united nations
educational, scientific
and cultural
organization

international atomic
energy agency

the
abdus salam
international centre for theoretical physics

SMR.1135 - 9

THIRD WORKSHOP ON
THIN FILMS PHYSICS AND TECHNOLOGY
(8 - 24 MARCH 1999)
including
TOPICAL CONFERENCE ON
MICROSTRUCTURE AND SURFACE MORPHOLOGY
EVOLUTION IN THIN FILMS
(24 - 26 MARCH 1999)

"Electron spectroscopies applied to thin film analysis"

Massimo SANCROTTI
Area di Ricerca
Laboratorio Nazionale TASC-INFM
Padriciano 99
34012 Trieste
ITALY

Trieste, Italy
The Abdus Salam ICTP
March 8-26, 1999

3rd Workshop on
Thin Films Physics and
Technology

ELECTRON SPECTROSCOPIES APPLIED TO THIN FILM ANALYSIS

Massimo SANCROTTI

Laboratorio Nazionale TASC-INFM
"Tecnologie Avanzate Superfici e Catalisi"
Istituto Nazionale per la Fisica della Materia
Padriciano 99, I-34012 Trieste, Italy
e-mail sancrotti@sci.area.trieste.it

and

Dipartimento di Fisica, Politecnico di Milano
Piazza L. da Vinci 33, I-20133 Milano, Italy

Trieste, Italy
The Abdus Salam ICTP
March 8-26, 1999

3rd Workshop on
Thin Films Physics and
Technology

OUTLINE

- Basic concepts on surface science
- Basic concepts on:
  - Photoemission spectroscopy
    Core levels & valence band states
  - Inverse photoemission
    Conduction band states
  - Auger electron spectroscopy
    Core-core-core transitions
    Core-core-valence transitions
    Core-valence-valence transitions
  - X-ray absorption spectroscopy
    Conduction band states
  - Low energy electron diffraction
  - Electron energy loss spectroscopy
    Valence & conduction band states

Surface Review and Letters, Vol. 2, No. 6 (1995) 859–883

QUALITATIVE AND QUANTITATIVE SURFACE ANALYSIS VIA X-RAY PHOTOEMISSION AND AUGER ELECTRON SPECTROSCOPIES

MASSIMO SANCROTTI*
Laboratorio Tecnologie Avanzate Superfici e Catalisi (TASC)
Istituto Nazionale per la Fisica della Materia (INFM)
Padriciano 99, I-34012 Trieste, Italy

1. Introduction

The last three decades have seen the birth and development of a wide variety of experimental techniques in solid-state research which share surface sensitivity as a key character.[1–5] These methods enable one to probe chemical and physical properties of solids in a spatial region confined to within a few atomic layers below the solid surface. This opportunity, which crucially benefited from the parallel advance of a wide series of technological areas such as electronic and vacuum industries, has ignited a progressively increasing number of fundamental and applicative researches on the peculiar properties of the surface and near-surface region of solids. At present, a set of these surface-sensitive techniques (SST) are routinely utilized over an unlimited series of technological domains encompassing metallurgic, electronic, chemical, and vacuum industries.

Depending on the specific technique, elemental and chemical information, surface morphology, surface topography, surface structure, or magnetic properties can be addressed. An in-depth understanding of a problem usually demands for the use of a combined series of SST such as photoemission spectroscopy, Auger spectroscopy, electron energy-loss spectroscopy, scanning tunneling microscopy and spectroscopy, secondary-ion mass spectroscopy, surface x-ray diffraction, electron diffraction, atom scattering, and x-ray absorption spectroscopy. Each of the SST is moreover characterized by specific figures of merit as far as, for example, the surface sensitivity, the spatial resolution, the elemental sensitivity and other significant parameters are concerned.

Whenever a solid interacts with a gas or liquid environment, like in corrosion, oxidation, and catalysis, the near-surface region of the solid plays a crucial role in determining the evolution of the process (Fig. 1). Thereby, an in-depth evaluation of the near-surface properties as a function of external parameters (temperature, chemical agents, humidity, etc.) is of major relevance to an understanding and a control of the technological applications.

However, SST can be of invaluable importance also in the characterization of processes occurring in the bulk of matter. This is, for example, the case of fracture and creep where nanosized segregations at grain boundaries of polycrystalline materials can govern the macroscopic behavior of massive matter (Fig. 1). In this case, SST can be applied to study fractured surfaces and find chemical species or compounds which can affect the macroscopic behavior.

Another field which is unavoidably linked to the use of SST is the synthesis of artificially structured materials spanning a wide variety of methods such as molecular beam epitaxy, ion implantation, ion-beam assisted deposition, and laser ablation (Fig. 1). For many of these applications, an evaluation of the growth process on a real-time scale and with atomic layer sensitivity is of fundamental importance, as

*Also at Dipartimento di Fisica, Politecnico di Milano, Italy.

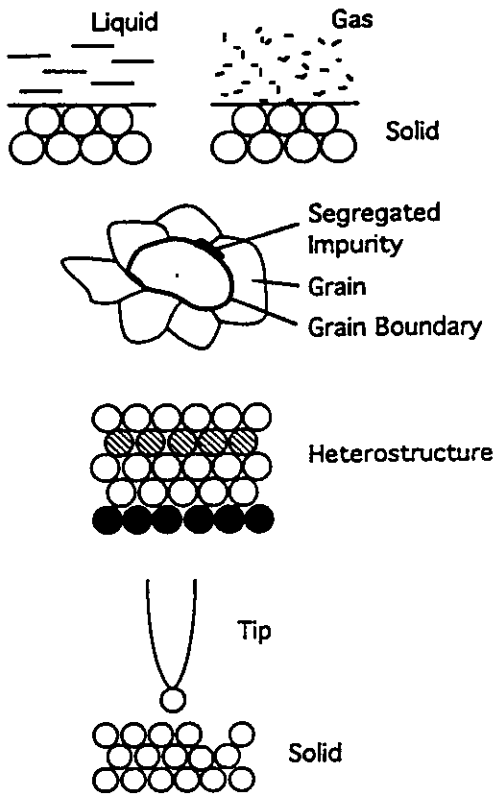

Fig. 1. Examples where SST can be usefully applied for studying surfaces and interfaces.

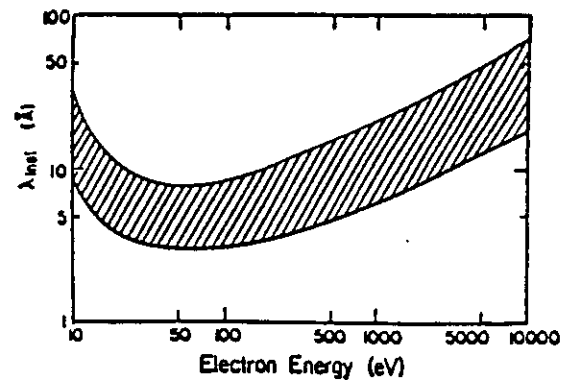

Fig. 2. Plot of the electron inelastic mean-free-path versus the electron kinetic energy. Shaded is the area where most of the experimental points measured from different solids fall.

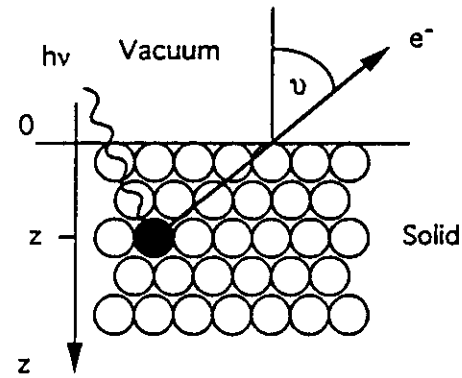

Fig. 3. Sketch of how an electron created at a depth z below the surface can escape from the solid.

well as a characterization *a posteriori* via SST combined with controlled erosion via ion sputtering.

What is moreover rapidly emerging is the possibility of using some SST for atomic manipulation and engineering at solid surfaces as can be done with the tips of scanning tunneling microscopes (Fig. 1).

In a simplified view, all SST are based on the excitation of a solid via particle bombardment and on the measurement of the response of the solid. In most cases, this response is the emission of particles whose properties (energy, charge, direction of emission, angular momentum, etc.) can be traced back to the properties of the solid. Surface sensitivity can be determined by differing causes. In the case of electron spectroscopies, surface sensitivity is mostly determined by the energy-dependent inelastic mean-free-path of electrons in solids (Fig. 2). Imagine an electron is excited at some energy value as a result of a specific excitation mechanism (Fig. 3). The probability that this energy is conserved is lower than one and depends on the path described by the particle within the solid. If $I_0(z)$ is the flux of electrons created at a selected depth (z) below the surface and at a specific energy value (E), the flux of electrons $[I(z)]$ which do not suffer an inelastic process prior to being emitted by the solid, and thereby conserving their energy, is related to z and the inelastic mean-free-path (λ) as follows

$$I(z) = I_0(z) \exp \frac{-z}{\lambda \cos \theta},$$

where θ is the angle of emission. It should now be clear that the exponential decay of the above formula makes a signal related to electrons of selected

energy more and more atenuated as electrons are created deeper in the solid, over a very wide energy range. If the final-state energy of the electrons is somehow tunable, as can be done in photoemission spectroscopy by tuning the excitation photon energy, one can control the degree of surface sensitivity.

It is worth mentioning that most of the SST require high-vacuum conditions for being operative. In the case of electron spectroscopies, this is primarily dictated by the limited number of inelastic scattering events that emitted electrons must suffer with the gas molecules of the residual gas prior to detection for not being sharply attenuated in intensity. Moreover, the full control of surface-science experiments imposes even more severe constraints that is to work in ultrahigh-vacuum conditions (10^{-11}–10^{-10} mbar range). On the basis of kinetic theory of gases and under the assumption that the sticking probability of a gas molecule at a solid surface is equal to one, it can be easily found that the adsorption of an atomic monolayer of molecules would be completed in 1 second at $\approx 1 \times 10^{-6}$ mbar. The lower the pressure, the longer the lifetime of a surface before being significantly contaminated.

Among the surface-sensitive experimental methods, x-ray photoemission spectroscopy (XPS) and Auger electron spectroscopy (AES) are easily recognized as the historical roots of the neverending development of SST and are also by far the most widely utilized techniques for both qualitative and quantitative analysis of solid surfaces. It is worth remarking that the large families of materials (single- and polycrystals, amorphous, adsorbates, polymers, conductors, semiconductors, insulators, etc.) can be fruitfully studied via XPS and AES, the only severe limitation being the vacuum compatibility of the specimen.

In this paper, we will give a survey of the basic principles, the instrumental aspects, and a selected set of applications of XPS and AES. The text is conceived as a primer for newcomers and a more profound level of understanding can be achieved in the quoted literature.

2. Basic Principles

2.1. *X-ray photoemission spectroscopy*

This technique[1–13] is based on the photoelectric effect. Figures 4 and 5 give a schematic view of a photoemission experiment along with the corresponding energy diagram sketched in a one-particle picture. Monochromatic photons are sent toward a solid and the emitted photoelectrons are analyzed in energy. This simplified view allows one to appreciate the inherent powerful characters of the technique. The distribution in energy (final-state kinetic energy) of the detected electrons (Fig. 5), which leave the system in a one-hole final state, is expected, to a first approximation, to mimic the distribution in energy of the occupied electron states in the ground state of the solid, the energy being conserved consistently with the following relation

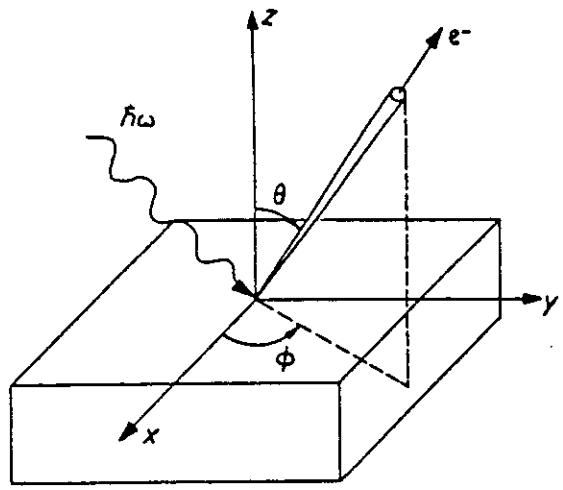

Fig. 4. Pictorial view of a photoemission experiment showing the impinging photon and the emitted electron.

$$E_f = h\nu - E_i - \Phi\,,$$

where E_f and E_i represent the final- and initial-state energies of the electron, respectively, $h\nu$ is the photon energy, and Φ is the solid work function.[14] Deviations from this simplified picture can occur and it will be described further below. Nevertheless, the real effectiveness of this technique stems essentially from the direct insight it can provide on the electronic structure (core levels and valence-band states) of a solid.

A real photoemission spectrum[15] is shown in Fig. 6. It is given as a function of the initial-state binding energy, consistently with the above formula. The measured profile is characterized by sharp structures which can be related to the atom and orbital

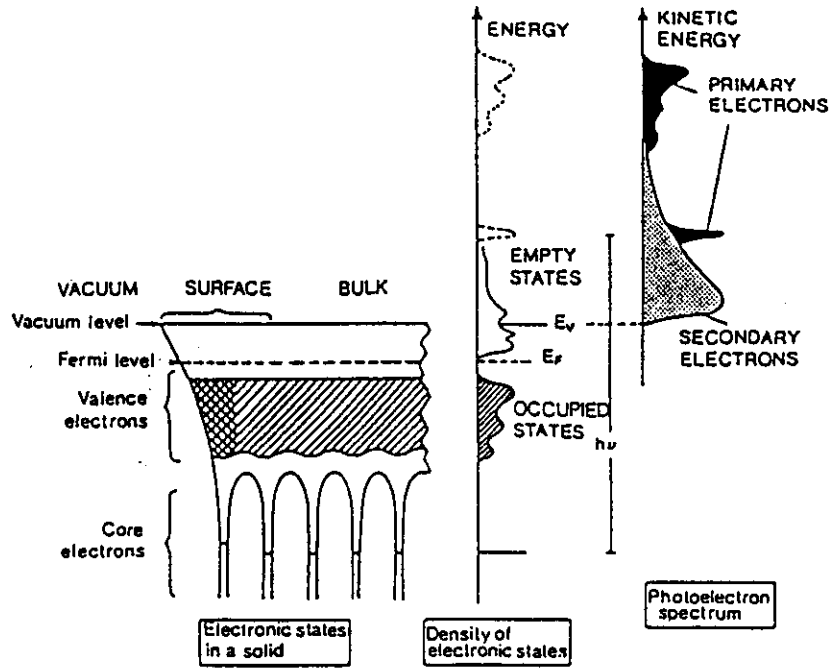

Fig. 5. Diagram of the energy levels relative to the ground state of a solid and a hypothetical photoemission spectrum where valence-band states and core levels are excited. E_V and E_F represent the vacuum level and the Fermi energy, respectively.

specific core levels. These features, usually called primary structures, are actually superimposed onto a mostly featureless background which exhibit a huge peak in the very low energy region ($\approx$ 5–10 eV) of the spectrum (see Fig. 5). This background is ascribed to the almost continuum distribution of the secondary electrons which are produced after inelastic scattering within the solid and have left memory of their primary energy. The excitation of most core levels requires at least soft x-rays and this explains the more usual acronym of the technique, i.e., x-ray photoemission spectroscopy (XPS). Also used is the acronym ESCA meaning electron spectroscopy for surface analysis.

The atom specificity of this technique is inherently related to the discreteness of the core-level energies in nature, i.e., each core-level distribution is a fingerprint of a specific chemical element. Handbooks[15,16] collecting XPS spectra for each elemental solid are currently available and are used as reference database for core-level identification.

A very important point which opens up the possibility for a profound understanding of the chemical state of an atom within a solid is related to the so-called *core-level shift* (CLS). Actually, a core-level binding energy depends on the chemical bonds and environment local to a specific atomic site. Thereby, if reference specimens are studied and quoted, the identification of the chemical state of an atom in *a priori* unknown solid system is made possible, consistently with the energy resolution and the actual size of the CLS. Figure 6 gives a list of core-level binding energies of Zr in a wide number of compounds.

Another key point for an analysis of the chemical state of a solid is related to the study of the energy distribution of the valence-band states. The typical feature of these shallow states, is their delocalized character, compared to the local nature of core levels. They are thus expected to markedly change their distribution in energy as the chemical bonds are changed.

In a one-particle framework, given an impinging flux of photons, the current density of photoelectrons can be expressed in terms of a Fermi golden rule formula where the matrix element, in the dipole approximation, can be written as

$$M_{fi} = \langle \Psi_f | \mathbf{A} \cdot \mathbf{p} + \mathbf{p} \cdot \mathbf{A} | \Psi_i \rangle ,$$

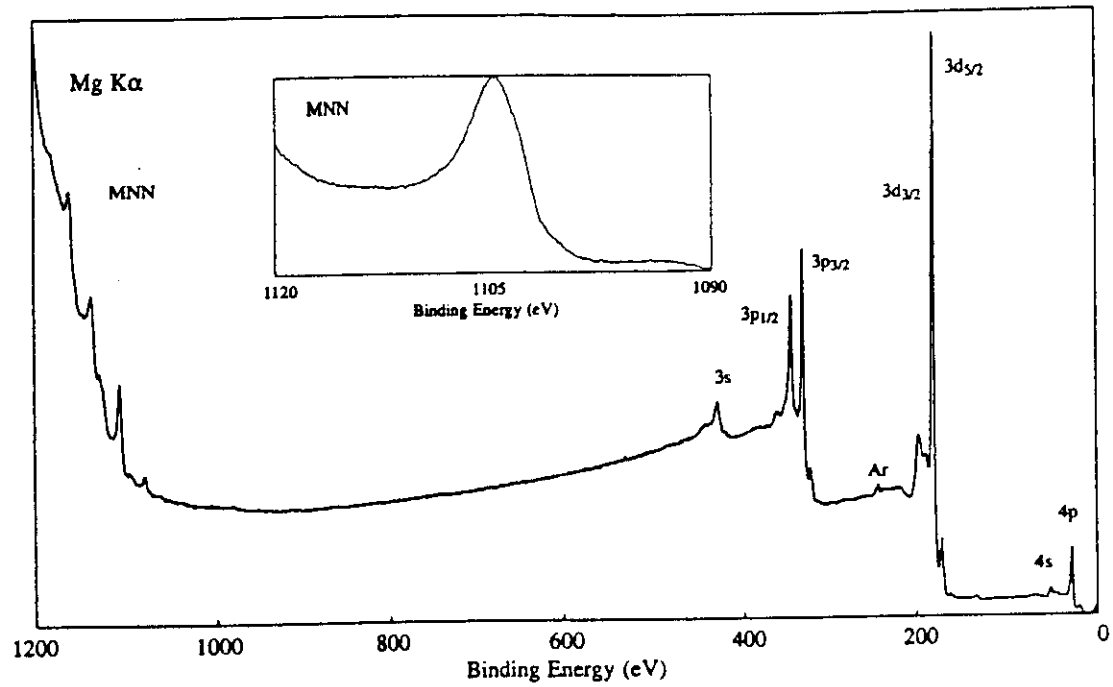

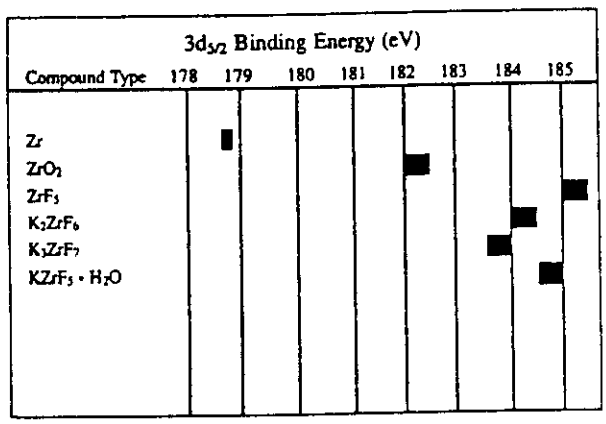

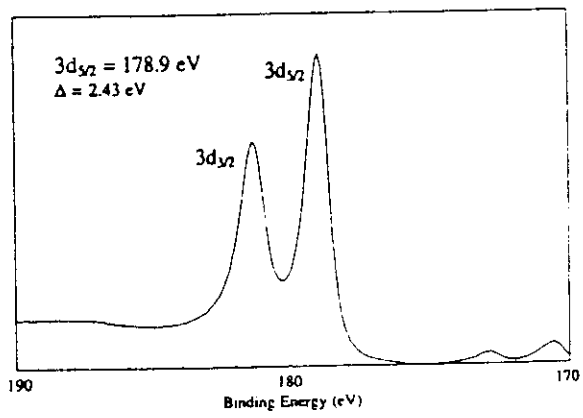

Fig. 6. Reference XPS spectrum excited from solid Zr with a Mg-anode x-ray source ($h\nu = 1253.6$ eV). Also shown are an expanded view of the spin–orbit split Zr-3d core-level emission and a table indicating the Zr-$3d_{5/2}$ core-level binding energy for a set of Zr compounds.

where Ψ_f and Ψ_i are the final- and initial-state electron wave functions, respectively. **A** is the electromagnetic vector potential, and **p** is the electron momentum.

The quantitative character of the technique resides in the behavior of the core-level photoionization cross sections. If a specific value of photon energy is selected, the probability of core-level photoemission for incident photon depends on the specific core level of the specific atom under study. This is shown, for example, in Fig. 7 where calculated cross sections are reported[17] for Yb. The relative intensities of core-level photoemission peaks for say element A and element B in *a priori* unknown composition, should thereby reflect the relative atomic concentrations of these elements in the spatial region of the solid probed via XPS, once the behavior of the corresponding core-level cross sections is known.

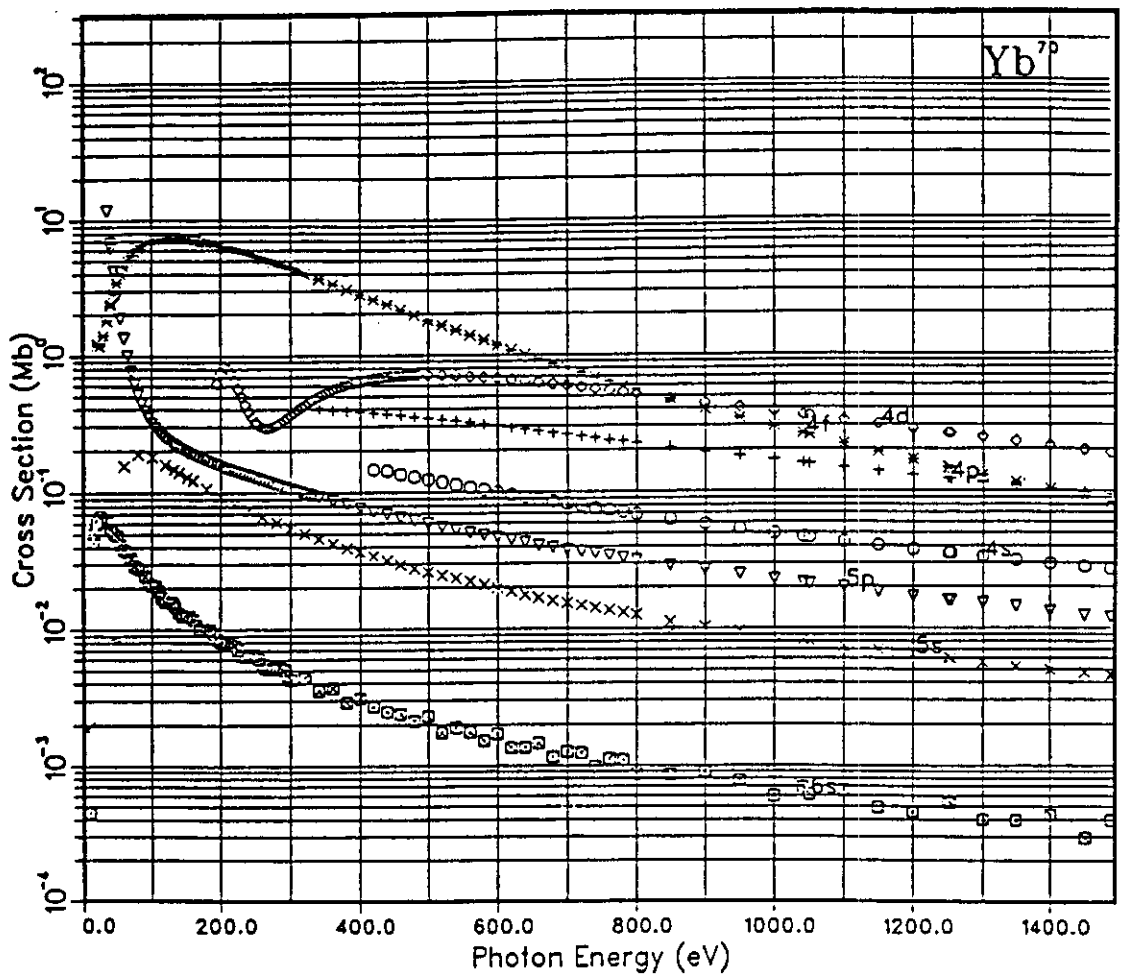

Fig. 7. Calculated photoionization cross sections for a set of Yb core levels in atomic Yb as a function of the photon energy.

2.2. *Auger electron spectroscopy*

Figure 8 depicts a view of the energy-diagram scheme relative to an Auger de-excitation process.[1–5,7,12,13,18–21] The starting point is to create a core hole inside the solid leaving an atomic site in an ionized state. This condition can be attained bombarding the solid with electrons, photons, ions, or other particles. The de-excitation of the system can occur along two distinct and competing processes: (i) an electron on a more shallow energy level can collapse over the core hole emitting a photon consistently with the fluorescence mechanism and leaving the system with $(N-1)$ electrons; (ii) an electron at lower binding energy can refill the initially created core hole, the energy of this electronic transition being transferred to another electron. Provided the

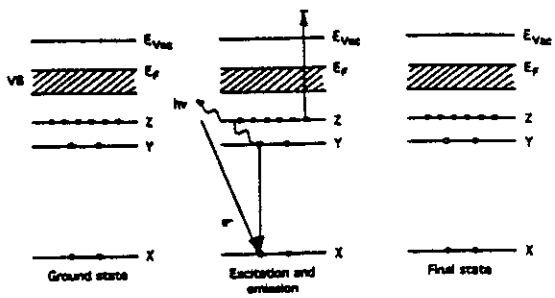

Fig. 8. Pictorial view of an energy-level scheme for an atom in a solid in its ground state (left), after creating a deep core hole and subsequent electron emission (center), and in the two-hole final state (right).

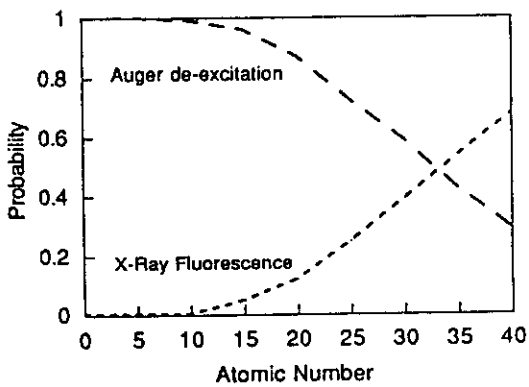

Fig. 9. Plot representing the Auger de-excitation probability and the x-ray fluorescence probability after creating a K hole as a function of the atomic number.

energy of the thus-excited electron falls above the vacuum level and the particle is able to escape from the solid, the electron is called an Auger electron and the overall de-excitation mechanism is called Auger process. The relative probability of the fluorescence versus Auger processes are plotted in Fig. 9 as a function of the atomic number (Z) for initial K core hole. The lower the atomic number, the higher the Auger yield.

In Auger spectroscopy, the system is left with two holes in the final state. The nomenclature of Auger spectroscopy indicates the transition with the sequence of the involved energy levels, say XYZ for the scheme of Fig. 8. The labeling of the energy levels is the same typically used in x-ray spectroscopy and

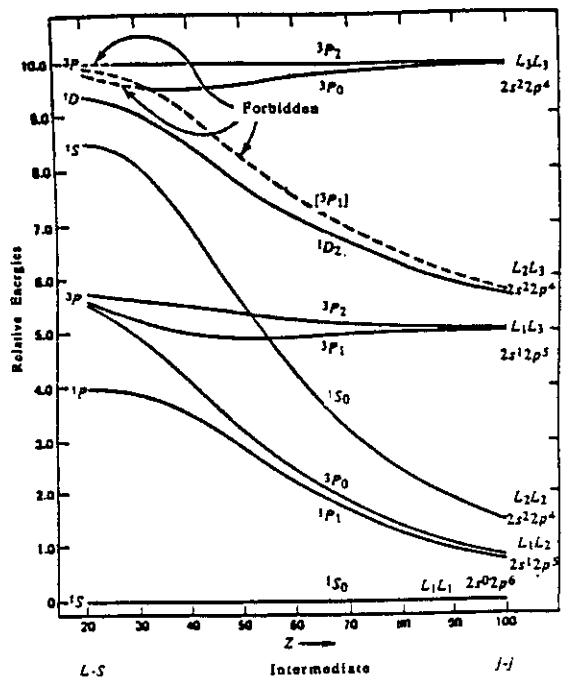

Fig. 10. Relative energies in the KLL Auger series. Also indicated is the transition from L–S to j–j coupling through intermediate coupling.

can change along with the atomic number depending on which scheme (j–j versus L–S versus intermediate) is more appropriate for the addition of the angular momenta of the electron states. (See Fig. 10 for Ref. 1.) The Auger process is characterized by the conservation of energy, angular momentum, and parity for the N-particle system. To a first approximation, the expression of the energy conservation is given below

$$E_{XUZ} = E_X - E_Y - E_Z - \Phi\,,$$

where E_X, E_Y, and E_Z are the one-particle core-level binding energies, E_{XUZ} is the Auger electron energy measured with respect to the vacuum level, and Φ is the solid work function. However, final-state effects can play a significant role. Therefore, corrections to the above formula are included such as

$$E_{XUZ} = E_X - E_Y - E_Z - \Phi - F_{YZ} + R_{YZ}\,,$$

where F_{YZ} and R_{YZ} represent a two-final-state correlation energy and a final-state relaxation energy (including intra- and extra-atomic contributions), respectively.

By relying on the one-particle electron scheme of Fig. 8, it should be clear that the distribution in energy of the emitted Auger electrons should be somehow reminiscent of the discrete distribution in energy of the electron states in the solid. Thereby, Auger spectroscopy is immediately recognized to be elemental sensitive. Handbooks with standard Auger spectra from elemental solids are currently available. In Fig. 11 a table with the principal Auger transitions is reproduced.[22]

Core-level chemical shifts are also expected to play a role in the Auger spectroscopy thereby providing, in principle, the chemical sensitivity to this technique. This means that Auger lines are to be measured for a wide series of standard elemental and compound solids for identification of the chemical

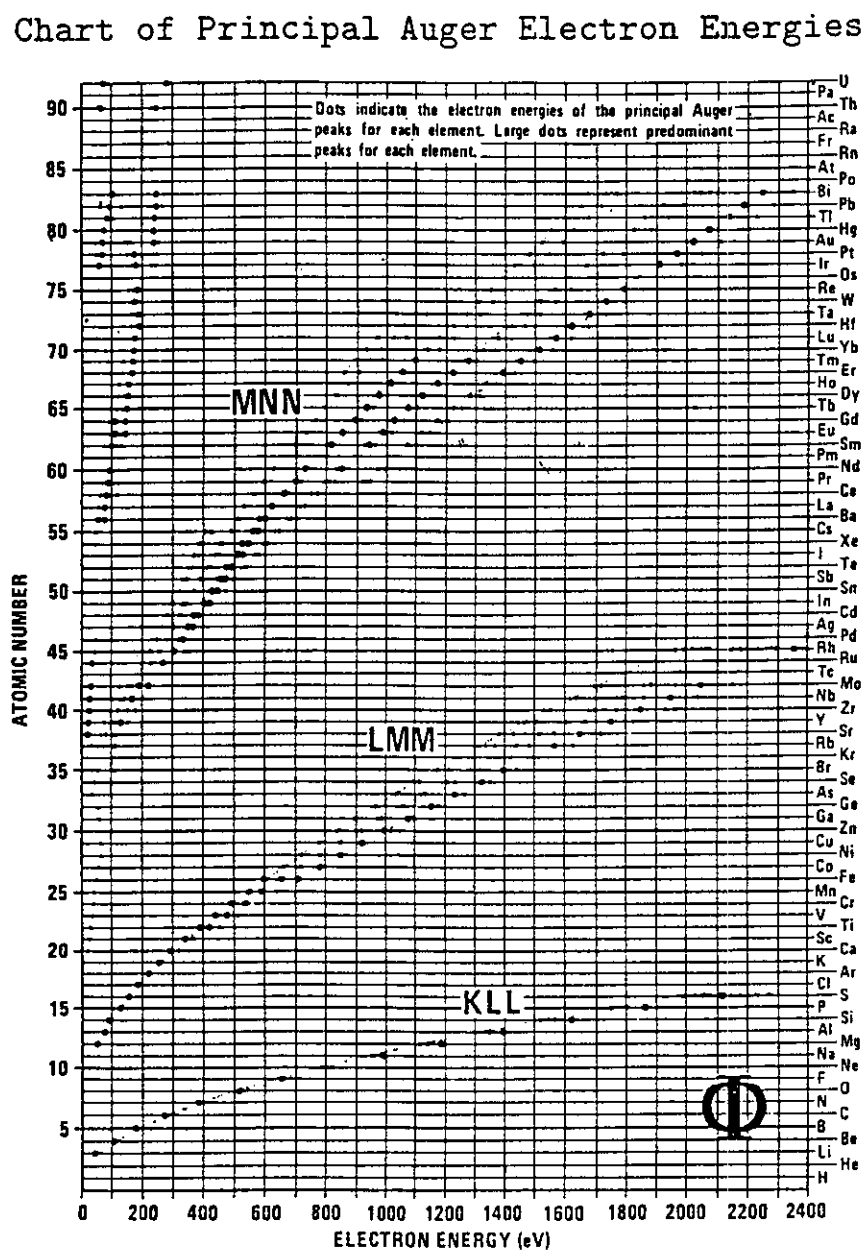

Fig. 11. Table of the principal Auger electron energies as a function of the atomic number.

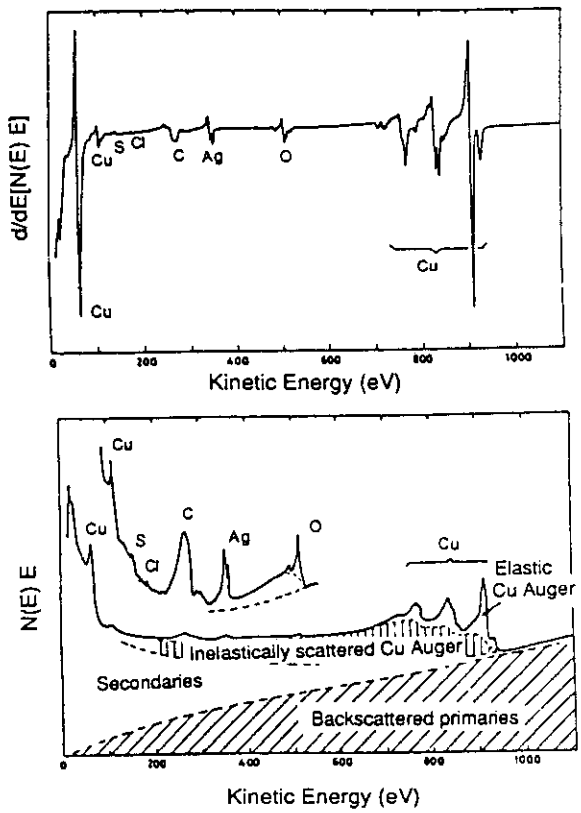

Fig. 12. Auger spectra from a contaminated Cu specimen as measured via pulse counting and derivative detection.

state of a specific element in an *a priori* unknown system. Chemical sensitivity will also be discussed further below in connection with Auger transitions involving valence-electron states.

An Auger spectrum from a contaminated Cu specimen[12] is shown in Fig. 12. Likewise the case of XPS, the corresponding spectroscopic features are superimposed on a secondary-electron background. Strictly speaking, Auger electron are secondary electrons as well. For the sake of clarity, they are usually referred to as elastic secondary electrons whereas the electrons which have lost memory of their initial excitation energy are called inelastic secondaries.

It is worth noting that the final-state energy of Auger electrons do not depend on the energy and on the nature of the particles used for creating the initial core hole. The ionizing particles can be classified depending on their ionization cross section. This is shown in the case of electrons in Fig. 13 where the

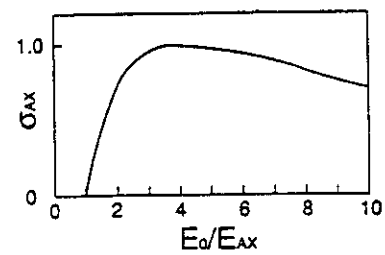

Fig. 13. Cross section of core-hole creation by electron impact as a function of the primary-beam energy (E_0) normalized to the core-hole energy (E_{AX}) for a set of selected species.

cross section for ionizing a core level is plotted as a function of the primary-electron energy normalized to the core-hole threshold. It is easily concluded that the best condition corresponds to selecting a primary energy approximately three times the core-hole energy.

Auger transitions are also classified as to the localized versus delocalized nature of the involved electron states. It is usual to distinguish between core–core–core (CCC), core–core–valence (CCV), and core–valence–valence (CVV) transitions depending on whether the electrons are core or valence electrons. We will come back to this point further below.

The Auger process is governed by a matrix element which can be expressed in the following way

$$M_{fi} = \langle f|H'_A|i\rangle\,,$$

where the final- and initial-state vectors $|f\rangle$ and $|i\rangle$ can be represented in a two-particle picture as $|\Psi_Y\Psi_Z\rangle$, $|\Psi_X\Psi_\lambda\rangle$, respectively. H'_A is the Hamiltonian describing the Auger transition which in the nonrelativistic limit becomes a Coulomb term. Ψ_λ refers to the Auger electron.

Since the Auger effect is a three-level transition and leaves the system in a doubly ionized state, multiplet effects are expected to dominate the energy distribution of the emitted Auger electrons, especially for CCC processes. This is, for example,[23,24] shown in Fig. 14. The nature of the matrix element dictates the character of the CCC transitions which is predominantly intra-atomic.

What makes Auger spectroscopy a quantitative method is the direct relation between the intensity of an Auger spectral feature and the number of

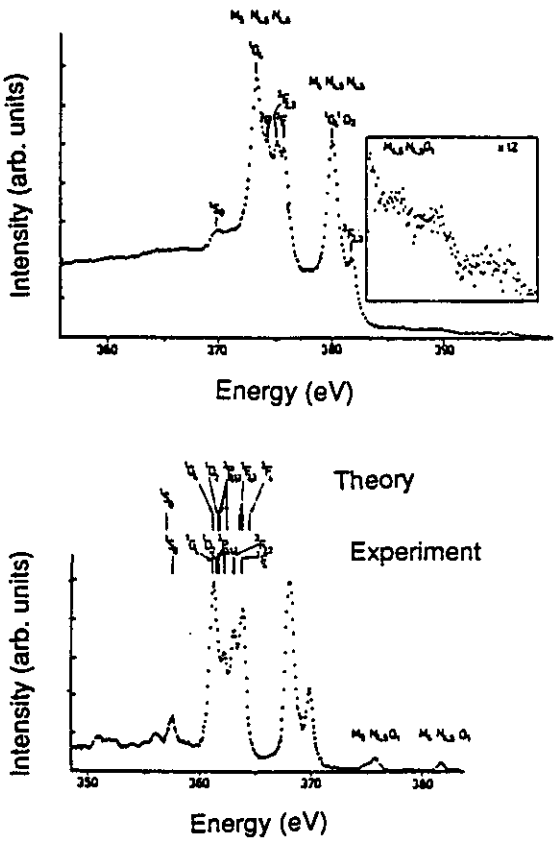

Fig. 14. Auger spectra of solid and vapor cadmium. The vertical bars represent the terms of the calculated multiplet distributions.

atoms supporting the Auger transitions through the transition-specific cross section. Similarly to the XPS case, atomic concentrations can be determined relative to the limited spatial volume which is probed by the surface sensitivity of the technique.

Of special importance are Auger transitions involving one or two valence-electron states. In a simple-minded scheme, the energy distribution of CCV or CVV Auger electrons is expected to mimic the valence density of states or the self-convolution of the valence density of states, respectively. See Fig. 15, for reference. More precisely, (i) the presence of a core-level wave function in the matrix element makes the valence density of states to be probed local to the atomic site where the initial core hole is created; (ii) the matrix element acts as a filter for the relative weights of the Auger structures depending on the angular momentum of the valence-band

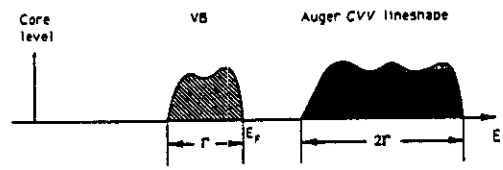

Fig. 15. Pictorial view of a one-particle energy-level scheme for a solid and the expected spectral distribution for a *CVV* Auger transition assuming a pure band-like picture.

states. This property of CCV or CVV line shapes yields additional chemical sensitivity to Auger spectroscopy. Deviations from the above picture can arise from the two-hole final state of the transitions. Let us therefore focus onto CVV line shapes whose cross sections are usually stronger than CCV transitions. Empirically speaking, there are many CVV transitions which can be successfully interpreted in terms of the density-of-states picture whereas other CVV line shapes resemble more closely the Auger response typical of free atoms where multiplet effects do play a dominant role. On a qualitative basis, it is reasonable to expect that, whenever the two holes left in the final state cannot efficiently delocalize from the ionized site, the electronic structure local to the Auger site can be significantly perturbed up to the breakdown of the Bloch theorem. The atom supporting the Auger transition can be envisioned as an impurity in the host solid with a peculiar local electronic structure. This will in turn determine an Auger response closer to that of free atoms. A general theory predicting the actual Auger CVV line shapes from solids is still lacking. However, in the late seventies a theory[25,26] has been formulated for filled band systems and is referred to as the Cini–Sawatzky theory. The criterion yielded by this theoretical approach can be schematized as follows

$$\Gamma \gg U_{\mathrm{h\text{-}h}} \qquad \text{band-like limit},$$

$$\Gamma \ll U_{\mathrm{h\text{-}h}} \qquad \text{atomic-like limit},$$

where Γ is the valence-bandwidth and $U_{\mathrm{h\text{-}h}}$ is the two-hole correlation energy. The band-like limit is typical of covalent systems while the atomic limit is often encountered in d-metals. The case of the Si-$L_{2,3}VV$ line shape in solid Si is shown[27] in Fig. 16 along with two theoretical predictions. The validity

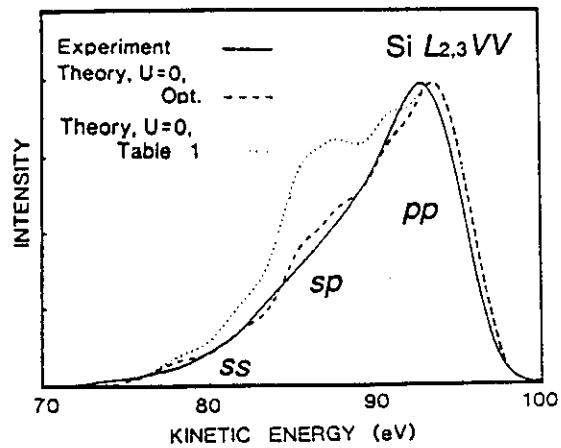

Fig. 16. Experimental Si-$L_{2,3}VV$ Auger line shape from solid silicon and theoretical spectral distributions calculated by setting the two-hole final-state energy equal to zero and by utilizing different sets of matrix elements.

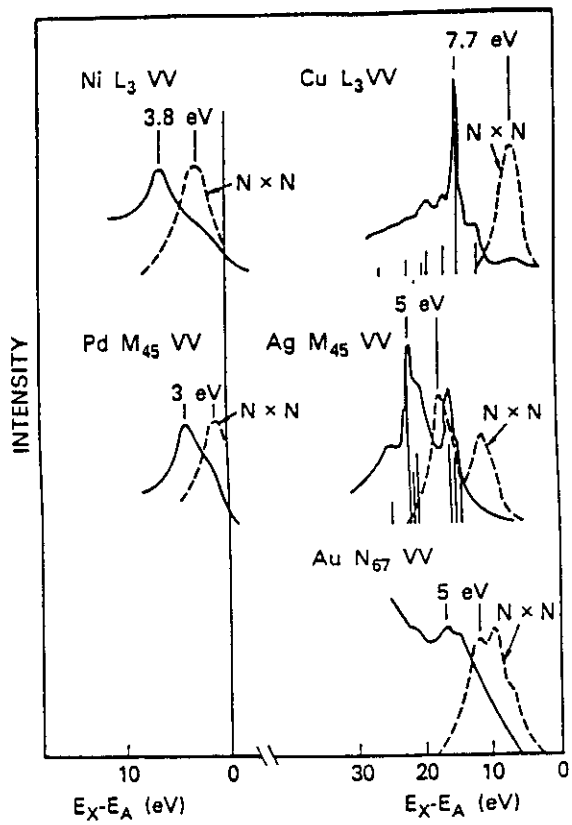

Fig. 17. Experimental CVV Auger line shapes from solid quasinoble and noble metals. Also indicated (dashed line) are the self-folded valence density of states ($N \times N$). The vertical bars (Cu and Ag) represent terms of multiplet distributions as predicted in an atomic-like calculation. The energy scale is the so-called two-hole final-state energy scale. E_X and E_A indicate the core-hole binding energy as determined via XPS and the measured Auger kinetic energy, respectively.

of a band-like approach is quite clear. Also noticeable is the role of the matrix elements in determining the relative weights to the main structures. In Fig. 17 a significant selection of experimental CVV Auger line shapes of d-metals[20] is compared with self-folded local density of states. Note the element-specific agreement versus disagreement of this comparison. The behavior of Γ and U_{h-h} in a selection of transitional metals[20] is given in Fig. 18.

2.3. *Extra-contributions to XPS and AES profiles*

Features other than the mentioned primary structures of XPS and the elastic secondary Auger features are usually found in experimental spectra. Moreover, the real line shapes are also affected by a wide series of effects. An understanding of these aspects is of fundamental importance for a reliable line-shape analysis. A significant selection of such effects is given[28] in Fig. 19 and is briefly discussed here. (i) *Lifetime broadening* – all electron spectroscopies measure the system in an excited state of finite lifetime. This is unavoidably reflected in the finite broadening of the lines according to the Heisenberg uncertainty principle. A wide number of core-hole lifetimes has been quoted in the literature. (ii) *Phonon broadening* – the vibrational motion of atoms in the solid occurs usually on a time scale longer than the temporal interval of the spectroscopic excitation. Thereby, atoms are probed in an infinite series of inhomogeneous positions during the acquisition of an XPS or AES spectrum. This is reflected in a Gaussian broadening of the final-state line shape. (iii) *Loss-induced broadening* – the excited electrons can promote inelastic scattering events while propagating in the solid such as excitation of plasmon modes of the Fermi gas or valence–to–conduction band state transitions. The result is typically the presence of extra features in the XPS or AES response. (iv) *Core-level asymmetry* – it is related to the many-body response of the solid to

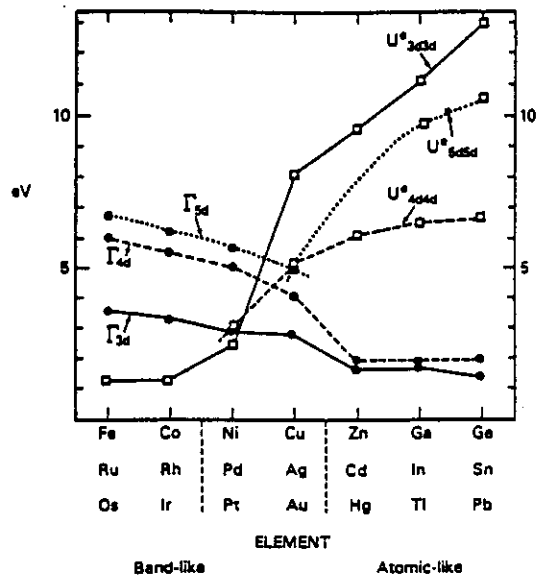

Fig. 18. Survey of the d valence-band state width (Γ_{nd}) and of the two-hole final-state correlation energy (U_{nd-nd}) for a wide selection of transitional metals. Also indicated are the regions where the pertinent CVV Auger line shapes are closer to the band-like versus atomic-like limit.

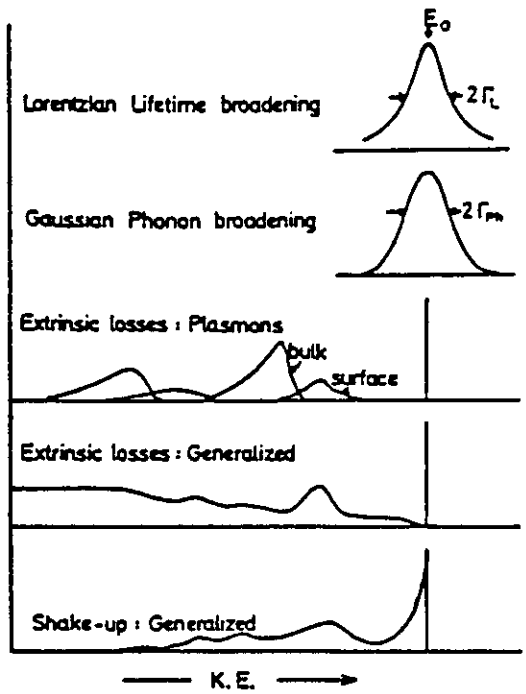

Fig. 19. Schematic view of the main processes which can affect the final line shape of a core-hole-excited experiment.

the creation of a core hole and it is the stronger the higher the density of states at the Fermi level. It is a typical marker of metallicity.

3. XPS Core-Level Line-Shape Fitting

A variety of fitting procedures has been proposed and utilized.[12] Regardless of the specific method of core-level fitting, some general remarks can be put forward.

A singlet contribution is expected from spherically symmetric orbitals for each of the homogeneous sites of a specific element in a solid. Orbitals of other than s-symmetry contribute with a spin–orbit split doublet. An exception to this scheme is the case of the shallow 4f states in the rare earths, where the partial filling of the orbitals is responsible of significant multiplet effects in the ionized final state.

Core-level fitting is usually accomplished via Voigt profiles which properly include both Lorentzian (lifetime) and Gaussian (phonons, instrumental width) broadening effects. Most of the fitting procedures also include the secondary-background line. Various models have been proposed for the secondaries profile.

As in any fitting procedure, the results must be critically examined. Any experimentalist is invited not to consider the recipes used for the core-level fitting as black boxes with *a priori* legitimate income and outcome. This means that for each core level, different choices of parameters must be explored. A fitting procedure will be considered reliable not only in terms of statistical criteria but also by checking whether the general trends emerging as outcome are crucially affected by small variations of the parameters.

4. Quantitative Analysis

It is not our intention to cover all the detailed aspects of quantitative analysis based on XPS or AES. For this, the reader is referred to monographs or review papers. Here, we just limit ourselves to give the fundamental elements for this analysis.

Assume we have an homogeneous multielement solid. The basic idea is that the intentisy I_i of an element-specific spectral feature is proportional to

Atomic Sensitivity Factors X-ray Sources at 90°

Element	Line	ASF	Element	Line	ASF	Element	Line	ASF	Element	Line	ASF
Ag	3d	5.198	Eu	4d	2.210	Na	1s	1.685	Si	2p	0.283
Al	2p	0.193	F	1s	1.000	Nb	3d	2.517	Sm	$3d_{5/2}$	2.907
Ar	2p	1.011	Fe	2p	2.683	Nd	3d	4.697	Sn	$3d_{5/2}$	4.095
As	3d	0.570	Ga	$2p_{3/2}$	3.341	Ne	1s	1.340	Sr	3d	1.578
Au	4f	5.240	Gd	4d	2.207	Ni	2p	3.653	Ta	4f	2.589
B	1s	0.159	Ge	$2p_{3/2}$	3.100	O	1s	0.711	Tb	4d	2.201
Ba	4d	2.627	Hf	4f	2.221	Os	4f	3.747	Tc	3d	3.266
Be	1s	0.074	Hg	4f	5.797	P	2p	0.412	Te	$3d_{5/2}$	4.925
Bi	4f	7.632	Ho	4d	2.189	Pb	4f	6.968	Th	$4f_{7/2}$	7.498
Br	3d	0.895	I	$3d_{5/2}$	5.337	Pd	3d	4.642	Ti	2p	1.798
C	1s	0.296	In	$3d_{5/2}$	3.777	Pm	3d	3.754	Tl	4f	6.447
Ca	2p	1.634	Ir	4f	4.217	Pr	3d	6.356	Tm	4d	2.172
Cd	$3d_{5/2}$	6.032	K	2p	1.300	Pt	4f	4.674	U	$4f_{7/2}$	8.476
Ce	3d	7.399	Kr	3d	1.096	Rb	3d	1.316	V	2p	1.912
Cl	2p	0.770	La	3d	7.708	Re	4f	3.327	W	4f	2.959
Co	2p	3.255	Li	1s	0.025	Rh	3d	4.179	Xe	$3d_{5/2}$	5.702
Cr	2p	2.201	Lu	4d	2.156	Ru	3d	3.696	Y	3d	1.867
Cs	$3d_{5/2}$	6.032	Mg	2s	0.252	S	2p	0.570	Yb	4d	2.169
Cu	2p	4.798	Mn	2p	2.420	Sb	$3d_{5/2}$	4.473	Zn	$2p_{3/2}$	3.354
Dy	4d	2.198	Mo	3d	2.867	Sc	2p	1.678	Zr	3d	2.216
Er	4d	2.184	N	1s	0.477	Se	3d	0.722			

Fig. 20. Table of relative XPS atomic sensitivity factors for the main core-line emissions. In this scale, the reference value is the sensitivity factor of fluorine which is set equal to one.

the flux F of incident particles (photons in XPS, photons or electrons in AES), the atomic concentration of the ith species, the cross-section (σ_i) of the spectral transition under examination, and the transmission function (T) of the instrumental apparatus for the corresponding energies. Moreover, this must be thought of as confined in the limited spatial volume sampled through the inelastic mean-free-path of the corresponding XPS or AES electrons. Joint analysis of the most intense spectral features for each element detected in a specific XPS or AES spectrum should allow one to determine the relative atomic concentrations in the solid.

An easier aproach makes use of the so-called sensitivity factors (s_i for the ith element). Tables of atomic sensitivity factors are given in Figs. 20 and 21 for XPS[15] and AES,[22] respectively. These factors are usually referred to a specific spectrometer operated in a well-defined mode, e.g., constant versus varying energy resolution, and are based on reference measurements made on elemental solids in well-controlled conditions. These factors include *ab-initio* cross-section effects. The evaluation of the atomic concentrations (x_i) is thus performed along the following formula for the ith element

$$x_i = \frac{\frac{I_i}{s_i}}{\sum_j \frac{I_j}{s_j}},$$

where the summation is performed over all the species detected in the specimen and I_i represents the spectroscopic intensity of the ith element.

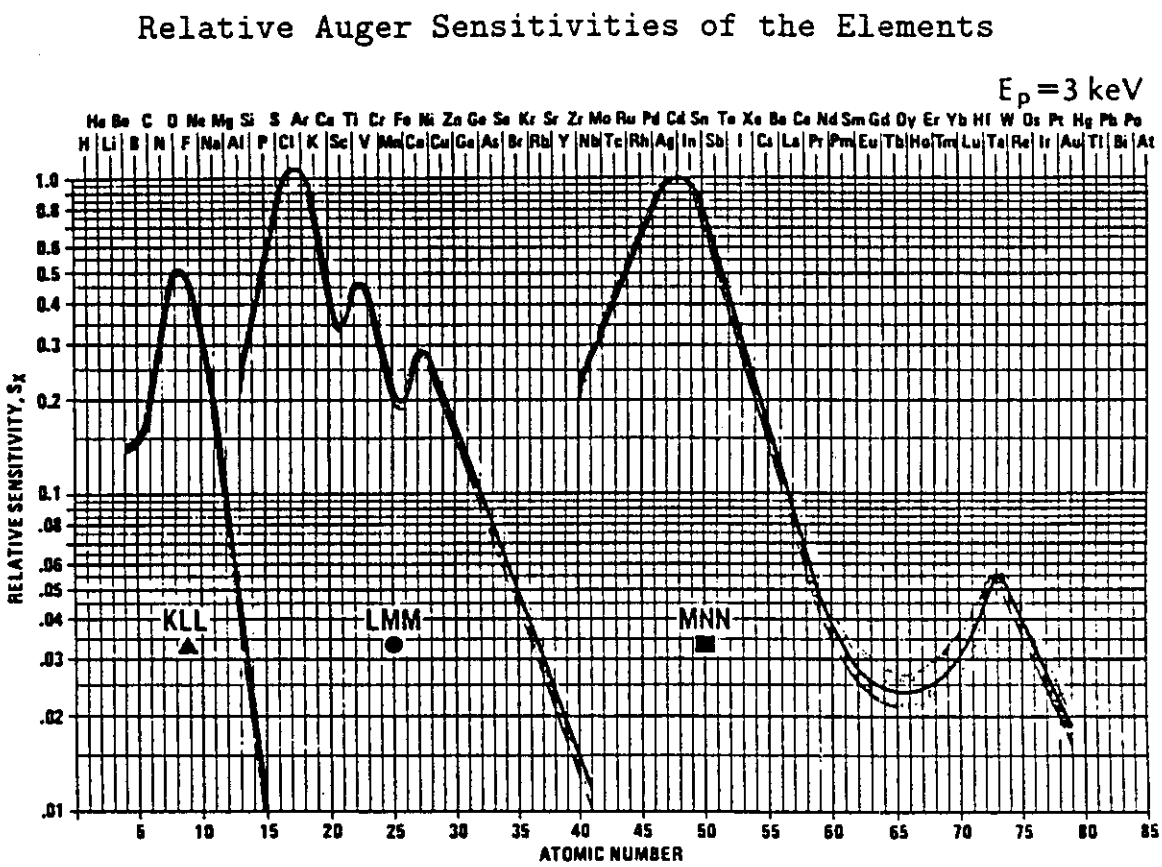

Fig. 21. Relative Auger sensitivity factors for various families of Auger transitions.

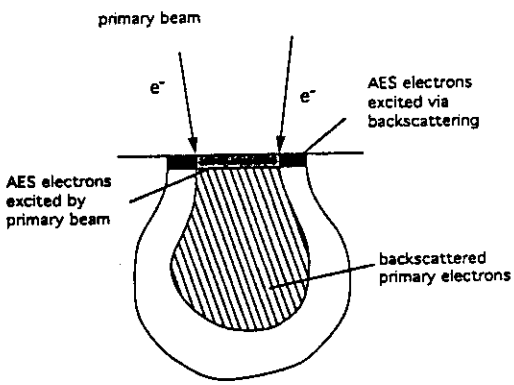

Fig. 22. Pictorial view of the spatial distribution of an electron beam after impinging a solid surface.

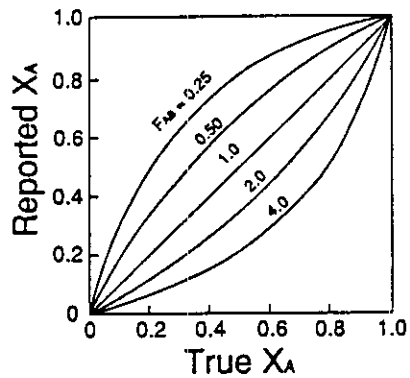

Fig. 23. Comparison of the real composition and that estimated ignoring matrix effects in a binary solid.

Various factors other than those already mentioned can affect the experimental intensity of the ith species in a solid. Just to make an example, Auger electrons in electron-excited spectra can be significantly produced by high-energy electrons backscattered well below the near-surface region (see Fig. 22).

The backscattering process depends unfortunately on the matrix and this poses limitations to the above-illustrated scheme. Figure 23 shows real versus reported atomic concentrations in homogeneous binary systems for different values of the matrix factor which includes the just-mentioned backscattering effect. For more details, see Ref. 12.

5. Instrumentation

Some instrumental elements needed for both XPS and AES are the same: (i) an UHV apparatus; (ii) a sample with related *in-situ* preparation facilities; (iii) an electron-energy analyzer; (iv) an electron detector; (v) a pulse-counting electronics; and (vi) a computer driving the instruments.

The excitation source can be different. XPS is based on photon sources while AES is primarily utilized in the electron-excited version therby needing an electron gun. For this latter application, a current signal is more usually detected and this implies the use of phase-sensitive lock-in amplifiers.

A schematic picture of an electron spectroscopy experiment is shown in Fig. 24. For the UHV technology and related apparatus the reader is referred to Refs. 12 and 29. Hereafter, we will provide some details concerning photon and electron sources, and electron-energy analyzers.

5.1. *Photon sources*

Most of the commercial photon sources are based on either gas discharges for UV photons or electron bombardment of properly chosen anodes for soft x-rays. An example of an anode-based x-ray source is given in Fig. 25. A hot filament is usually the source of thermally emitted electrons which are then accelerated toward the anode. A thin window is usually inserted between the anode and the sample for cutting a significant fraction of the continuum bremsstrahlung radiation and preventing electrons from reaching the sample. In Fig. 26, a selection of the most promising lines provided by nature is given along with their natural width. It is noteworthy, that the charging effects which typically occur when doing photoemission of insulators are usually neutralized by low-energy electron beam sent toward the specimen surface.

Of fundamental and progressively increasing importance is the use of storage rings used as synchrotron radiation sources. The key features of these sources are (i) the continuum distribution of photon energies which can be properly selected by inserting a monochromator prior to the analysis chamber; (ii) the polarization of the synchrotron light whose electric-field vector is naturally parallel to the plane of the storage-ring orbit. Right-hand or left-hand circular polarization can be achieved by working

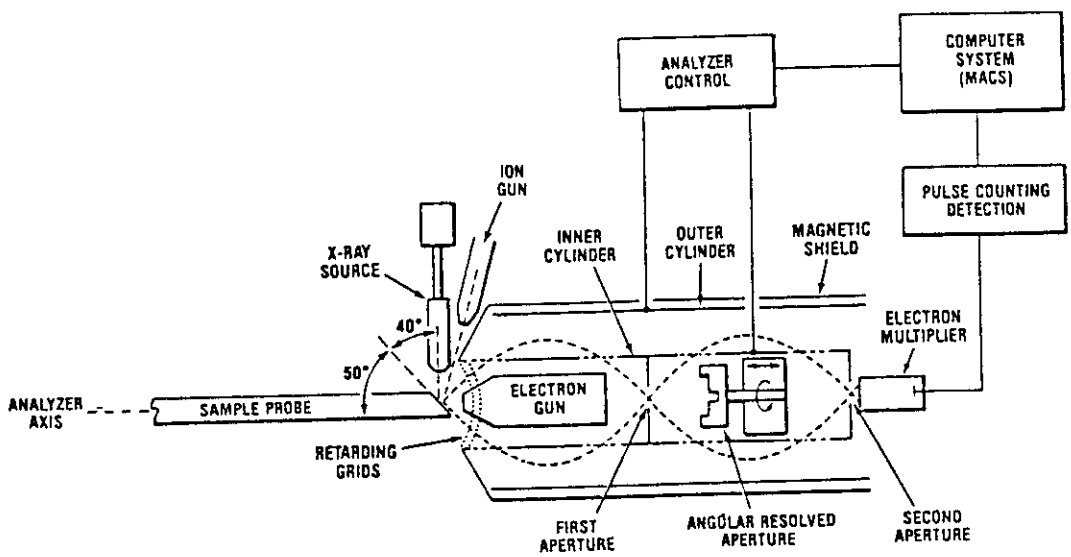

Fig. 24. Pictorial view of a surface-science spectroscopic experiment.

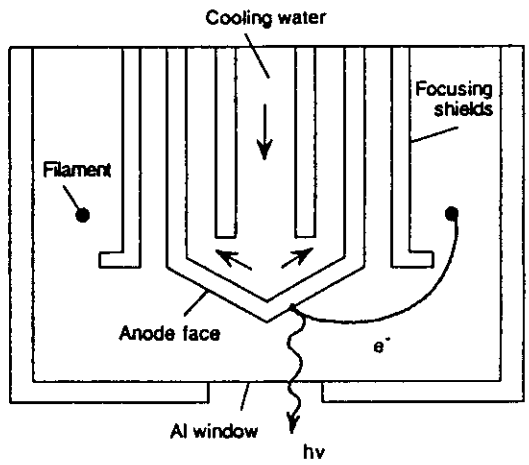

Fig. 25. Schematic view of an anode-based x-ray source.

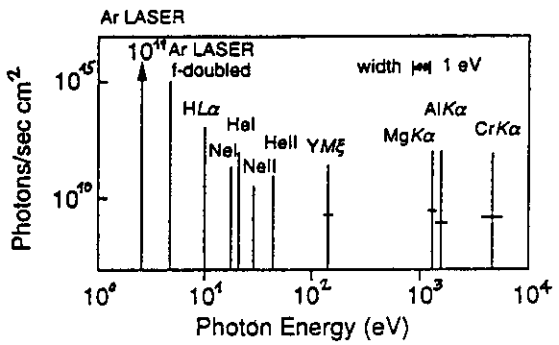

Fig. 26. A significant selection of characteristic UV and x-ray lines provided by nature.

in off-plane geometry; (iii) the high flux of photons achievable over a very wide photon energy range; (iv) the high brilliance of the photon beams. This is crucially important for high energy-resolution experiments and spectromicroscopy. The recent use of insertion devices in storage rings has allowed an advance in the achievements of most of the above-mentioned parameters as is reported in some papers in this volume.

5.2. *Electron sources*

Strictly speaking, AES poses less severe constraints to the design and construction of electron sources rather than other electron-excited spectroscopies such as electron energy loss and inverse photoemission. Actually, an ultrahigh energy resolution is not required, the energies of Auger electrons not being determined by the excitation source. Typically, a beam with good stability in intensity and a fine spot are required. Most of the electron guns use thermionic emitters. Also used are emission-field sources.

5.3. *Electron-energy analyzers*

Various families of analyzers have been designed and constructed. They are usually classified along with the specific trajectory the electrons describe. The mostly utilized analyzers are the double-cylindrical-mirror analyzer (CMA) and the hemispherical analyzer (HSA). Both of them can work for XPS and AES. The latter is fruitfully used when angular resolution is required as for angle-resolved UPS or photoelectron or Auger electron diffraction experiments. Electron-energy analyzers have been recently designed allowing one to target spectromicroscopy by selecting small areas of the photoelectron-emitting specimens.

6. Applications

Here, a selected set of scientific cases will be given for showing the potential of the XPS and AES techniques in studying problems in surface and interface sciences. The possibility of addressing elemental and chemical aspects of any kind of solid material (single- vs poly-crystals; chemisorbed and variously surface-treated systems), being limited just for the vacuum compatibility, should be appreciated. For more details concerning the examples which will be shown, the reader is referred to the original literature. The following overview is far from being complete but it should in any case be considered a good starting point for a further thorough examination.

Before we continue, it is worth mentioning the typical figures of merit of XPS and AES. For XPS, the constraints on energy resolution reside in the photon source (best values achieved so far: ≈ 0.3 eV for commercial apparatus; $\approx$ 0.02–0.05 eV at synchrotron sources). The best lateral resolution attained so far is of the order of 5 μm for commercial apparatus and tens of nanometer at synchrotron beamlines. The elemental sensitivity amounts to

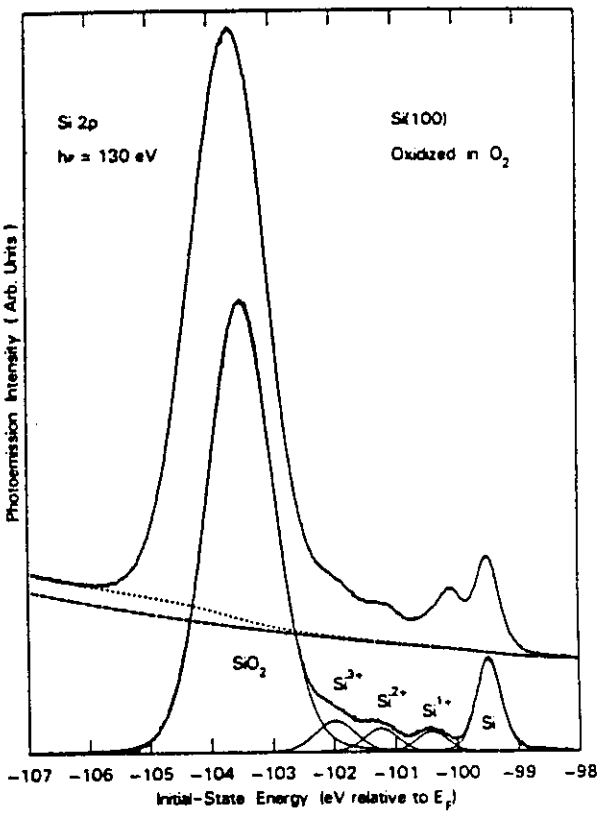

Fig. 27. Oxidation states at the SiO_2/Si(100) interface, as measured by the Si 2p core levels. The top curve represents the raw data. The bottom curve has the Si-$2p_{1/2}$ line and the secondary-electron background subtracted.

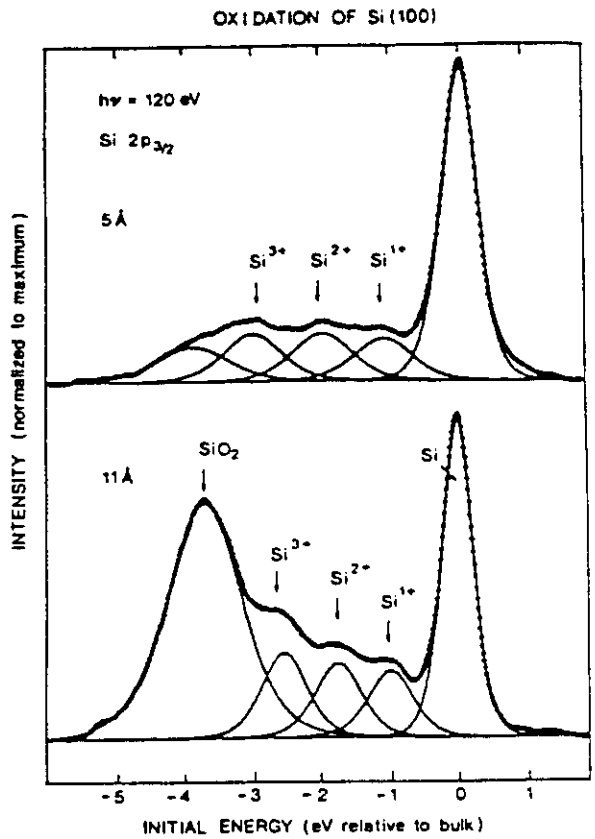

Fig. 28. Si-$2p_{3/2}$ core-line emission for two distinct oxide thicknesses at the SiO_2/Si(100) interface.

$\approx 0.1\%$, this value being subject to change markedly by making use of ultrabright synchrotron radiation. XPS can directly detect all the elements of the periodic Table except H and He.

For AES, the best lateral resolution is of the order of 5 nm while the elemental sensitivity is of the order of 0.1%. Energy resolution is not usually a bottleneck, the Auger line shapes being spread over extended energy ranges. Like XPS, AES cannot directly measure H and He.

In Figs. 27 and 28 are shown XPS Si-2p spectra[30] from silicon surfaces after oxygen chemisorption combined with thermal annealing. All these treatments were performed in UHV starting from *in-situ* cleaned Si surfaces. Clearly identified, even in the raw data are the various chemically distinct contributions of Si atoms reflecting differing chemical environments and spanning the Si^0, Si^{1+}, Si^{2+}, Si^{3+}, and Si^{4+} oxidation states. The sizeable oxidation-dependent core-level shift enables one to distinguish the various components within the instrumental resolution without sophisticated line-shape fitting. In this case, the use of the tunable synchrotron radiation allowed the authors to enhance the photoemission signal of the topmost layers, i.e., the final-state kinetic energies of the Si-2p photoelectrons fall in the broad minimum of the inelastic mean-free-path (Fig. 2). Also noticeable is the different relative weights of the various oxidation states depending on the evolution of the oxide thickness grown on the pristine substrate.

The effects of controlled exposure of different Si surfaces to fluorine, studied by XPS,[31] is shown in Fig. 29. A variety of oxidation states is found in both cases. These test cases are then compared with the results of fluorine etching. This shows that SiF_3 is the dominant contribution left after the etching

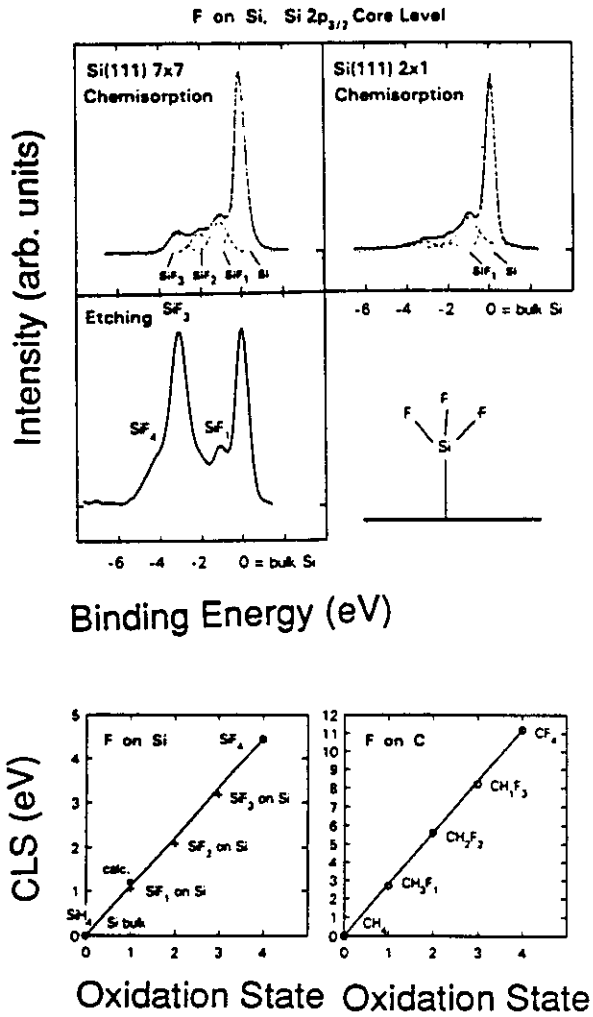

Fig. 29. Background subtracted Si-$2p_{3/2}$ core-level spectra Si surfaces after chemisorption of one monolayer of fluorine (top panels) and after etching. Also shown is the relation between core-level shift and oxidation state in fluorinated silicon and carbon.

treatment. Removal of SiF_3 is thus the bottleneck of the etching reaction. Needless to say, this is an important information in the domain of solid-state electronics. Figure 29 also shows the behavior of the core-level shift spanning a wide variety of oxidation states for fluorinated silicon and carbon.

Core-level XPS has been proven to be quite effective for addressing the evolution of interface growth both for the chemical state identification and for the quantitative description of the growth mode. In Fig. 30 a series of Si-2p spectra measured at the

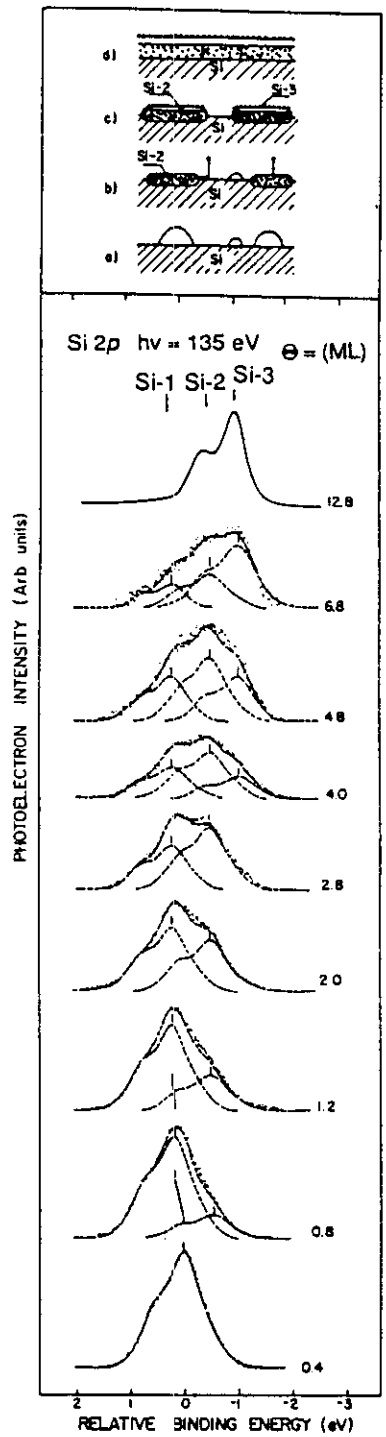

Fig. 30. Si-2p core-level photoemission spectra from the Ce/Si(111) interface as a function of the Ce coverage. Also shown are the fitting components which are assigned to clean Si (Si-1), reacted Ce–Si pseudosilicide (Si-2), and surface segregated Si (Si-3).

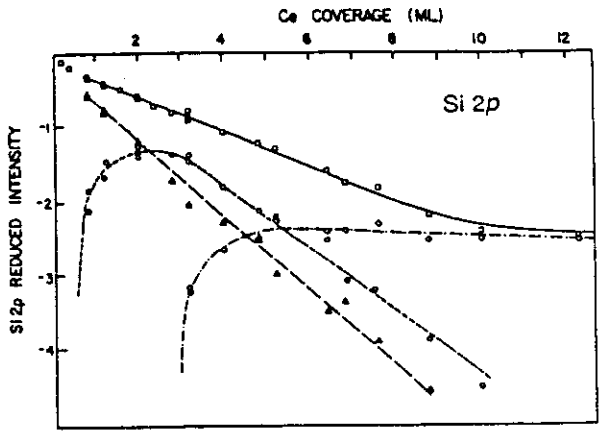

Fig. 31. Attenuation curves for the Si-2p core-level intensity relative to the total and distinct component signals shown in Fig. 30.

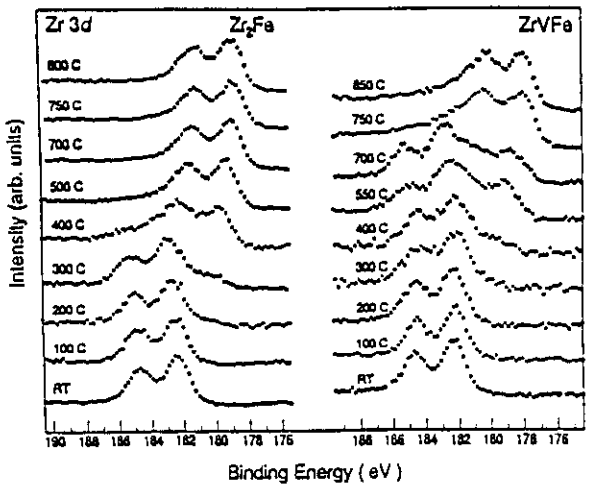

Fig. 32. Zr-3d core-level XPS spectra from ZR_2Fe and ZrVFe alloys after annealing treatments at selected temperatures.

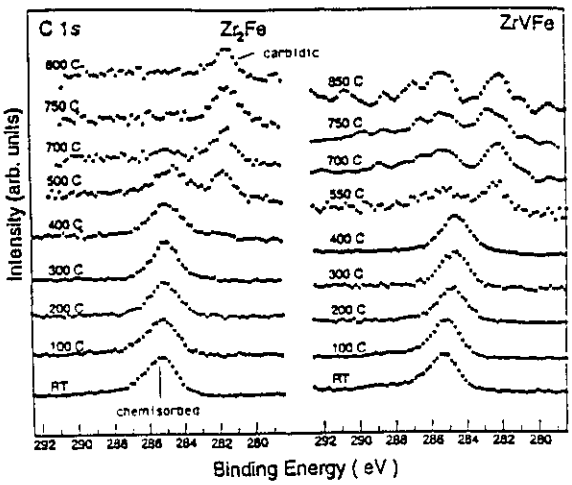

Fig. 33. C-1s core-level XPS spectra from ZR_2Fe and ZrVFe alloys after annealing treatments at selected temperatures.

Ce/Si(111) interface as a function of the Ce coverage is reported.[32] Line-shape fitting allowed the authors to identify up to three different Si sites. The plot of the intensities of such components as a function of the Ce thickness is also shown (Fig. 31). Comparison with reference models for the interface growth (layer-by-layer versus island formation versus layer-plus-island formation) suggests the real growth models as indicated in the top panel of Fig. 30. Studies of this kind have been widely performed for semiconductor–metal, metal–metal, and semiconductor–semiconductor interfaces.

An increasing number of studies have been recently devoted to evaluate the near-surface behavior of the so-called nonevaporable gettering alloys. The key feature of these systems, which can include d-metals, rare earths, or alkali atoms, is the ability of absorbing huge amounts of gases after proper thermal activation procedures. This property can also be engineered so as to be molecular-selective. Applications of these alloys are found in vacuum industry (pumping elements), in the field of gas purification (selective filters), and in the nuclear-fusion technology (tritium recycling). XPS spectra[33] from two important Zr-based alloys are shown in Figs. 32 and 33 as a function of the annealing temperature. In both cases, the alloys have been fractured in air and then inserted in the UHV apparatus where they have been thermally treated at selected steps (annealing duration $\approx$ 20 min) and measured after each annealing.

The XPS spectra hereby reported refer to Zr-3d and C-1s core levels. It is noteworthy that:

(i) the surfaces of fractured specimens exhibit predominantly Zr-3d core levels associated to ZrO_2 and C-1s signal typical of chemisorbed C-containing molecules such as hydrocarbons, CO, and CO_2;

(ii) the progressively increasing annealing promotes the growth of intermediate oxidation states of Zr which appear at lower binding energies at the expenses of the Zr^{4+} component and the appearance of a more shallow contribution in the C-1s spectra which is ascribed to the formation of metal carbides in the near-surface region of the alloys. The joint Zr_2Fe versus ZrVFe analysis allows one to appreciate the different behavior of the two alloys after the same annealing steps thus enabling one to explore differences in the kinetics;

(iii) the high-temperature treatments enrich the near-surface region in Zr atoms which are predominantly in a metallic environment (alloyed or elementally segregated);

(iv) the residual content of carbon in Zr_2Fe at high temperature is typical of solely metal carbides whereas ZrVFe shows also contributions ascribed to chemisorbed molecules and graphitic carbon.

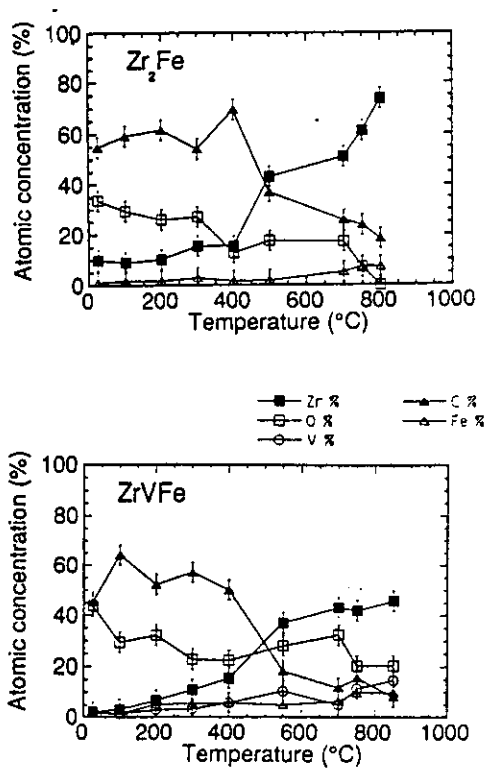

Fig. 34. Relative atomic concentrations as a function of the annealing temperatures from ZR_2Fe and ZrVFe.

If the line-shape analysis allows one to establish how the chemistry local to the different species sites evolves, an analysis of the signal intensities does establish how the relative atomic concentrations are affected in the near-surface region by the thermal treatments. This is shown in Fig. 34. The main messages are the progressive increase, as the temperature is raised, of Zr content at the expenses of carbon. Moreover, Zr_2Fe is able to remove all the oxygen atoms whereas a sizeable oxygen contribution is seen in ZrVFe even after the highest temperature annealing. Remarkable is the fact that the temperature range ($\approx$ 400–500°C for Zr_2Fe and $\approx$ 400–600°C for ZrVFe) where the Zr (C) sharply increases (decreases) has a direct correspondence with the temperature ranges found by studying the macroscopic gettering efficiencies of these alloys. This gives a fruitful example of systems where macroscopic measured properties can be accounted by an investigation focused onto the atomic-scale behavior.

The case of Fig. 35 deals with the combined use of a SST (AES) with controlled ion-induced erosion.[34] An important point is that both qualitative and quantitative aspects are addressed altogether within the same approach. In the domain of metallurgy a relevant point is to check whether surface properties of solid materials can be properly engineered, e.g., increase of the resistance to wear or to chemical agents. The use of thin films deposited via novel techniques seems to be promising, implying at the same time to find out good recipes for good adhesion with the substrate. Here, steel and copper specimens have been coated with an a-SiC film to increase the hardness of the surface. Samples of SiC films have also been nitrogen-implanted for improving the adhesion with the substrate. The depth profiles give the distribution of the atomic species as a function of the depth below the surface and, in particular, make evident the presence of nitrogen just across the film–substrate interface. Moreover, the evolution of both N-KLL and C-KLL Auger line shapes (Fig. 36) for the a-SiC/steel sample enables one to recognize the formation of Si–(N, C)–Cr complexes at the interface. These determine the improved film-to-substrate adhesion for the ion-implanted specimen.

A way for enhancing surface sensitivity is to exploit the dependence on the angle of emission of the electrons consistently with Fig. 3. This is especially important when the electron kinetic energy is not

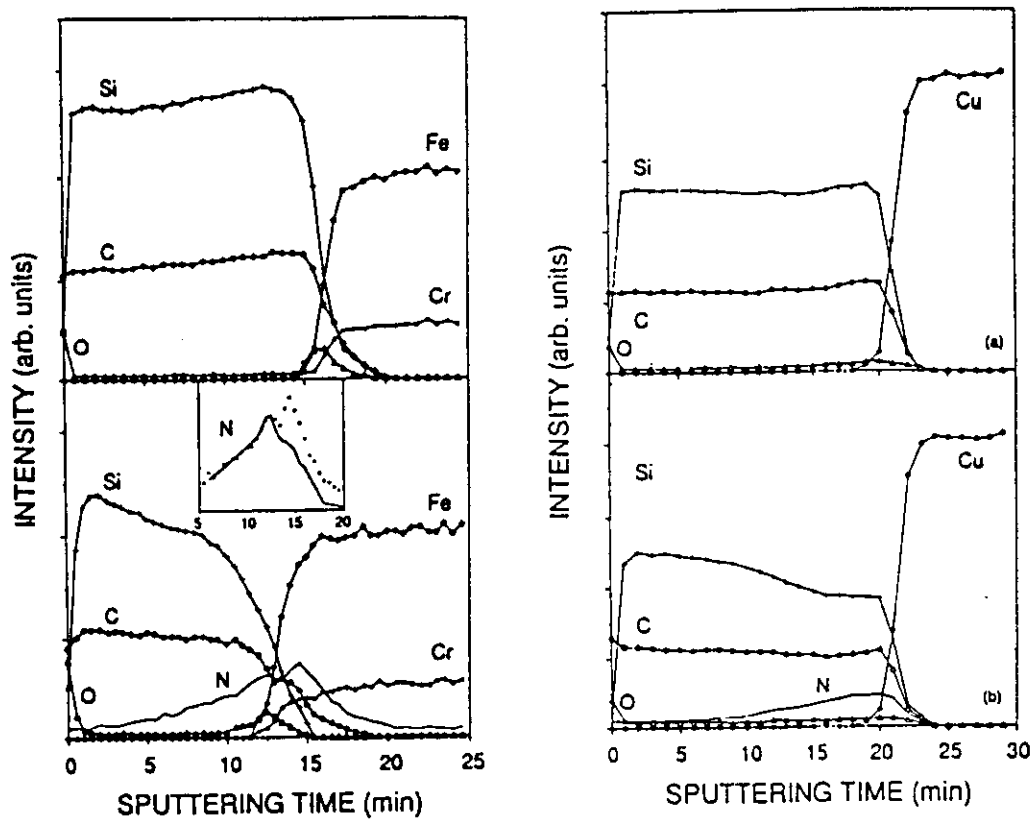

Fig. 35. Auger signal amplitudes as a function of sputtering time from as-deposited a-SiC film on a steel substrate (left side, top panel), N-implanted (1×10^{17} ions/cm^2) SiC–steel sample (left side, bottom panel), as-deposited a-SiC film on a Cu substrate (right side, top panel), N-implanted (1×10^{17} ions/cm^2) a-SiC/Cu bilayer.

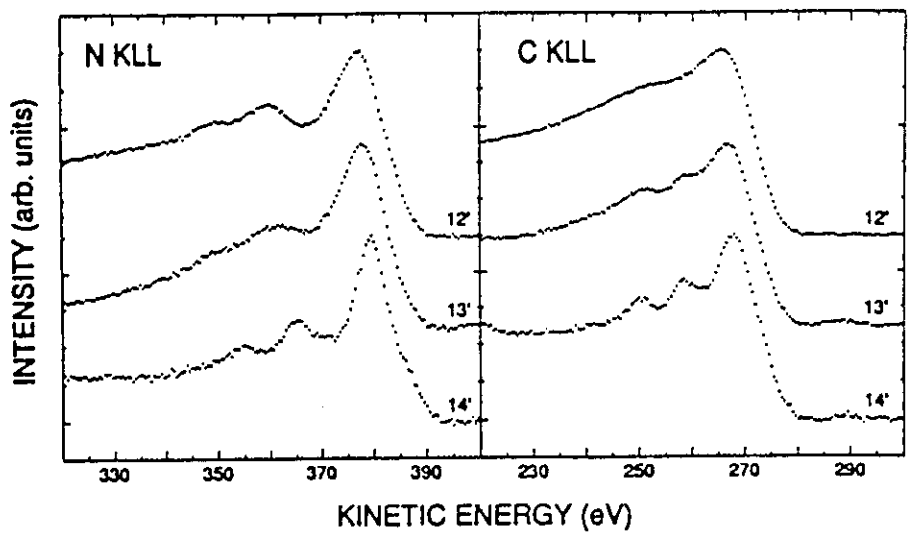

Fig. 36. N-KLL and C-KLL Auger spectra at three selected points of the N-implanted a-SiC/steep specimen of Fig. 35.

tunable and the corresponding inelastic mean-free-path is sizeable. Figure 37 collects a series of XPS spectra from polycrystalline gold taken with a conventional x-ray source.[35] A significant Au-4$f_{7/2}$ line shape change is visible as the angle of emission is varied. Line-shape fitting allows one to identify two

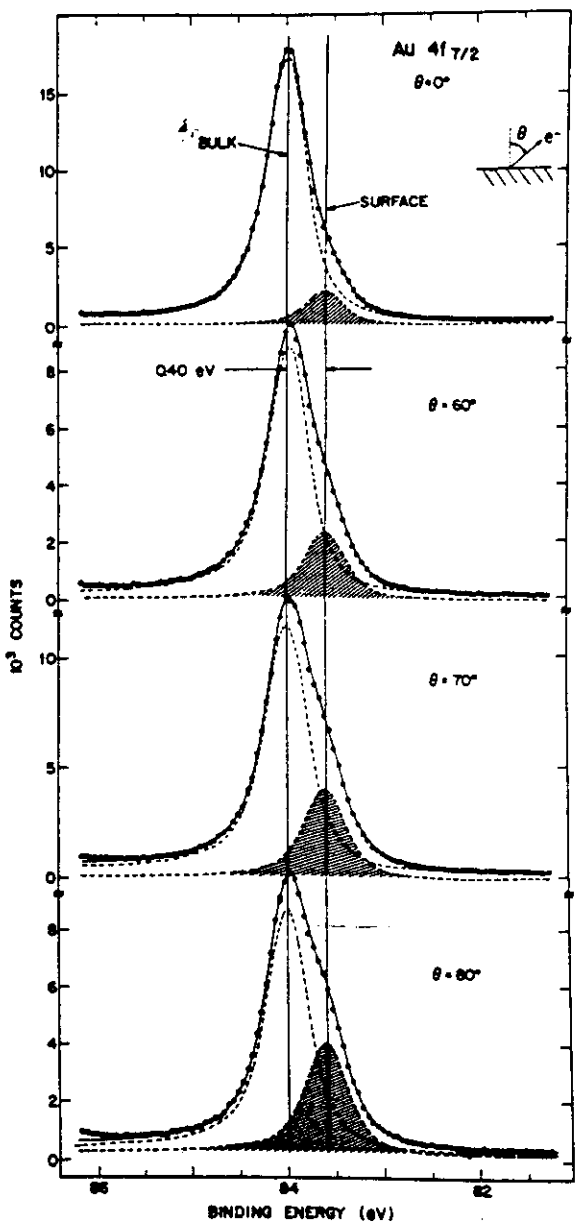

Fig. 37. Least-squares fits to Au-4$f_{7/2}$ XPS line shape as a function of the angle of emission of the electrons from poly-Au. The surface components are shaded.

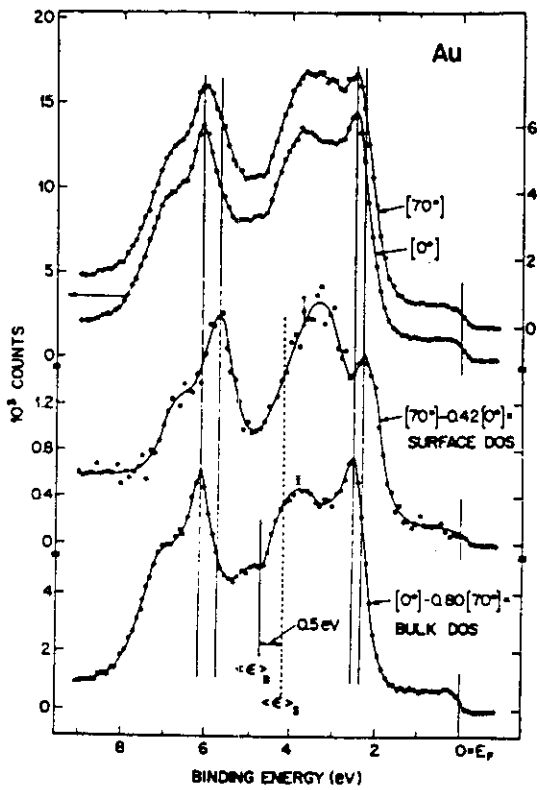

Fig. 38. Separation of bulk versus surface contributions in the valence-band photoemission spectra of poly-Au.

prominent contributions, which are respectively ascribed to two inhomogeneous families of gold sites: bulk and surface atoms. The behavior of the energy distribution of the 5d-derived valence-band states is shown in Fig. 38. The intensity analysis of the Au-4f core level allowed the authors to discriminate the energy distribution local to the surface sites with respect to the bulk matter.

The following example illustrates how the tunability of the photon energy of synchrotron radiation can be exploited for discriminating surface versus bulk contributions. Figure 39 shows Ga-3d and As-3d core levels measured from a GaAs(110) single crystal.[36] By changing the surface sensitivity, the surface-related core-level contribution is significantly enhanced or depressed compared to the bulk components.

An example of spectromicroscopy via AES[37] is given in Fig. 40. The annealing of thin noble-metal films grown *in situ* on Si substrates promotes the

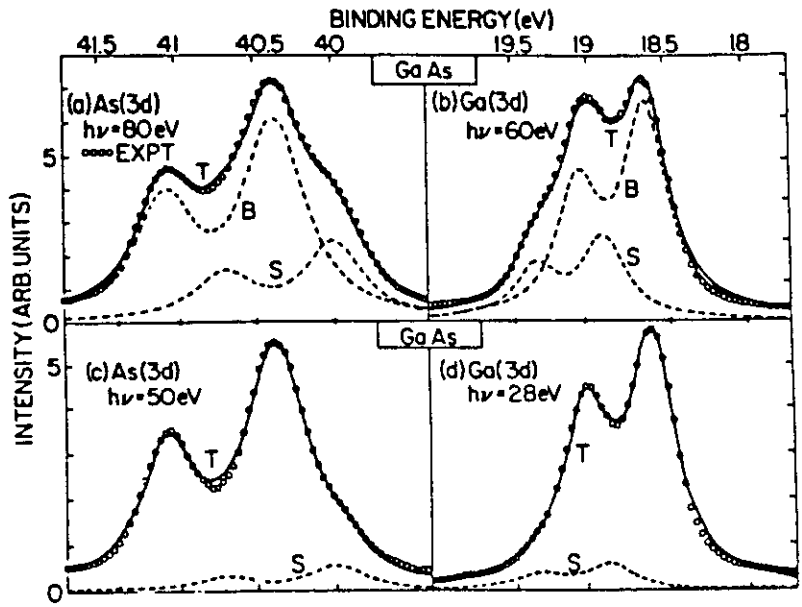

Fig. 39. Ga-3d and As-3d core-level photoemission spectra of the GaAs(110) surface. Shown are the bulk- and surface-related contribution as determined after line-shape fit.

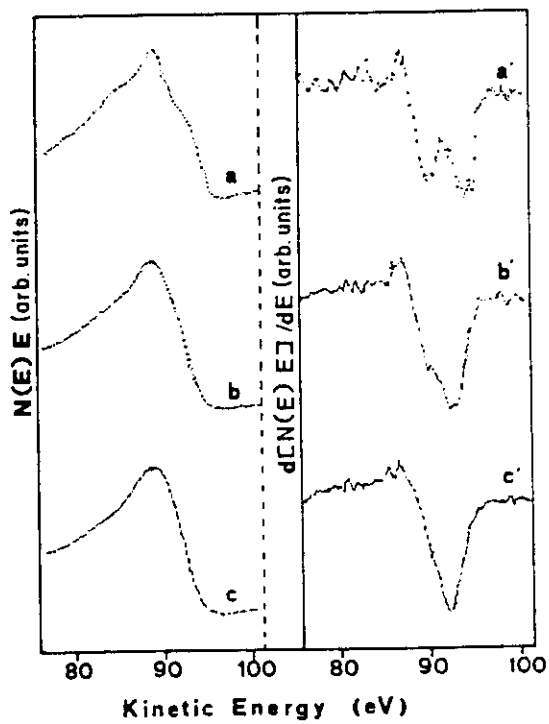

Fig. 40. Laterally resolved ($\approx$ 200 nm) Si-$L_{2,3}VV$ Auger line shapes from a thermally agglomerated Cu/Si(111) interface. (a) island, (b) flat region, and (c) flat region after soft Ar^+ sputtering.

formation of an inhomogeneous pattern with micron-sized islands superimposed on flat regions. AES, XPS, and low-energy electron diffraction (LEED) performed by averaging over an extended lateral area reveal an ordered two-dimensional phase where Cu and Si atoms are arranged to give rise to a superstructure with a weak chemical interaction between Cu and the topmost Si atoms. However, when a laterally resolved Auger analysis (lateral resolution $\approx$ 200 nm) is performed on the various morphologies, one finds that (i) the islands are Cu-rich systems where Si is also present and the Si-$L_{2,3}VV$ Auger line shape is typical of a Cu–silicide (see Fig. 41 for reference); (ii) the flat regions are characterized by Auger spectra which closely resemble the laterally averaged profiles. This example combines both the line-shape analysis for chemical identification and the intensity evaluation for the distribution of the atomic species. Imagine now to record the intensities of the Auger Cu- and Si-related signals as the narrow electron beam is focused onto a specific surface point and to do this while scanning over a laterally extended region. The result is the map of the chemical elements as they are distributed over the explored area. Examples of spectromicroscopy via XPS are widely discussed in the paper by Coluzza and Moberg in this volume.

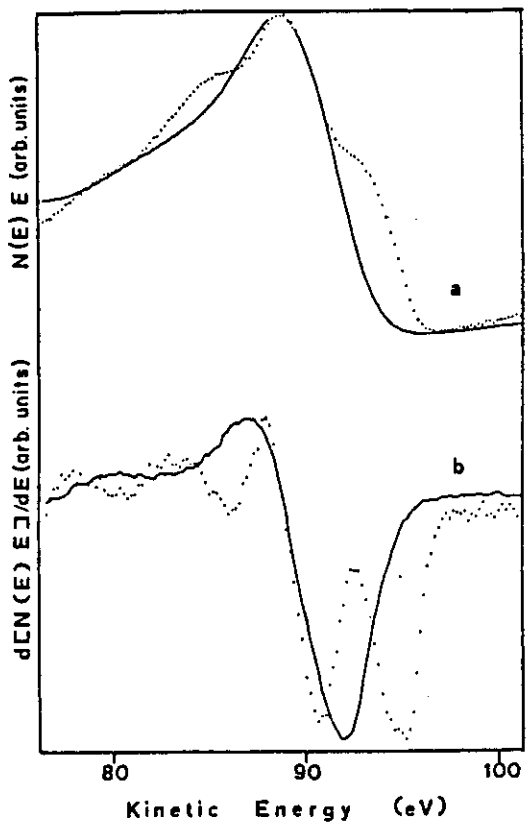

Fig. 41. Si-$L_{2,3}VV$ Auger line shape from Si(111) (solid lines) and Si(111) + ≈ 25 Cu monolayers (room-temperature growth) (points). Spectra (a) as measured in the pulse counting mode and (b) after numerical differentiation. The data refer to an averaged extended area of the specimens.

7. Other Topics

Other versions of photoemission and Auger spectroscopies have been developed since the birth of these techniques. Some of them are discussed in other papers of this volume such as angle-resolved photoemission, photoelectron diffraction, and spin-resolved photoemission. At present, they are mainly utilized for fundamental and applicative research but not for routine analysis in industrial environments. The next few years will certainly make these exotic approaches more familiar in the industrial areas.

Acknowledgments

The author is indebted to Sophie Vandré for helping in the figures editing and Lucia Sorba for critical reading of the manuscript.

References

1. K. D. Sevier, *Low Energy Electron Spectrometry* (John Wiley & Sons, New York, 1972).
2. *Electron Spectroscopy for Surface Analysis*, ed. H. Ibach (Springer-Verlag, Berlin, 1977).
3. *Electron Spectroscopy: Theory, Techniques and Applications*, eds. C. R. Brundle and A. D. Baker (Academic Press, New York).
4. D. P. Woodruff and T. A. Delchar, *Modern Techniques of Surface Science* (Cambridge University Press, Cambridge, 1986).
5. A. Zangwill, *Physics at Surface* (Cambridge University Press, Cambridge, 1988).
6. *Handbook of X-ray and Ultraviolet Photoemission Spectroscopy*, ed. D. Briggs (Heyden, London, 1978).
7. T. A. Carlson, *Photoelectron and Auger Spectroscopy* (Plenum Press, New York, 1976).
8. *Synchrotron Radiation: Techniques and Applications*, ed. C. Kunz (Springer-Verlag, Berlin, 1979).
9. *Photoemission in Solids*, Vols. I & II, eds. L. Ley and M. Cardona (Springer-Verlag, Berlin, 1979).
10. G. Margaritondo, *Introduction to Synchrotron Radiation* (Oxford University Press, Oxford, 1988).
11. *Photoemission and the Electronic Properties of Surfaces*, eds. B. Feuerbacher, B. Fitton, and R. F. Willis (John Wiley & Sons, New York, 1978).
12. *Practical Surface Analysis, Auger and X-ray Photoelectron Spectroscopy*, Vol. 1, eds. D. Briggs and M. P. Seah (John Wiley & Sons, New York, 1990).
13. *Methods of Surface Analysis*, ed. J. M. Walls (Cambridge University Press, Cambridge, 1989).
14. When the energy distribution of the photoelectrons is measured, the work function of the spectrometer should be considered in the above formula.
15. J. F. Moulder *et al.*, *Handbook of X-ray Photoelectron Spectroscopy*, ed. J. Chastain (Perkin–Elmer Corp., Eden Prairie, 1992).
16. C. D. Wagner *et al.*, *Handbook of X-ray Photoelectron Spectroscopy*, ed. G. E. Muilenberg (Perkin–Elmer Corp., Eden Prairie, 1979).
17. J. J. Yeh and I. Lindau, *At. Data Nucl. Data Tables* **32**, 1 (1985).
18. R. Weissmann and K. Müller, *Surf. Sci. Rep.* **1**, 251 (1981).
19. P. Weightman, *Rep. Prog. Phys.* **45**, 753 (1982).
20. D. E. Ramaker, in *Chemistry and Physics of Solid Surfaces*, Vol. IV, eds. R. Vanselow and R. Howe (Springer-Verlag, Berlin, 1982).
21. D. E. Ramaker, *Critical Rev. Solid State Mater. Sci.* **17**, 211 (1991).
22. L. E. Davis *et al.*, *Handbook of Auger Electron Spectroscopy* (Perkin–Elmer Corp., Eden Prairie, 1978).

23. H. Aksela and S. Aksela, *J. Phys.* **B7**, 1262 (1974).
24. P. Weightman, *J. Phys.* **C9**, 1117 (1976).
25. M. Cini, *Solid State Commun.* **20**, 605 (1976); *Phys. Rev.* **B17**, 2788 (1978).
26. G. A. Sawatzky, *Phys. Rev. Lett.* **39**, 504 (1977).
27. C. O. Almbladh and A. L. Morales, *Phys. Rev.* **B39**, 3503 (1989).
28. J. C. Fuggle, in *Electron Spectroscopy: Theory, Techniques and Applications*, Vol. 4, eds. C. R. Brundle and A. D. Baker (Academic Press, New York, 1981).
29. A. Roth, *Vacuum Technology* (North-Holland, Amsterdam, 1990).
30. F. J. Himpsel *et al.*, *Phys. Rev.* **B38**, 6084 (1988).
31. F. R. McFeely *et al.*, *Phys. Rev.* **B30**, 764 (1984).
32. M. Grioni *et al.*, *Phys. Rev. Lett.* **53**, 2331 (1984); M. Grioni *et al.*, *Phys. Rev.* **B30**, 7370 (1984).
33. J. Kovac, O. Sakho, P. Manini, and M. Sancrotti, *Surf. Interf. Anal.* **22**, 327 (1994).
34. N. Laidani, A. Miotello, L. Guzman, S. Tuccio, and L. Calliari, *J. Appl. Phys.* **76**, 785 (1994).
35. P. H. Citrin, G. K. Wertheim, and Y. Baer, *Phys. Rev.* **B27**, 3160 (1983).
36. D. E. Eastman *et al.*, *Phys. Rev. Lett.* **45**, 656 (1980).
37. L. Calliari, F. Marchetti, and M. Sancrotti, *Phys. Rev.* **B34**, 521 (1986).

APPLICABILITY OF SURFACE SCIENCE TECHNIQUES

- Metal manufacture

  Nitriding, carburizing, welding, machining, powders, coatings, corrosion, oxidation, tribology, rubber adh.

- Electronics

  Thin films, adhesion, doping, cleaning, contacts

- Motor vehicles

  Paint adhesion, corrosion, wear, fatigue failures

- Chemicals

  Catalysis, plastics, pharmaceuticals

- Vacuum

  Getters, hydrogen storage, plasma/wall

SURVEY OF SURFACE SCIENCE TECHNIQUES

Technique	Info	Best spatial resolution	Sampling depth (ML)	Sensitivity	
AES	E, C, S	5 nm	3	0.3%	
EELS	E, C	1 mm	3	1%	
ISS	E	1 mm	1	1%	
RBS	E	1 mm	100	1%	
Static SIMS	C	1 μm	2	0.01%	
Dynamic SIMS	E	20 nm	10	< 1 ppm	
SNMS	E	50 μm	10	< 1 ppm	
UPS	C	100 nm	3	1%	
XPS	E, C, S	100 nm	3	0.3%	
AFM				Atomic	
STM		2÷3 Å lateral 0.01 Å vertical		Atomic	
LEED	S	1 mm	3		
AS	S		1		

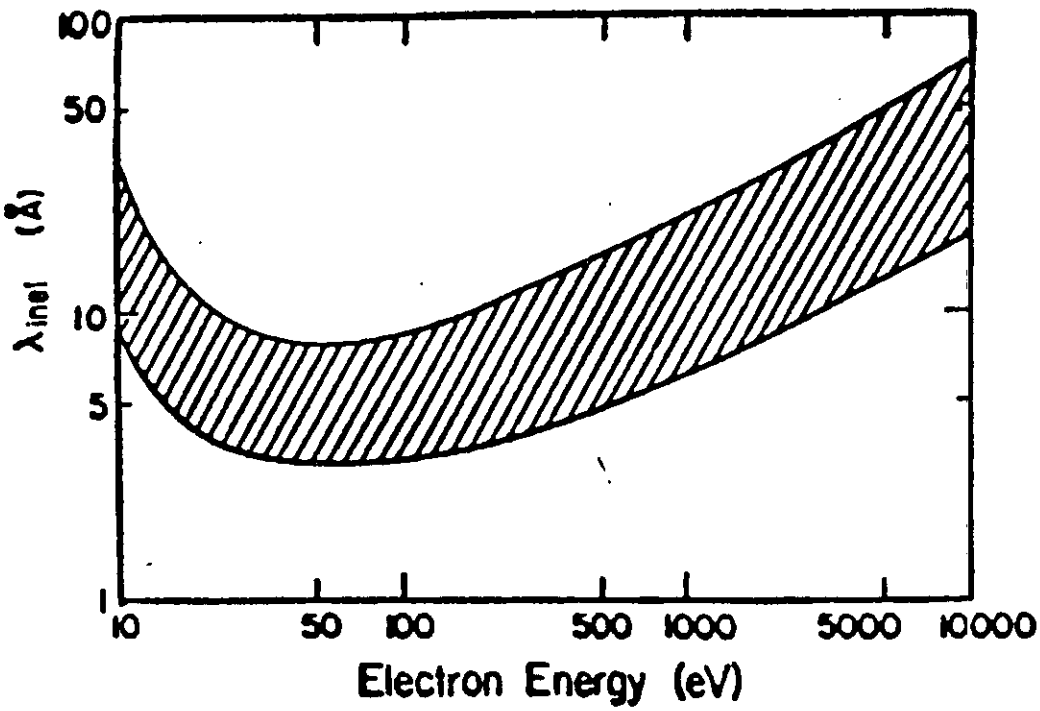

INELASTIC ELECTRON MEAN FREE PATH AS A FUNCTION OF ELECTRON ENERGY

SIGNAL ATTENUATION versus DEPTH

e^- PROBABILITY FOR NOT BEING INELASTICALLY SCATTERED $\propto e^{-z/\lambda \sin\vartheta}$

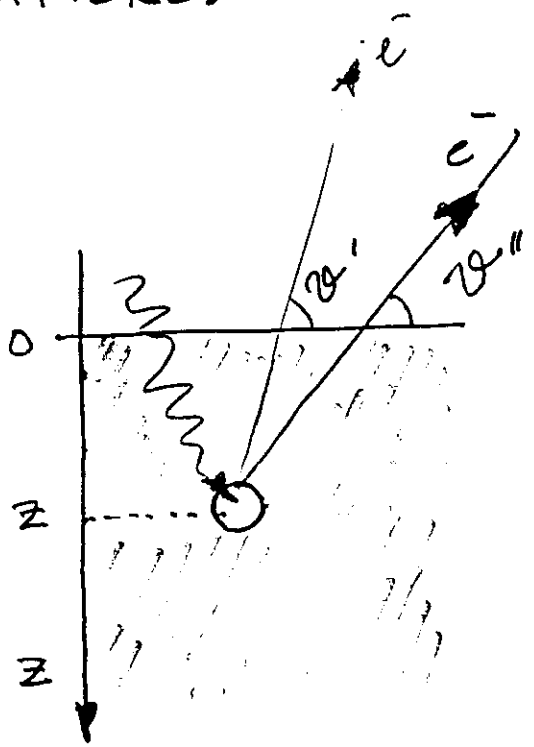

$$I_1 = I_0\, e^{-z_1/\lambda \sin\vartheta}$$

$$I_2 = I_0\, e^{-2z_1/\lambda \sin\vartheta}$$

$$I_i = I_0\, e^{-iz_1/\lambda \sin\vartheta}$$

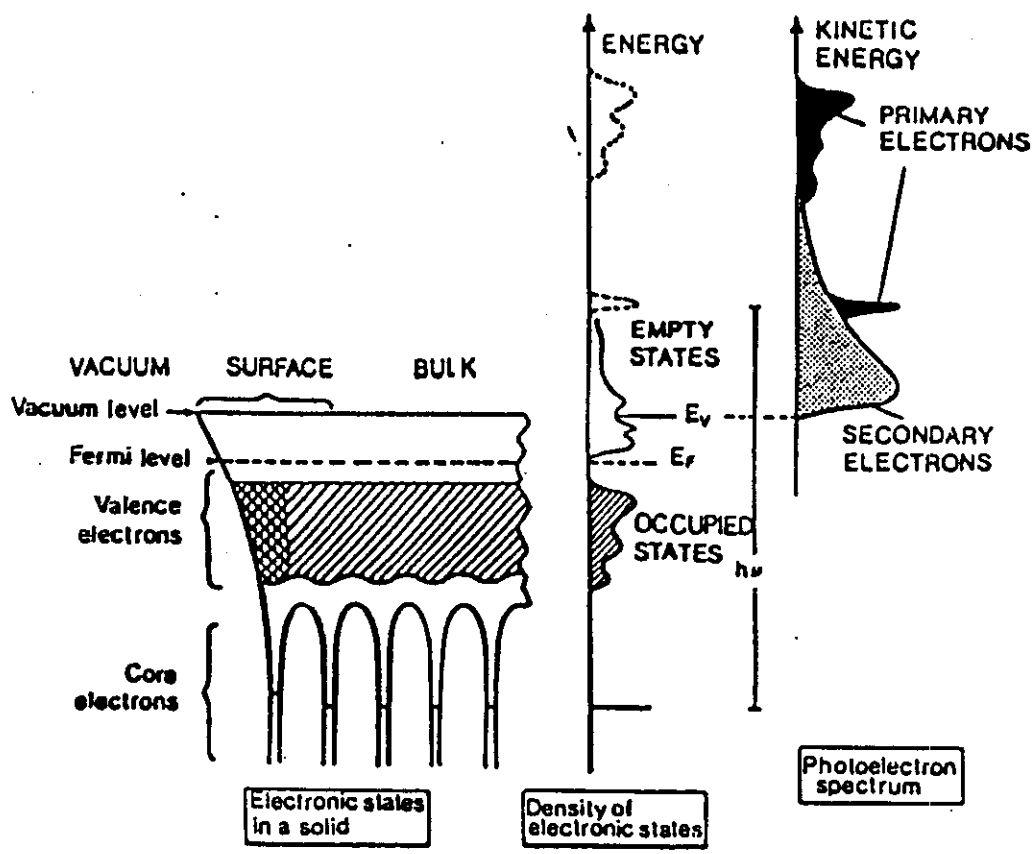
VACUUM
SURFACE
BULK
Vacuum level
Fermi level
Valence electrons
Core electrons
Electronic states in a solid
ENERGY
EMPTY STATES
E_V
E_F
OCCUPIED STATES
hν
Density of electronic states
KINETIC ENERGY
PRIMARY ELECTRONS
SECONDARY ELECTRONS
Photoelectron spectrum

Fig. 5

Carbon C

Atomic Number 6

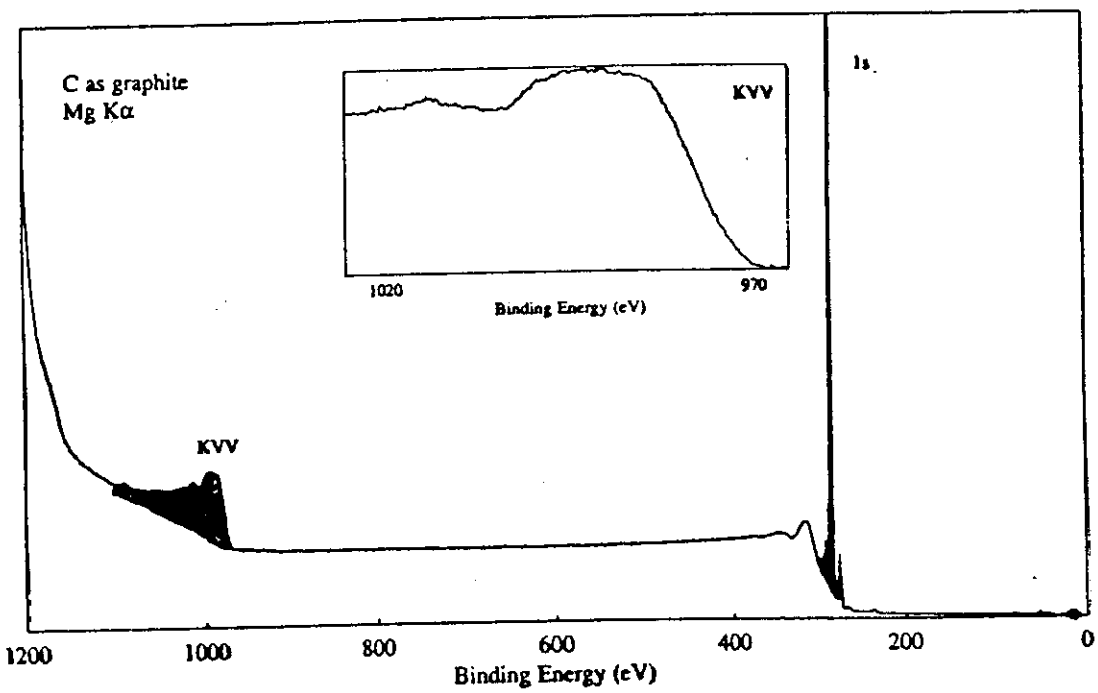

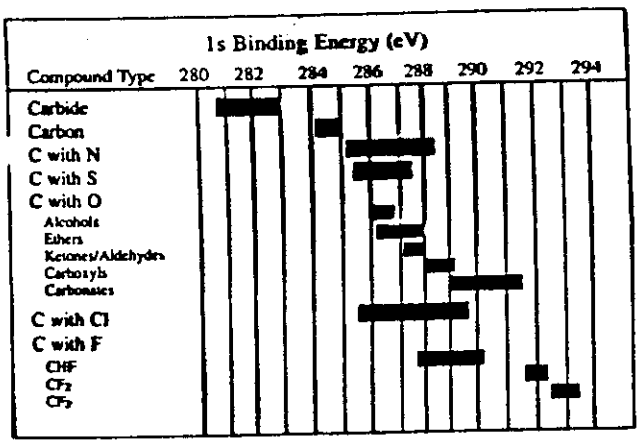

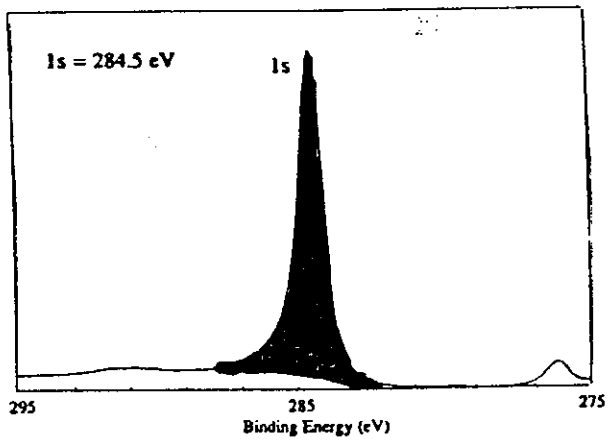

Perkin-Elmer Corporation
Physical Electronics Division

Zirconium Zr

Atomic Number 40

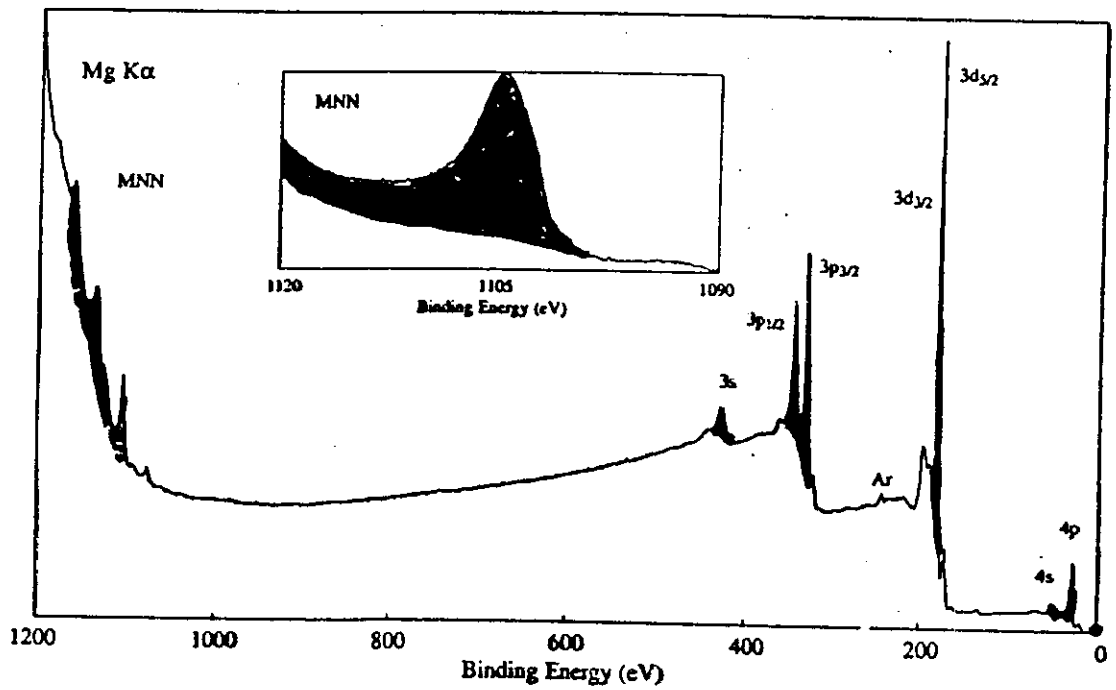

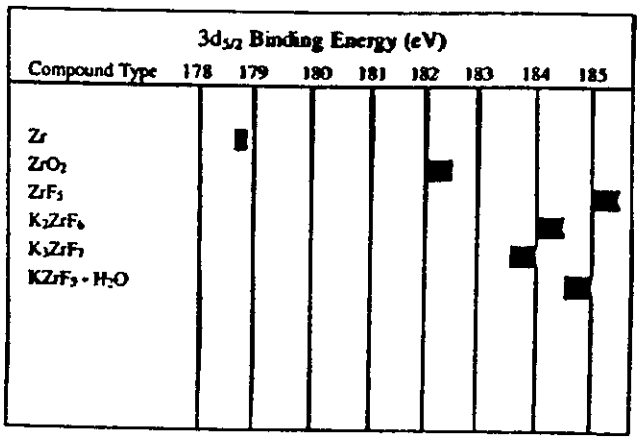

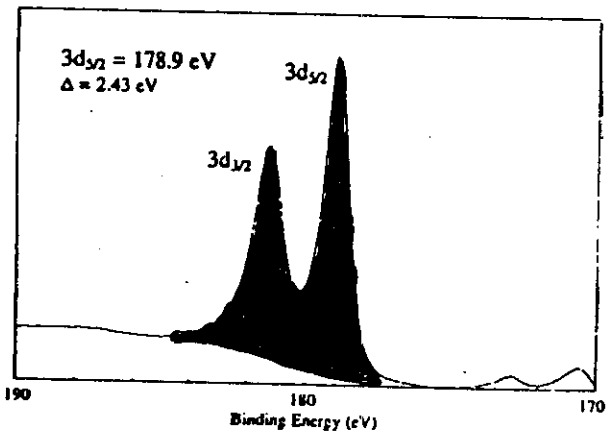

Perkin-Elmer Corporation
Physical Electronics Division

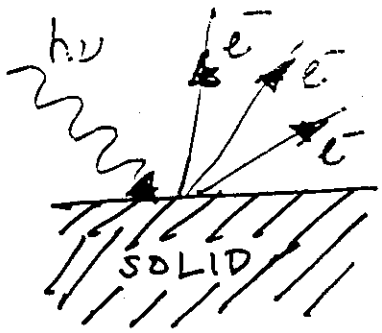

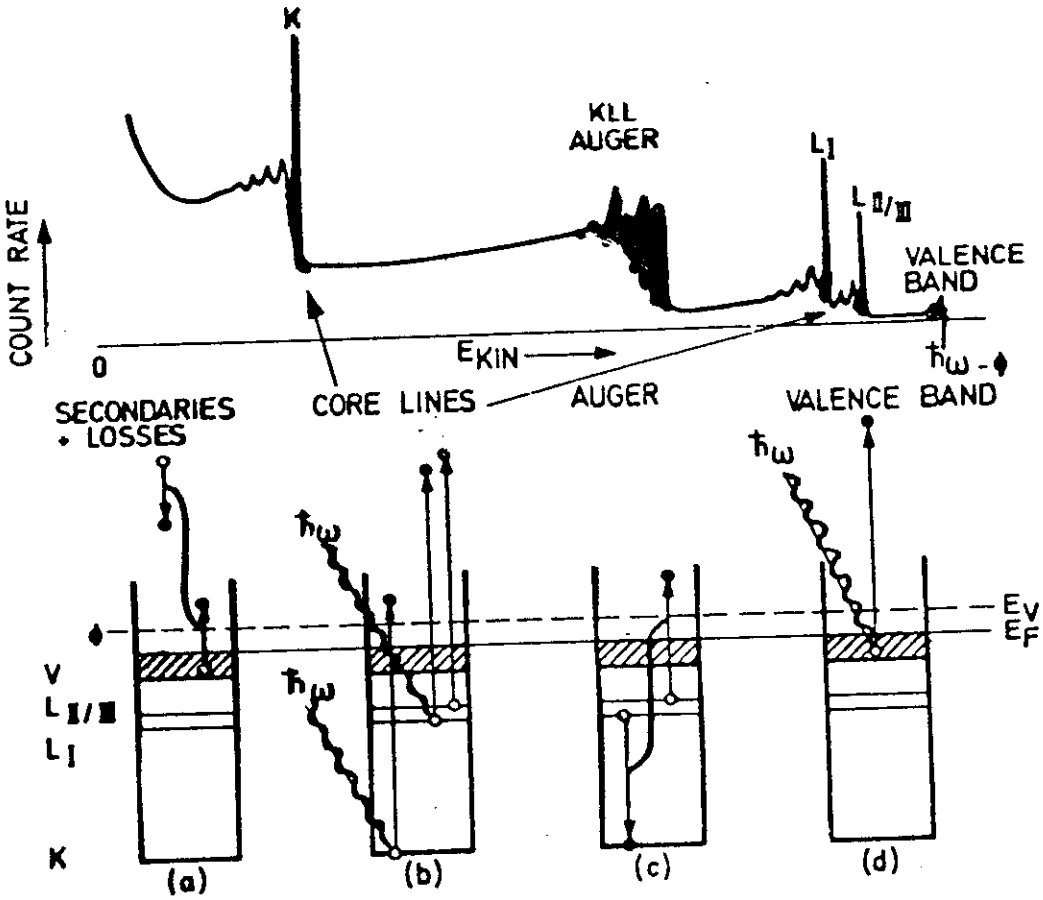

Figure 1.8 The basic processes contributing to an XPS spectrum (top) include: (b) direct optical excitation of core electrons; or (d) valence electrons; (c) hole de-excitation via the Auger process; and (a) inelastic losses giving rise to secondary electrons, and plasmon satellites

BASIC COMPONENTS FOR XPS

- UHV APPARATUS
- SAMPLE
- PHOTON SOURCE
- ELECTRON ENERGY ANALYSER
- ELECTRON DETECTOR
- PULSE COUNTING ELECTRONICS

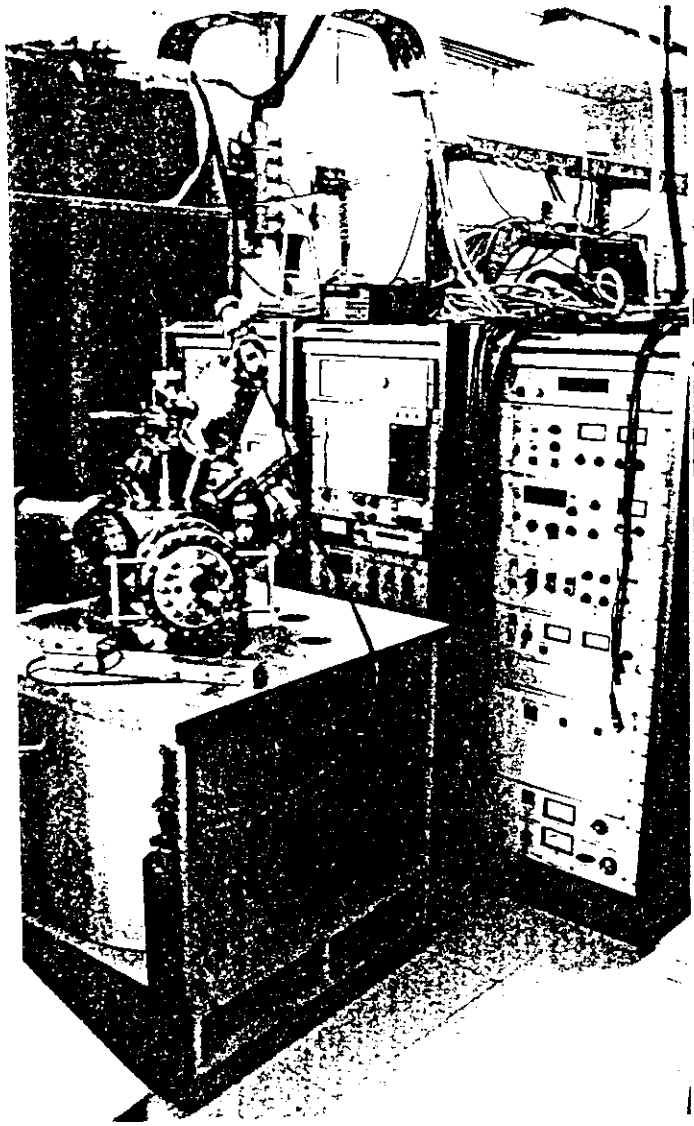

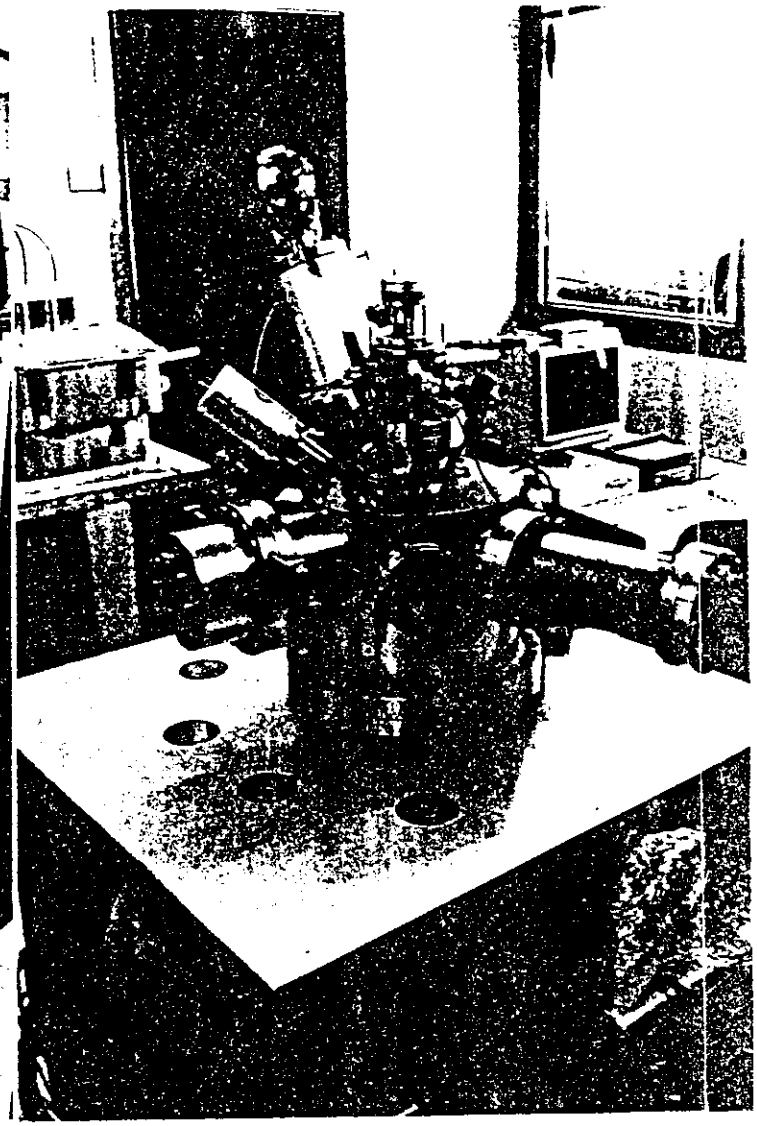

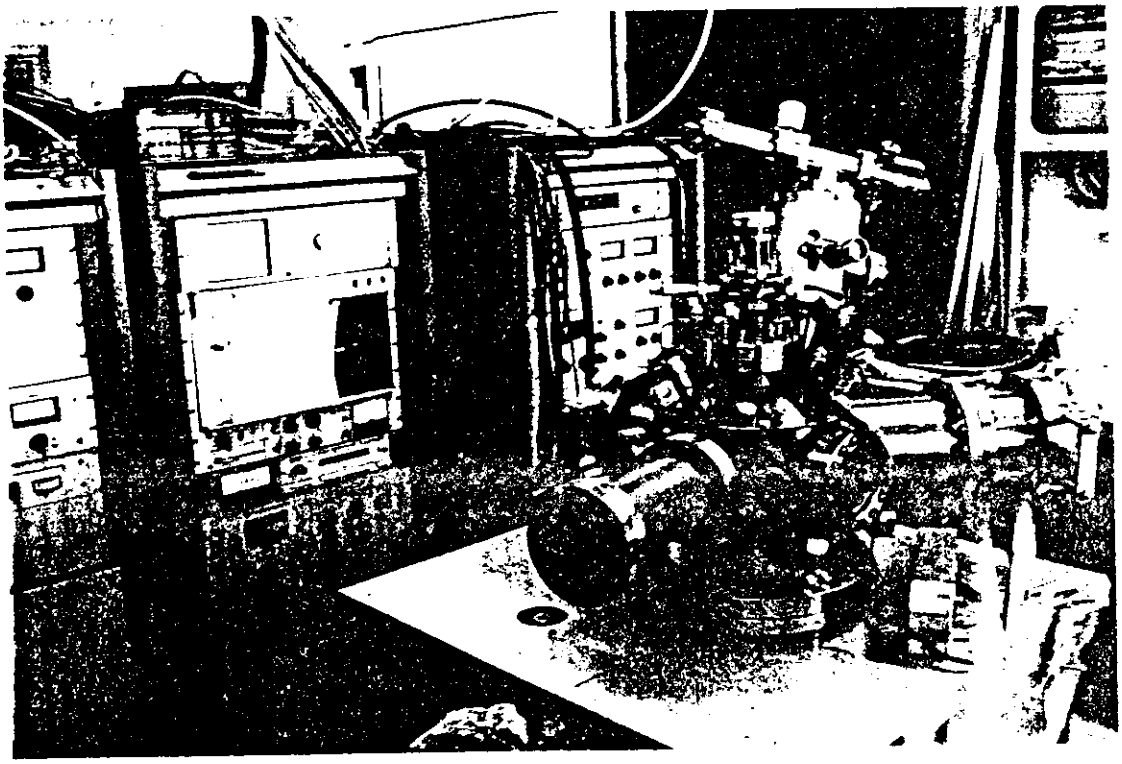

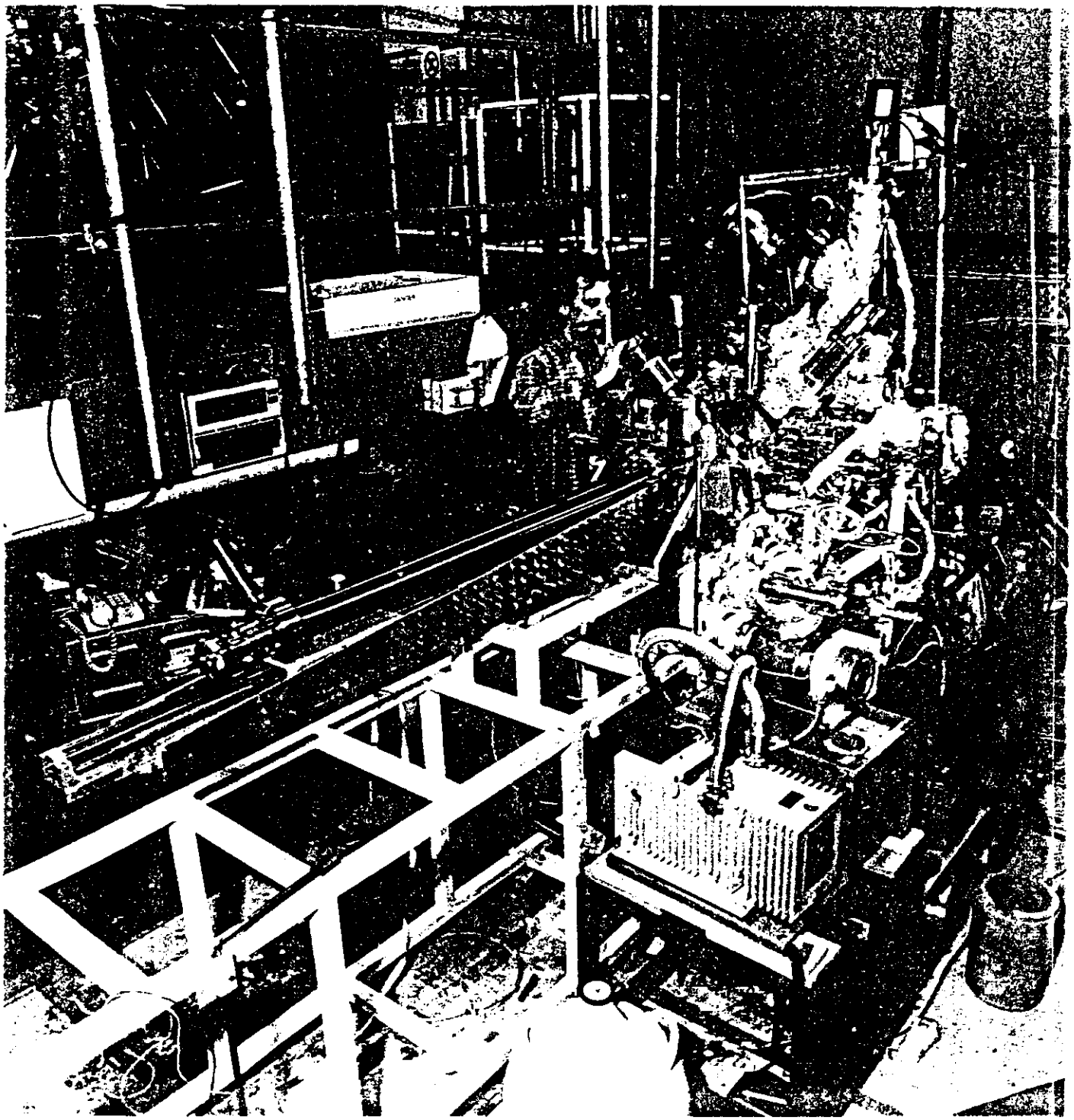

PHOTON SOURCES

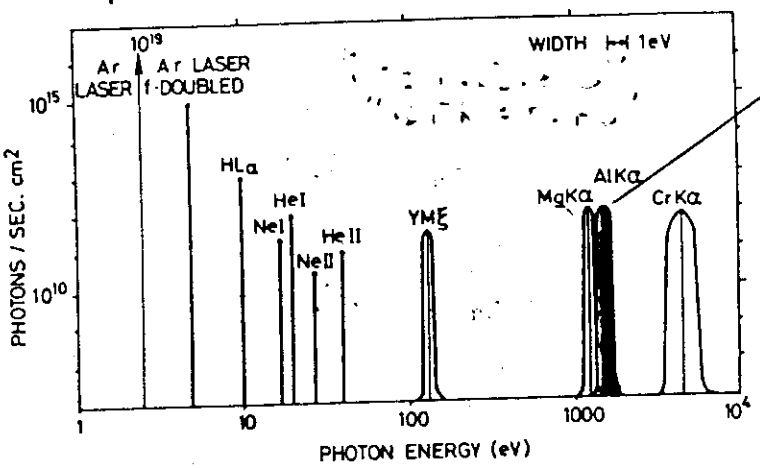

$\hbar\omega = 1486.6eV$
WIDTH = 0.85eV

Fig. 5.5 Photon energies and intensities for line sources commonly used in photoemission experiments. Intensities are given for a 10 x 10 mm illuminated area at the sample position. Line widths are indicated on an expanded scale as shown in the top right corner. The AlK_α line is also shown after monochromatization (full peak)

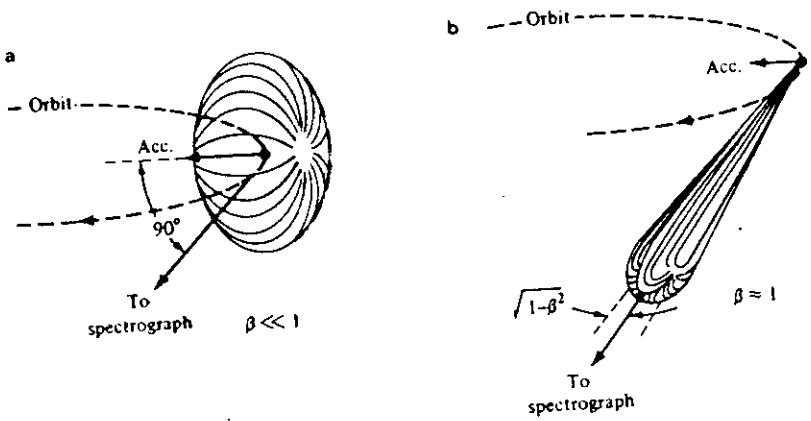

Fig. 6.1a and b. Angular distribution of emitted intensity **a** from a slow electron on a circular orbit, **b** from a relativistic electron moving with the velocity βc. The dipole pattern **a** is distorted into a narrow cone **b** in the instantaneous direction of motion of the electron [6.7]

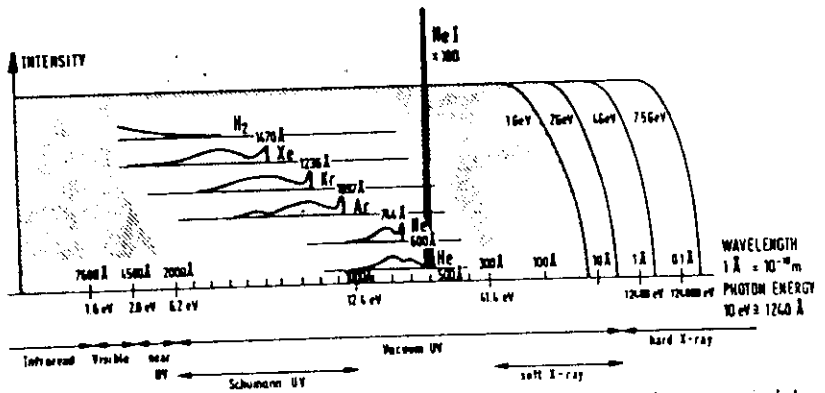

Schematic comparison of the spectral emission of radiation from a typical large synchrotron (e.g., DESY) with that of classical discharge sources. The intensities are roughly on the same relative scale [6.17]

X-RAY SOURCE

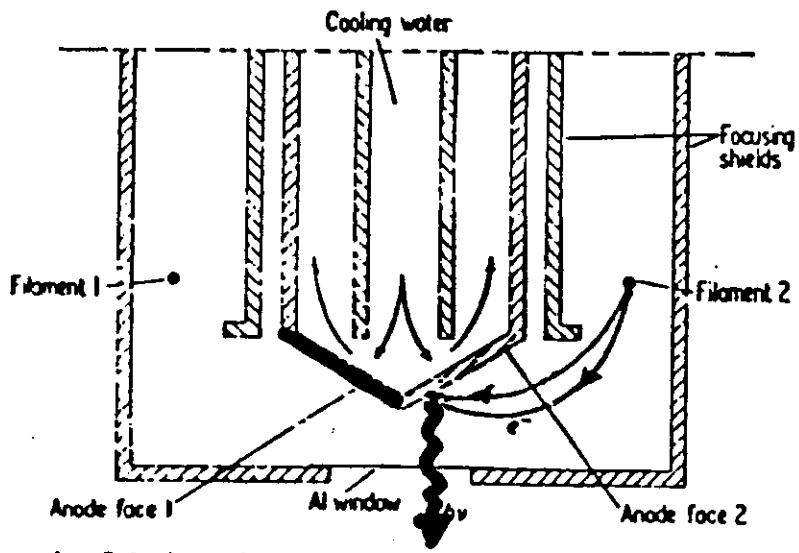

Figure 2.18 Schematic of dual-anode X-ray source. The tapered anode has two faces, on which films of magnesium and aluminium respectively are deposited. Each anode face has its own semi-circular filament, near ground potential, from which electrons are accelerated through a potential of up to 15 kV to the anode face nearer to it. Switching from one anode face to another can be accomplished without the need to break the vacuum. (Reproduced from Yates, Barrie and Street[8] by permission of The Institute of Physics)

——— ELECTRON TRAJECTORY

ANODE FACE #2

[redacted] ANODE FACE #1

XPS TECHNICALITIES

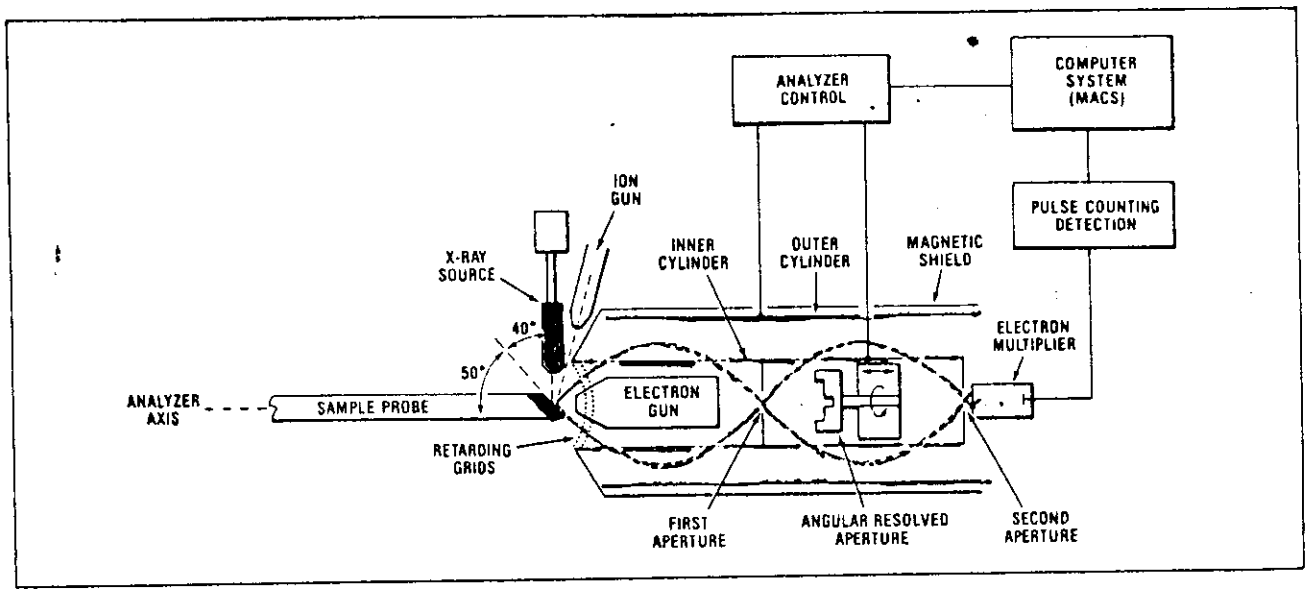

ELECTRON ENERGY ANALYSER

PHOTON SOURCE

ELECTRON PATH

ELECTRON DETECTOR

SAMPLE

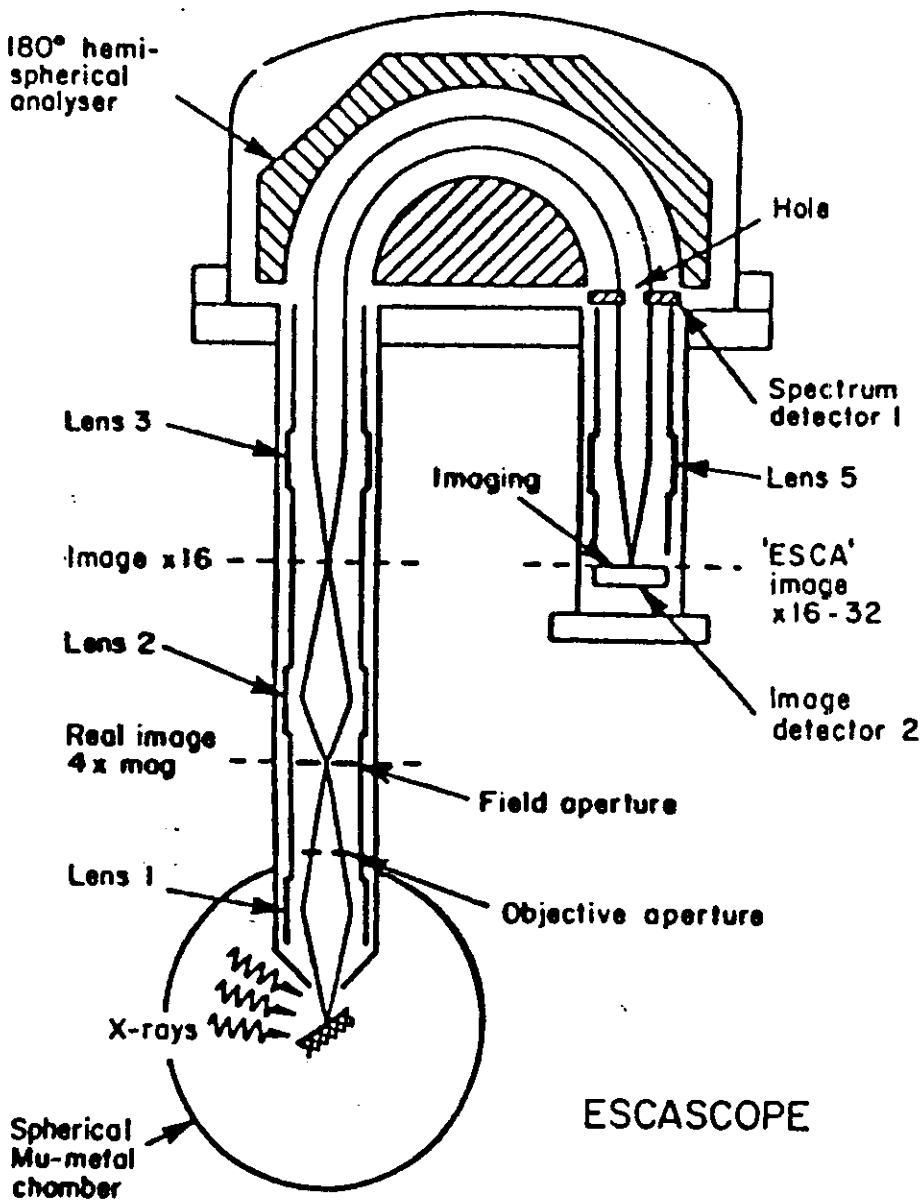

Figure 2.32 Diagram showing the electron optical arrangement in the ESCASCOPE instrument designed to produce energy-resolved two-dimensional images of the surface of a sample. Compared to the conventional lens-plus-analyser system, the additional elements are the input lens (3) the output lens (5) and the channel plate image detector. The principles of the imaging technique are discussed in the text. (Reproduced from Coxon *et al.*[24] by permission of Elsevier Science Publishers)

XPS OF INSULATORS: CHARGING EFFECTS ! NEUTRALIZATION

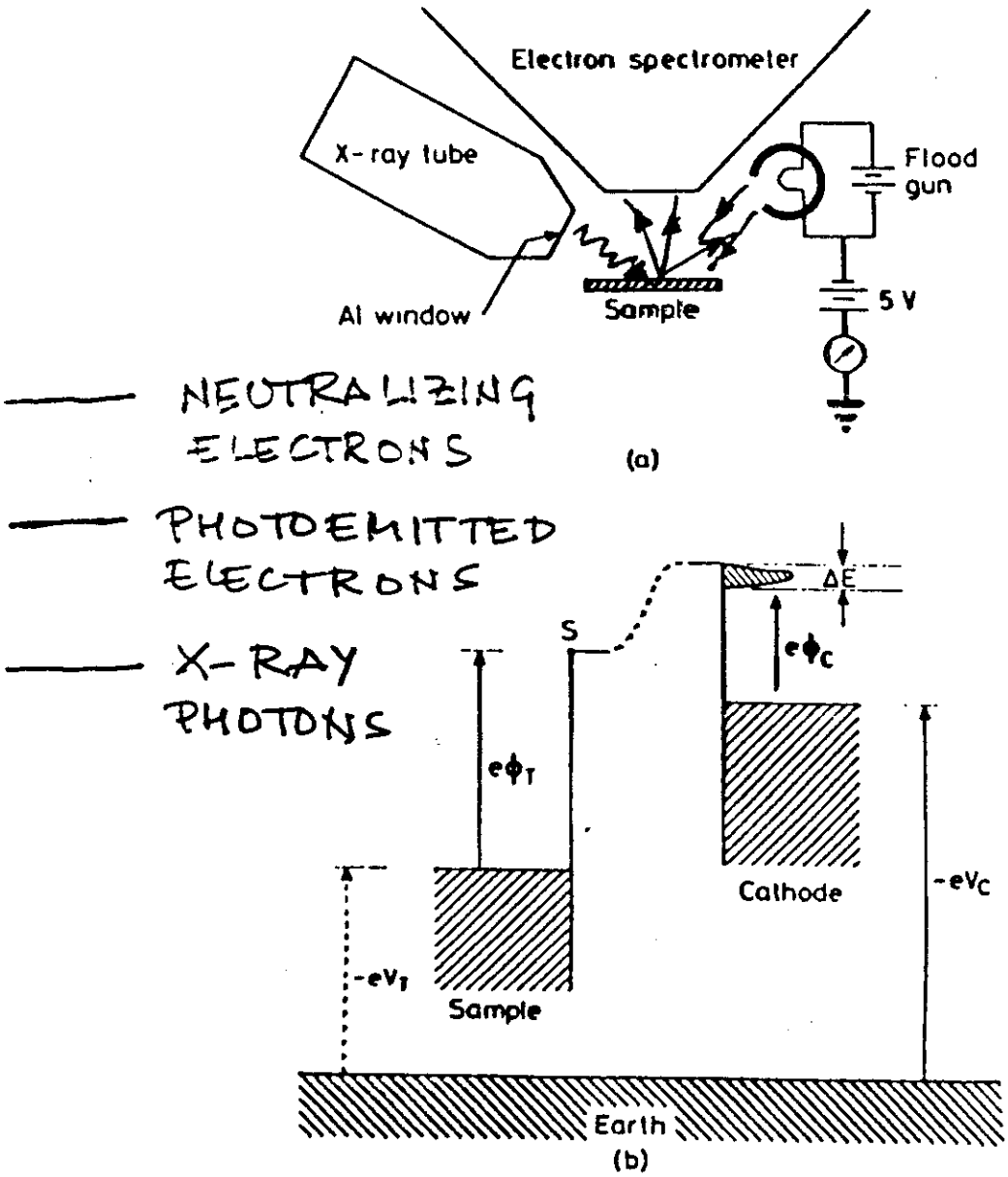

Figure A2.2 Stabilization of surface potential using an electron flood gun: (a) schematic flood gun arrangement (After Huchital and McKeon.[42]), (b) potential energy diagram for the sample and flood gun system with respect to earth (After Hunt, Stoddart and Seah[43])

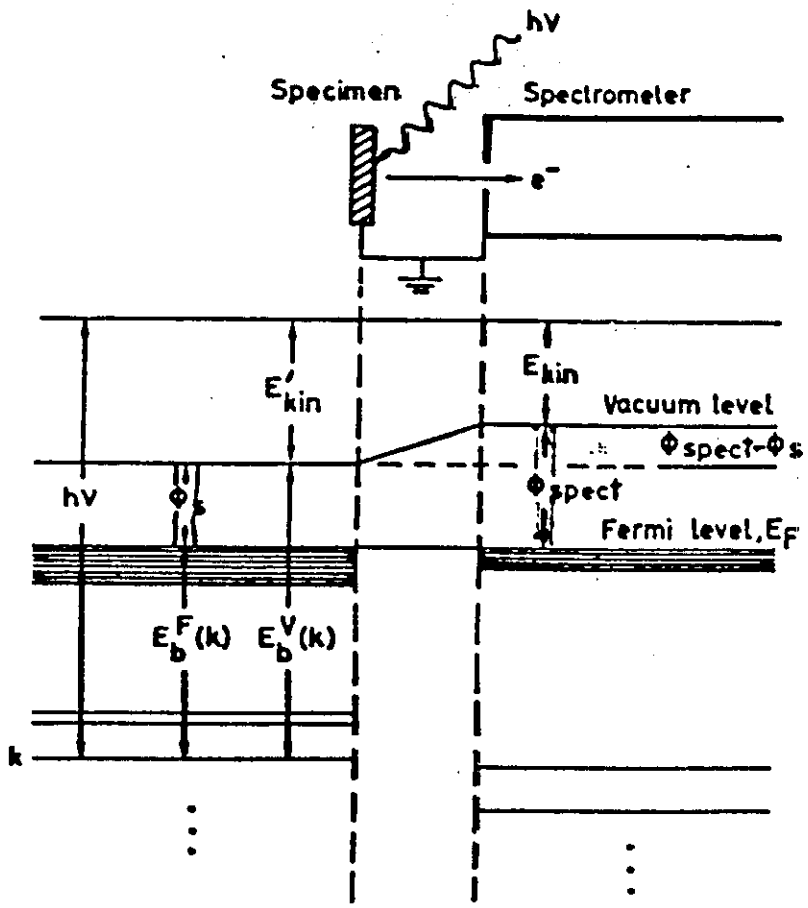

Fig. 3. Energy level diagram for a metallic specimen in electrical equlibrium with an electron spectrometer. The closely spaced levels near the Fermi level E_F represent the filled portions of the valence bands in specimen and spectrometer. The deeper levels are core levels. An analogous diagram also applies to semi-conducting or insulating specimens, with the only difference being that E_F lies somewhere between the filled valence bands and the empty conduction bands above.

HOW TO MEASURE THE SAMPLE ϕ_s

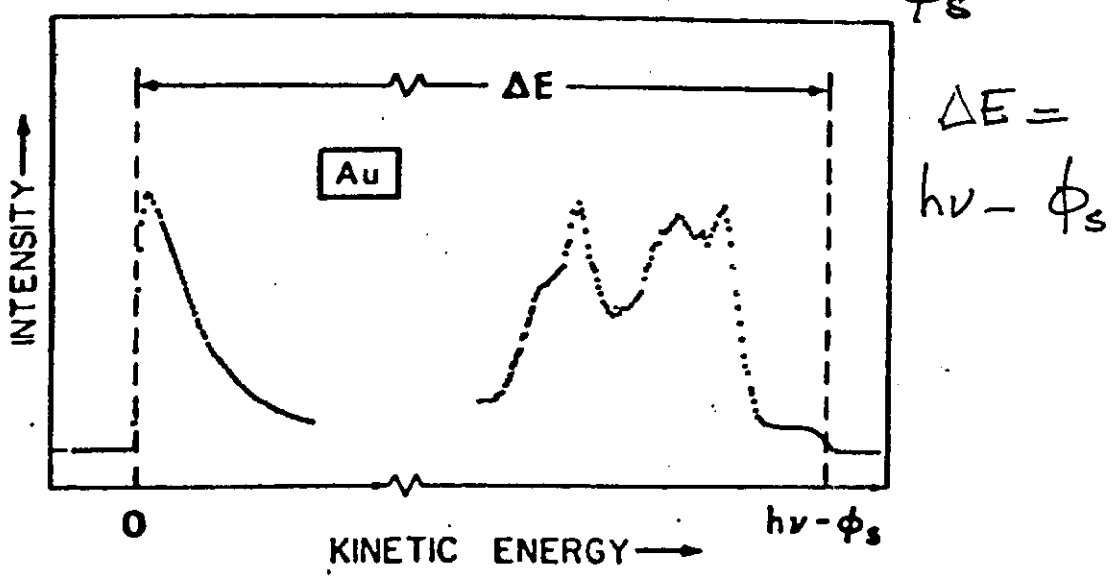

$\Delta E = h\nu - \phi_s$

Fig. 4. Full XPS spectral scan for a polycrystalline Au specimen, showing both the cut-off of the secondary electron peak at zero kinetic energy and the high-energy cut-off for emission from levels at the metal Fermi level. The measurable distance ΔE thus equals $h\nu - \phi_s$, provided that suitable specimen biasing has been utilized. For this case, $h\nu$ was 1253·6 eV and ϕ_s was 5·1 eV. (From Baer, ref. 56.)

VALENCE STATES

XPS PROFILE
Versus
DENSITY OF STATES
CALCULATION

HOW TO MEASURE
THE INSTRUMENTAL
RESOLUTION

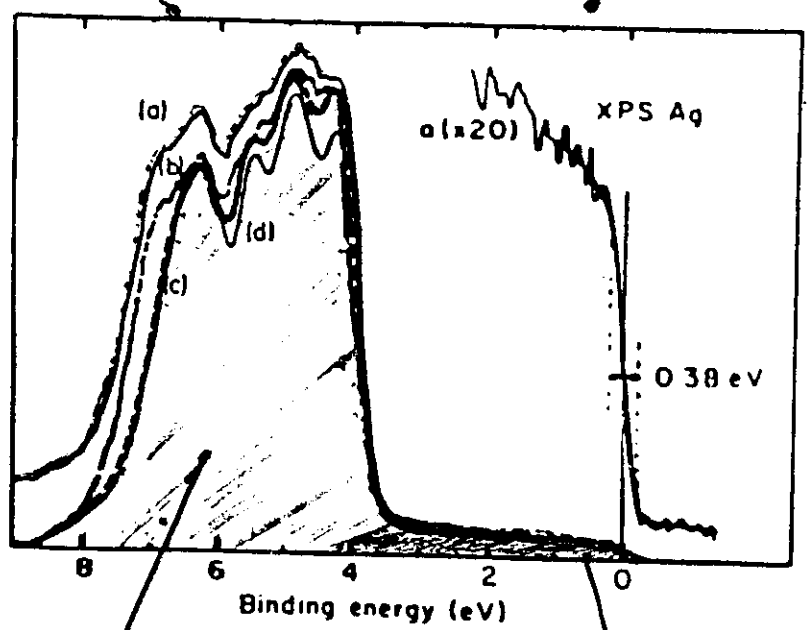

Ag

Figure 3.21 **XPS valence spectrum for polycrystalline silver excited by monochromatic Al Kα radiation in comparison with the theoretical density of states:** (a) raw XPS data; (b) data after substraction of smooth inelastic background; (c) and (d) total theoretical density of states after two different line shape broadenings to include lifetime and shake-up effects. The Fermi edge has been expanded to reveal the instrumental resolution. (After Barrie and Christensen[24])

MOSTLY
Ag 4d STATES

MOSTLY
Ag 5(SP) STATES

XPS

CORE LEVEL ASYMMETRY

via

DONIACH - ŠUNJIĆ EFFECT

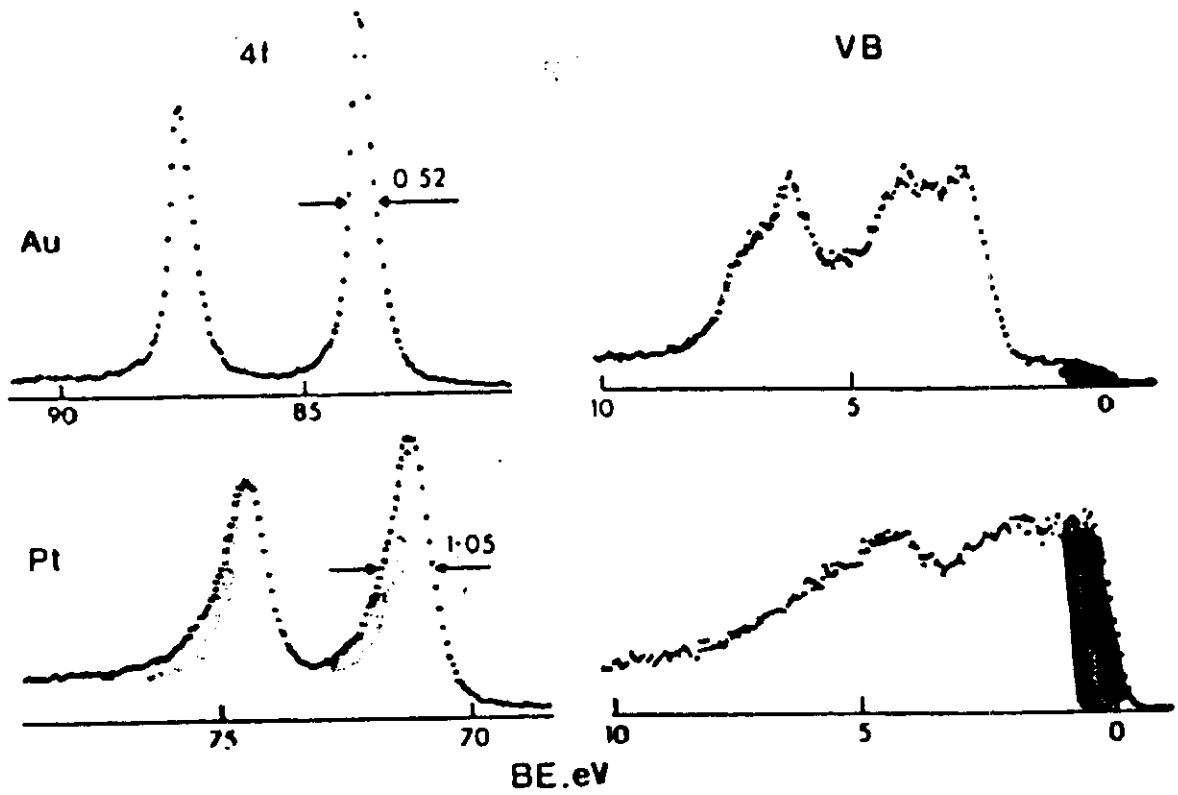

Figure 1.33 Core (4f) and valence (VB) photoelectron spectra of gold and platinum recorded using monochromatic Al Kα radiation. Note the relationship between the degree of core level asymmetry and the density of states at the Fermi level (BE = 0 eV). (After Barrie, Swift and Briggs[49])

ELECTRON-HOLE PAIRS EXCITED AT THE FERMI LEVEL AS A RESPONSE TO THE CORE HOLE

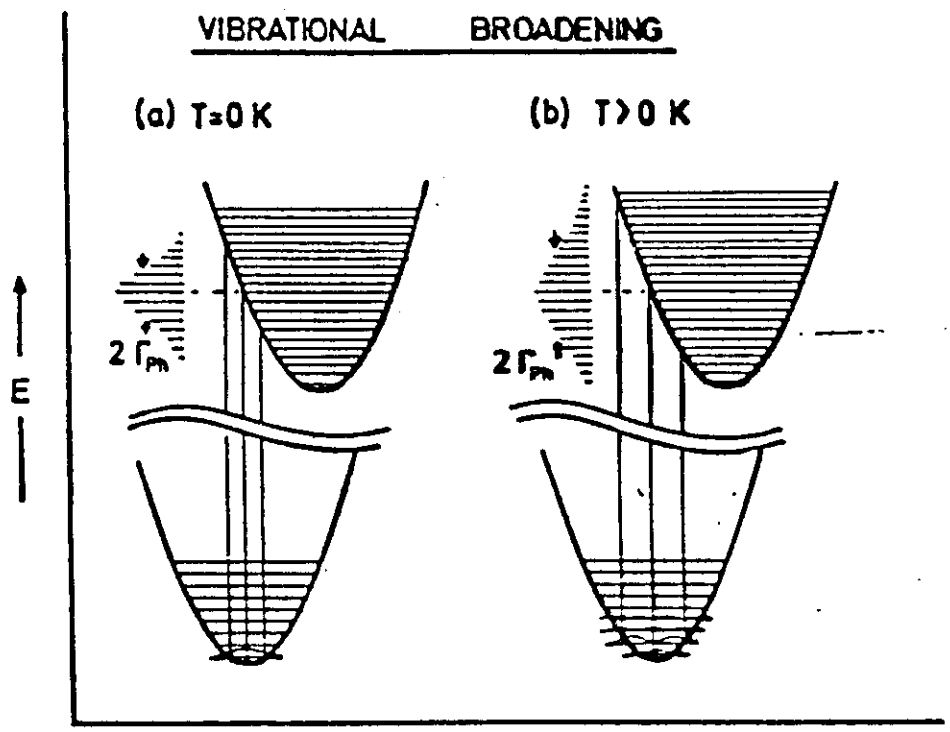

Fig. 11. The origin of phonon broadening in XPS and Auger lines.

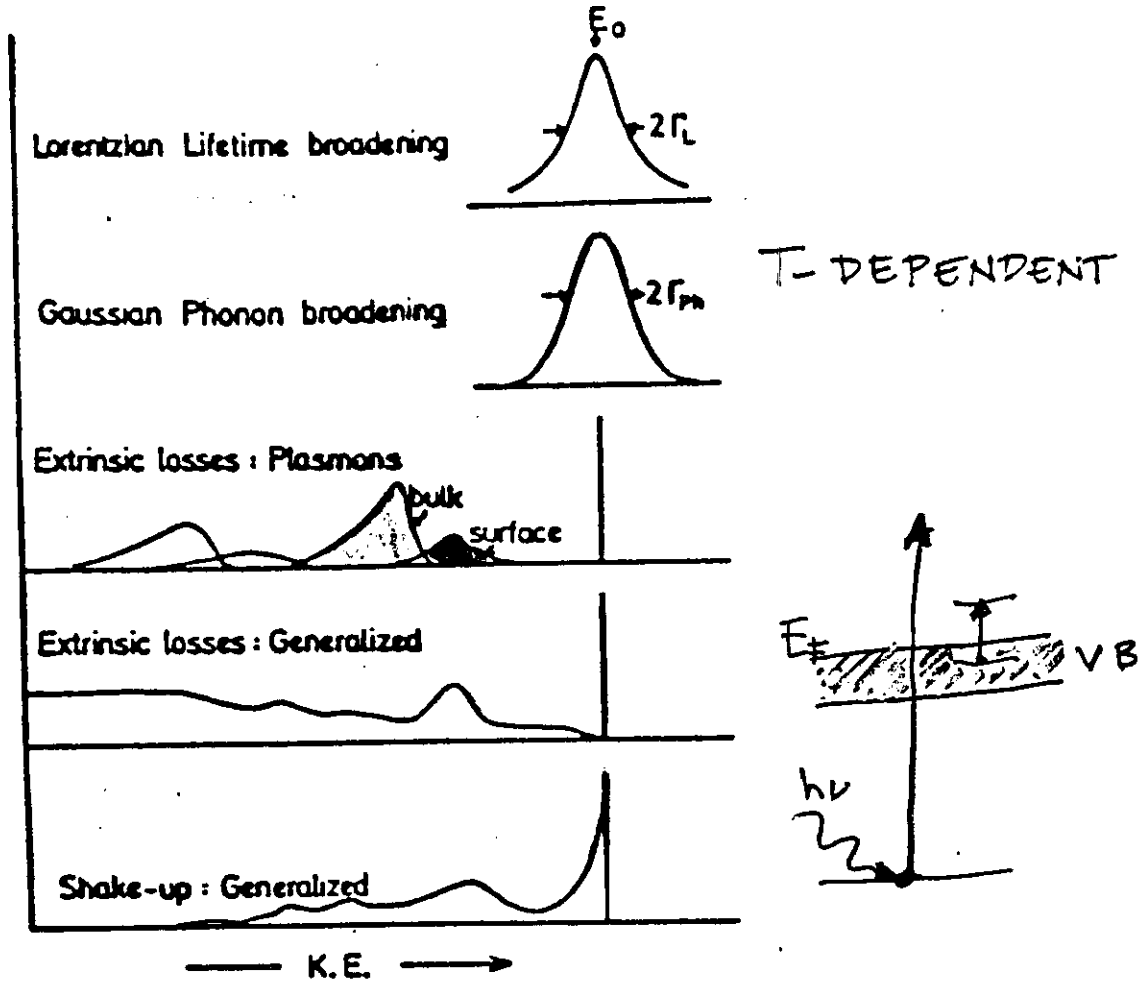

Fig. 10. Summary of the effects on line shapes in electron spectroscopies. Note that phonon broadening is associated with an energy shift not shown here.

OVERVIEW OF THE PHYSICAL EFFECTS AFFECTING THE LINE SHAPE IN ELECTRON SPECTROSCOPIES

INELASTIC SCATTERING: PRIMARY versus SECONDARY PHOTOELECTRONS

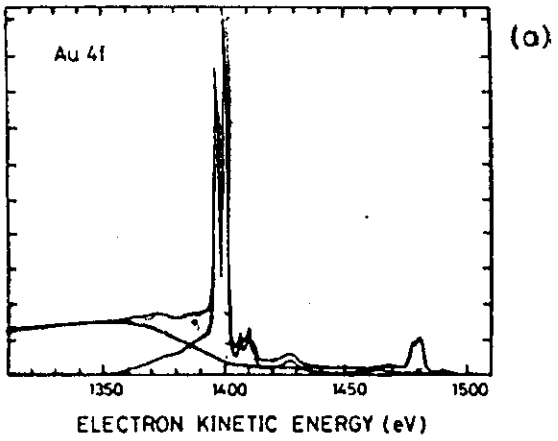

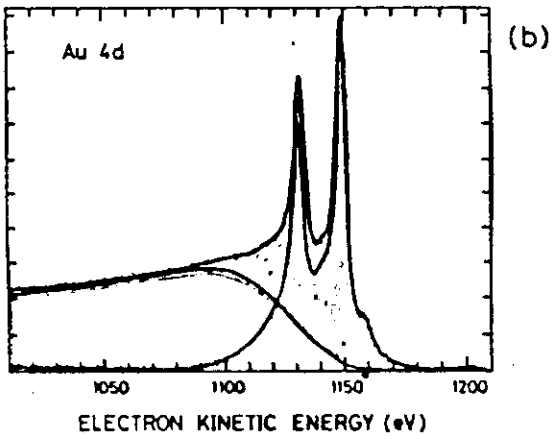

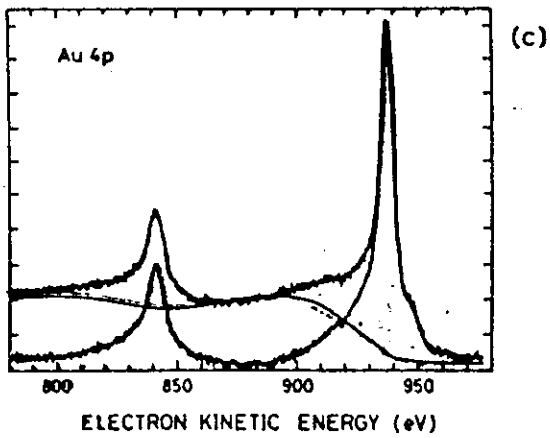

BACKGROUND LINE

PRIMARY PHOTOELECTRON SIGNAL

FIG. 3. Experimental Al $K\alpha$ excited spectra of gold (upper curves) and the primary excitation spectra as determined by Eq. (1) (lower curves). The difference curves are the background signal of inelastically scattered electrons. The inelastic scattering cross section $K(E,T)$ (Ref. 21) for $E=1400$, 1145, and 950 eV and the corresponding inelastic mean free paths $\lambda=21.5$, 17.1, and 14.0 Å (Ref. 26), respectively, were used.

XPS MODEL IN SOLIDS

- THREE STEP MODEL
  - PHOTON ABSORPTION
  - ELECTRON TRANSPORT INSIDE THE SOLID (λ)
  - ESCAPE INTO VACUUM ($k_{\parallel}$ vs $k_{\perp}$)

XPS THEORY

ONE-PARTICLE PICTURE

- ELECTROMAGNETIC FIELD – MATTER INTERACTION
- SEMI-CLASSICAL TREATMENT OF THE ELECTROMAGNETIC FIELD

$$H = \frac{1}{2m}\left(\vec{p} - \frac{e}{c}\vec{A}\right)^2 + e\varphi + V$$

$\vec{p}$ ELECTRON MOMENTUM

e ELECTRIC CHARGE

m PARTICLE MASS

$\vec{A}$ VECTOR POTENTIAL

φ SCALAR POTENTIAL

H HAMILTONIAN

V POTENTIAL ENERGY

$$i\hbar \frac{\partial}{\partial t}|\psi\rangle = \left[-\frac{\hbar^2}{2m}\nabla^2 + \frac{ie\hbar}{mc}\vec{A}\cdot\vec{\nabla} + \right.$$

$$\left. + \frac{ie\hbar}{2mc}\vec{\nabla}\cdot\vec{A} + \frac{e^2}{2mc^2}\vec{A}^2 + e\varphi + V\right]|\psi\rangle$$

- $\frac{eA}{cp}$ FIRST ORDER PERTURBATION THEORY
  DIPOLE APPROXIMATION
- GAUGE CONDITIONS

$$i\hbar \frac{\partial}{\partial t} |\psi\rangle = \left(H_0 + H'\right) |\psi\rangle$$

$$H_0 = -\frac{\hbar^2}{2m} \nabla^2 + V(\vec{r})$$

$$H' = \frac{ie\hbar}{mc} \left(\vec{A} \cdot \vec{\nabla} + \vec{\nabla} \cdot \vec{A}\right)$$

- TRANSITION PROBABILITY BETWEEN EIGEN STATES OF THE UNPERTURBED HAMILTONIAN H_0

$$\frac{d^2 J}{dE\, d\Omega} \propto \left(E_f - E_{VAC}\right)^{1/2} \cdot \sum_i |M_{fi}|^2 \, \delta\left(E - \hbar\omega - E_i\right)$$

(ENERGY CONSERVATION CONDITION)

J PHOTOELECTRON CURRENT THROUGH AN ENERGY ANALYZER SET AT E ! WITHIN A SOLID ANGLE $d\Omega$ (PRIMARY EMISSION)

E_f; E_i FINAL STATE ENERGY; INITIAL STATE ENERGY

E_{VAC} VACUUM LEVEL

$\hbar\omega$ PHOTON ENERGY

M_{fi} MATRIX ELEMENT

XPS THEORY

ONE-PARTICLE PICTURE

$$H = H_0 + H'$$

$$H_0 = \frac{\vec{p}^2}{2m} + V(\vec{r})$$

$\vec{p}$ ELECTRON MOMENTUM

m ELECTRON MASS

$V(\vec{r})$ SCALAR POTENTIAL

H_0 UNPERTURBED HAMILTONIAN

H' INTERACTION HAMILTONIAN

$$H' \propto \vec{p} \cdot \vec{A} + \vec{A} \cdot \vec{p}$$

$\vec{A}$ VECTOR POTENTIAL OF THE ELECTROMAGNETIC FIELD

QUANTITATIVE EVALUATION

- HOMOGENEOUS SOLIDS

- $$X_A = \frac{I_A}{I_A^{\infty}}$$

X_A = MOLAR FRACTION OF COMPONENT "A"

I_A = INTENSITY FROM ELEMENT "A" IN THE SOLUTION

I_A^{∞} = INTENSITY FROM ELEMENT "A" IN PURE "A"

- ASSUME YOU KNOW $\frac{I_A^{\infty}}{I_B^{\infty}}$

THEN

$$X_A = \frac{I_A / I_A^{\infty}}{\sum_{i=A,B} I_i / I_i^{\infty}}$$

XPS

$$I_i \propto I X_i \sigma_i \lambda(E_k) T$$

I = PHOTON FLUX

X_i = ATOMIC CONCENTRATION OF THE SPECIES "i"

σ_i = PHOTO-IONIZATION CROSS SECTION FOR A SPECIFIC CORE LEVEL OF THE SPECIES "i"

λ = ESCAPE DEPTH FOR THE PHOTOELECTRON OF ENERGY E_k

T = INSTRUMENTAL FACTOR

XPS

ATOMIC SENSITIVITY FACTORS

Appendix E. Atomic Sensitivity Factors for X-ray Sources at 90°

This table is based upon empirical peak area values corrected for the system's transmission function. The values are only valid for and should only be applied when the electron energy analyzer used has the transmission characteristics of the spherical capacitor type analyzer equipped with an Omni Focus III lens supplied by Perkin-Elmer. The data are calculated for x-rays at 90° relative to the analyzer.*

Element	Line	ASF
Ag	3d	5.198
Al	2p	0.193
Ar	2p	1.011
As	3d	0.570
Au	4f	5.240
B	1s	0.159
Ba	4d	2.627
Be	1s	0.074
Bi	4f	7.632
Br	3d	0.895
C	1s	0.296
Ca	2p	1.634
Cd	$3d_{5/2}$	3.444
Ce	3d	7.399
Cl	2p	0.770
Co	2p	3.255
Cr	2p	2.201
Cs	$3d_{5/2}$	6.032
Cu	2p	4.798
Dy	4d	2.198
Er	4d	2.184

Element	Line	ASF
Eu	4d	2.210
F	1s	1.000
Fe	2p	2.686
Ga	$2p_{3/2}$	3.341
Gd	4d	2.207
Ge	$2p_{3/2}$	3.109
Hf	4f	2.223
Hg	4f	5.797
Ho	4d	2.189
I	$3d_{5/2}$	5.337
In	$3d_{5/2}$	3.777
Ir	4f	4.217
K	2p	1.300
Kr	3d	1.096
La	3d	7.708
Li	1s	0.025
Lu	4d	2.156
Mg	2s	0.252
Mn	2p	2.420
Mo	3d	2.867
N	1s	0.477

Element	Line	ASF
Na	1s	1.685
Nb	3d	2.517
Nd	3d	4.697
Ne	1s	1.340
Ni	2p	3.653
O	1s	0.711
Os	4f	3.747
P	2p	0.412
Pb	4f	6.968
Pd	3d	4.642
Pm	3d	3.754
Pr	3d	6.356
Pt	4f	4.674
Rb	3d	1.316
Re	4f	3.327
Rh	3d	4.179
Ru	3d	3.696
S	2p	0.570
Sb	$3d_{5/2}$	4.473
Sc	2p	1.678
Se	3d	0.722

Element	Line	ASF
Si	2p	0.283
Sm	$3d_{5/2}$	2.907
Sn	$3d_{5/2}$	4.095
Sr	3d	1.578
Ta	4f	2.589
Tb	4d	2.201
Tc	3d	3.266
Te	$3d_{5/2}$	4.925
Th	$4f_{7/2}$	7.498
Ti	2p	1.798
Tl	4f	6.447
Tm	4d	2.172
U	$4f_{7/2}$	8.476
V	2p	1.912
W	4f	2.959
Xe	$3d_{5/2}$	5.702
Y	3d	1.867
Yb	4d	2.169
Zn	$2p_{3/2}$	3.354
Zr	3d	2.216

*C.D Wagner, et al. *Surf. Interface Anal.* 3, 211 (1981).

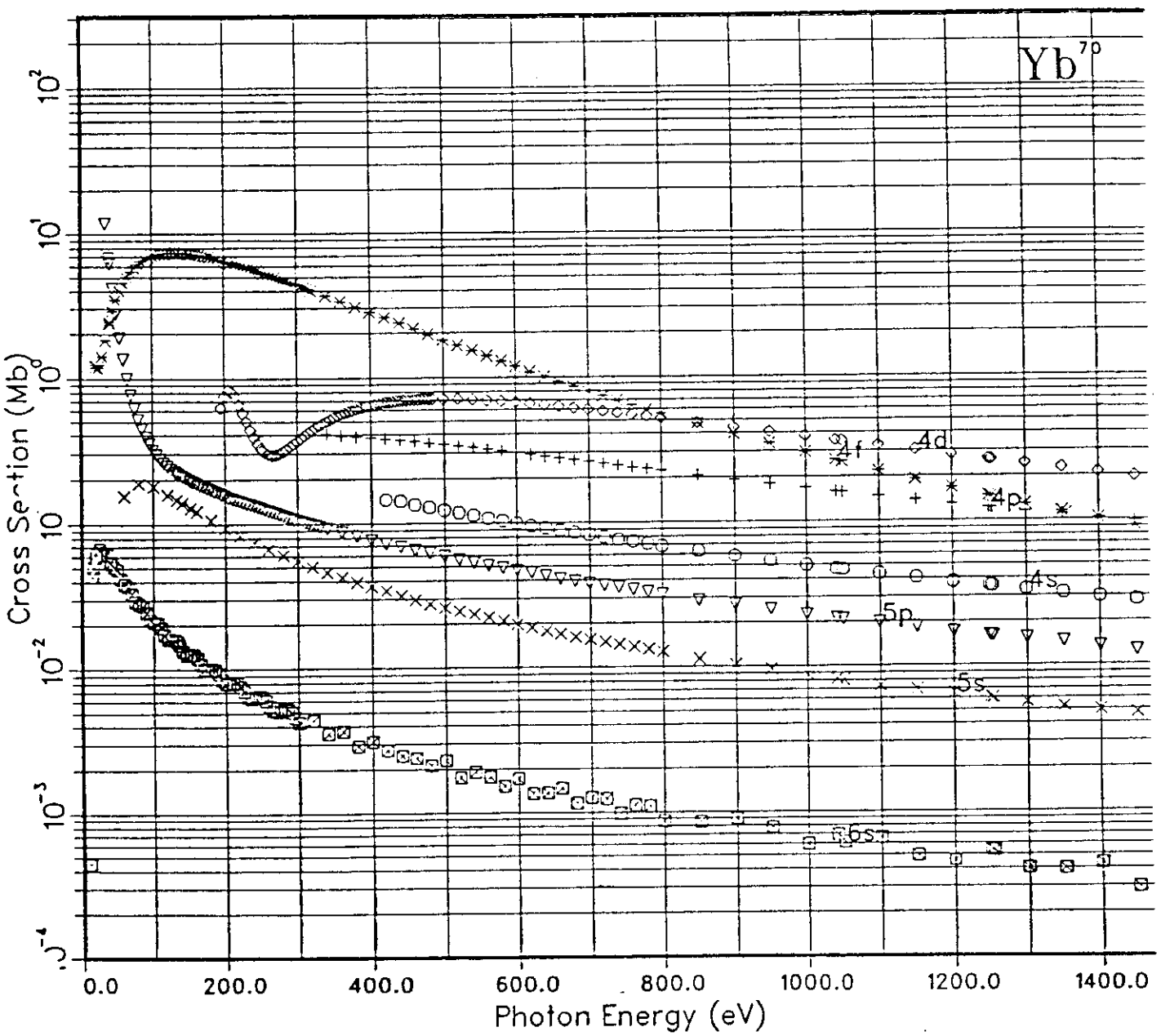

Yb binding energies(eV) are:

1s(2) 57009.8	2s(2) 9290.78	2p(6) 8897.20
3s(2) 2086.76	3p(6) 1904.14	4s(2) 402.610
3d(10) 1561.01	4p(6) 327.461	5s(2) 50.8637
4d(10) 190.652	5p(6) 30.7582	6s(2) 5.16038
4f(14) 15.9818		

XPS

- **Elemental sensitivity**
  via
  Core level binding energies

- **Chemical environment sensitivity**
  via
  Core level chemical shift

- **Quantitative evaluation**
  via
  Core level intensity analysis
  & cross section evaluation

- **Structural information**
  via
  Photoelectron diffraction

- **Access key to many body realm**
  via
  Spectral line shape analysis

XPS

- ELEMENTAL SENSITIVITY
  via
  CORE LEVEL BINDING ENERGIES

- CHEMICAL ENVIRONMENT SENSITIVITY
  via
  CORE LEVEL CHEMICAL SHIFT

- QUANTITATIVE EVALUATION
  via
  CORE LEVEL INTENSITY ANALYSIS
  & CROSS SECTION EVALUATION

- STRUCTURAL INFORMATION
  via
  PHOTOELECTRON DIFFRACTION

- ACCESS KEY TO MANY BODY REALM
  via
  SPECTRAL LINESHAPE ANALYSIS

XPS Si 2p

Si(100) OXIDIZED IN O_2

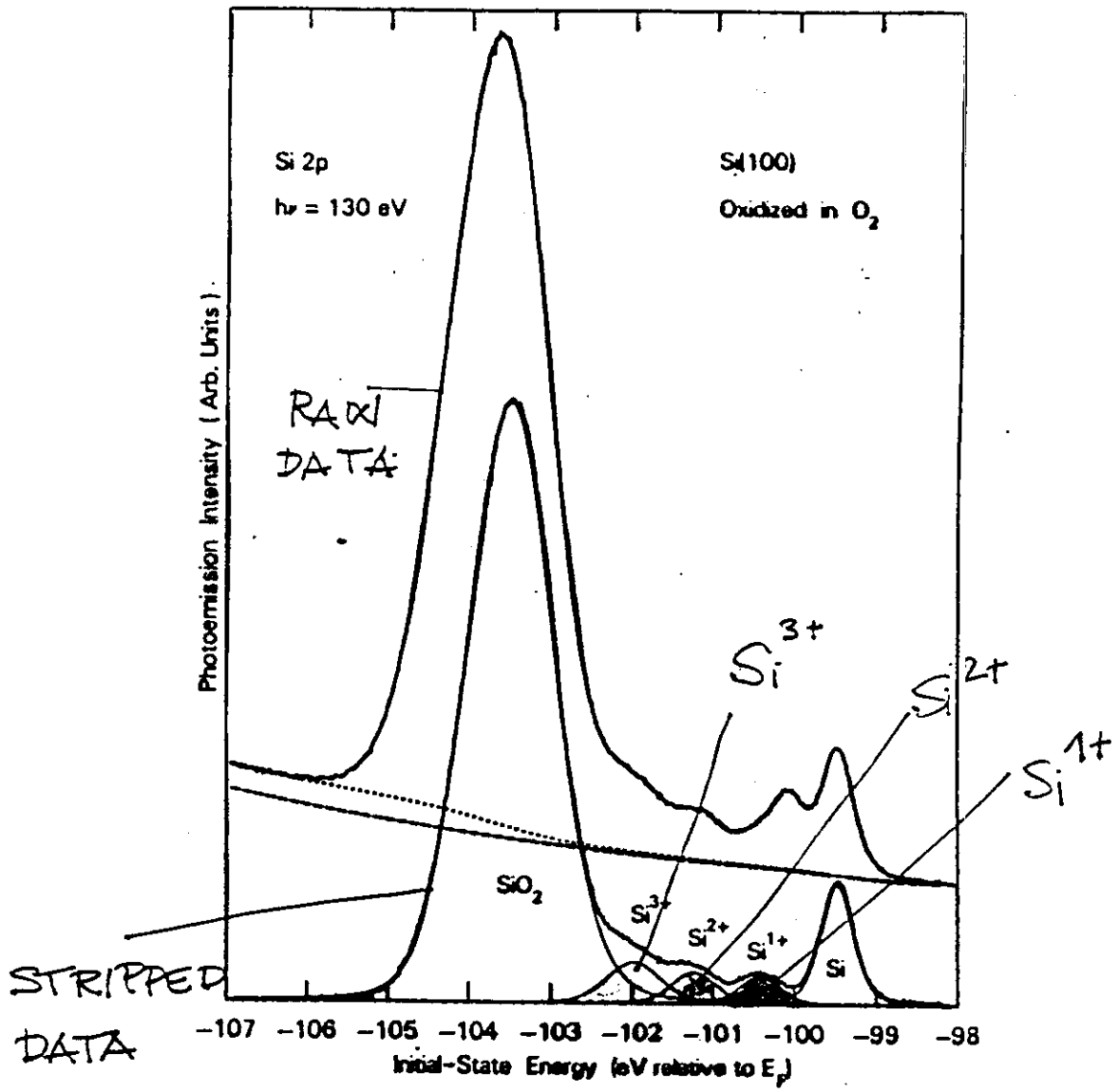

FIG. 1. Intermediate-oxidation states at the SiO_2/Si(100) interface, identified by their Si 2*p* core-level shifts. The top curve represents the raw photoemission data for the Si $2p_{1/2,3/2}$ core levels. The bottom curve has the Si $2p_{1/2}$ line and the secondary electron background subtracted. All three intermediate-oxidation states are seen. For a truncated bulk structure only Si^{2+} would be present since the Si(100) surface has two broken bonds per atom.

HIMPSEL ET AL PHYS REV. B 38 (1988) 6084

XPS Si 2p 3/2

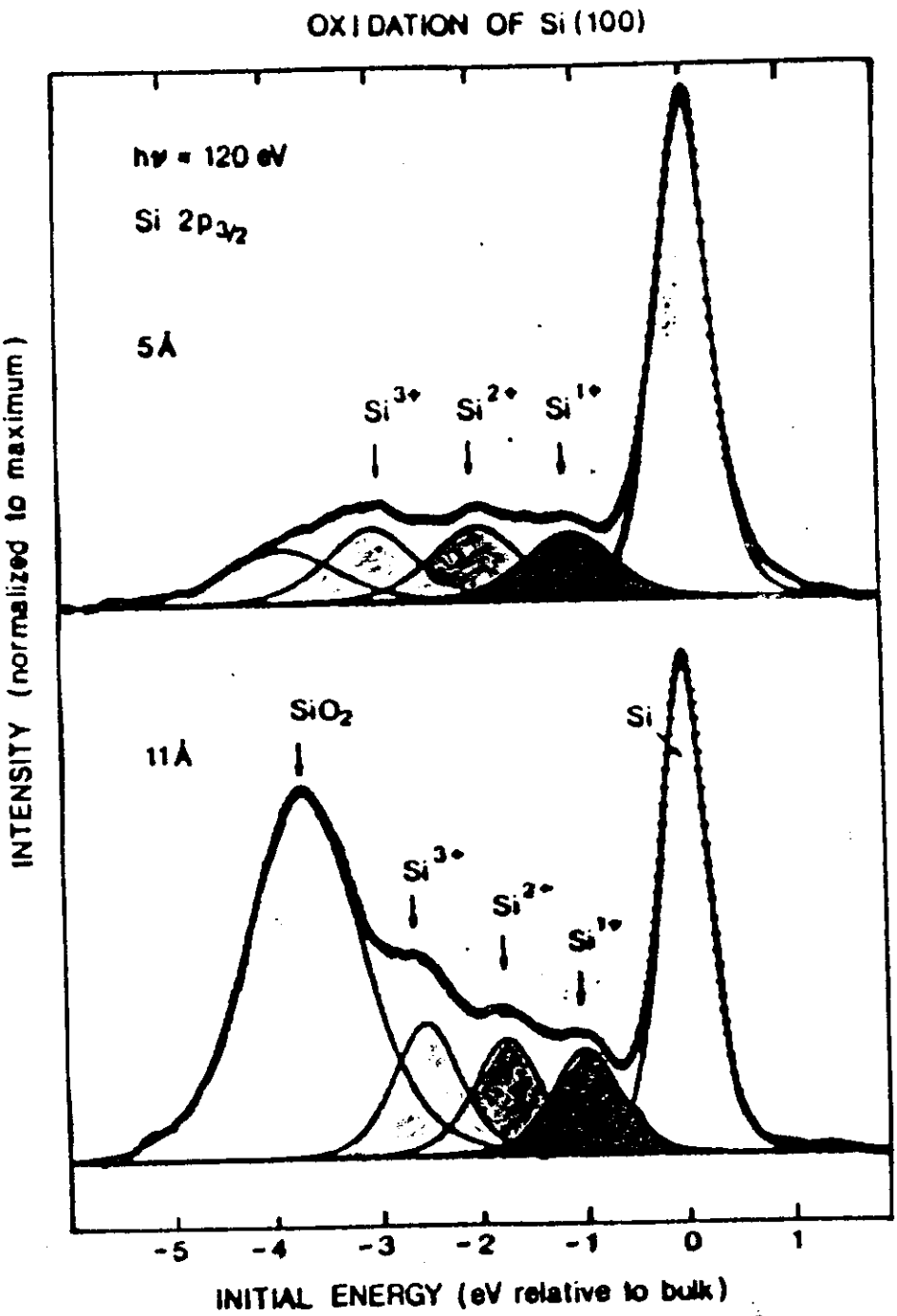

5 Å

11 Å

FIG. 3. Si $2p_{3/2}$ core level spectra for 5 and 11-Å-thick oxides decomposed into five components. The black crosses represent the experimental spectra and the solid lines indicate the theoretical functions and the different components.

XPS Si $2p_{3/2}$

Si(100) versus Si(111)

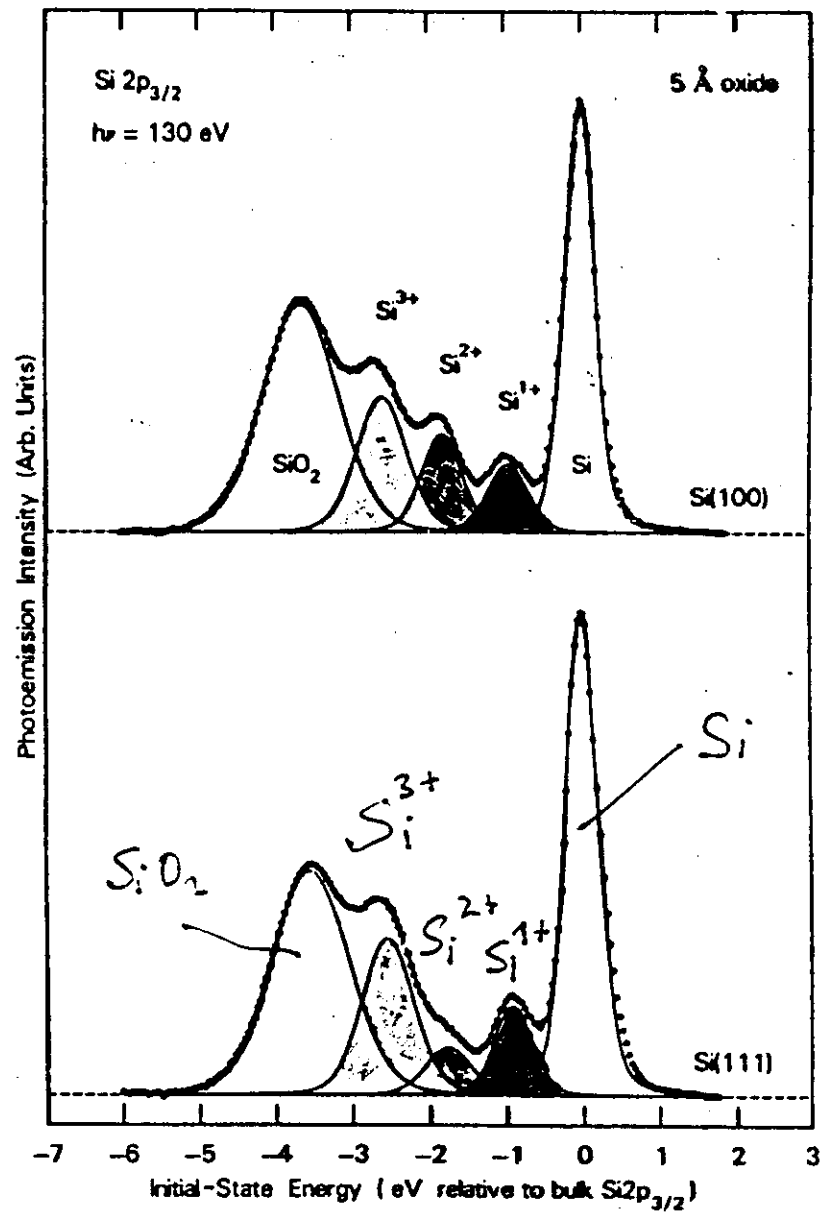

FIG. 4. Core-level spectra from ultrathin SiO_2 overlayers on Si(100) and Si(111) surfaces. The Si(111) substrate has less Si^{2+} and more Si^{1+} than the Si(100) substrate. Si^{3+} is enhanced by a factor of 1.7 at this photon energy due to a cross-section resonance (see Table II). The films were grown in 2×10^{-5} Torr O_2 at 750 °C for 20 sec.

XPS

Si 2p3/2

F on Si

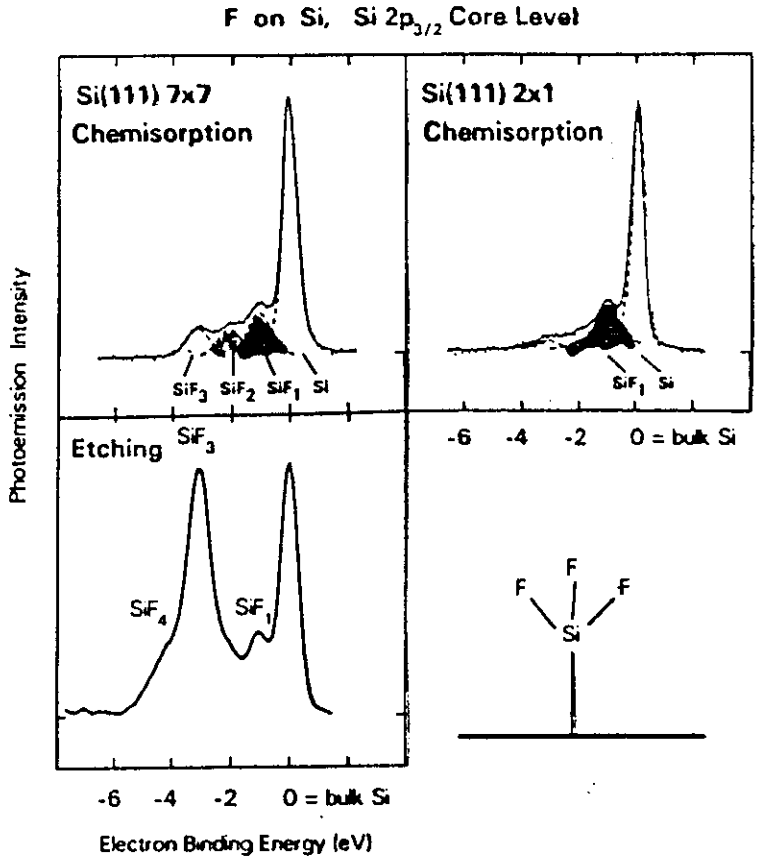

Fig. 6. Si $2p_{3/2}$ core level spectra for fluorine-exposed Si surfaces [21]. The Si $2p_{1/2}$ contribution has been subtracted. At low exposure, about a monolayer of fluorine is chemisorbed and exhibits a distribution of oxidation states that varies with the surface structure. At high exposure, where the surface is etched, one finds predominantly SiF_3 indicating that the removal of SiF_3 from the surface is the bottleneck of the etching reaction

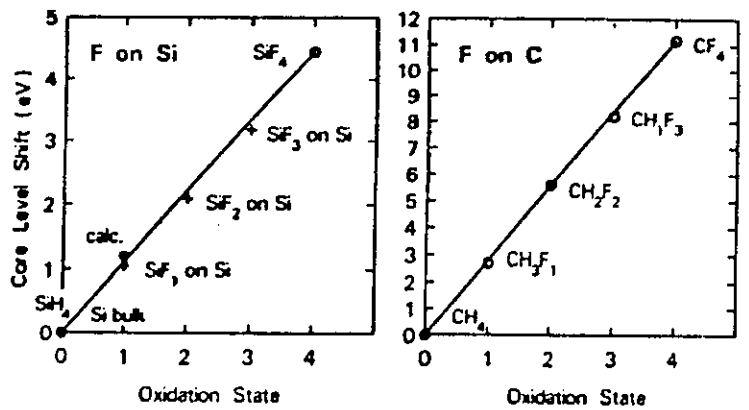

CORE LEVEL SHIFT versus OXIDATION STATE

Fig. 5. Linear relation between core level shift [18] and oxidation state for fluorinated silicon and carbon. Fluorine on Si surfaces (crosses, from [21]; see Fig. 6) exhibits similar core level shifts as expected from an interpolation between SiH_4 and SiF_4. The calculated shift (dot) is for a fluorine-terminated Si(111) 1 × 1 surface [22]

Mc FEELY & al PHYS. REV. B 30 (1984) 764

SURFACE ATOMS
Au 4f STATES

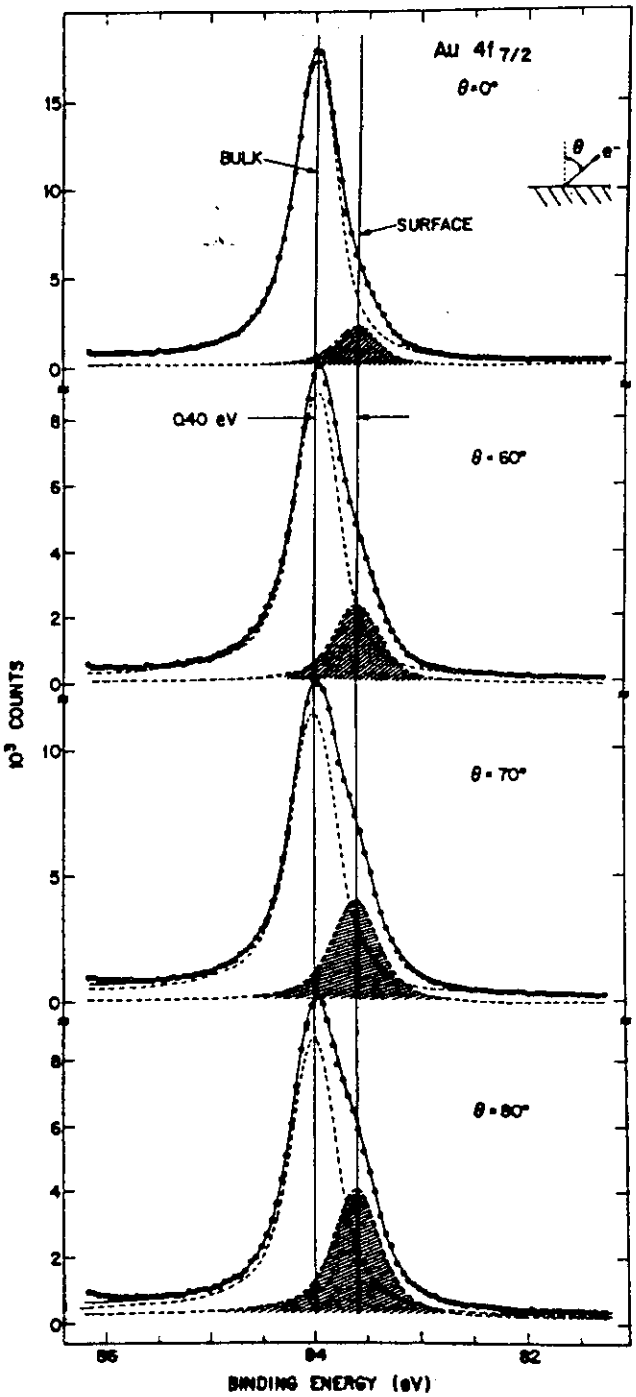

Least-squares fits to Au $4f_{7/2}$ photoemission data as a function of θ. Each spectrum was fitted *individually* assuming two lines of equal shape with all line-shape parameters and line positions freely adjustable. The surface component is shaded. Note excellent consistency in binding energy of the bulk and surface components for each data set.

SURFACE DOS

BULK DOS

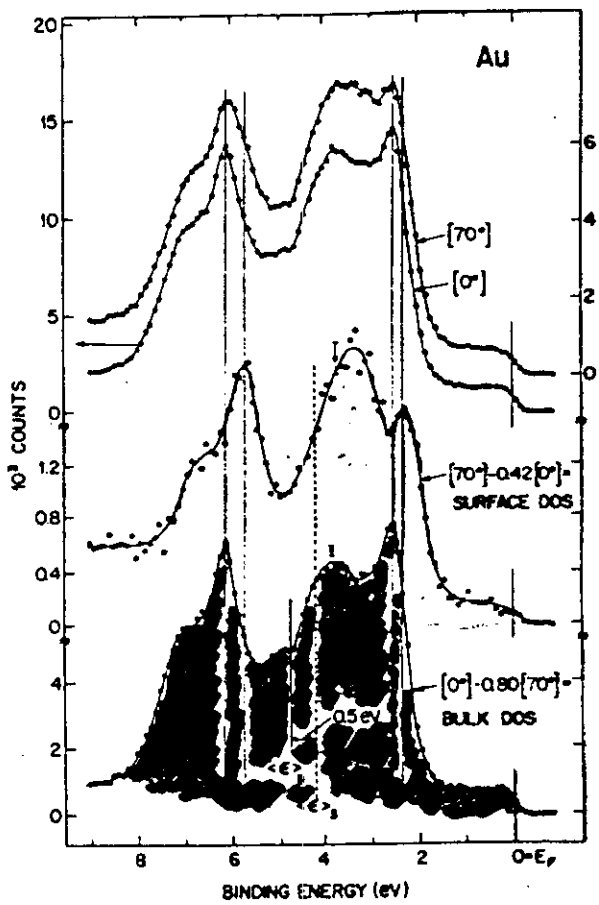

Separation of Au bulk and surface density of states from the difference between $\theta=0°$ and 70° spectra. Note different scales for raw data. Weighting factors 0.42 and 0.80 were determined from corresponding *core*-level spectra as in Fig. 2. Centers of gravity $\langle\epsilon\rangle$ for bulk and surface DOS are also shown.

$\vartheta = 0°$

$\vartheta = 60°$

$\vartheta = 70°$

$\vartheta = 80°$

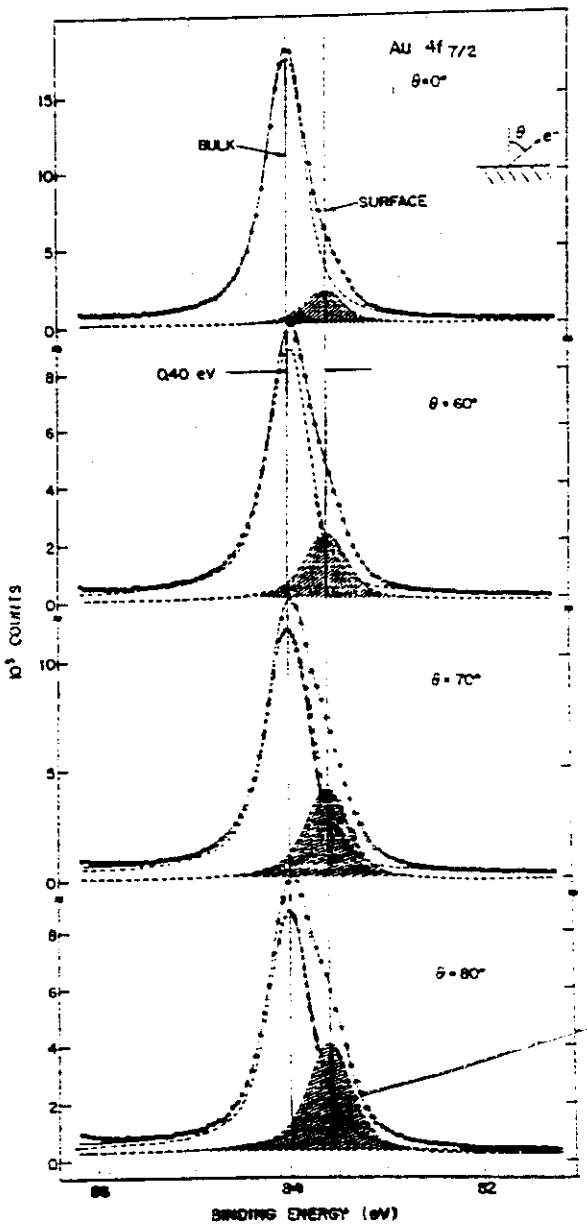

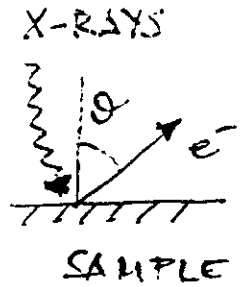

Al K_α RADIATION

SURFACE Au ATOMS

FIG. 3. Least-squares fits to Au $4f_{7/2}$ photoemission data as a function of θ. Each spectrum was fitted *individually* assuming two lines of equal shape with all line-shape parameters and line positions freely adjustable. The surface component is shaded. Note excellent consistency in binding energy of the bulk and surface components for each data set.

POLYCRYSTALLINE GOLD

Au $4f_{7/2}$ CORE LINE PHOTOEMISSION

BULK- VS SURFACE-SPECIFIC CORE LEVEL CONTRIBUTIONS

FROM P.H. CITRIN *et al.*, PHYS REV LETT 41 (1978) 1425

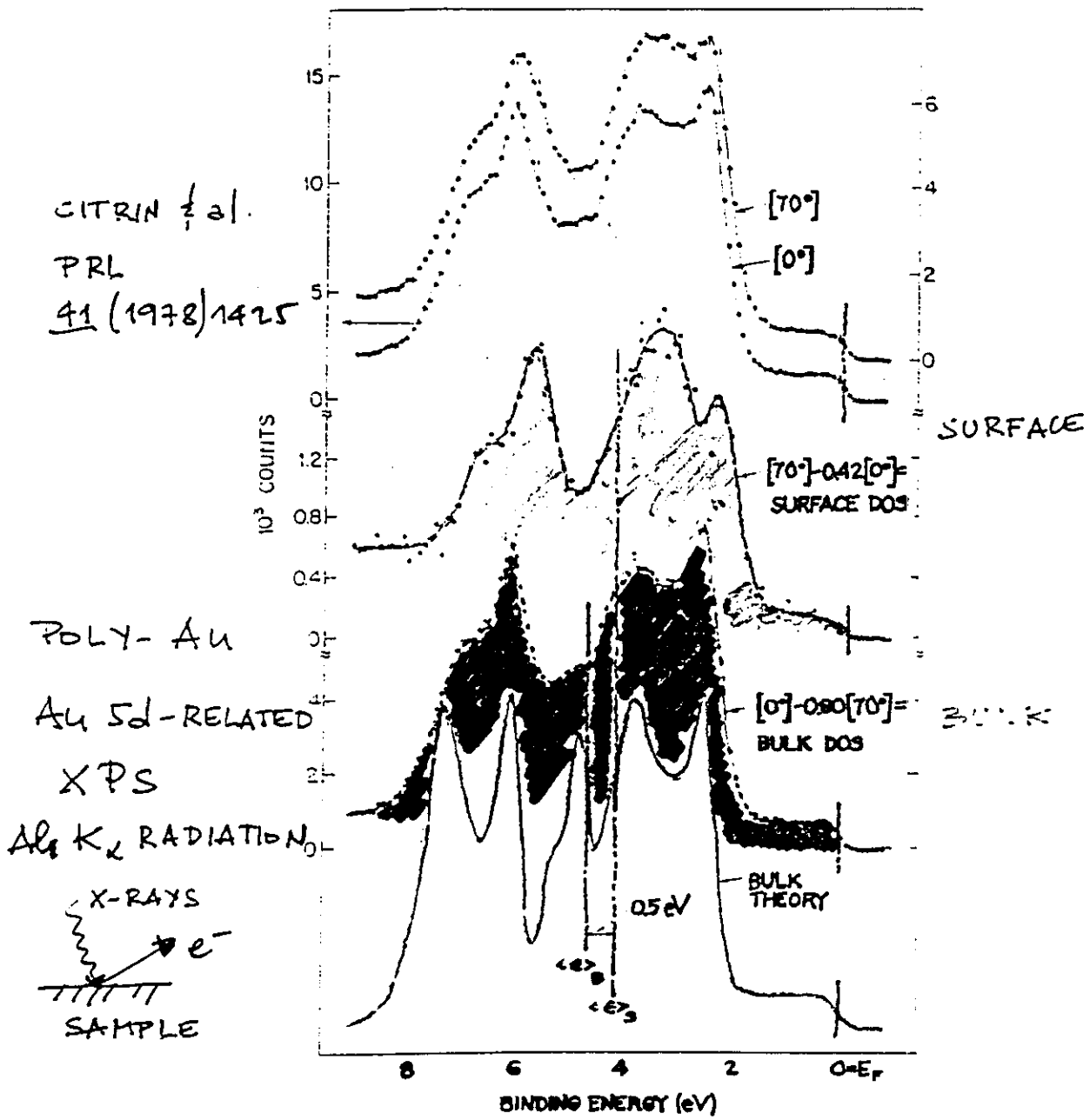

FIG. 3. Separation of bulk and surface DOS from the difference of 0° and 70° spectra (note scale assignments). The weighting factors were determined from the corresponding 0° and 70° *core*-level spectra as in Fig. 2. The bulk theory is from Ref. 16.

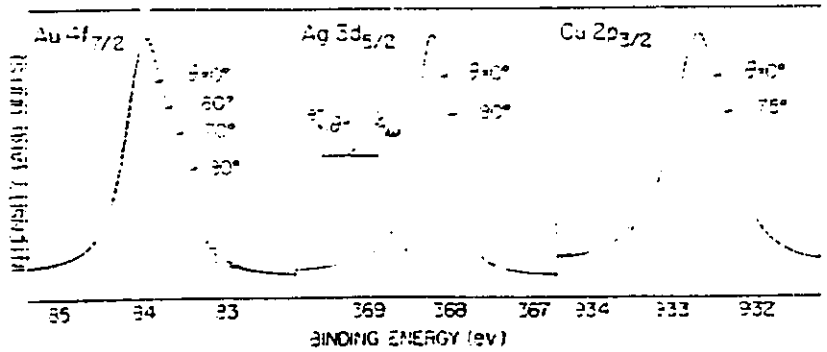

FIG. 1. Normalized x-ray photoemission spectra from Au, Ag, and Cu as a function of increasing surface sensitivity (increasing θ).

GaP (110)

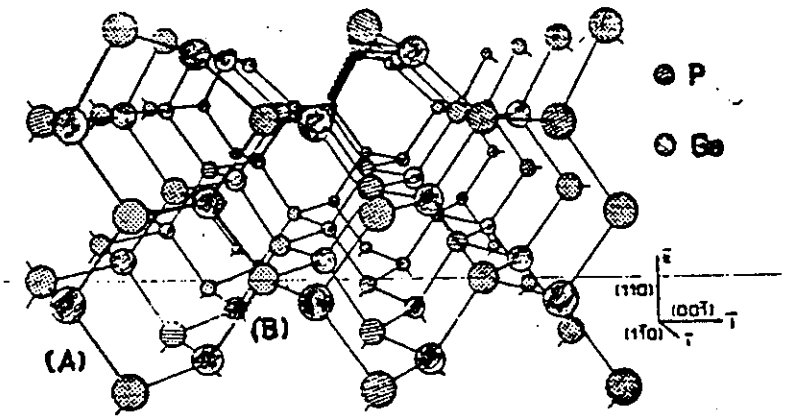

Side view of a slab of five GaP(110) layers. The surface layer is relaxed according to the rotation-relaxation model with a surface bond-rotation angle θ =27.5°. Chains of atoms along a (1$\bar{1}$0) plane passing either through P (chain *A*) or through Ga (chain *B*) surface atoms are shown.

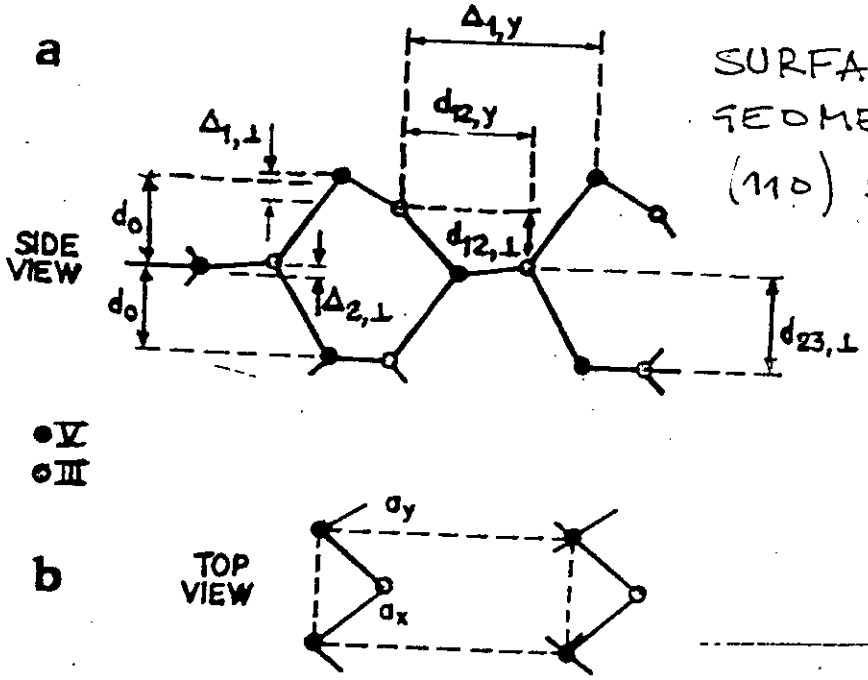

SURFACE ATOMIC GEOMETRY (110) SURFACE OF III-V SEMICONDUCTOR

Panel (a): Schematic indication of the surface atomic geometry for the (110) surface of III–V semiconductor compounds. The layer spacing is $d_0 = a_0/2\sqrt{2}$, where a_0 is the bulk lattice constant. Panel (b): Surface unit cell. Space lattice parameters are $a_y = a_0$ and $a_x = a_0/\sqrt{2}$, where a_0 is the bulk lattice constant.

SURFACE & BULK

CORE LINE COMPONENTS

As 3d
hν = 80eV

Ga 3d
hν = 60eV

As 3d
hν = 50eV

Ga 3d
hν = 28 eV

Sb
hν = 70eV

Ga 3d
hν = 60eV

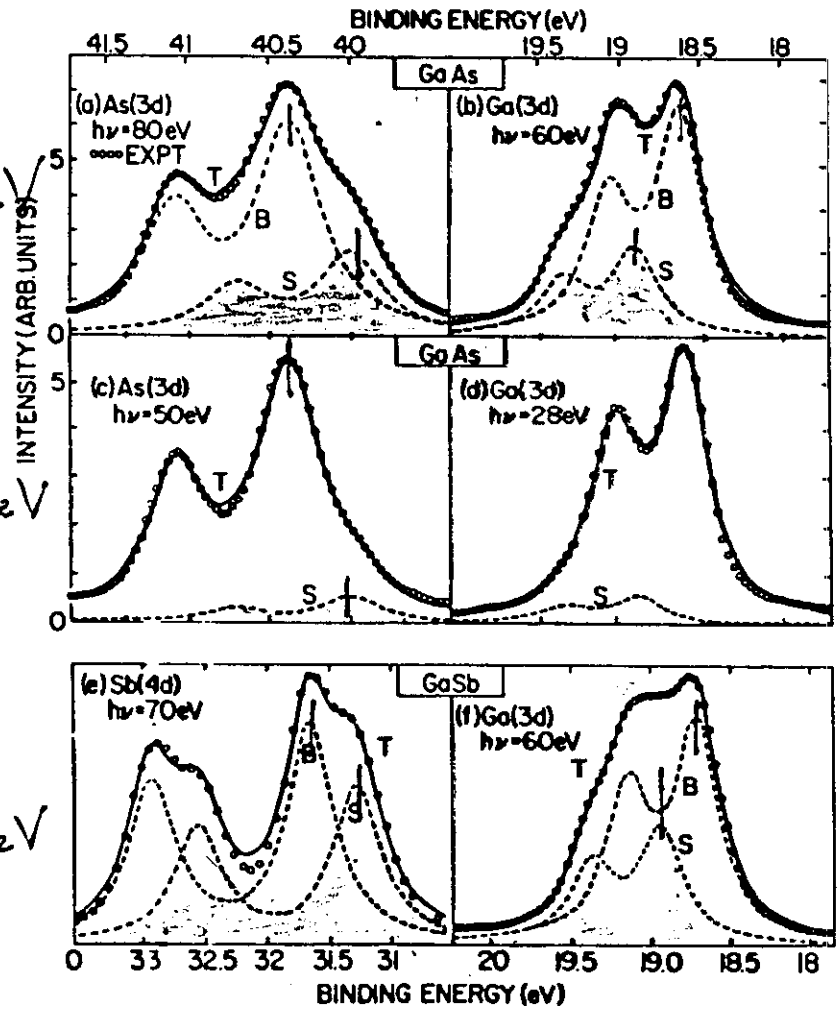

FIG. 1. Photoemission spectra for 3*d* and 4*d* core levels in GaAs(110) and GaSb(110). Spectra for low photon energies (~10 eV above threshold) show mainly bulk emission (B) while spectra for higher photon energies (~40 eV above threshold, small escape depth) show additional surface core-level emission (S). BG denotes the inelastic secondary-electron background.

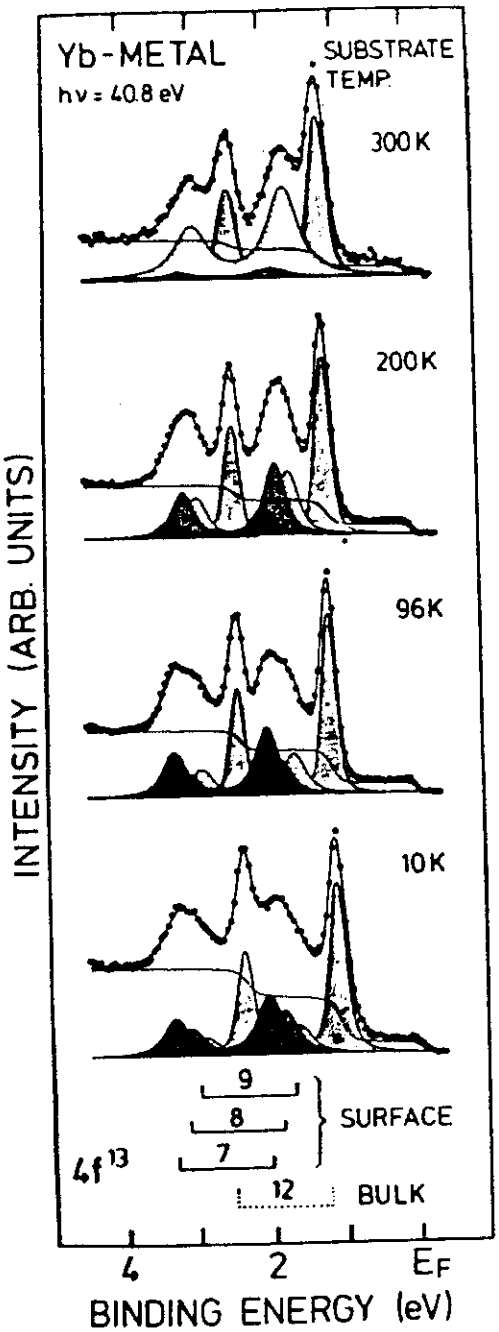

BULK ATOMS
Yb 4f STATES

FIG. 1. Valence-band photoemission spectra of evaporated Yb metal at different substrate temperatures. The heavy solid line represents the result of a least-squares-fit analysis of the data points of four $4f^{13}$ final-state multiplets originating from the bulk [light solid curve (dotted bar diagram)] and the surface [shaded curve areas (solid bar diagram)]. The dotted line represents the integral background. The correlation between the surface peaks and the corresponding surface atom coordination numbers is indicated. Note the strong intensity variation of the surface peaks with substrate temperature.

COORDINATION DEPENDENCY
OF Yb-4f STATES
IN Yb-METAL

INTERFACE GROWTH STUDIED VIA CORE LEVEL XPS AS A FUNCTION OF THE ELECTRON ESCAPE DEPTH

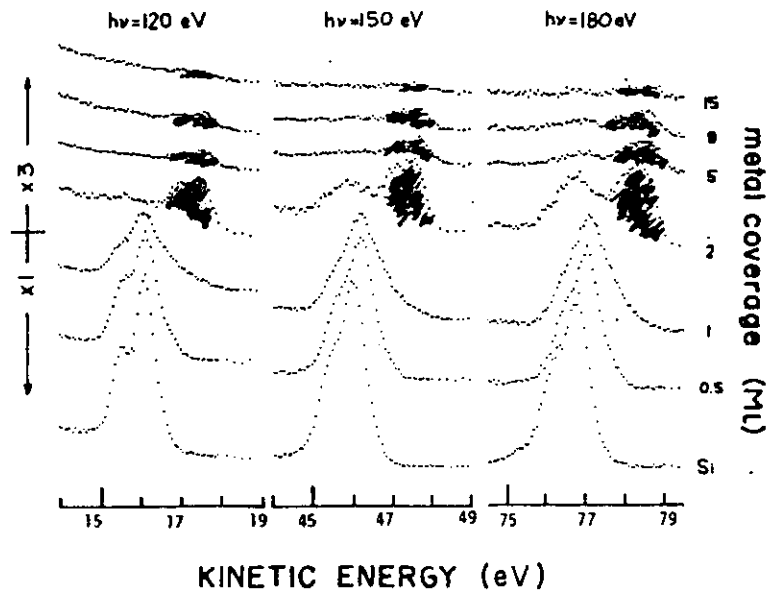

Fig. 58. Si 2p photoemission as a function of the photoelectron escape depth parameter, and of the coverage at the Eu–Si(111) interface. Tails of chemically shifted signal are seen, at lower binding energy of the bulk Si peak, already at 0.5 ML, but a fully shifted reacted component is manifest above 1 ML [161].

EUROPIUM / Si(111)

Si 2p XPS

[redacted] REACTED COMPONENT

CLEAN Si

REACTED PHASE

Si SEGREGATED

CERIUM / Si (111)

Si 2p XPS

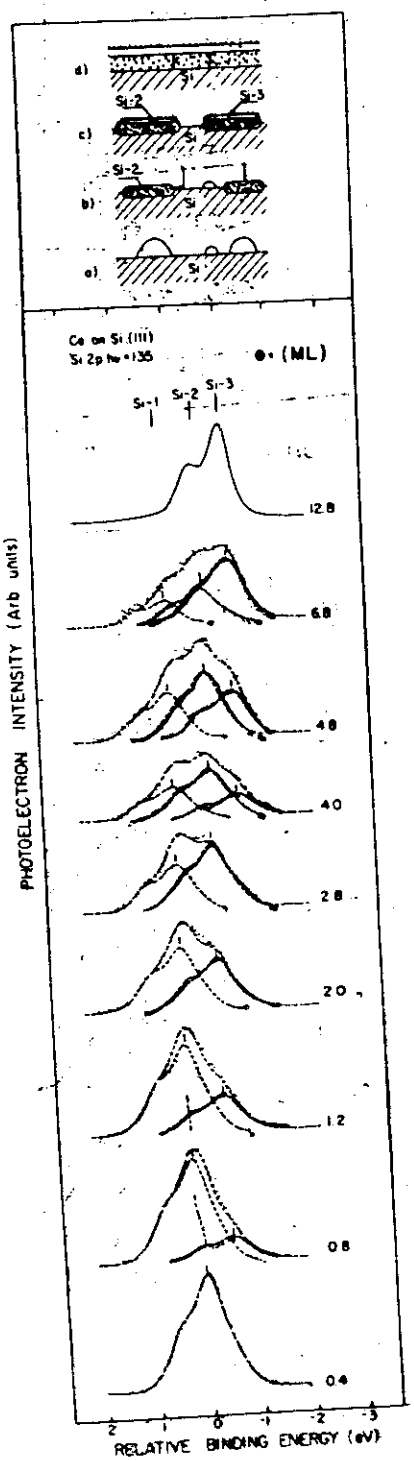

Fig. 69. Si2p core photoemission spectra for Sm–Si(111) interfaces. The spectra are fitted with components representing clean Si (Si-1), a reacted phase (Si-2), and surface segregated Si (Si-3). The model for the interface proposed by Grioni et al. is represented in the top panel of the figure [170].

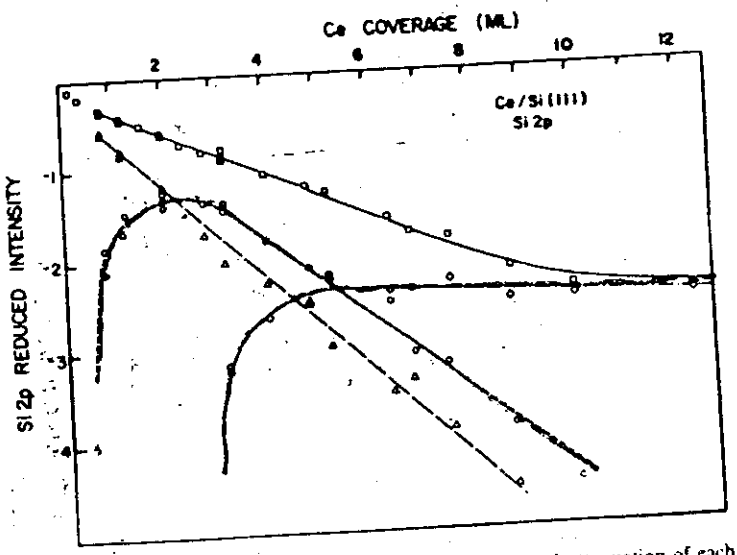

Fig. 70. Attenuation of the total Si2p emission (solid line at top) and attenuation of each of the three Si2p components deconvoluted in fig. 69. Although the substrate attenuation is monotonic, the reacted component grows to a maximum near 2.5 ML and is then attenuated. The surface segregated component appears only after the reacted component is covered up by Ce and is nearly constant in magnitude to high coverage [170].

PLASMA-TREATED STAINLESS STEELS

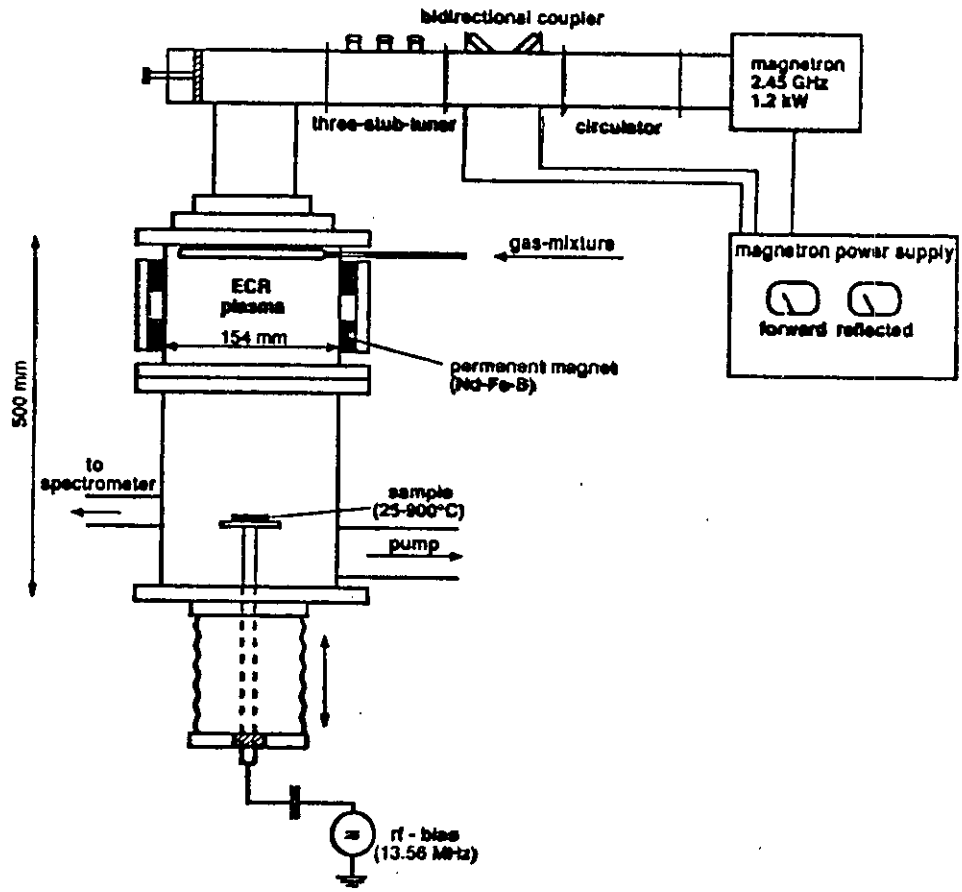

Fig. 1. Experimental set-up of the ECR plasma chamber.

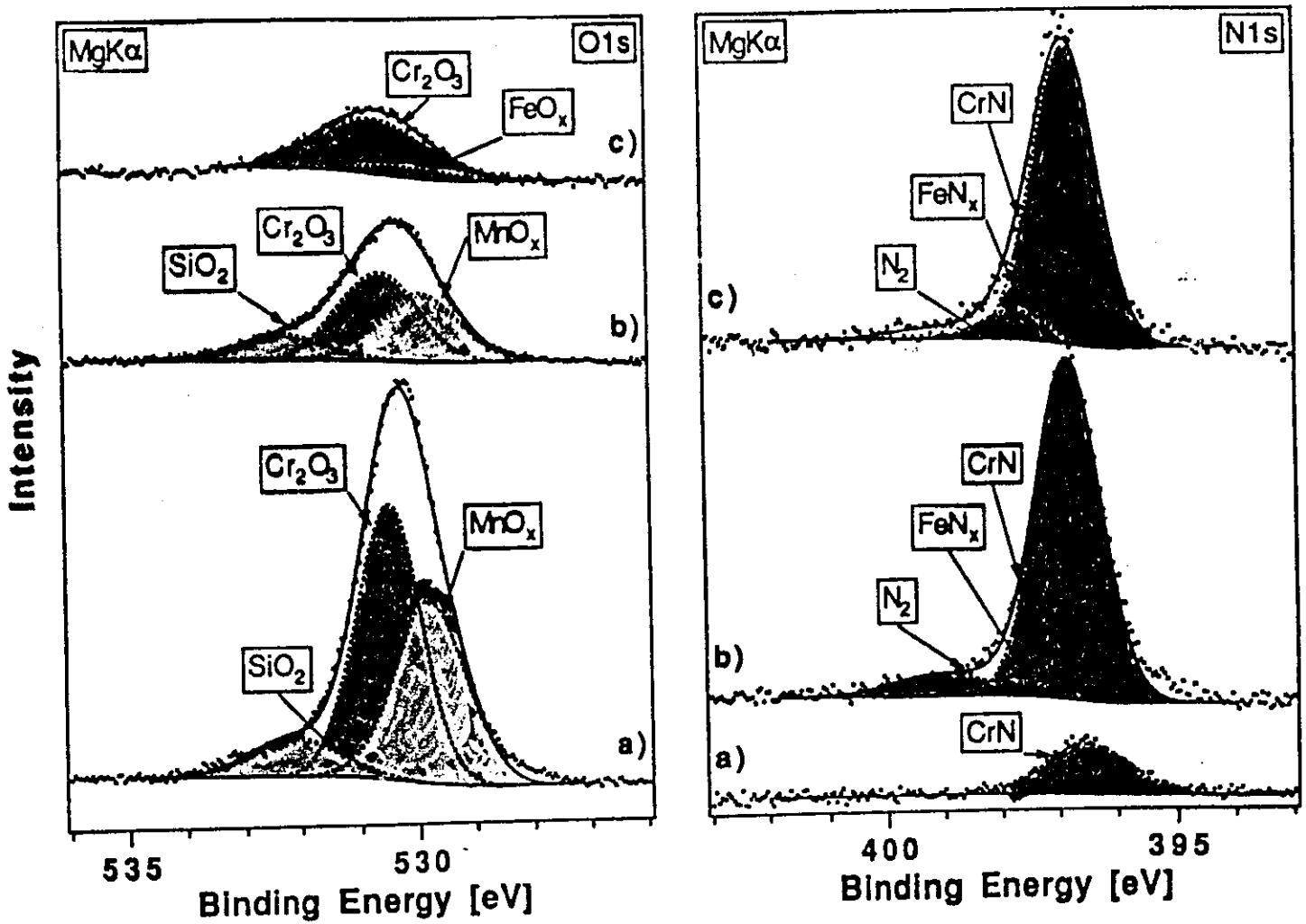

Fig. 8. Curve fitting for the N 1s and O 1s photoemission spectra of AISI 440C after treatment at $T = 600°C$ in: (a) N_2 gas; (b) N_2 plasma without bias ($U_s = 0$ V); (c) N_2 plasma with bias ($U_s = -100$ V).

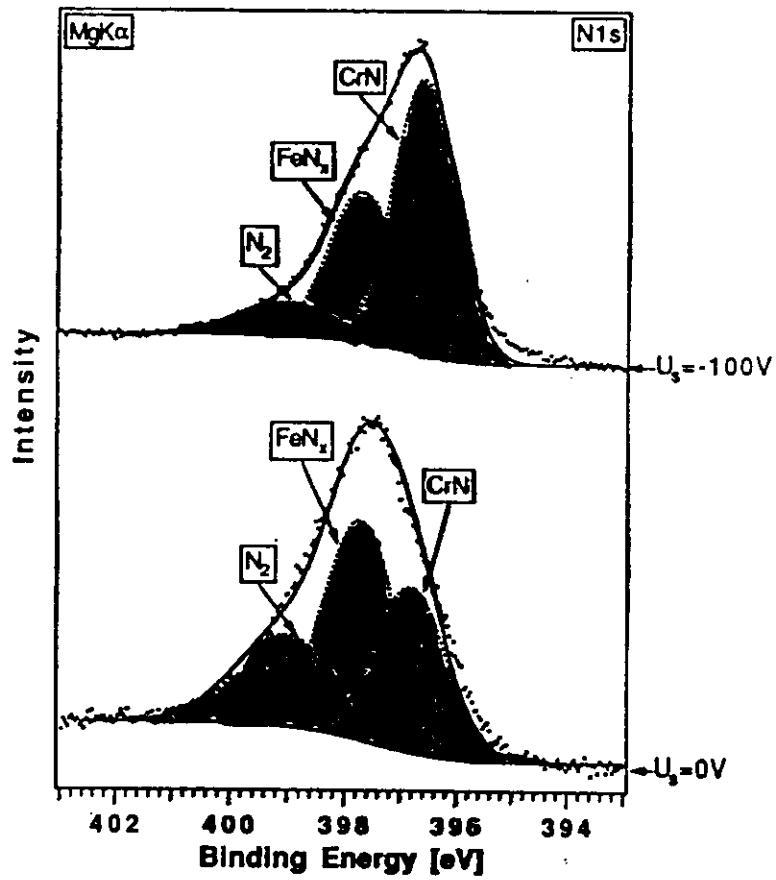

Fig. 5. Curve fitting for the N1s photoemission spectra of AISI 440C after N_2 plasma treatment at room temperature, with and without bias U_s.

P. GRÖNING, S. NOVAK, & L. SCHLAPBACH
APPL. SURF. SCIENCE 64 (1993) 265

NON EVAPORABLE GETTERING ALLOYS

METALLIC Zr

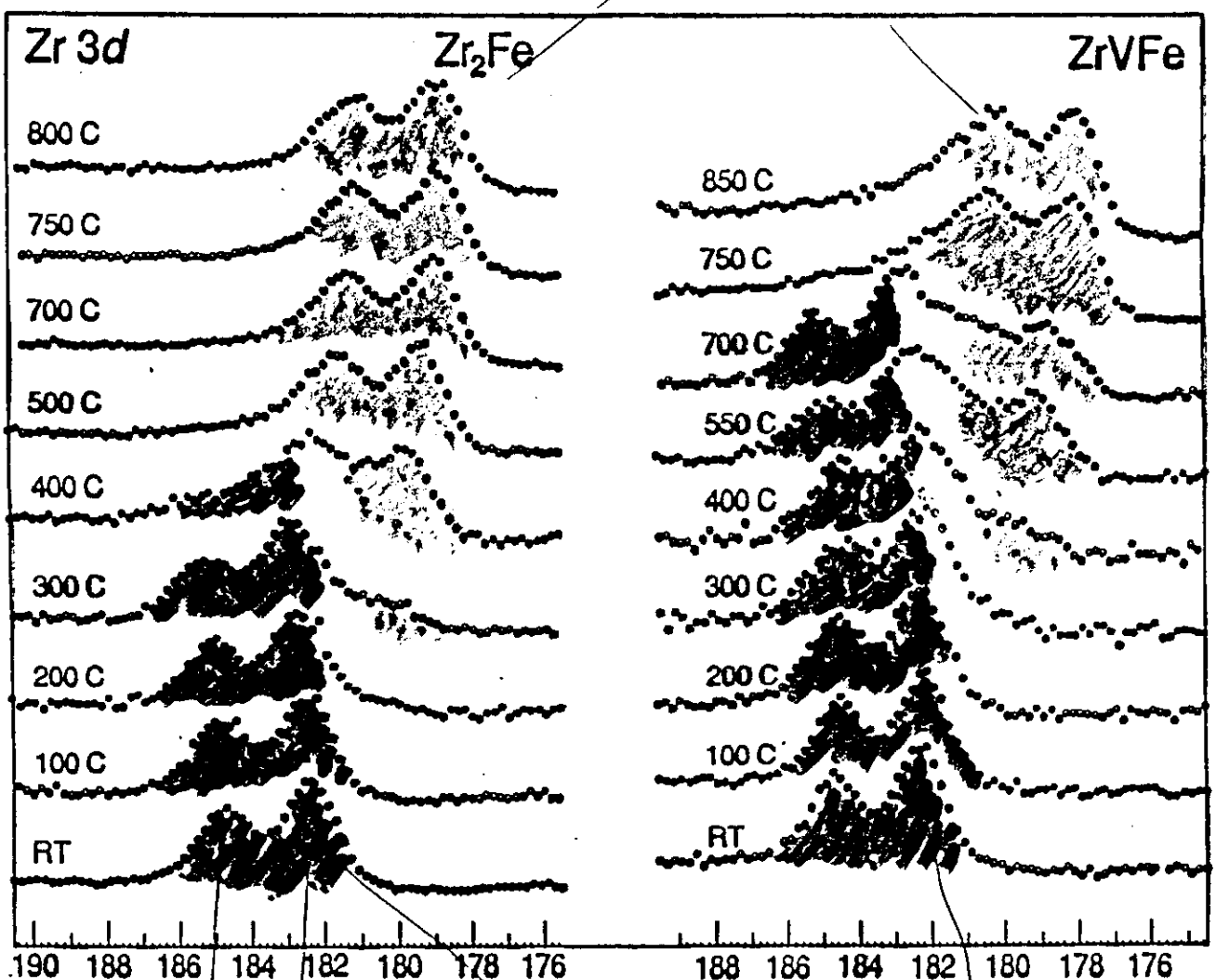

J. KOVAČ, D. SAKHO, P. MANINI, & M. SANCROTTI
CIRF & INT. ANALYSIS (1994)

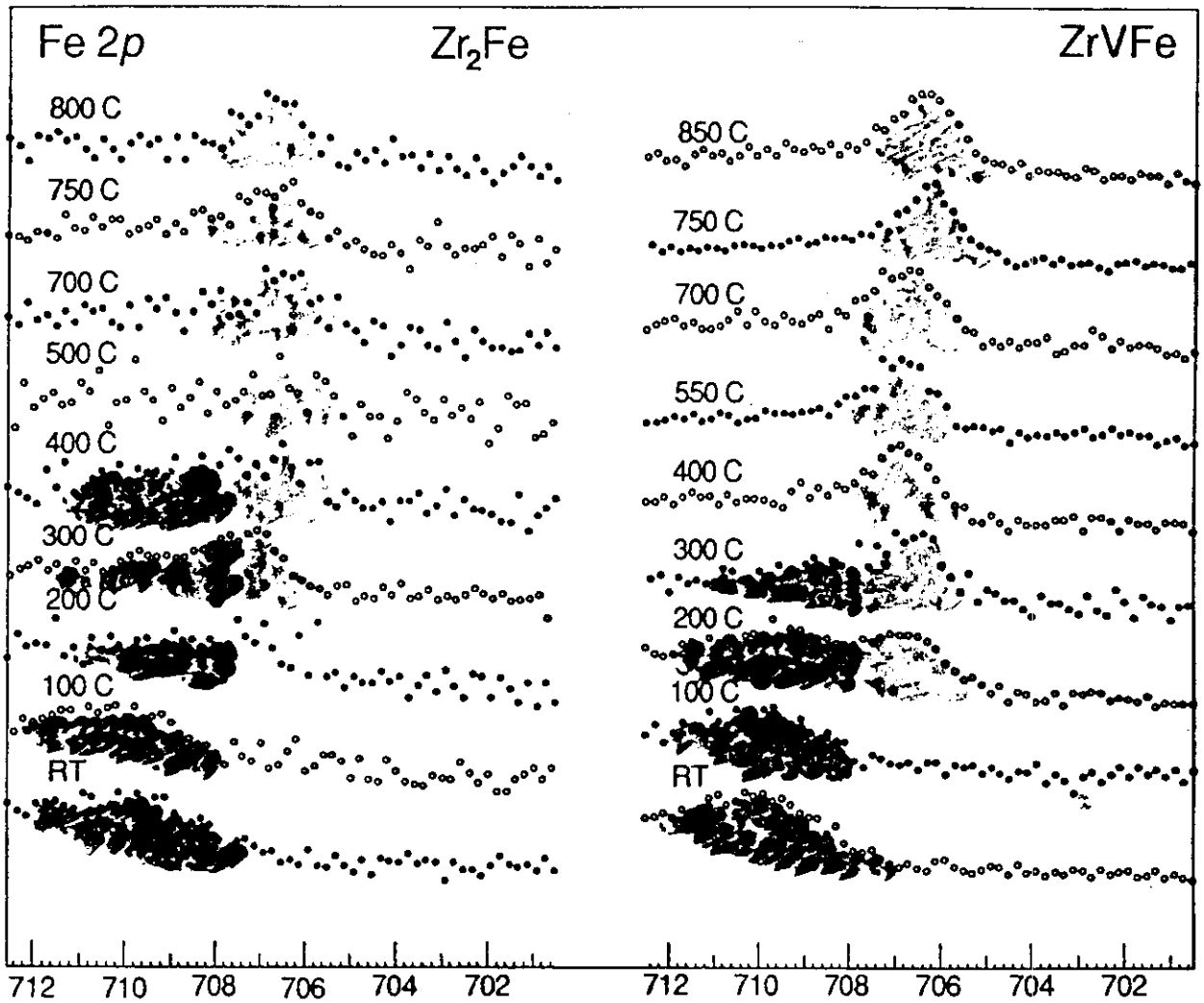

OXIDIZED IRON

METALIC IRON

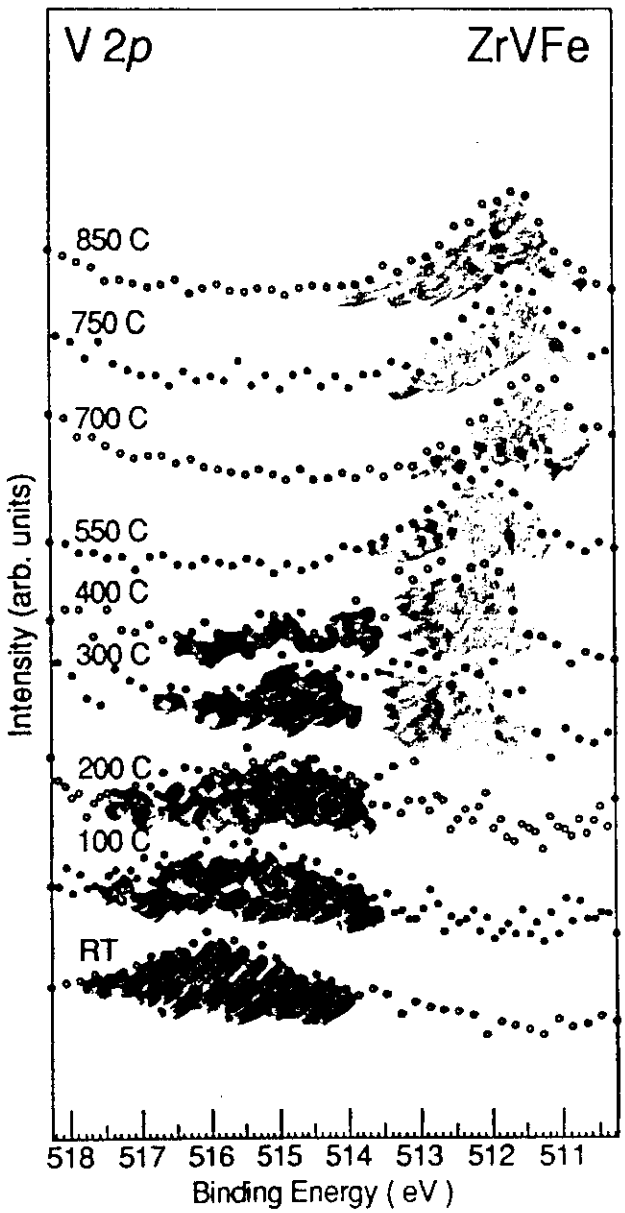

OXIDIZED VANADIUM

METALLIC VANADIUM

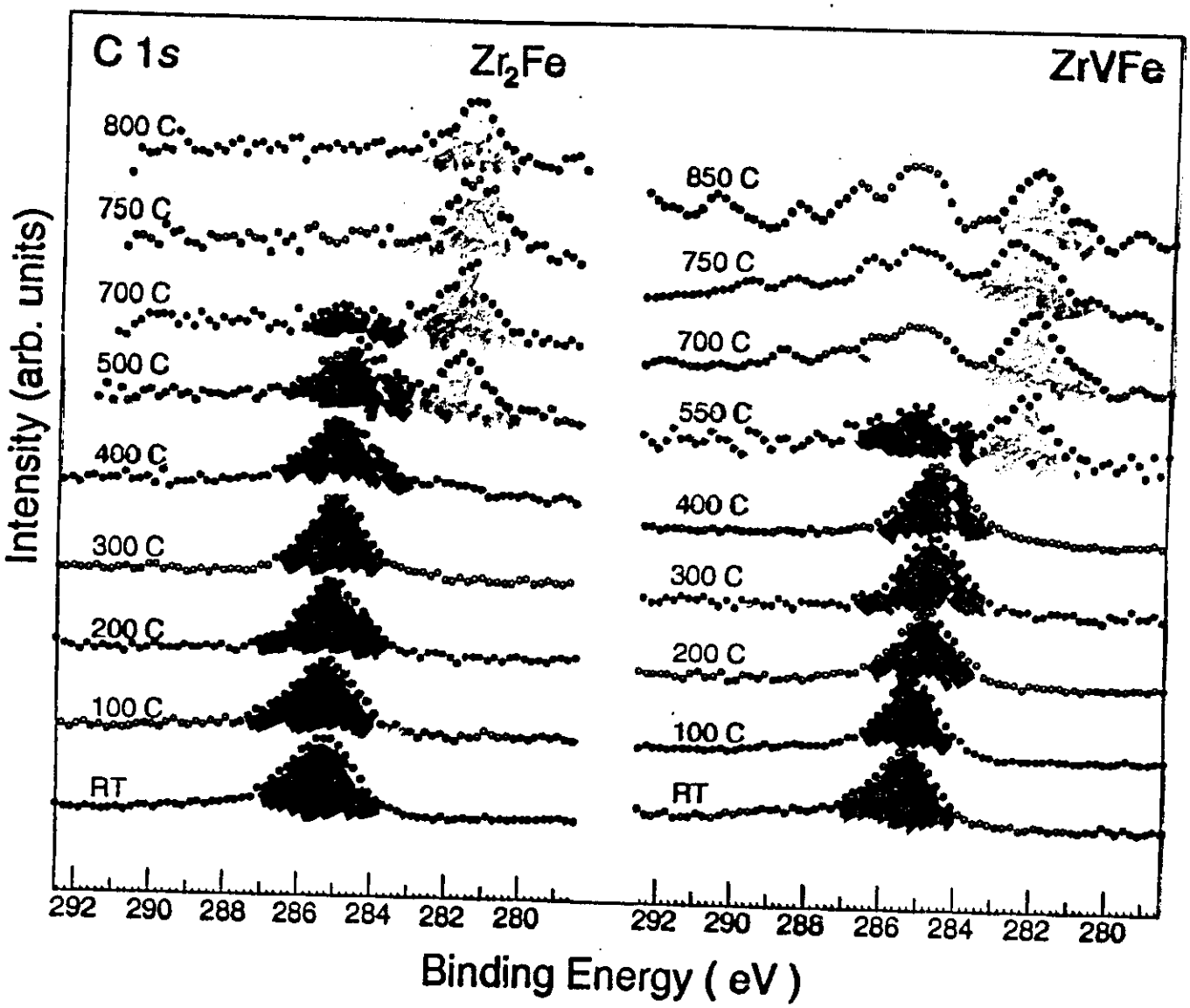

METAL CARBIDES

GRAPHITIC CARBON

C-BASED CONTAMINANTS

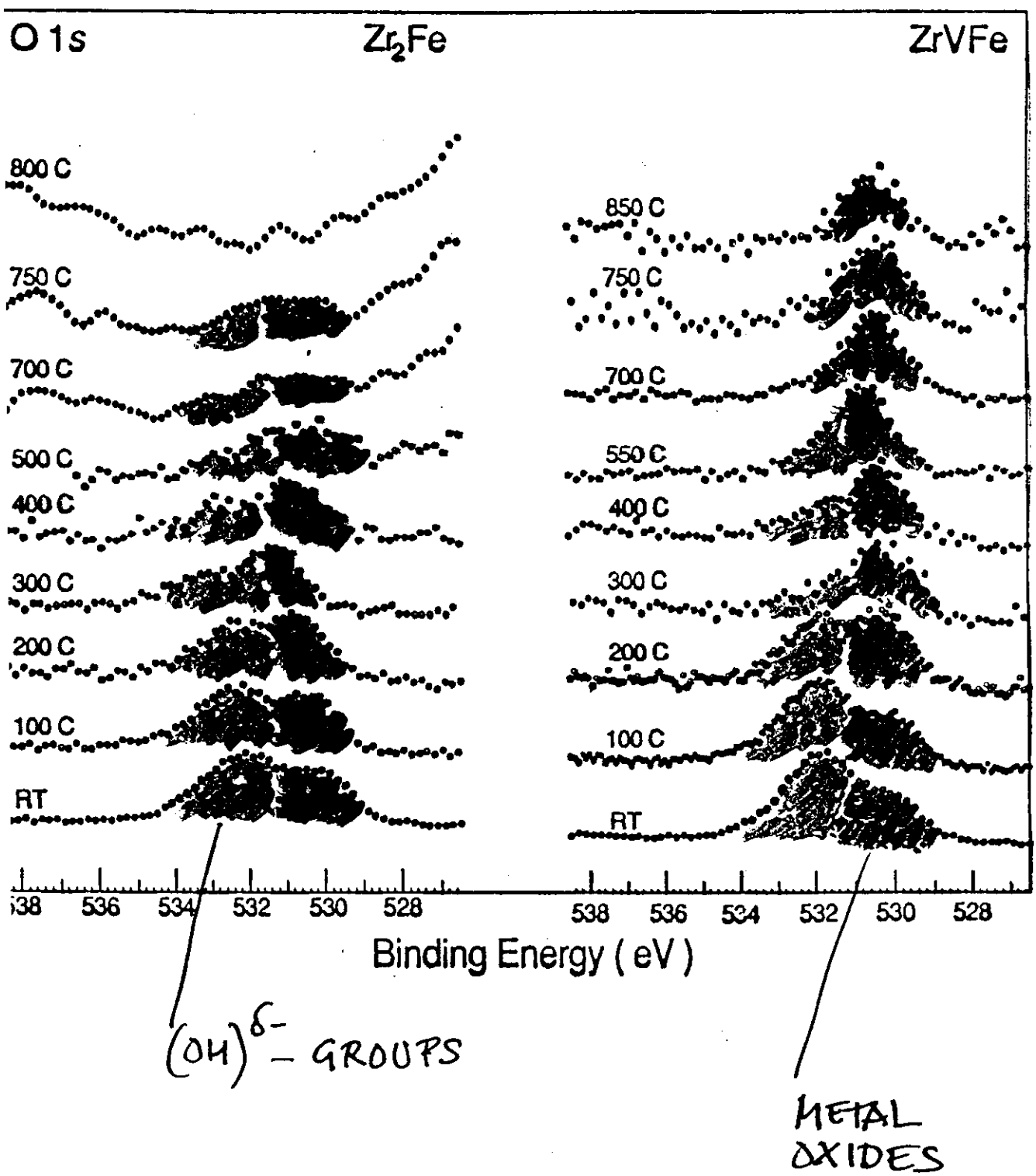
(OH)δ− GROUPS
METAL OXIDES
O 1s
Zr2Fe
ZrVFe
800 C
750 C
700 C
500 C
400 C
300 C
200 C
100 C
RT
850 C
750 C
700 C
550 C
400 C
300 C
200 C
100 C
RT
538 536 534 532 530 528
538 536 534 532 530 528
Binding Energy (eV)
(OH)δ− GROUPS
METAL OXIDES

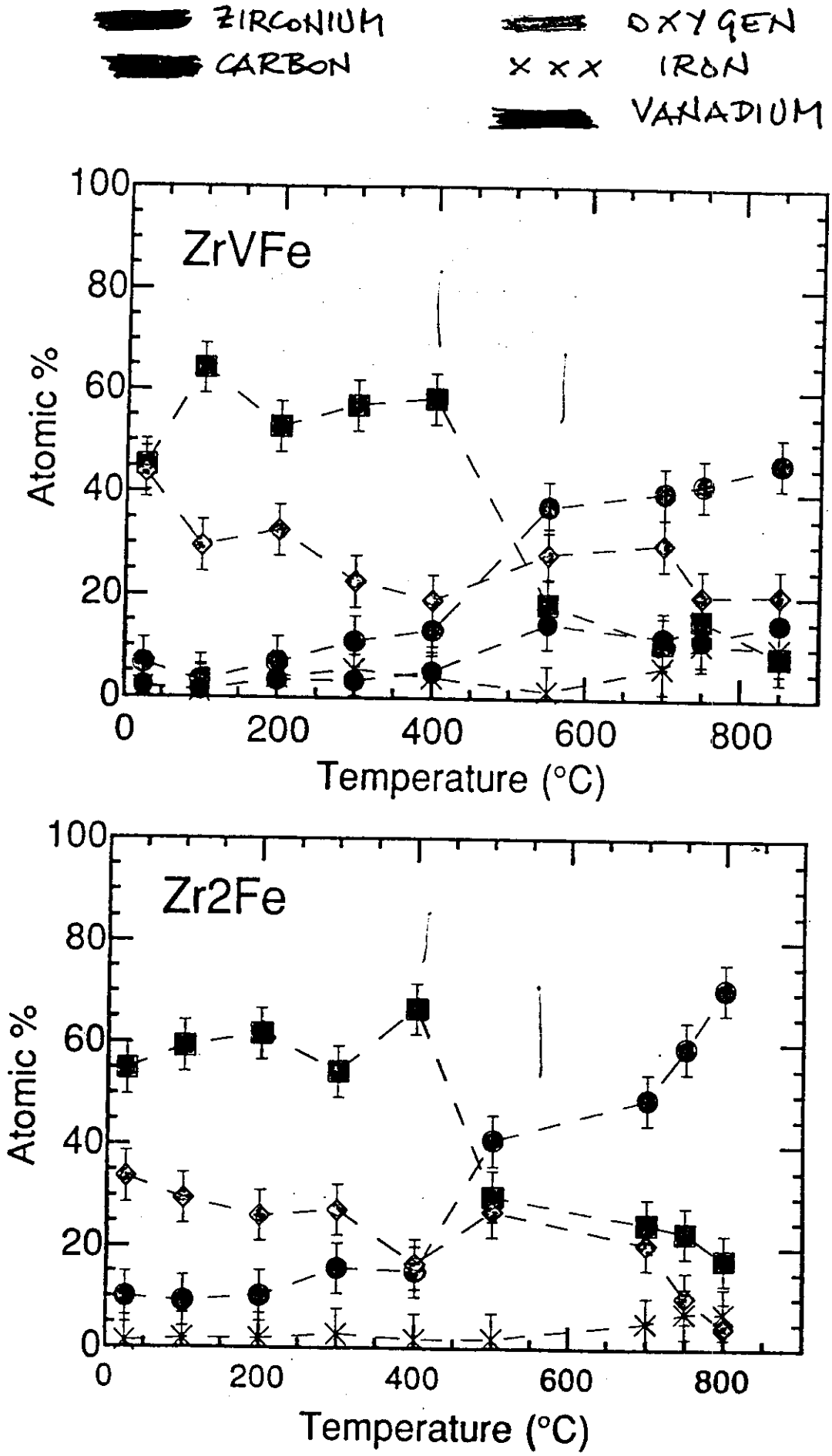
ZIRCONIUM
CARBON
OXYGEN
IRON
VANADIUM
ZrVFe
Atomic %
Temperature (°C)
Zr2Fe
Atomic %
Temperature (°C)
0
20
40
60
80
100
0
200
400
600
800

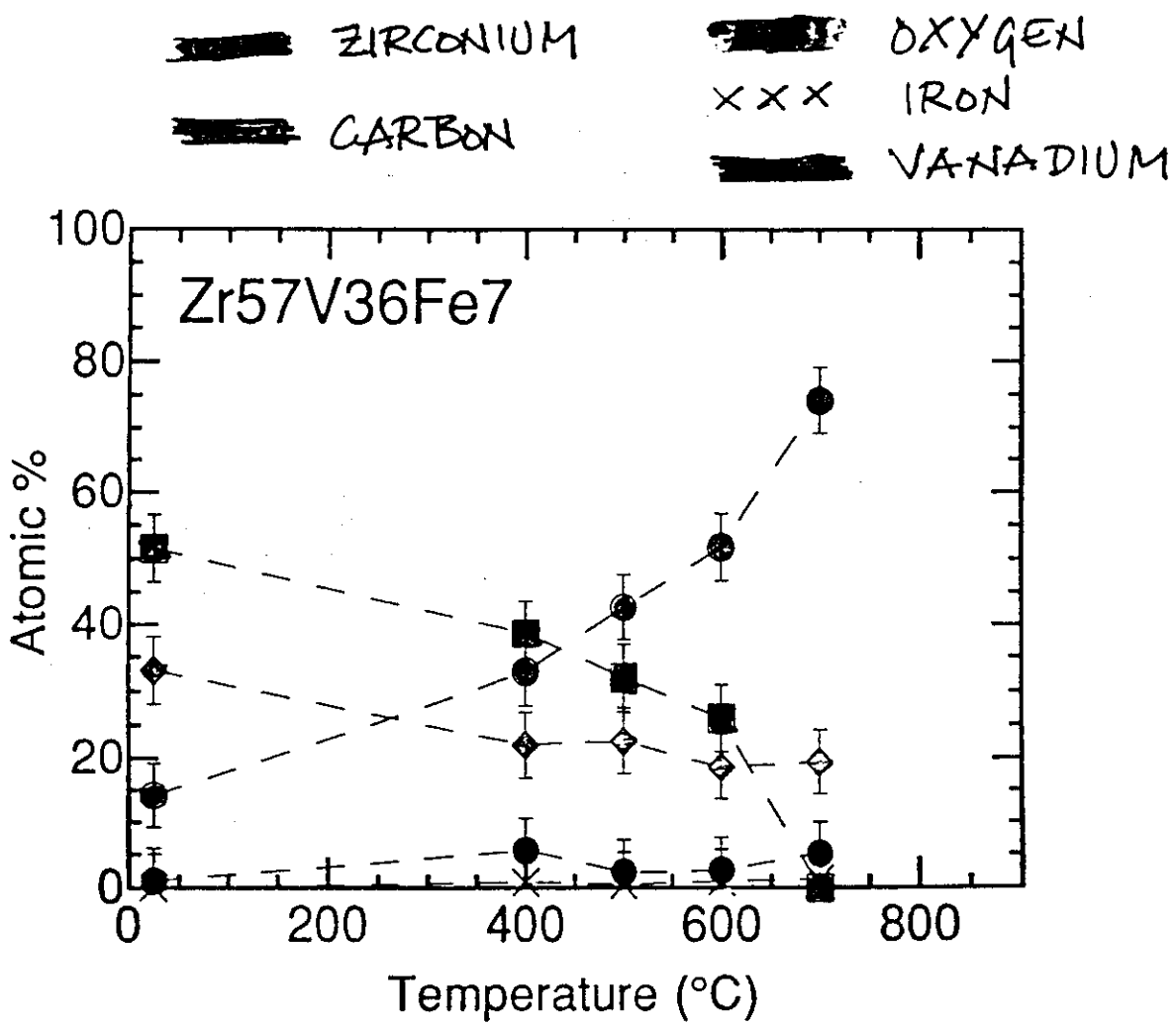
ZIRCONIUM
OXYGEN
CARBON
IRON
VANADIUM
Zr57V36Fe7
Atomic %
Temperature (°C)
0
20
40
60
80
100
0
200
400
600
800

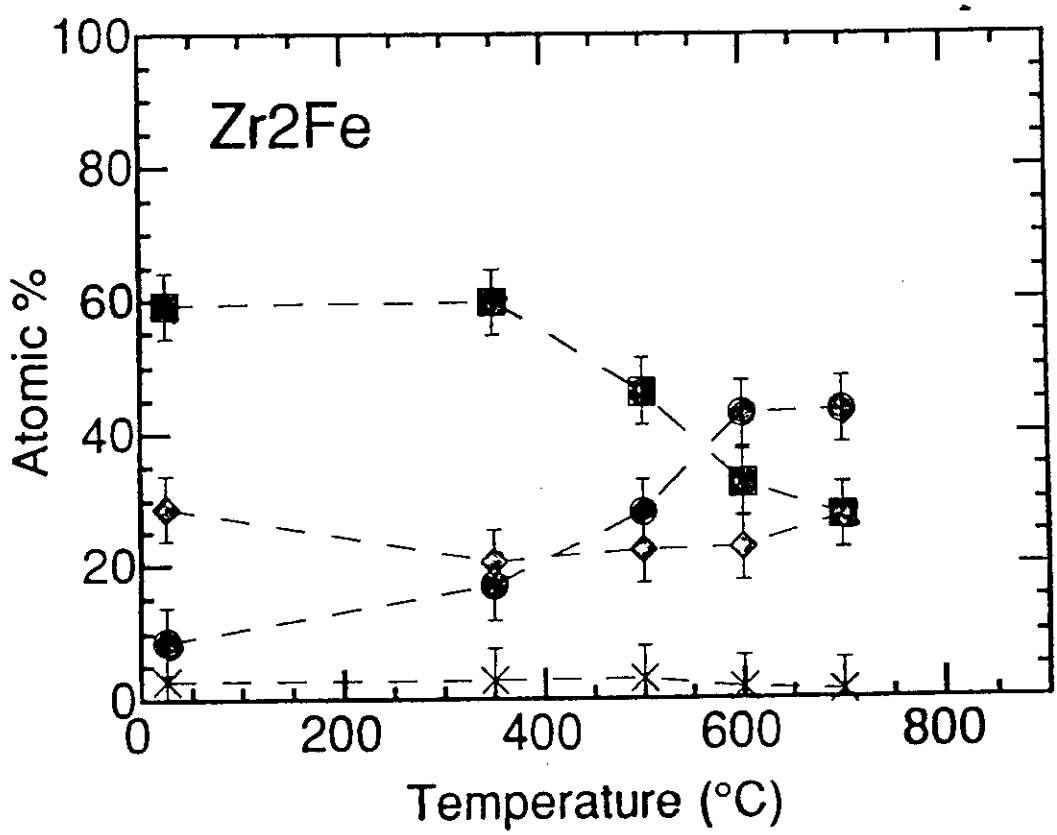
Zr2Fe
Atomic %
Temperature (°C)
0
20
40
60
80
100
0
200
400
600
800

ELECTRON SPECTROSCOPIES

&

ION SPUTTERING

DEPTH PROFILING

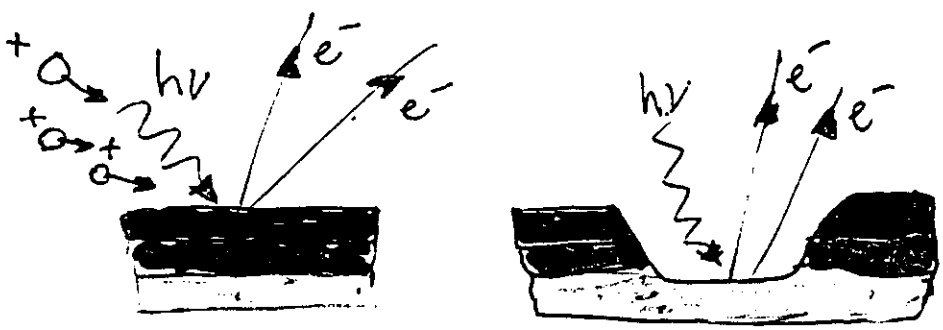

SPECTROSCOPIC SIGNAL

versus

SPUTTERING TIME

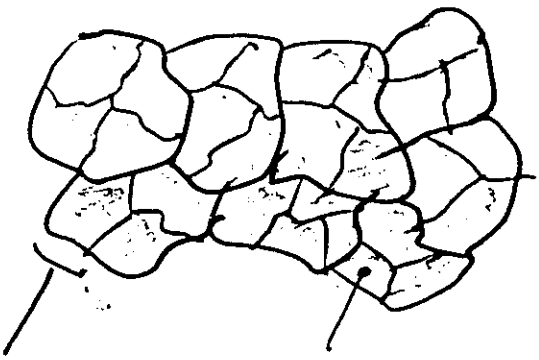

POWDER GRAIN

SINGLE CRYSTAL GRAIN

SCRAPING

↓

INTERGRANULAR PHYSICS, PRIMARILY

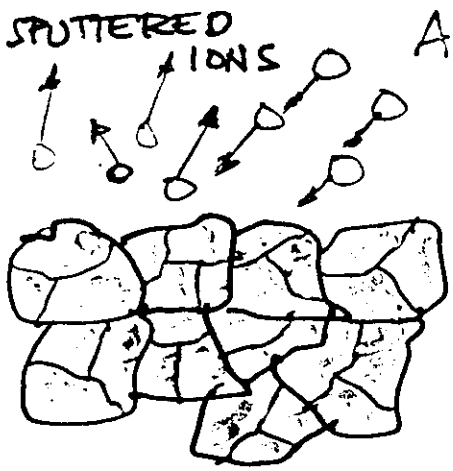

LAYER-BY-LAYER EROSION

SPUTTERING

↓

INTRAGRANULAR PHYSICS

WATER-PROCESSED
$Zr[V_{0.5}Fe_{0.5}]_2$ ALLOY AFTER SPUTTERING

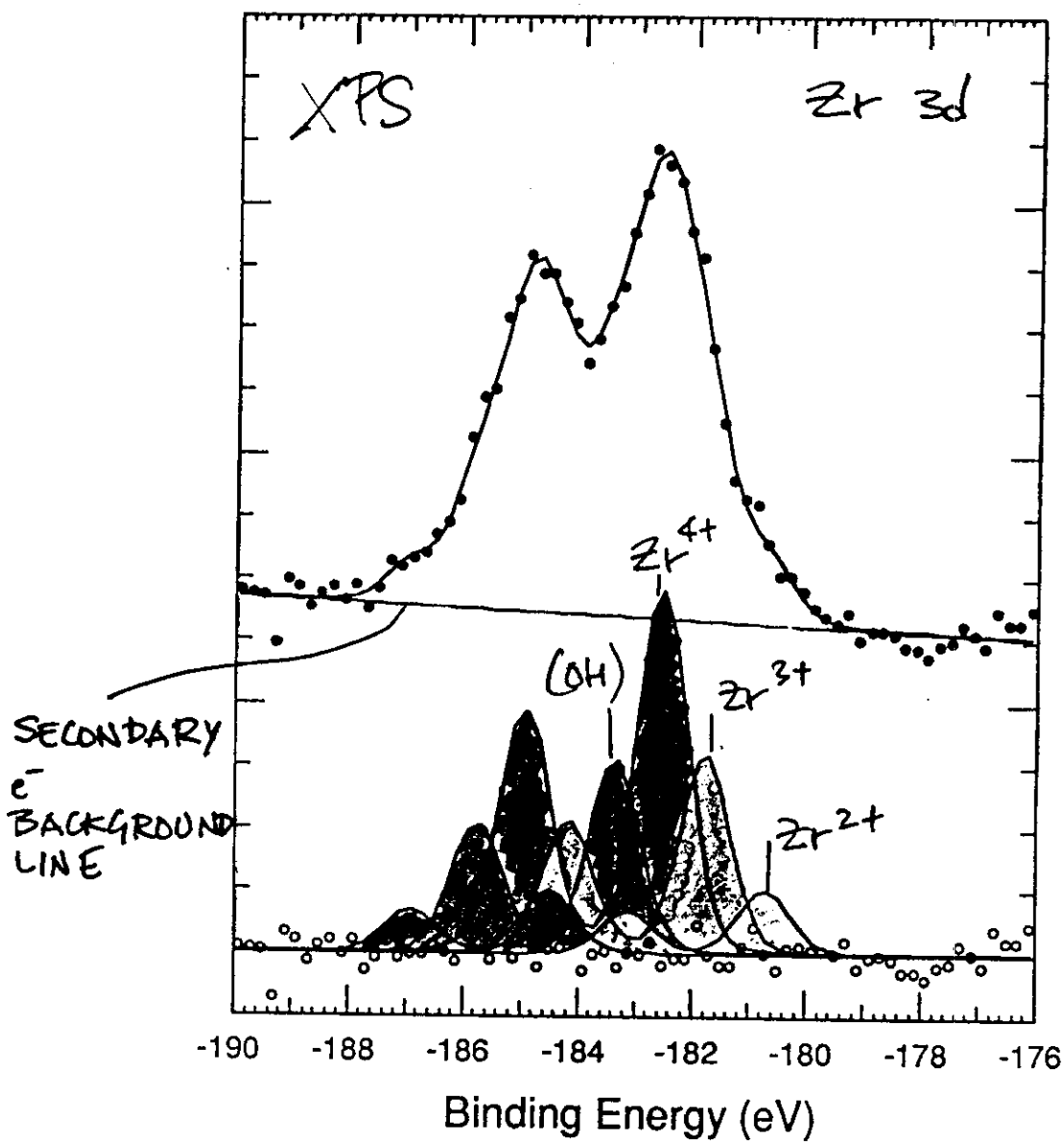

Zr 3d CORE LINE FIT
RESOLVING THE CHEMICALLY
DISTINCT Zr COMPONENTS

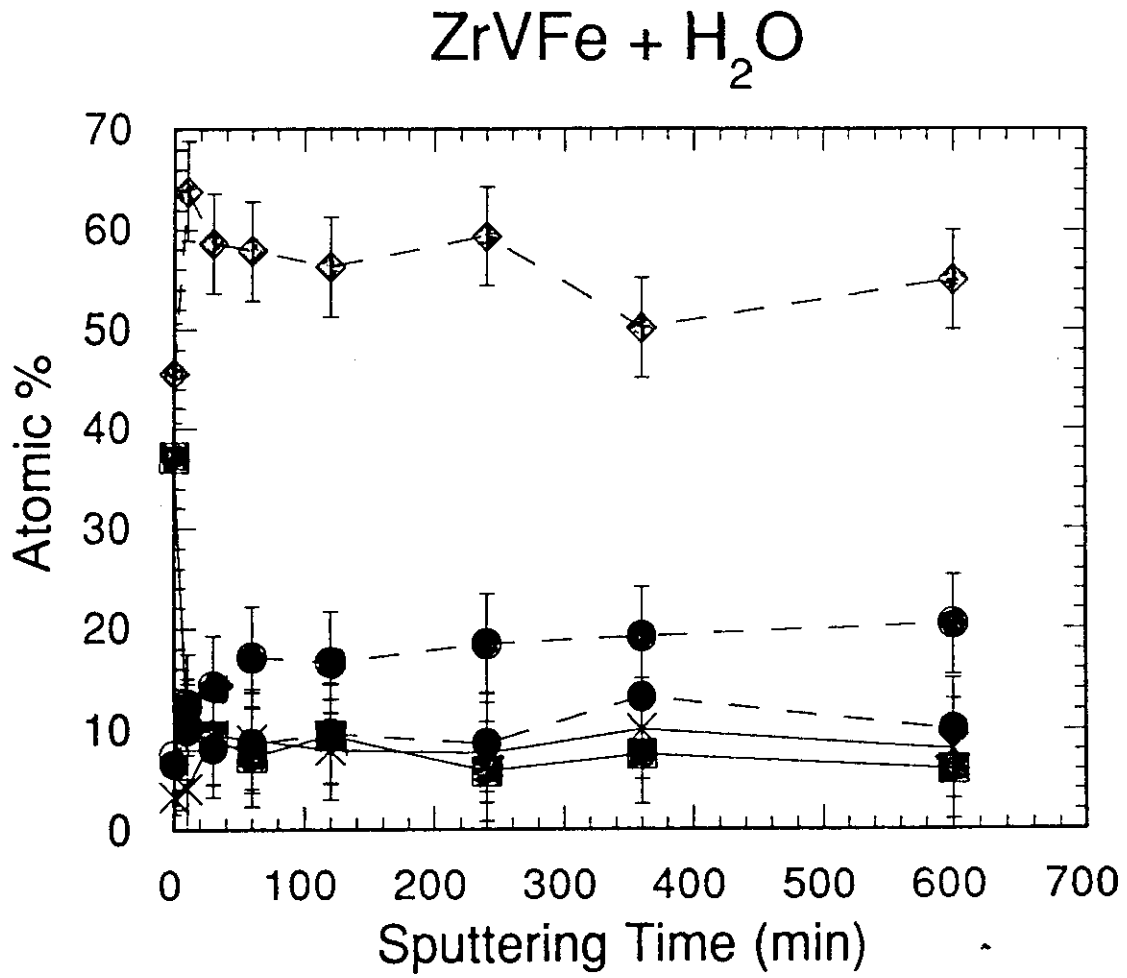

ZIRCONIUM

IRON

CARBON

VANADIUM

OXYGEN

TOTAL DEPTH PROBED = 0.6 μm

- INITIAL TRANSIENT
- ALMOST UNIFORM COMPOSITION VS DEPTH
- HUGE AMOUNT OF OXYGEN

WATER-TREATED ZrVFe

XPS Fe $2p_{3/2}$

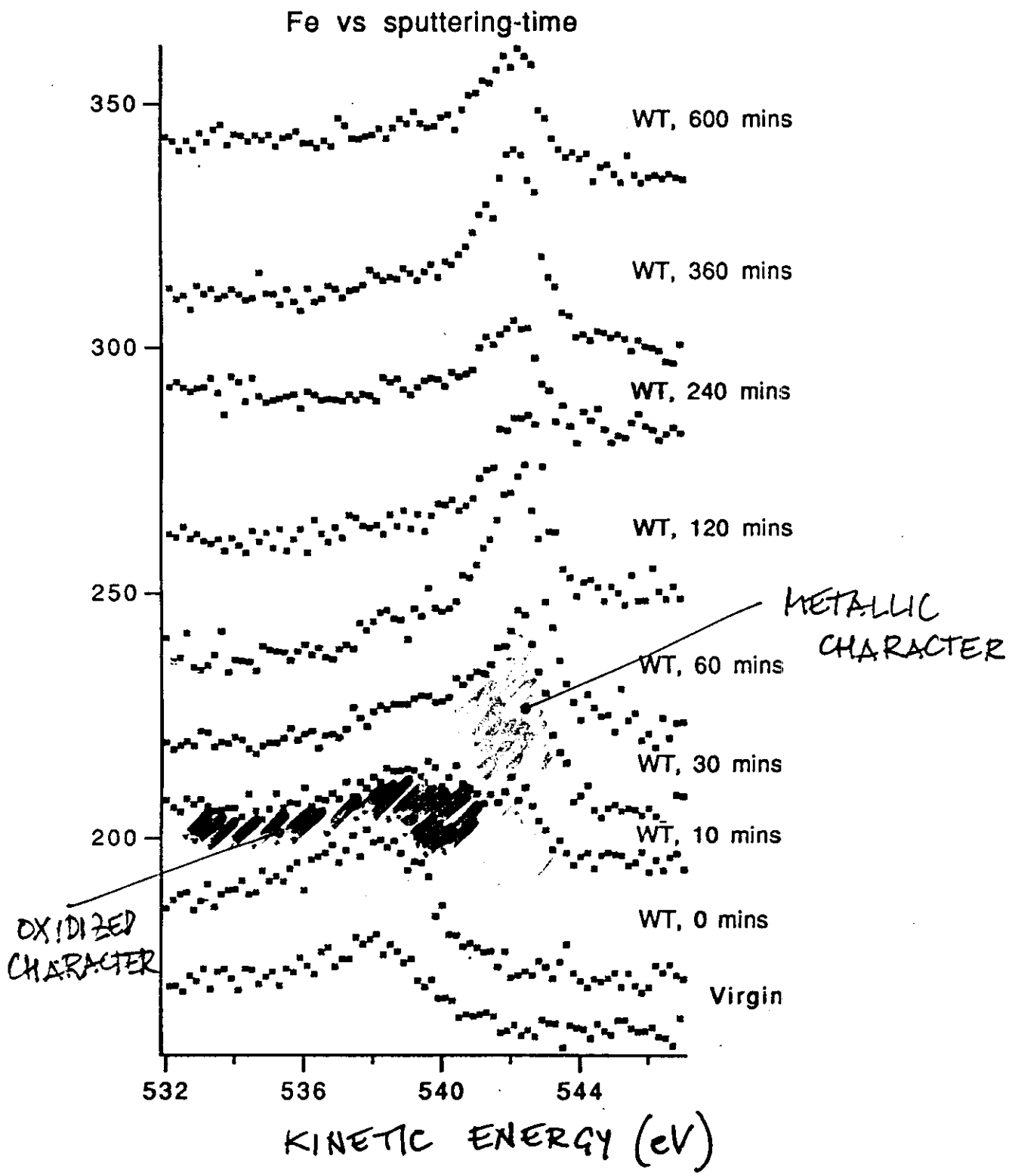

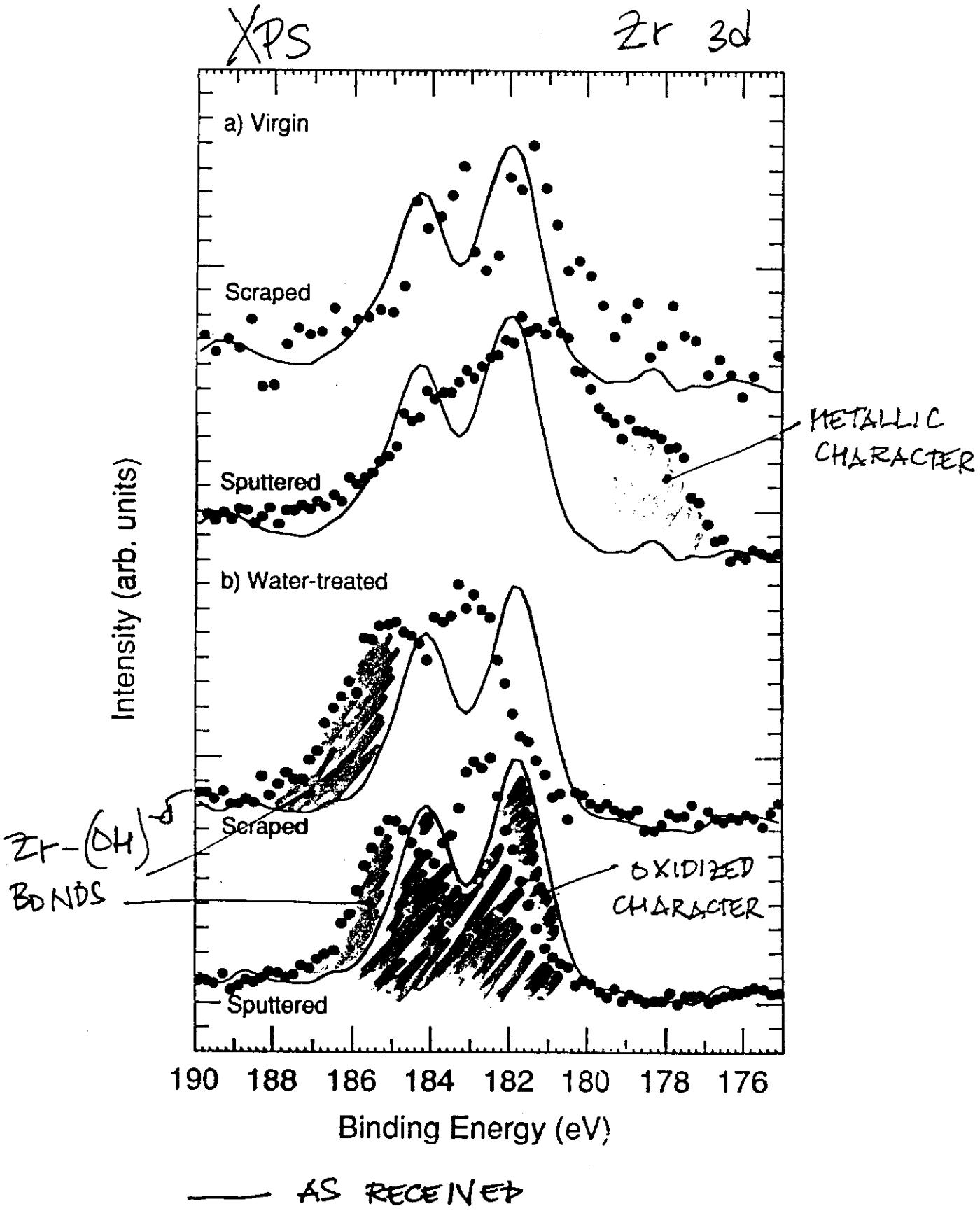
XPS
Zr 3d
a) Virgin
Scraped
Sputtered
METALLIC CHARACTER
b) Water-treated
Intensity (arb. units)
Zr-(OH)
BONDS
Scraped
OXIDIZED CHARACTER
Sputtered
190 188 186 184 182 180 178 176
Binding Energy (eV)
AS RECEIVED

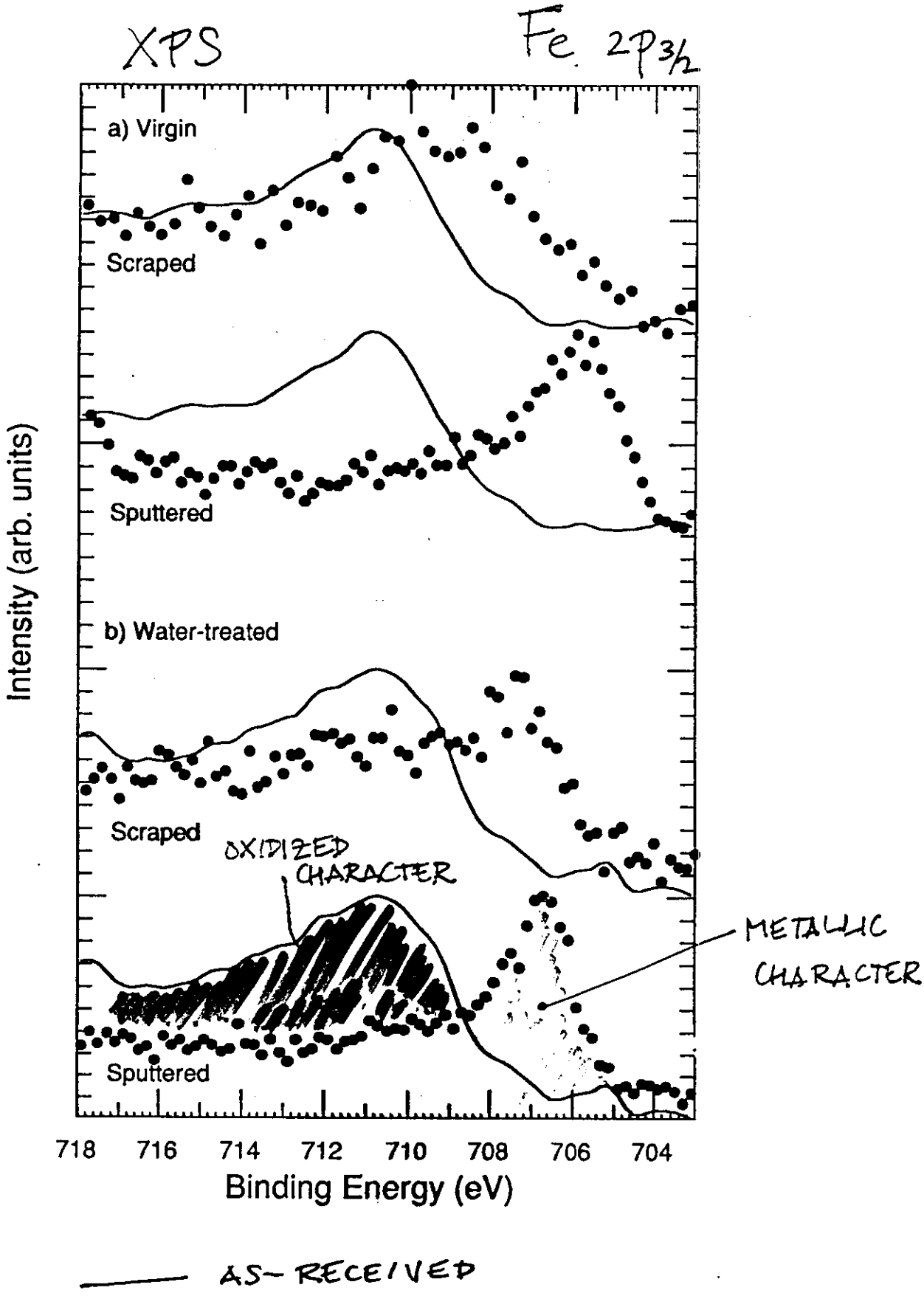
XPS
Fe 2p3/2
a) Virgin
Scraped
Sputtered
b) Water-treated
Scraped
OXIDIZED CHARACTER
METALLIC CHARACTER
Sputtered
Intensity (arb. units)
718 716 714 712 710 708 706 704
Binding Energy (eV)
AS-RECEIVED

CHEMICALLY DISTINCT Zr COMPONENTS AS A FUNCTION OF THE SPUTTERED LAYERS

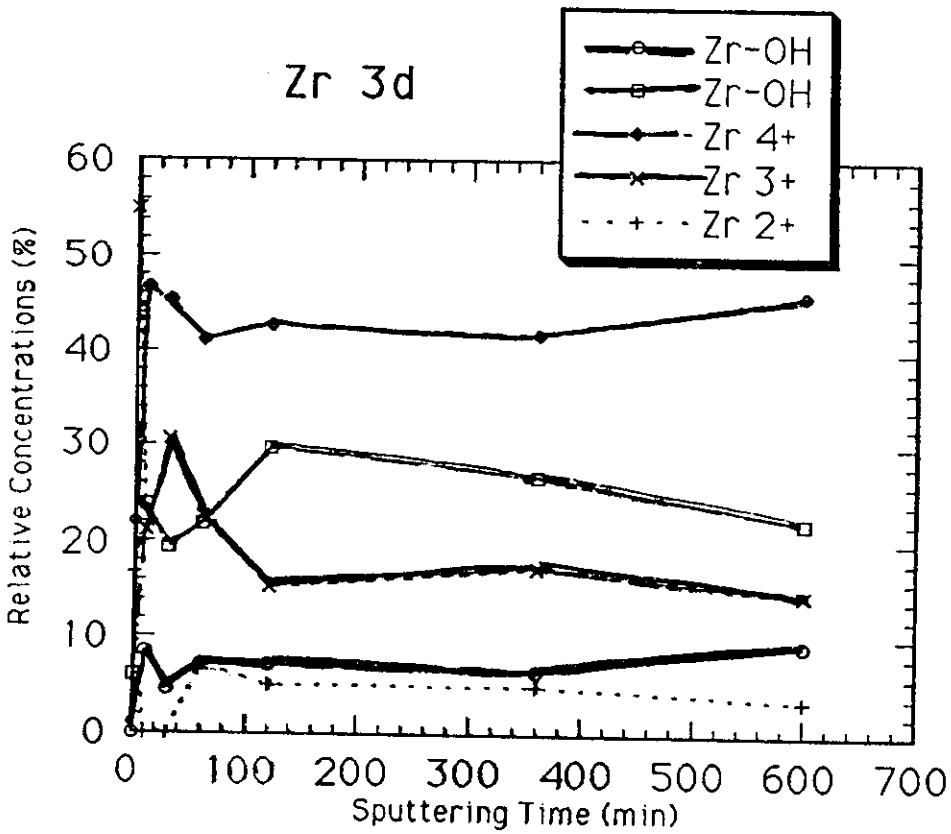

- MAJOR CONTRIBUTION OF Zr^{4+} (ZrO_2)
- SIZEABLE AMOUNTS OF Zr BONDED WITH HYDROXYL GROUPS
- NO TRACES OF METALLIC-LIKE Zr

MIXED - VALENCY VIA VALENCE - FLUCTUATIONS

$$4f^{N} \rightleftharpoons 4f^{N-1} + e^{-}$$

YTTERBIUM Yb

ATOMIC CONFIGURATION

$[Xe]\ 4f^{14}\ 5d^{0}\ 6s^{2}$

METALLIC STATE CONFIGURATION

$[Xe]\ 4f^{14}\ (5d\ 6s)^{2}$ DIVALENT

MIXED-VALENT Yb-COMPOUNDS

$$4f^{14} \rightleftharpoons 4f^{13} + e^{-}$$

DIVALENT TRIVALENT

FLUCTUATION TIME $\simeq 10^{-13}$ sec.

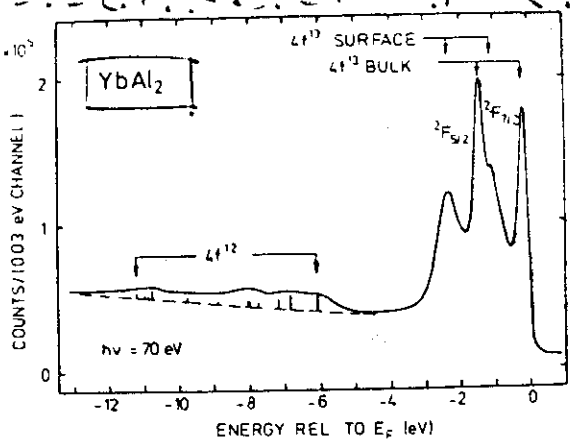

Fig. 1 Photoemission spectrum of $YbAl_2$ at hν=70 eV. Two final-state $4f^{13}$ doublets are seen, a narrow bulk doublet and a much wider surface doublet shifted to higher binding energy. Weaker bulk final-state $4f^{12}$ multiplet lines are also seen.

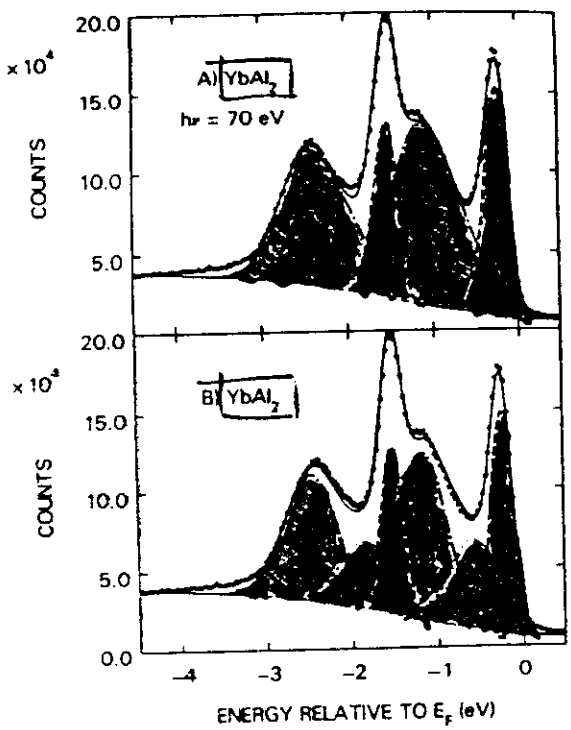

Fig. 2 Least-squares fit analysis of the $4f^{13}$ final-state multiplet spectrum using (a) two doublets and (b) three doublets of asymmetric gaussian lines plus background. Dashed lines represent emission from the bulk. In Fig. 2b dash-dotted (dotted) lines represent the first (second) surface layer.

G. KAINDL, B. REIHL, D.E. EASTMAN, R.A. POLLAK, N. MARTENSSON, B. BARBARA, T. PENNEY & T.S PLASKETT SOLID STATE COMMUN 41 (1982) 757

STRUCTURAL DATA

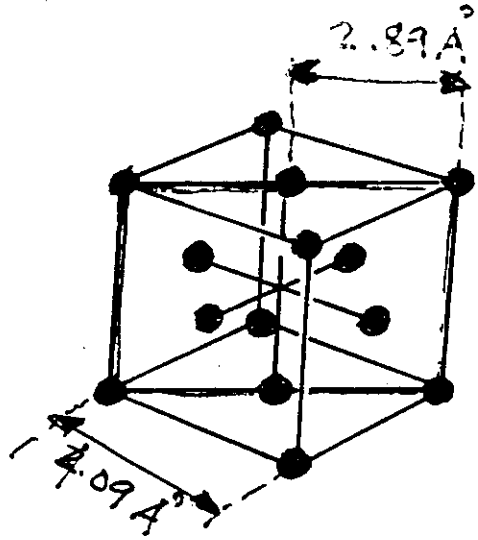

fcc

Ag (110)

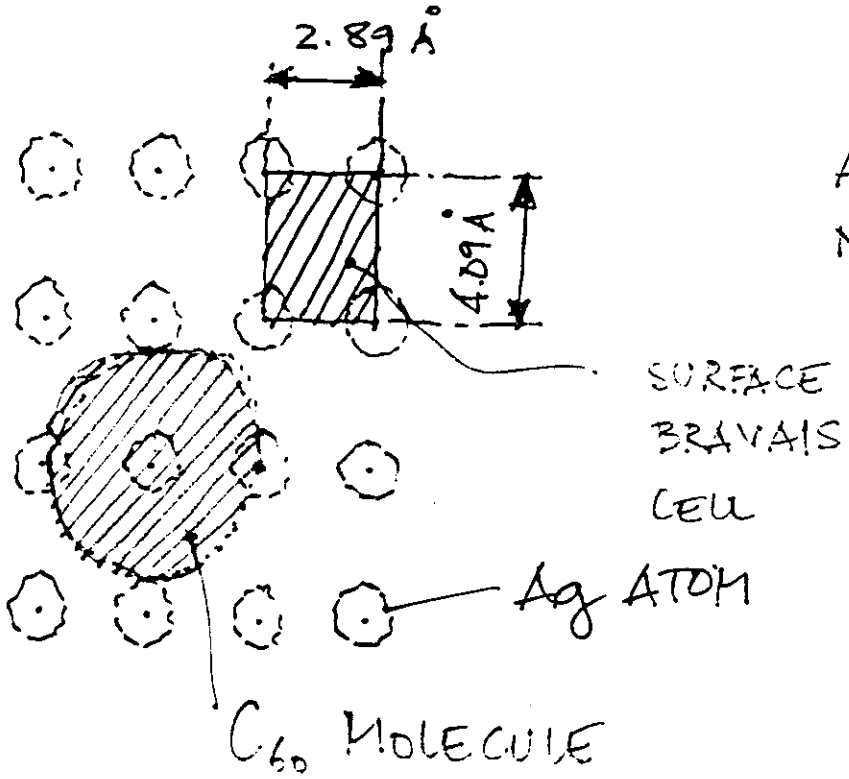

Ag (110)
NO RECONSTRUCTION

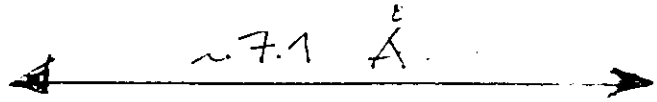

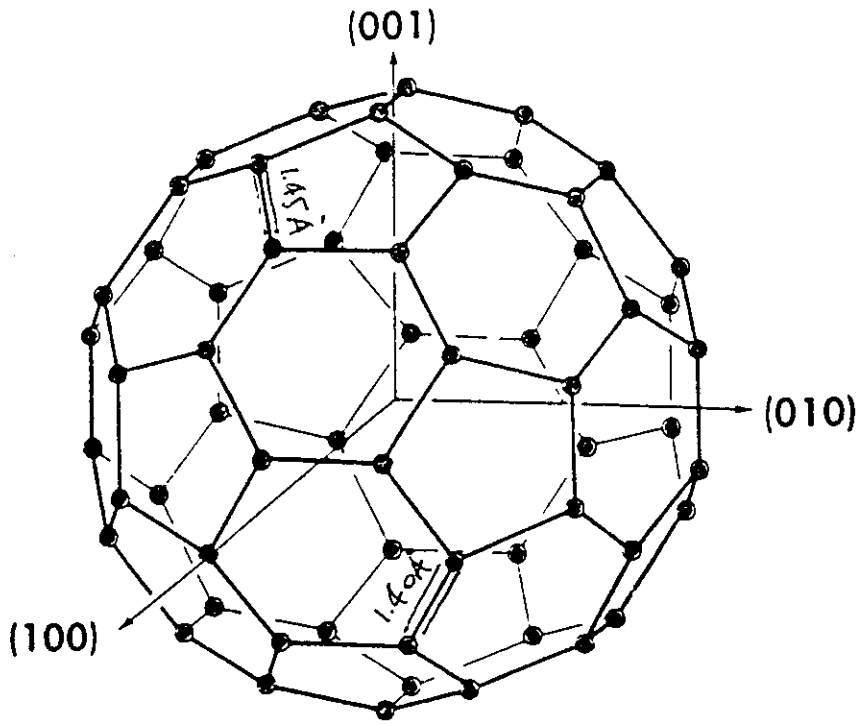

C_{60} MOLECULE

—— SINGLE BOND

—— DOUBLE BOND

- TRUNCATED - ICOSAHEDRON STRUCTURE
- "MAGIC" CLUSTER
- BUCKMINSTER FULLERENE
- ALL C ATOMS ARE EQUIVALENT

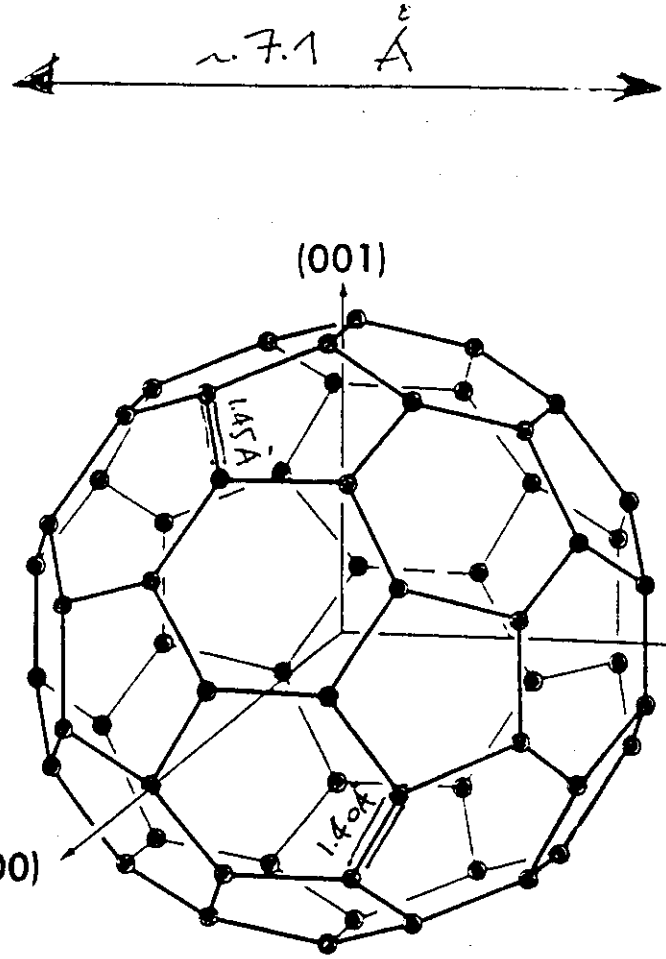

C_{60} MOLECULE

— SINGLE BOND

— DOUBLE BOND

- TRUNCATED - ICOSAHEDRON STRUCTURE
- "MAGIC" CLUSTER
- BUCKMINISTER FULLERENE
- ALL C ATOMS ARE EQUIVALENT

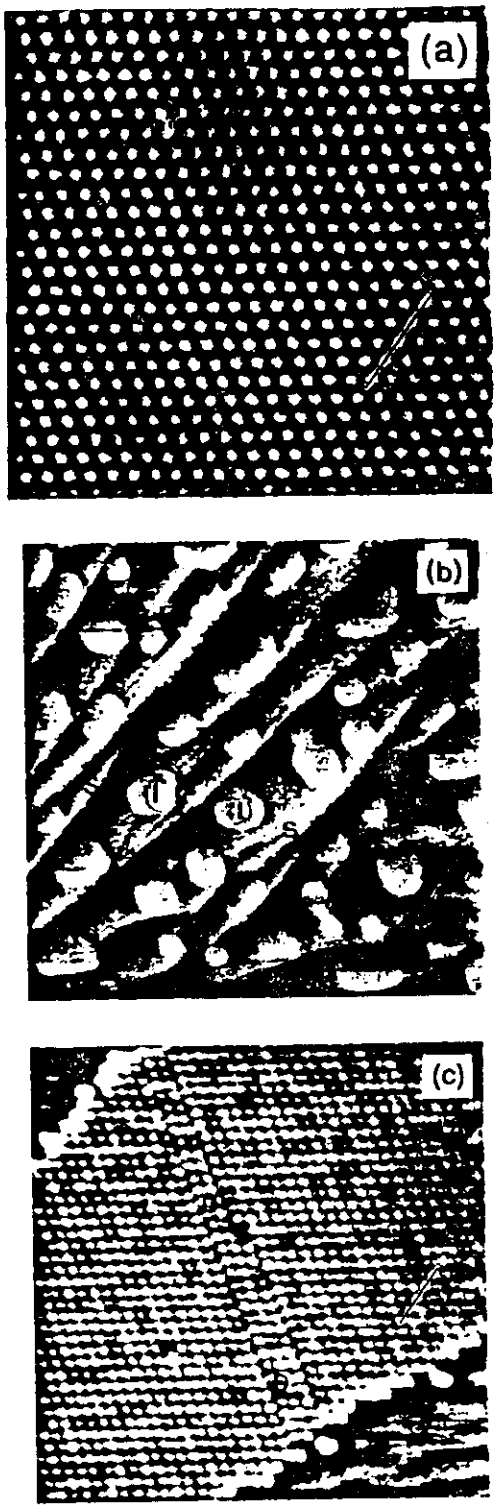

WELL ORDERED
C_{60} ON Ag(...)
AFTER ANNEALING
AT 700 K

CLOSE-PACKED DIRECTION
PARALLEL TO [1$\bar{1}$0]
Ag(110) c(4×4) C_{60}

C_{60} ISLAND FORMATION

FIG. 2. Topographs of (a) well-ordered C_{60} monolayer on Ag(110) with nearest neighbor distance of ~9.4 Å. The line indicates Ag[1$\bar{1}$0] direction. (b) C_{60} island formation (*I*) on terraces and Ag steps (*S*) running along [1$\bar{1}$0] indicated by the line. (2400×2400 Å) V_t=0.3 V, i_t=1 nA. (c) Defect (*D*) indicated in hexagonal layer on one of the islands. The line indicates Ag[1$\bar{1}$0] direction.

REFERENCE #1
J VST 3 1 2 (1 9 4 4) 1942

WELL ORDERED
C_{60} ON Ag(1..)
AFTER ANNEALING
AT 700 K

CLOSE-PACKED DIRECTION
PARALLEL TO [1T0]
Ag(1..)c(4x4)C_{60}

C_{60} ISLAND FORMATION

FIG. 2. Topographs of (a) well-ordered C_{60} monolayer on Ag(110) with nearest neighbor distance of ~9.4 Å. The line indicates Ag[1$\bar{1}$0] direction. (b) C_{60} island formation (*I*) on terraces and Ag steps (*S*) running along [1$\bar{1}$0] indicated by the line. (2.400×2.400 Å) V_t=0.3 V, i_t=1 nA. (c) Defect (*D*) indicated in hexagonal layer on one of the islands. The line indicates Ag[1$\bar{1}$0] direction.

SIMEONSKI ET AL
J VST 3(2) (1985) 1742.

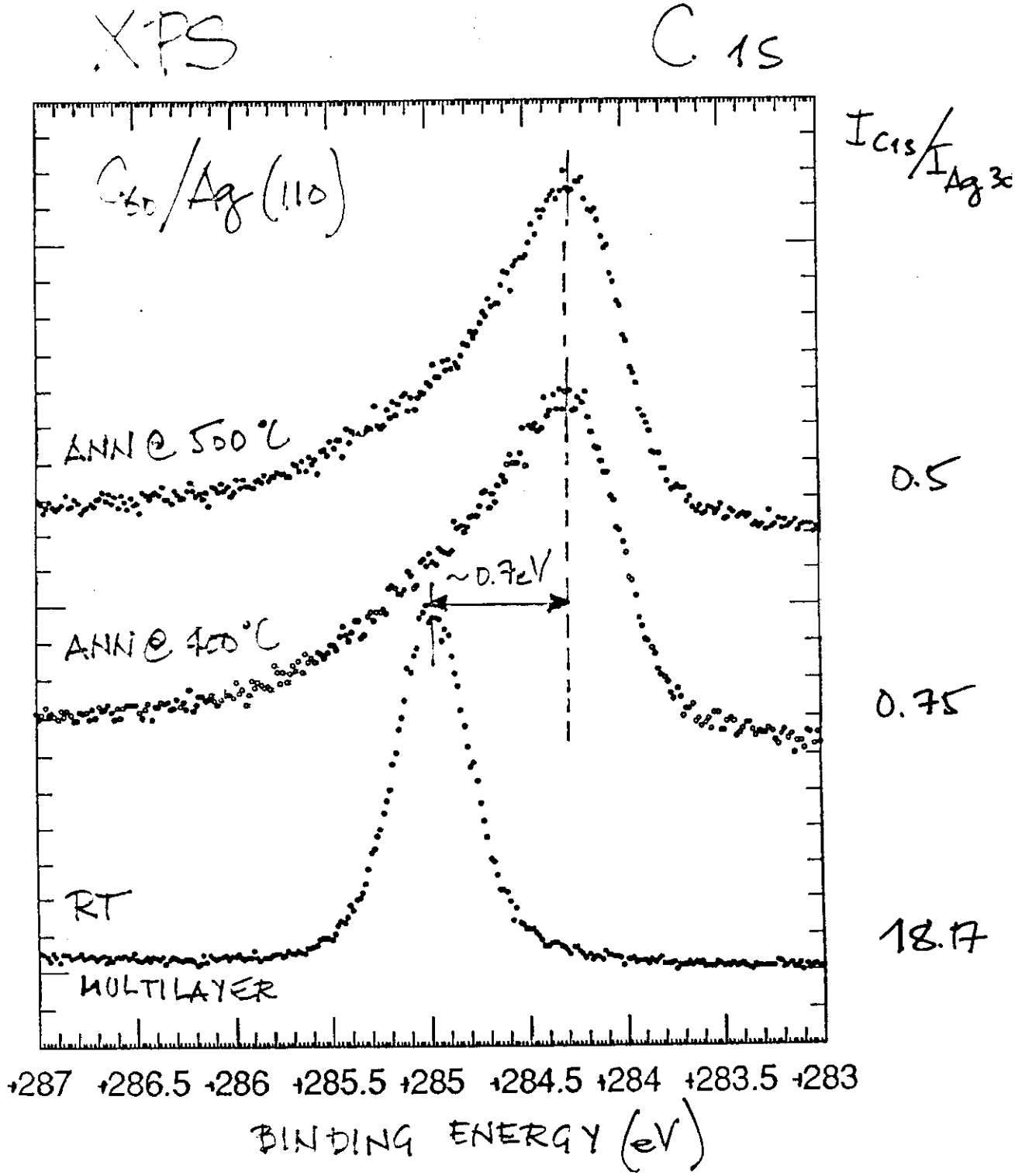
XPS
C 1s
C_{60}/Ag(110)
I_{C1s}/I_{Ag3c}
ANN @ 500°C
0.5
~0.7eV
ANN @ 400°C
0.75
RT
18.17
MULTILAYER
+287 +286.5 +286 +285.5 +285 +284.5 +284 +283.5 +283
BINDING ENERGY (eV)

XPS C 1S

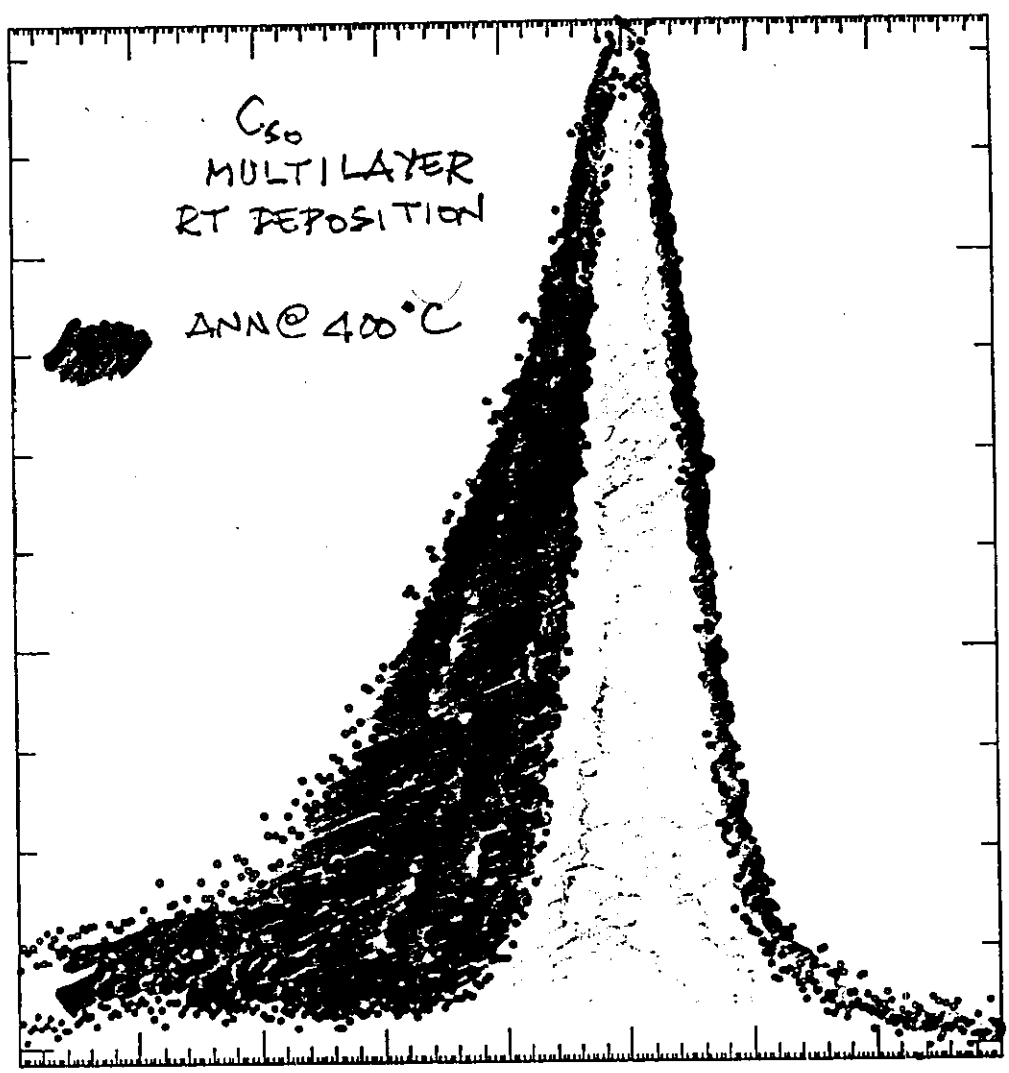

+287.5 +287 +286.5 +286 +285.5 +285 +284.5 +284 +283.5

BINDING ENERGY (eV)

C_{60} / Ag (110)

AFTER ALIGNMENT WITH RESPECT TO THE MULTILAYER PEAK

ANGLE-INTEGRATED
PHOTOEMISSION

C_{60}/Ag(110)

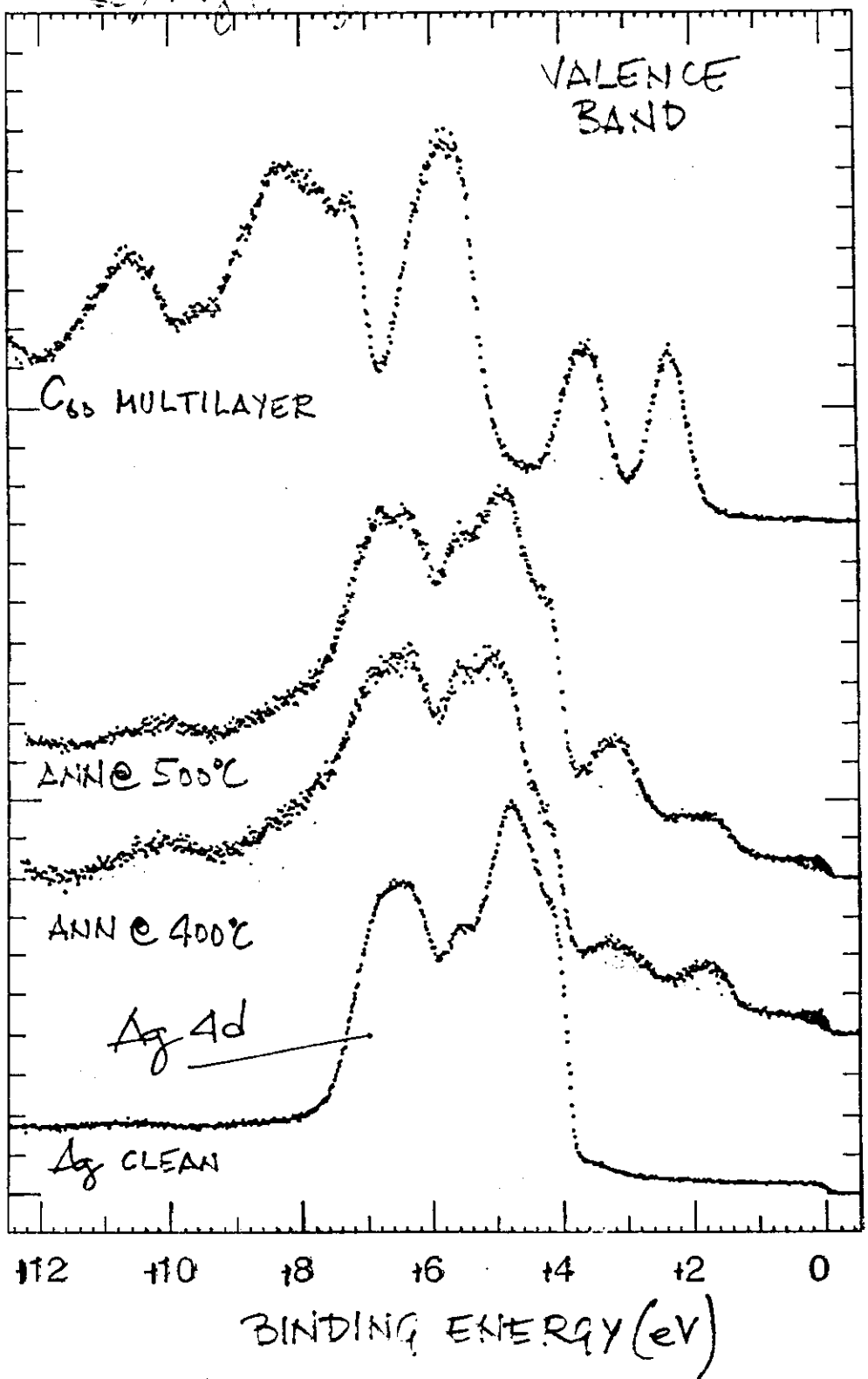

Ag 4d COOPER MINIMUM

ANGLE-INTEGRATED PHOTOEMISSION

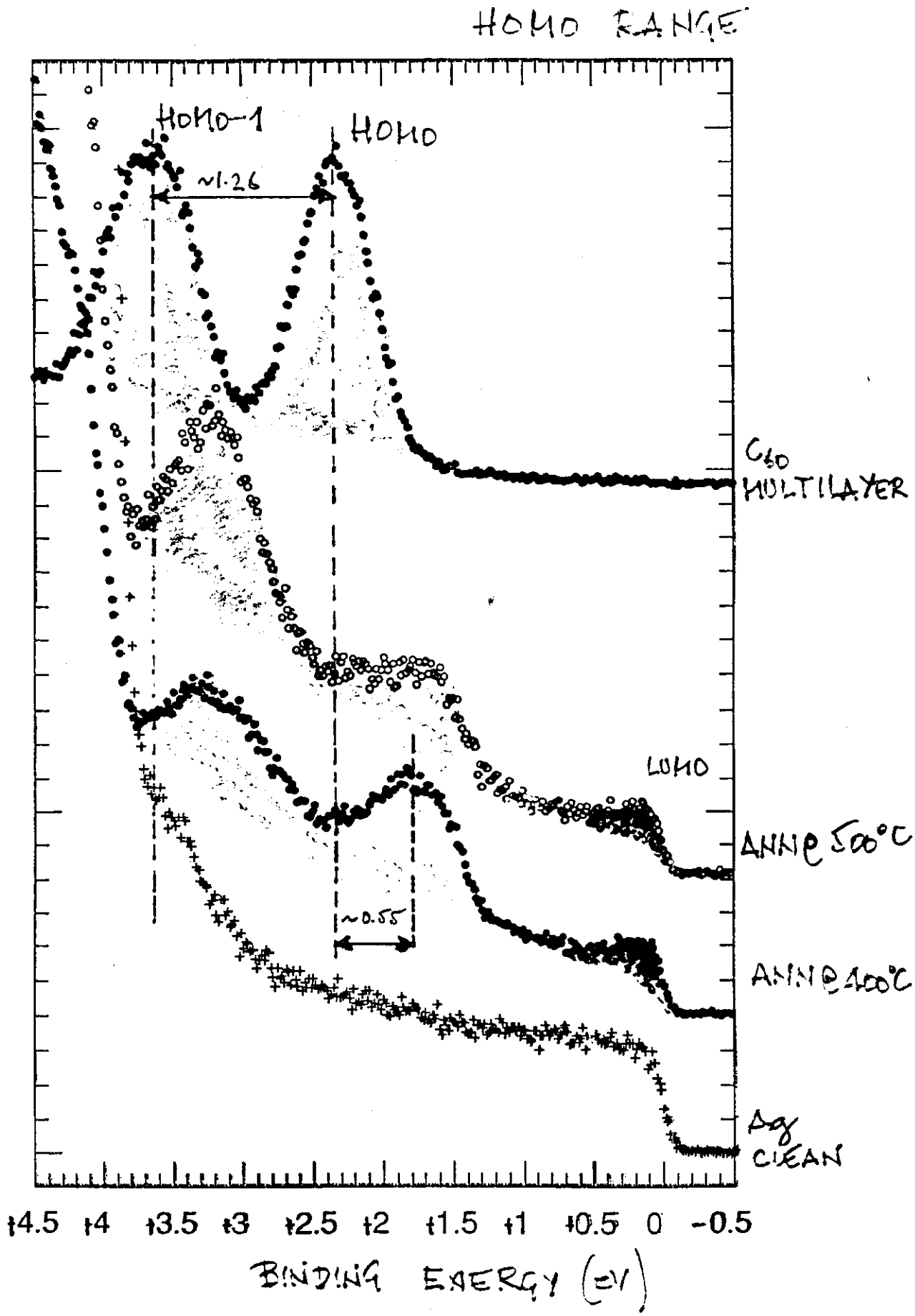

C_{60}/Ag(110)

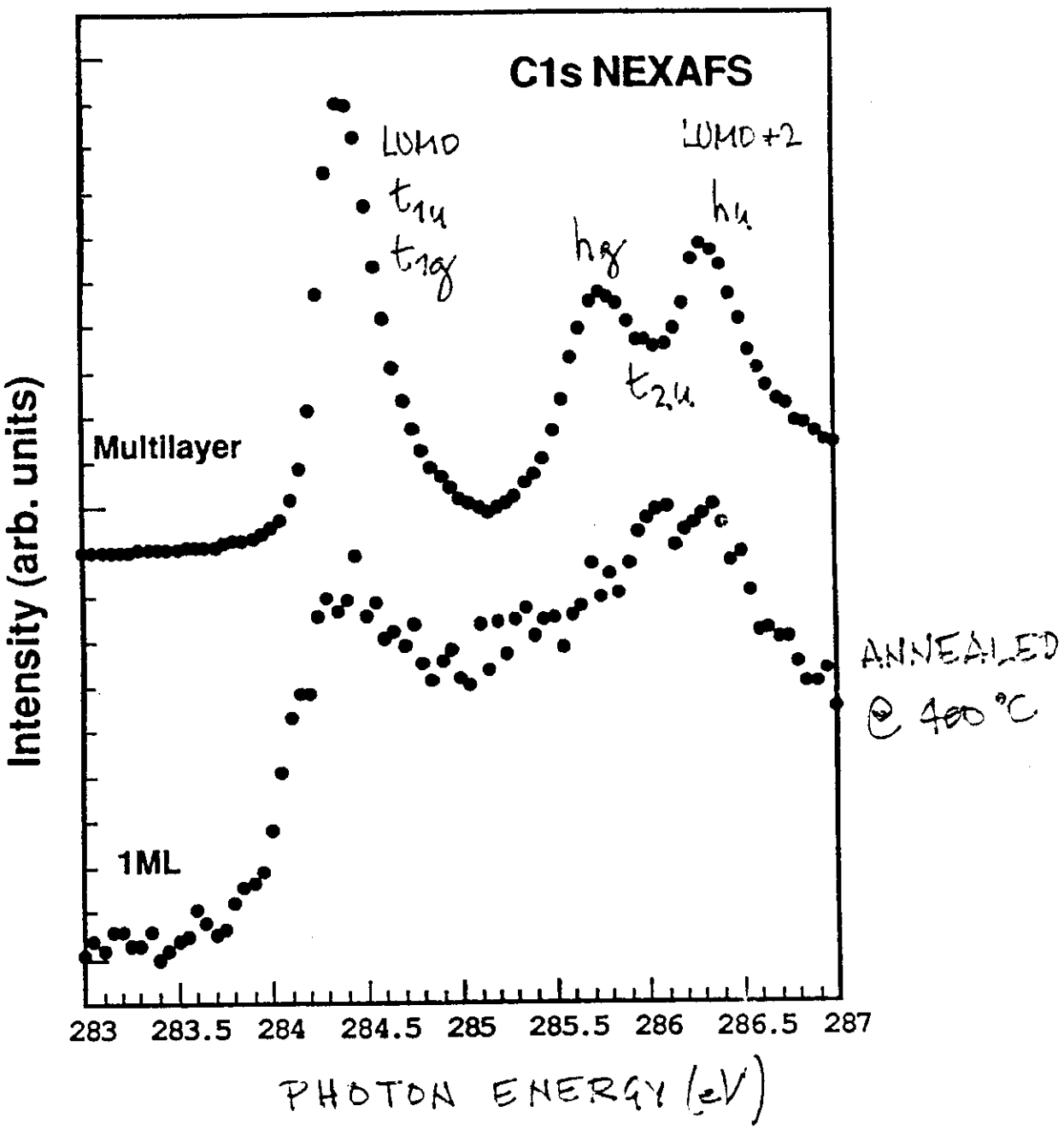

π^* ORBITALS

C 1s NEXAFS

COOPER MINIMUM PHOTOEMISSION

HOW TO DISCRIMINATE BETWEEN 4d (5d) - & sp VALENCE BAND STATES

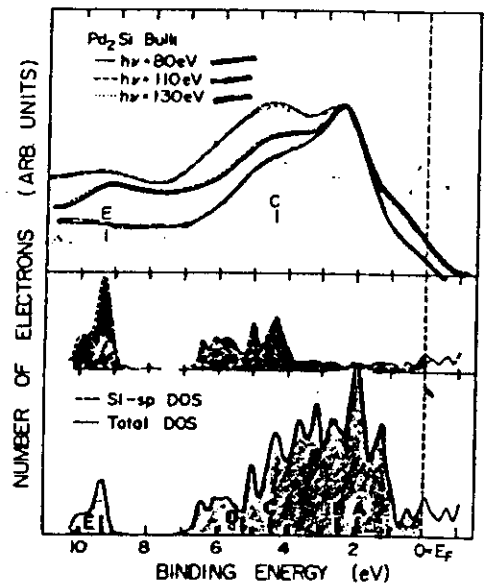

Pd_2Si

Pd 4d STATES

VS

Si 3(sp) STATES

FIG. 2. EDC's for the valence-band emission of Pd_2Si at $h\nu=80$, 110, and 130 eV are shown (top) normalized to the main 4*d* structure. In the lower part of the figure we show, for comparison, the total DOS (solid line) and the Si-derived *s-p* partial DOS as calculated by Bisi and Calandra in Ref. 14. The vertical bars mark the experimental features $A-E$ identified in Fig. 1. Experimentally, the suppression of the Pd-derived *d* emission at the 4*d* Cooper minimum ($h\nu>100$ eV) results in the emergence of the Si-derived *s* states at 9.3 eV and of the Si *p* states in bonding combination with metal *d* orbitals 3.5–6.5 eV below E_F. Theory does not show a similar one-to-one correspondence for the other experimental features but the qualitative agreement suggests that structures *A* and *B* arise from 4*d* nonbonding states. The emission within 1.5 eV from E_F is strongly enhanced at the Cooper minimum but the nature of the corresponding states is less clear. Either a substantial amount of metal *s-p* character is present near E_F or the antibonding Si *p*–metal-*d* orbitals are partially occupied.

FRANCIOSI ET AL

PHYS REV B

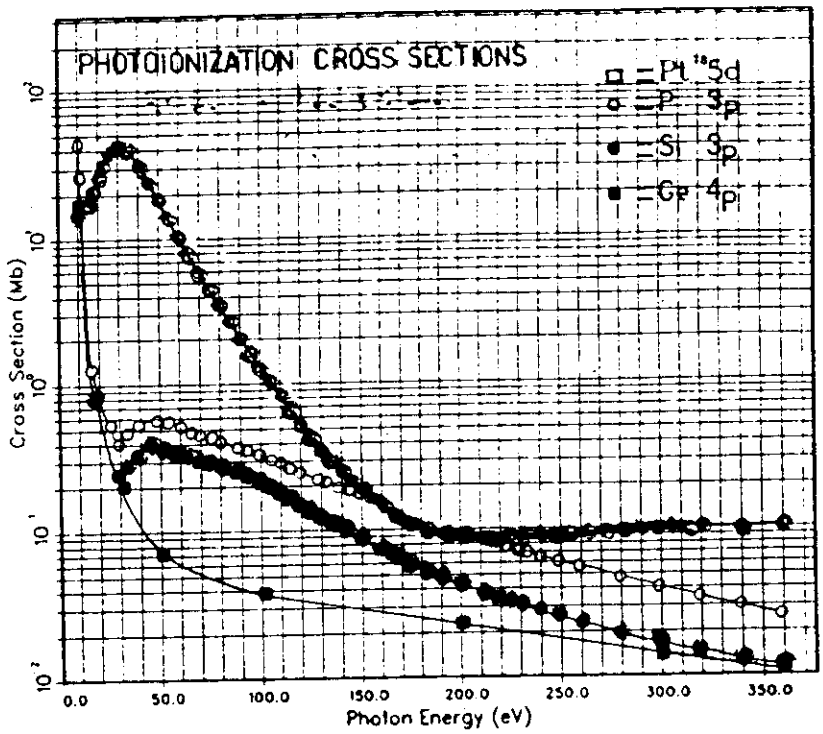

. Photoionization cross section for 4d and 5d subshells in the energy range 0–200 eV compared to the cross sections for the 3ps and 4sp valence states of the semiconductors [21].

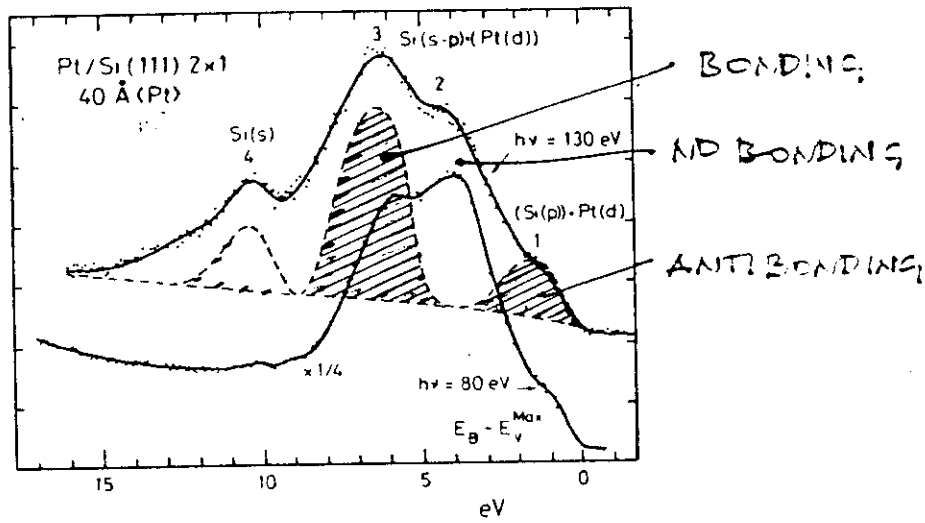

. Analysis of the Si sp partial DOS at the Pt–Si(111) reacted interface (40 Å Pt–Si(111) at room temperature). The top panel displays the CM and the $h\nu = 80$ eV photoemission data, and a three-peak partial DOS that accounts for the Si hybridized 3sp charge at the interface: a gap is present in correspondence to the localized Pt 5d states. The same three-peak partial DOS is then self-convoluted and compared to the integrated Si $L_{2,3}VV$ lineshape. The correspondence of all peaks and relative intensities (a part of the known reduction of the Si 3s contribution) confirms the CM derivation of the Si sp partial DOS [159].

AFTER P. MORGEN & al
SURFACE SCIENCE (1987)

RESONANT PHOTOEMISSION

HOW TO SUPPRESS OR ENHANCE d- CHARACTER STATES IN VALENCE BAND STATE PHOTOEMISSION

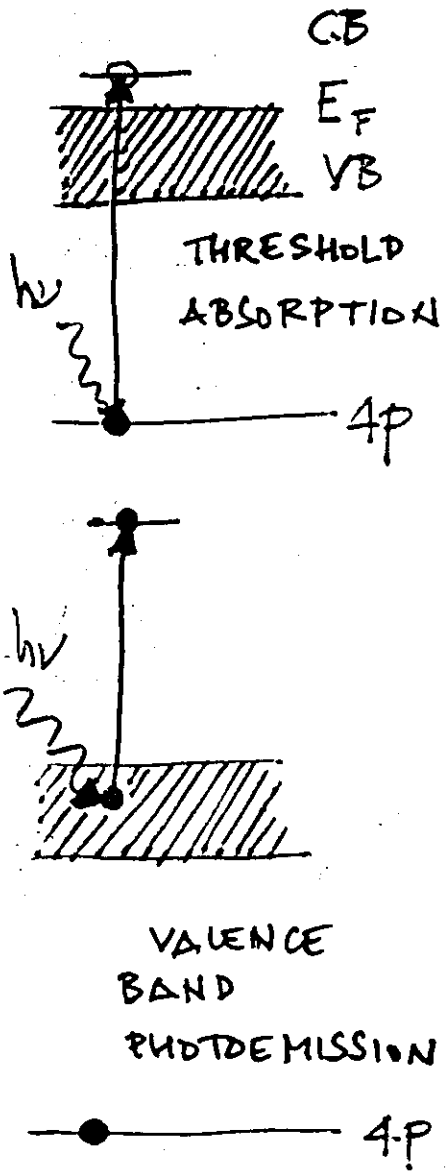

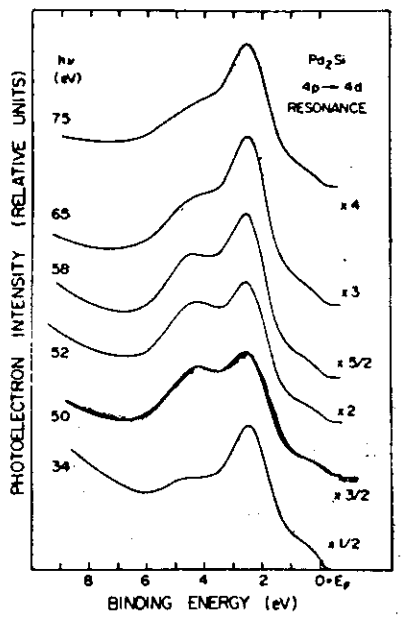

FIG. 4. Representative spectra of the valence-band emission of Pd_2Si for photon energy near the $4p \rightarrow 4d$ resonance. The spectra were normalized for monochromator output (Ref. 29) and are given in relative units. The modulation of the relative intensity of the experimental features reflects the suppression of the 4*d* character at antiresonance, where the Si-derived states are more visible ($h\nu \sim 50$ eV), and the following reenhancement at resonance (see Fig. 3). Resonant photoemission represents an important tool for analyzing the different orbital contributions to the valence states and, unlike the Cooper minimum technique, can in principle be applied to all *d* systems.

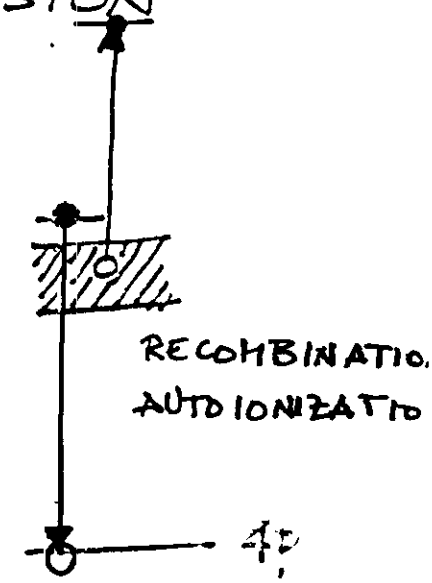

QUANTUM
INTERFERENCE
BETWEEN
TWO EXCITATION
CHANNELS

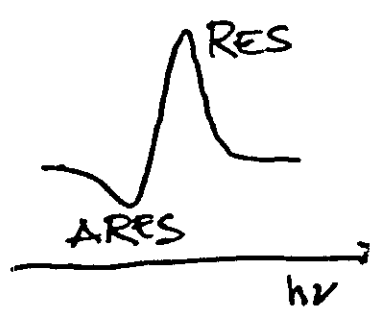

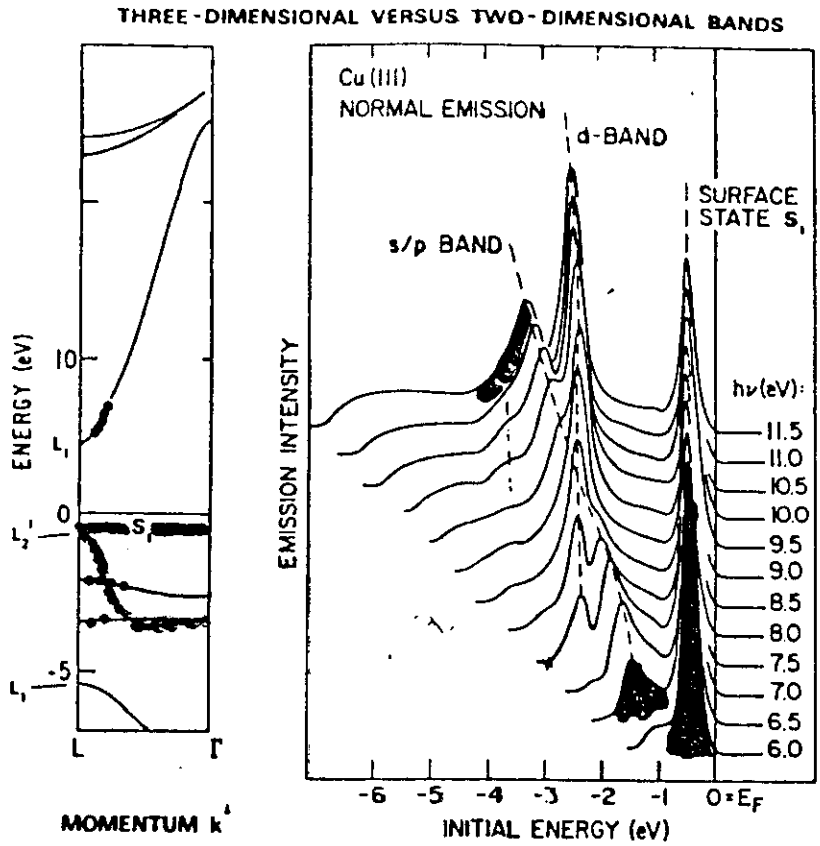

Surface and bulk states for Cu(111). The structure S_1 at $E_f - 0{\cdot}4$ eV in the normal emission photoelectron spectra is a surface state; the other peaks are bulk states. Two characteristics of a surface state can be seen: S_1 is located in the L_2'–L_1 gap of bulk states. The binding energy of the surface state is independent of the photon energy $h\nu$ in contrast to the bulk states which move due to dispersion along the $k^{\perp}$ axis as shown on the left-hand side.

FRANCIOSI et al

PHYS REV B

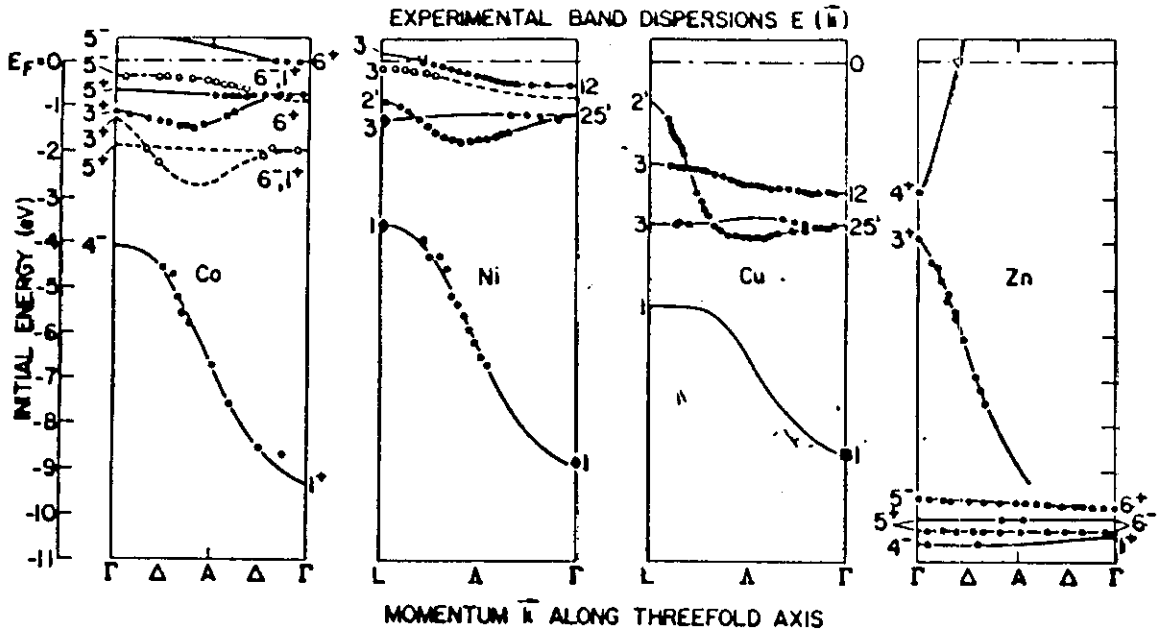

Overview of three-dimensional experimental energy band dispersions along the first row of transition and noble metals (from Eastman and Himpsel 1980b including data from Eberhardt and Plummer 1980 (diamonds) and Thiry *et al.* 1979 (square)). The flat 3*d* bands become filled with increasing atomic number and move down relative to the strongly dispersing *s*, *p* bands.

Fig. 20

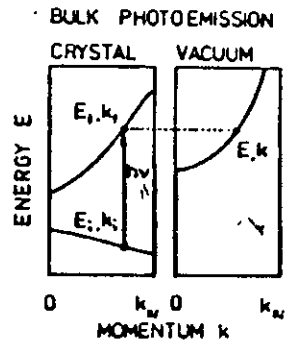

Electronic states for photoemission from the bulk (from Smith and Himpsel 1983).

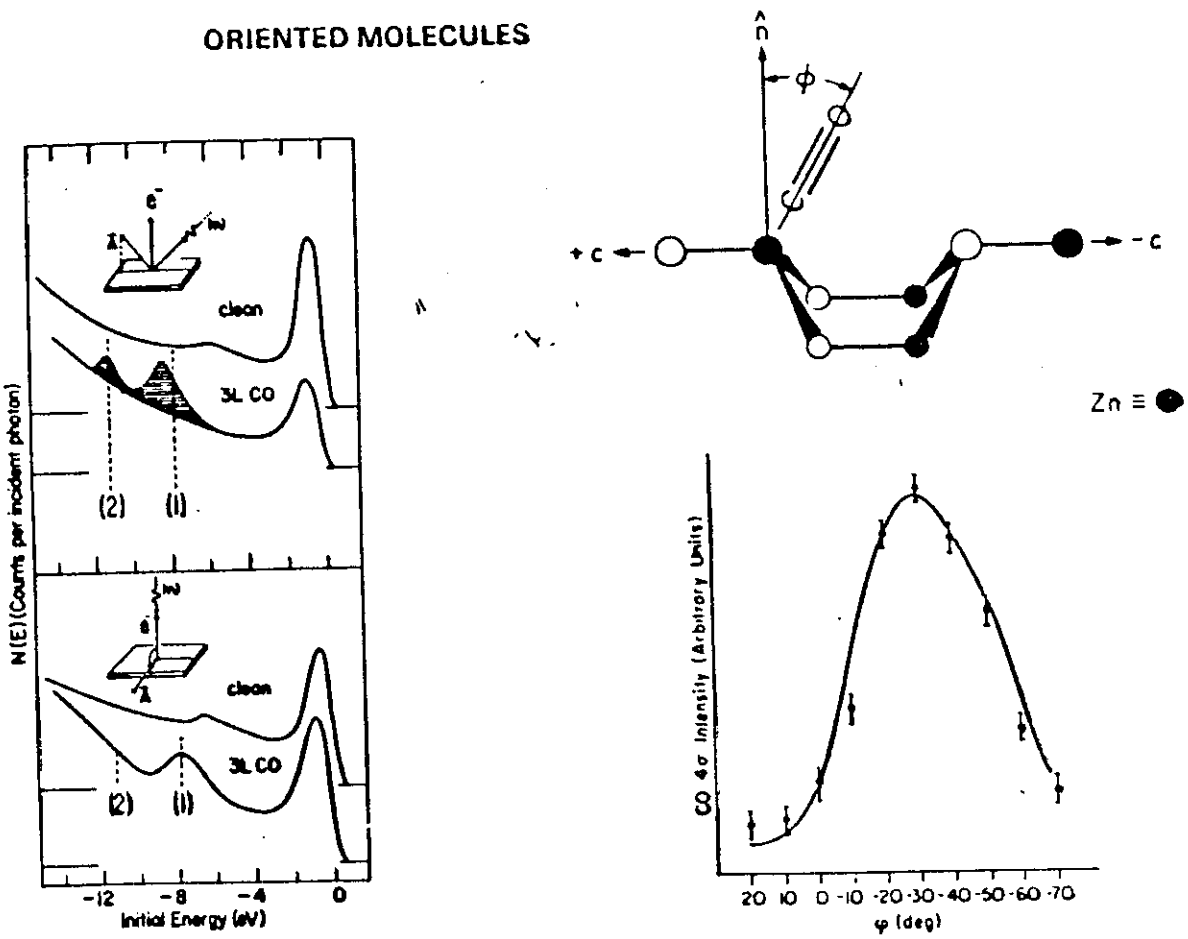

(*a*) Polarization-dependent angle-resolved photoelectron spectra for CO on Ni(100) which demonstrate that the axis of the CO molecule is perpendicular to the surface (after Smith *et al.* 1976 b). For normal emission and with the electric field vector parallel to the surface (bottom) the emission from the lowest orbital (4σ; structure 2) is symmetry forbidden. (*b*) Photoemission from CO on a ZnO($10\bar{1}0$) surface giving evidence for inclined CO (from D'Amico *et al.* 1980) by comparing the angular dependence of the 4σ emission (dots) with oriented-molecule calculations (line, see Davenport 1976).

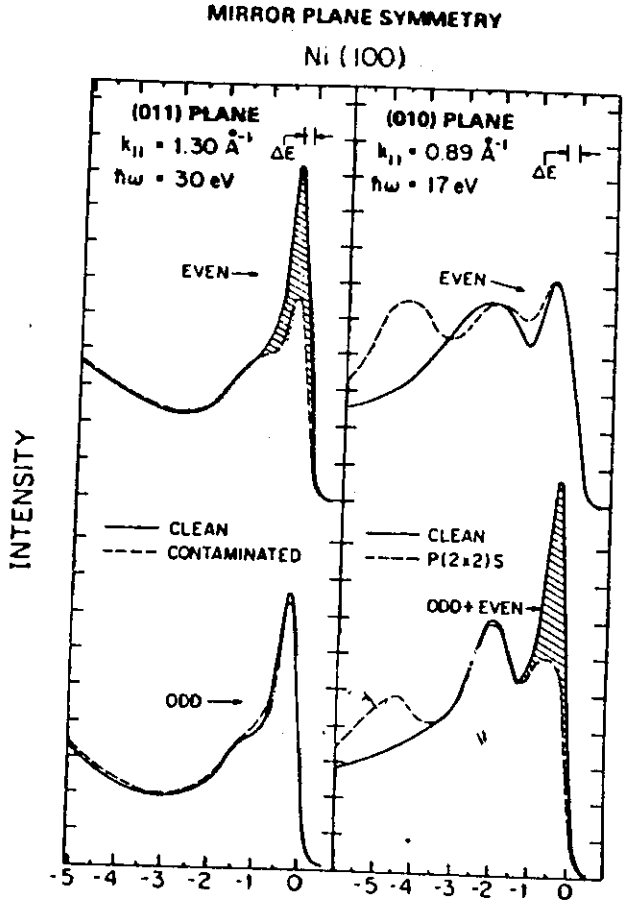

Surface states with even and odd mirror symmetry on Ni(100) selected by aligning the electric field vector parallel and perpendicular to the mirror plane, respectively, and detecting photoelectrons in the mirror plane (from Plummer and Eberhardt 1979).

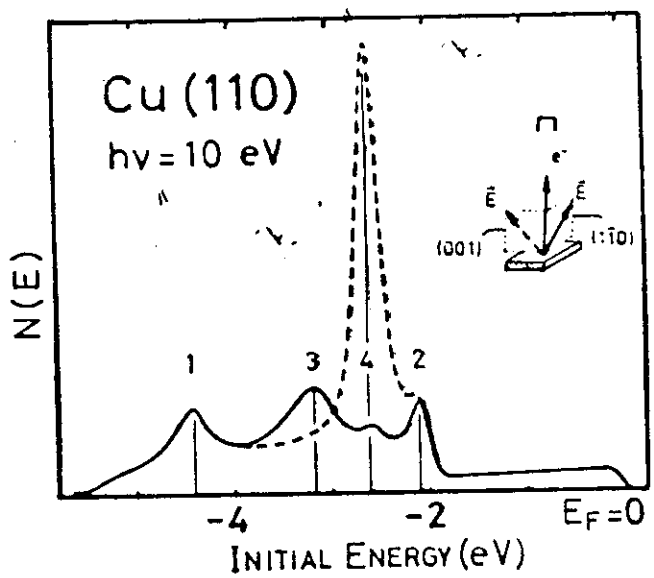

Fig. 5. Photoelectron spectra for normal emission from Cu(110), which demonstrate polarization selection rules. With the electric field vector **E** parallel to the (001) plane (dashed lines), states of Σ_4 symmetry are excited; with **E** parallel (1$\bar{1}$0), Σ_3 states are excited (after Ref. 23).

INVERSE PHOTOEMISSION

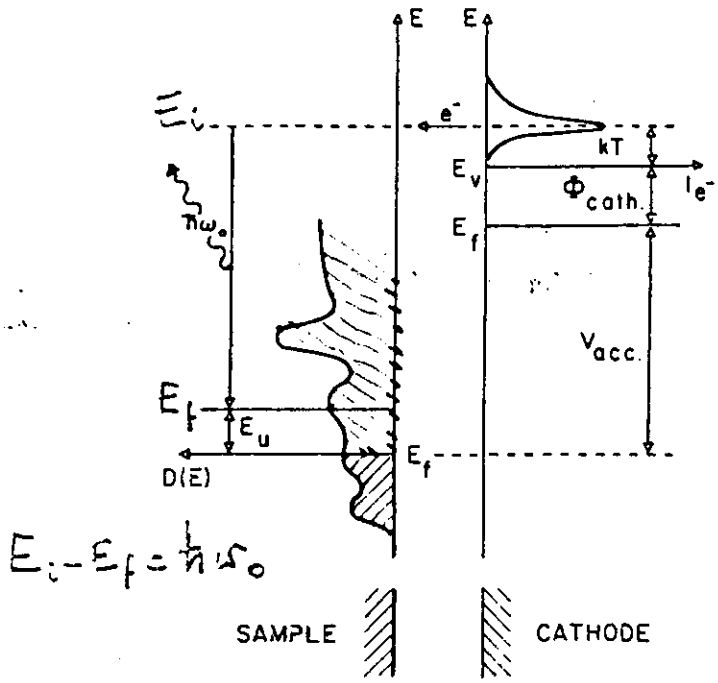

$E_i - E_f = \hbar\omega_0$

Energy diagram of the system cathode-sample. E_F—Fermi level; E_v—vacuum level; V_{acc}—acceleration potential of the electrons; ϕ_{cath}—work function of the cathode; T—temperature of the cathode; $\hbar\omega_0$—x-ray photon energy; E_u—unoccupied state energy; I_e—intensity distribution of the emitted electrons (thermionic emission); and $D(E)$—density of states.

$$E_{kin} = V_{ACC} + \Phi_{CATH} + kT - \hbar\omega_0$$

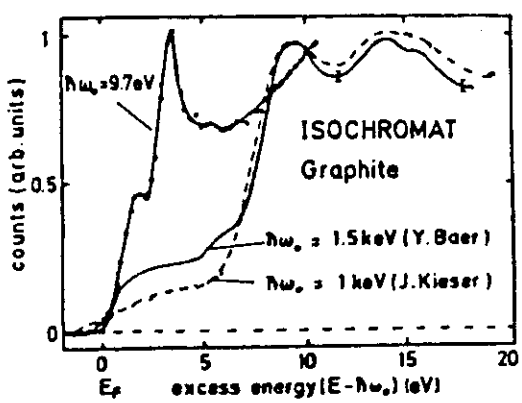

Bremsstrahlung isochromat spectra from graphite for photon energies in the UV and X-ray regime [18.37-39]

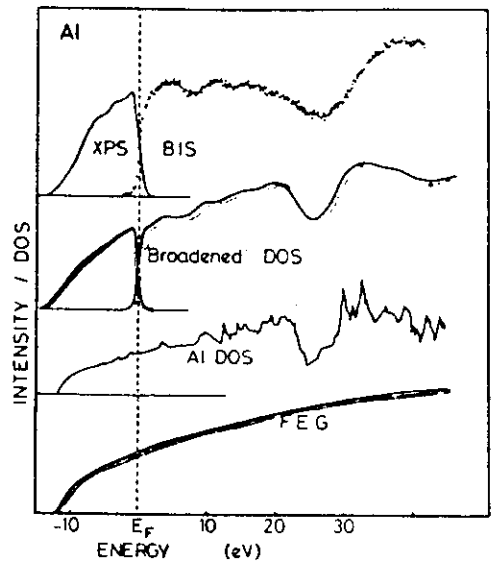

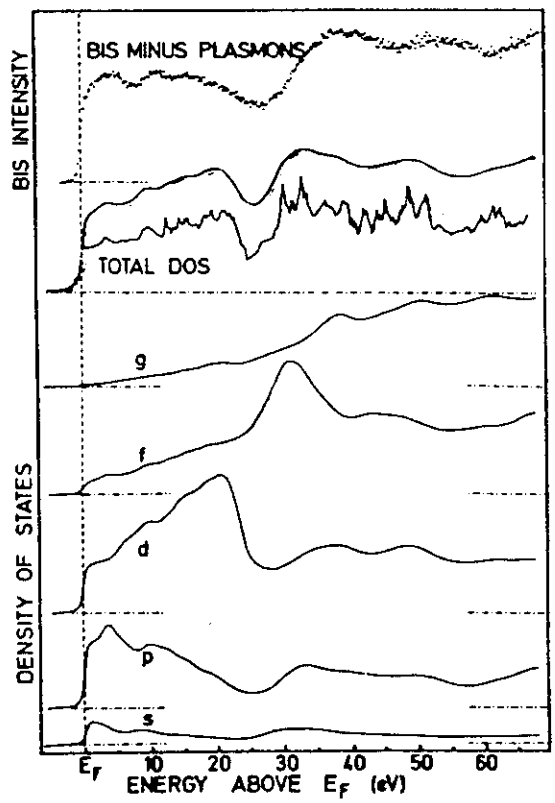

FIG. 5. The partial (s,p,d,f,g) and total density of states curves for Al as compared to the measured BIS spectrum corrected for plasmon losses. With the exception of one total DOS curve, the DOS have been broadened to account for instrumental and lifetime broadening effects (see text).

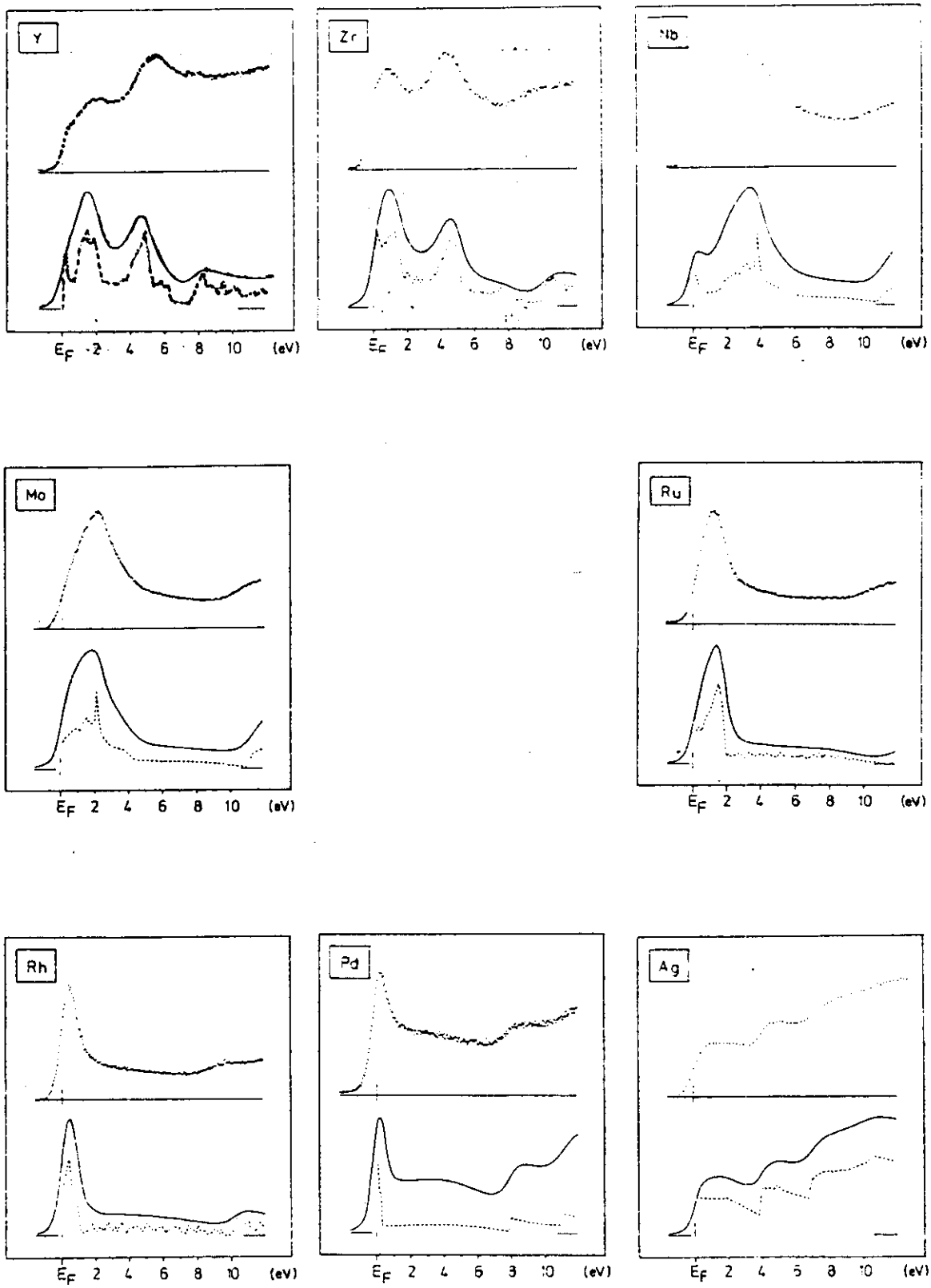

..... EXPERIMENT

---- CALCULATED DOS's

——— GAUSSIAN & LORENTZIAN BROADENED DOS's

PES

$E_i = E_f - \hbar\omega$

$\vec{k}_{i\parallel} = \vec{k}_{f\parallel} - \vec{q}_{\parallel} - \vec{q}_{ph}$

IPES

$E_f = E_i - \hbar\omega$

$\vec{k}_{f\parallel} = \vec{k}_{i\parallel} - \vec{q}_{\parallel} - \vec{q}_{ph}$

$J_{ph} \propto \nu^2 \cos^2\theta \, / \, 2 E c^2 \cos\varphi$

J_{el} – ELECTRONS PER UNIT TIME PER UNIT AREA PER PHOTON

J_{ph} – PHOTONS PER UNIT TIME PER UNIT AREA PER UNIT ENERGY

ν – PHOTON FREQUENCY

c – VELOCITY OF LIGHT IN APPROPRIATE UNITS

ϑ – POLAR ANGLE OF PHOTON SPECIFICATION

φ – POLAR ANGLE OF ELECTRON SPECIFICATION

Ω – SOLID ANGLE IN APPROPRIATE UNITS

$\nu = \frac{1}{\text{WAVELENGTH}}$

J. B. PENDRY
PRL 45 (1980) 1356
J. PHYS. C14 (1981) 1381

d-BAND NOBLE METAL

$\hbar\omega = 0.4$ hartree

OCCUPIED SURFACE STATES

UNOCCUPIED SURFACE STATES

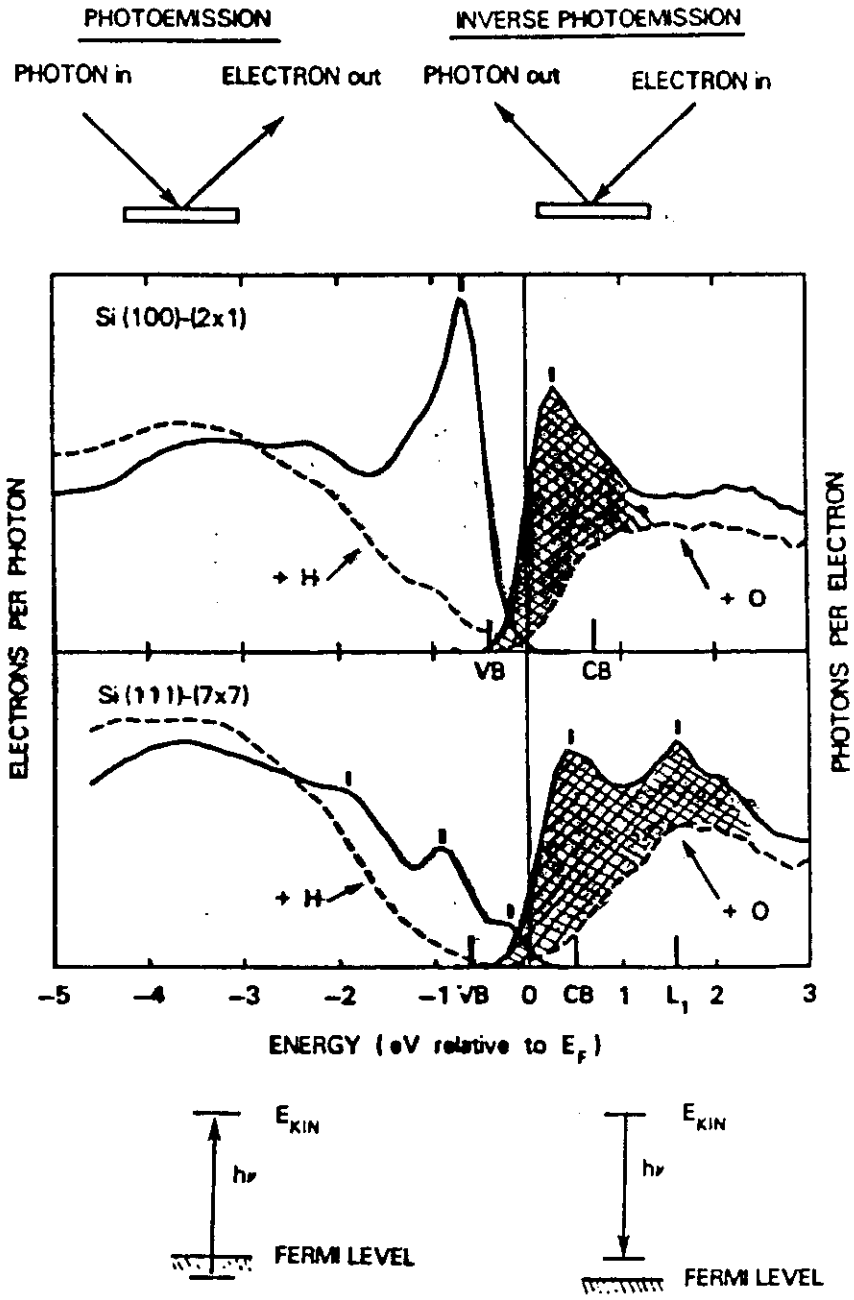

Fig. 4. Comparison between photoemission and inverse photoemission for surface states (tickmarks) on different Si surfaces [17]. Photoemission measures occupied states whereas inverse photoemission measures unoccupied states

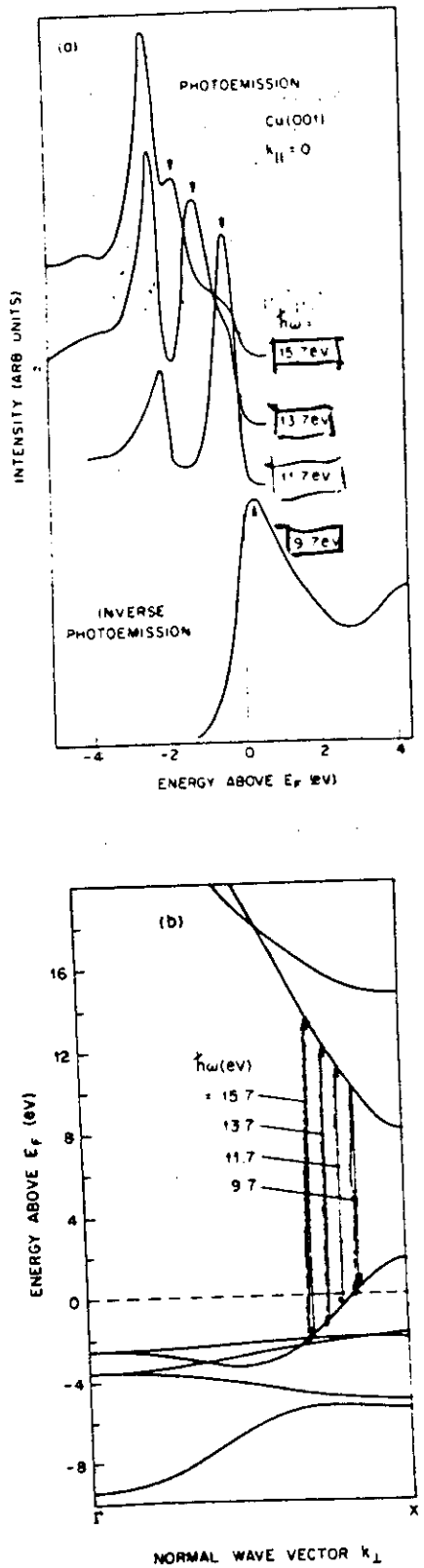

FIG. 3. Complementarity of photoemission and inverse photoemission: (a) comparison of angle-resolved photoemission spectra on Cu(001) taken for normal emission with a k-resolved inverse photoemission spectrum taken for normal electron incidence; (b) corresponding direct k-conserving transitions in the ΓX direction of the bulk band structure.

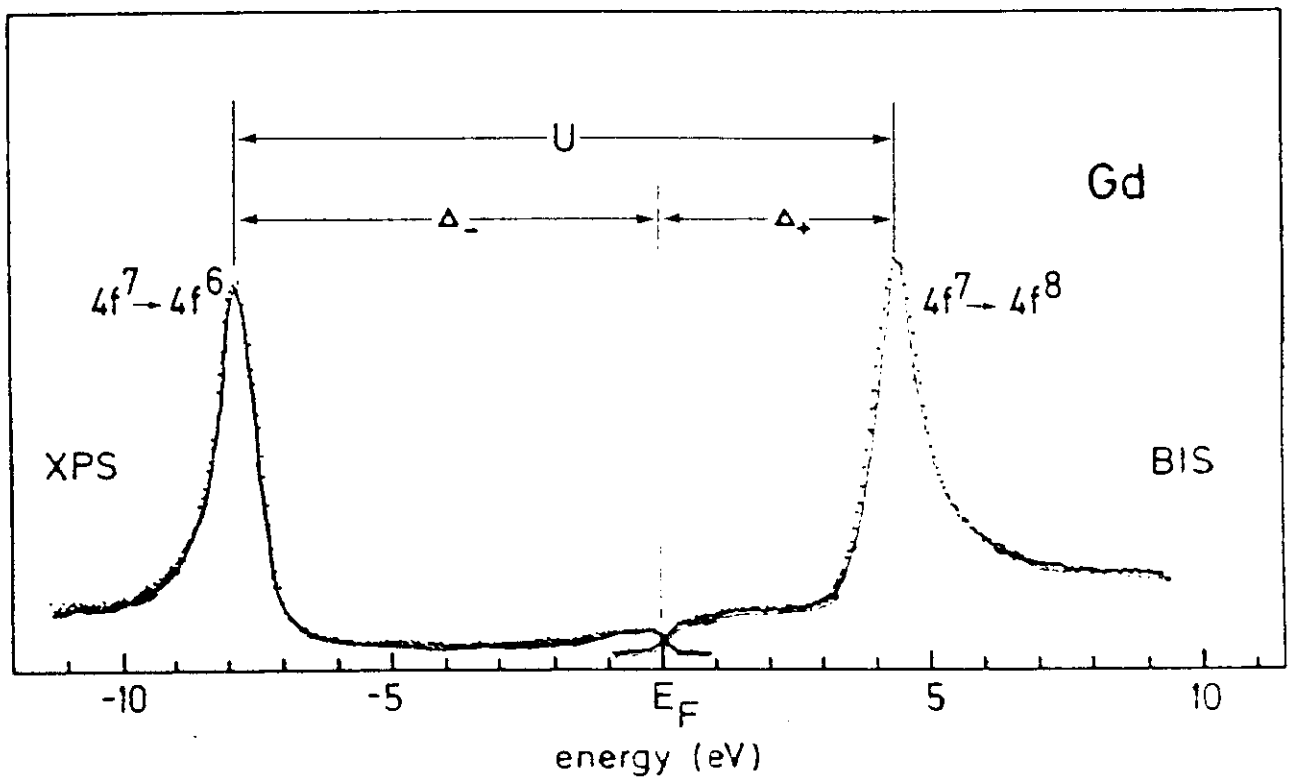

U CORRELATION ENERGY (COULOMB + EXCHANGE)

Δ_- IONIZATION ENERGY OF $4f^n$

Δ_+ AFFINITY ENERGY OF $4f^{n+1}$

$$U = \Delta_- + \Delta_+$$

INVERSE PHOTOEMISSION
VIA GRATING SPECTROMETER

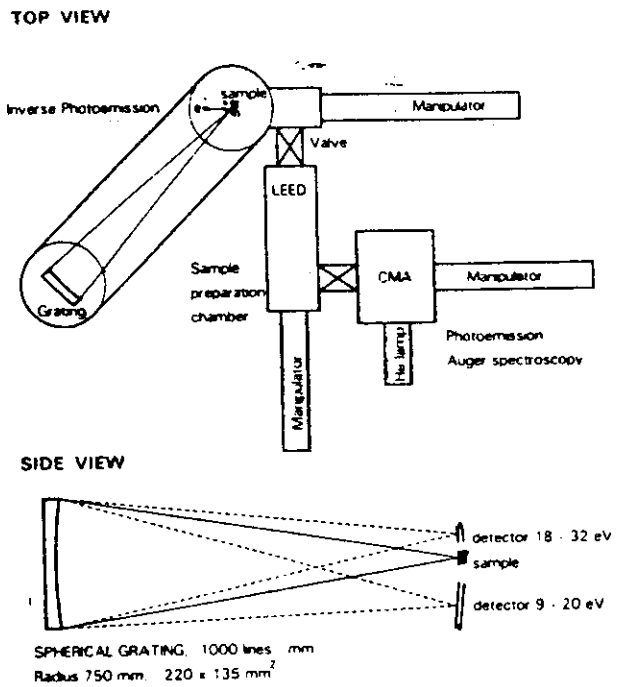

FIG. 2. Schematic of a newly developed system combining photoemission with inverse photoemission in the ultraviolet.

Th. FAUSTER et al
Z. Phys. B 56 (1984) 121

$\hbar\omega_0 = 1486.6\,eV$

J. K. LANG & Y. BAER

RSI 50 (1979) 221

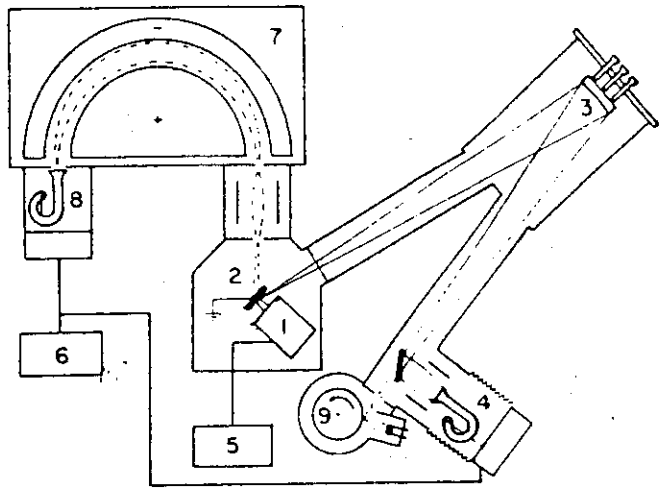

Combined XPS–BIS apparatus. 1—Electron gun; 2—sample; 3—x-ray monochromator; 4—x-ray photon detector; 5—electron gun power supply; 6—counting electronics and data outputs; 7—photoelectron energy analyzer; 8—photoelectron detector; and 9—x-ray tube.

Y. DOSE

APL PHYS 15 (1977) 117

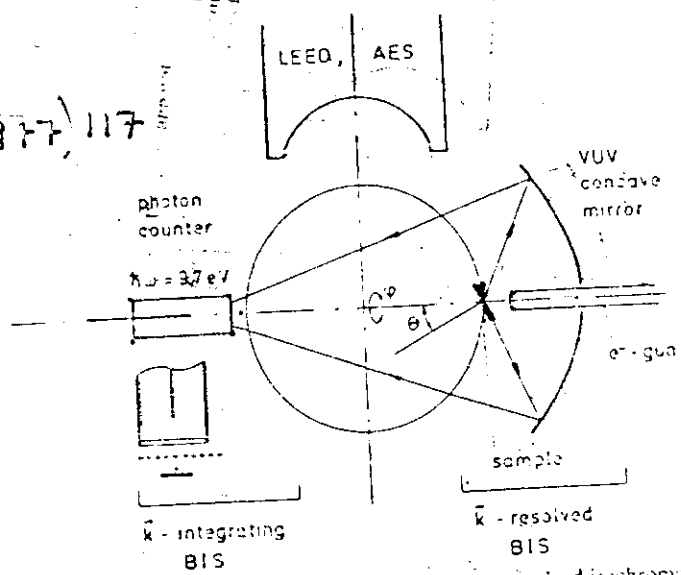

Schematic of an apparatus for momentum-resolved isochromat spectroscopy. An enlarged view of the detector position is given in the lower left corner.

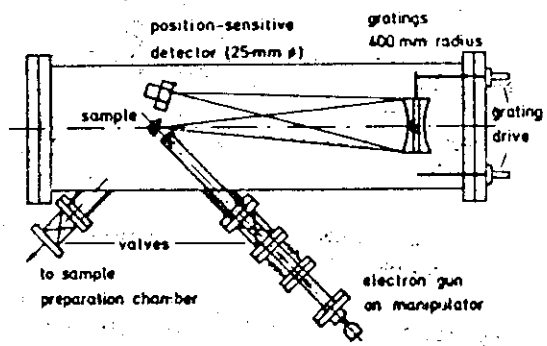

Fig.18.3. Top view of a grating spectrograph for inverse photoemission showing retractable electron source and sample. The light from the sample is dispersed by one of the two gratings and focused on a position-sensitive detector. Sample preparation is performed in a separate vacuum chamber

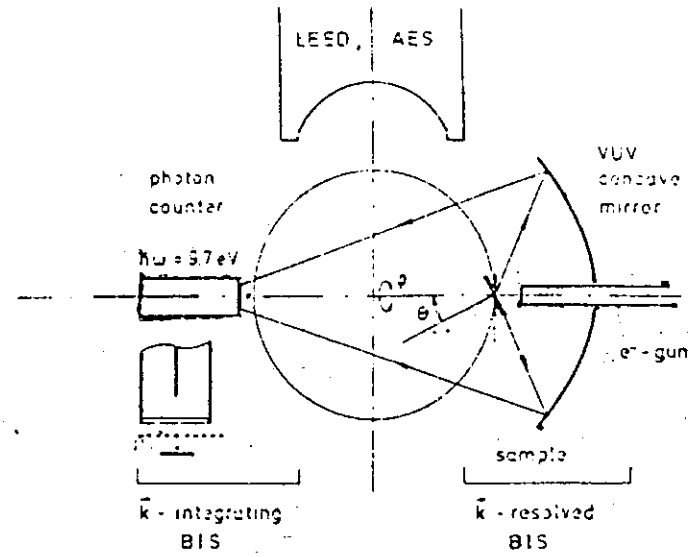

Schematic of an apparatus for momentum-resolved isochromat spectroscopy. An enlarged view of the detector position is given in the lower left corner.

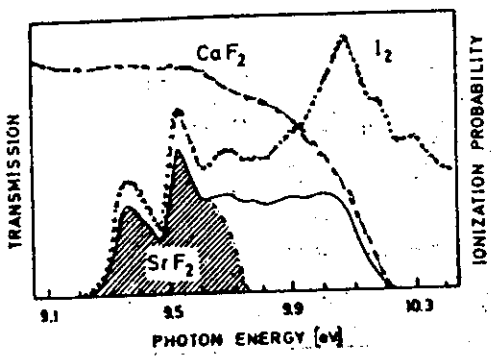

Fig.18.2. Energy dependence of the photoionization efficiency of I_2 (•••) and of the optical transmission of CaF_2 (---). The combined effect provides a bandpass (——) centered at 9.7 eV. For SrF_2 the resulting bandpass (*shaded area*) has an improved energy resolution and is centered at 9.5 eV.

P.M.G. ALLEN & al
JVST A5 (1987) 3346

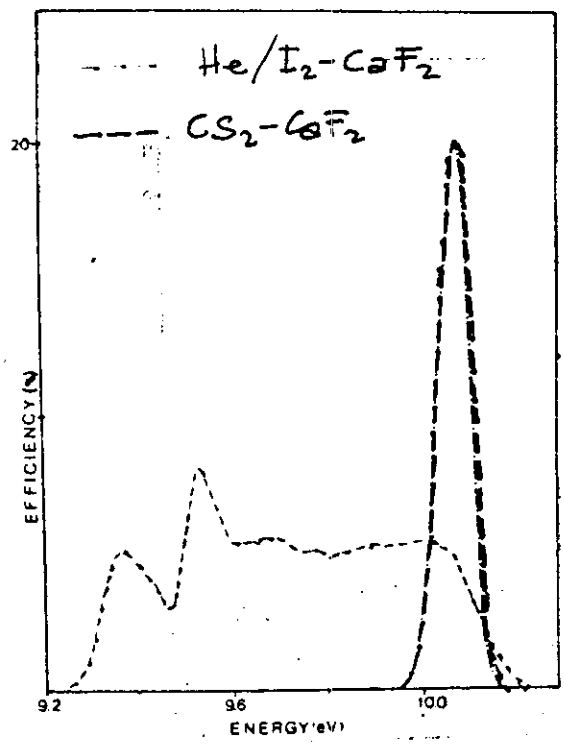

FIG. 4. Comparison of functional response of ··· CS_2–CaF_2 counter, and —— He/I_2–CaF_2 Geiger counter (Ref. 1).

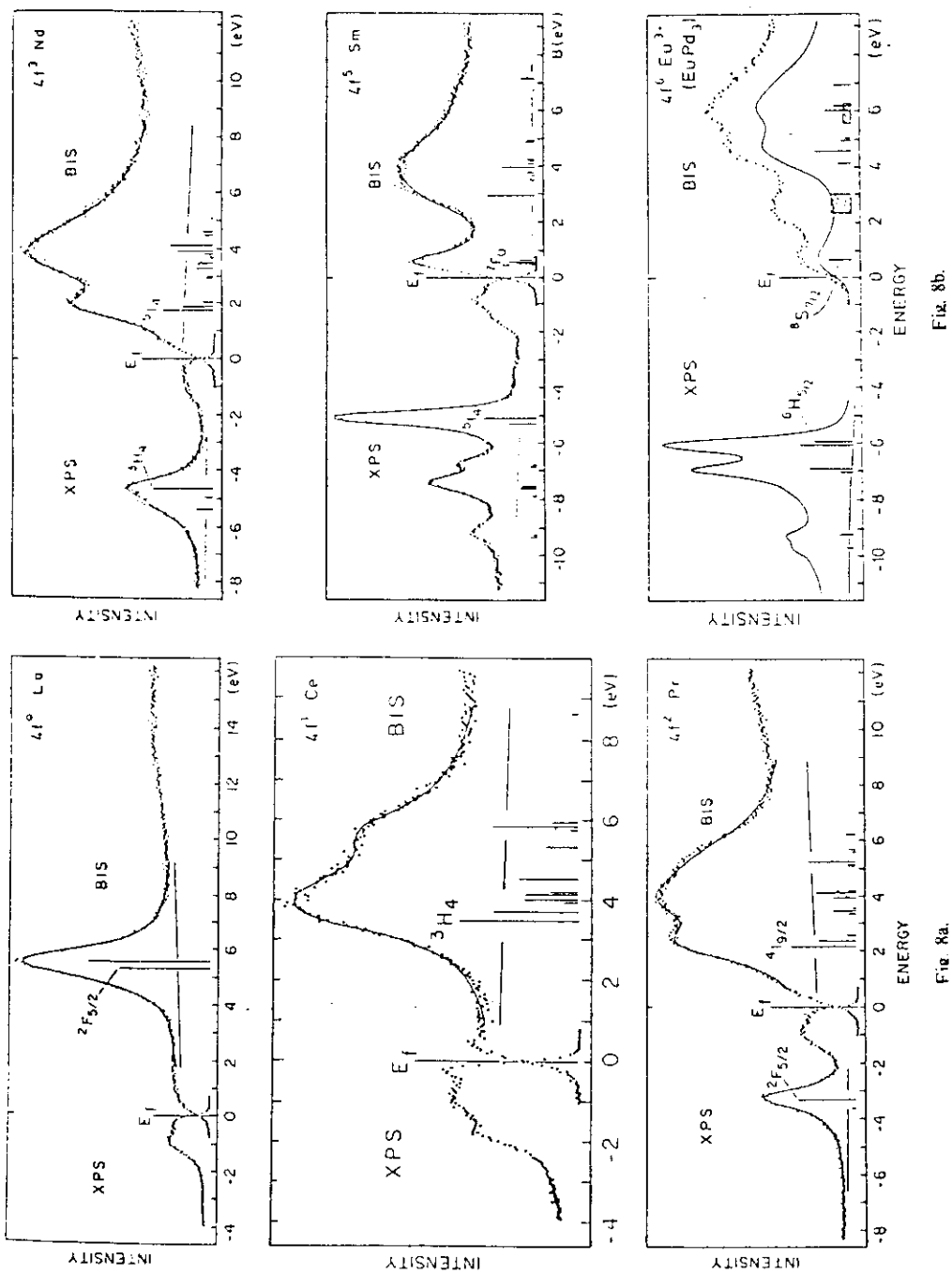
4f⁰ La
4f¹ Ce
4f² Pr
4f³ Nd
4f⁵ Sm
4f⁶ Eu³⁺ (EuPd₃)
XPS
BIS
INTENSITY
ENERGY
E_f
²F_5/2
³H_4
⁴I_9/2
⁶H_5/2
⁸S_7/2

Fig. 8a.

Fig. 8b.

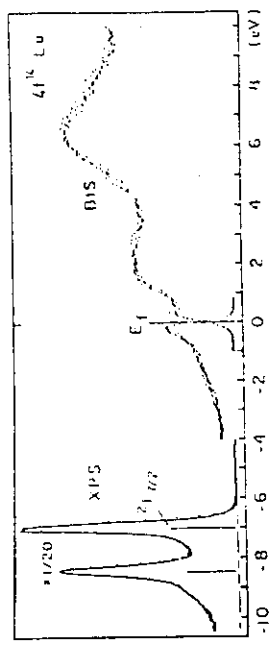

Fig. f.

Fig. 8. Atomic-like analysis of XPS and BIS spectra for all $4f^n$ initial states. The spectra of the pure metals are taken from Lang et al. (1981), the spectra of YbP from Wuilloud et al. (1986) and the BIS spectrum of $EuPd_3$ from Laubschat et al. (1984). The coefficients of fractional parentage shown as vertical bars have been calculated in the *LS* coupling scheme (Nielson and Koster 1964, Cox et al. 1981), except for the XPS process from the initial configurations f^n to f^{13} where the intermediate coupling scheme has been used (Gerken 1983). The particular situation met in Ce is discussed in sections 6 and 7.

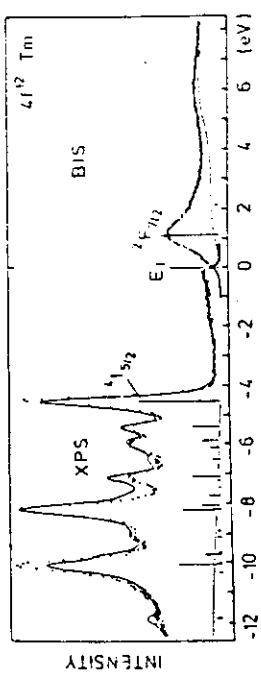

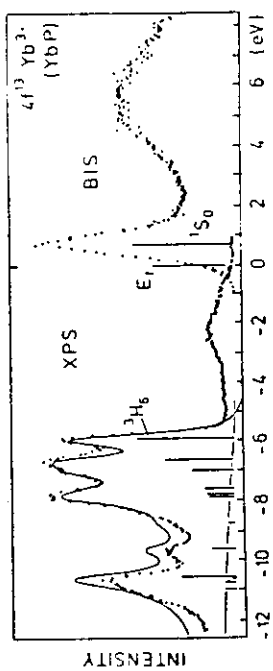

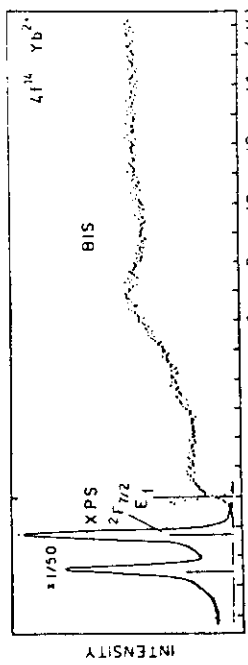

Fig. 8c.

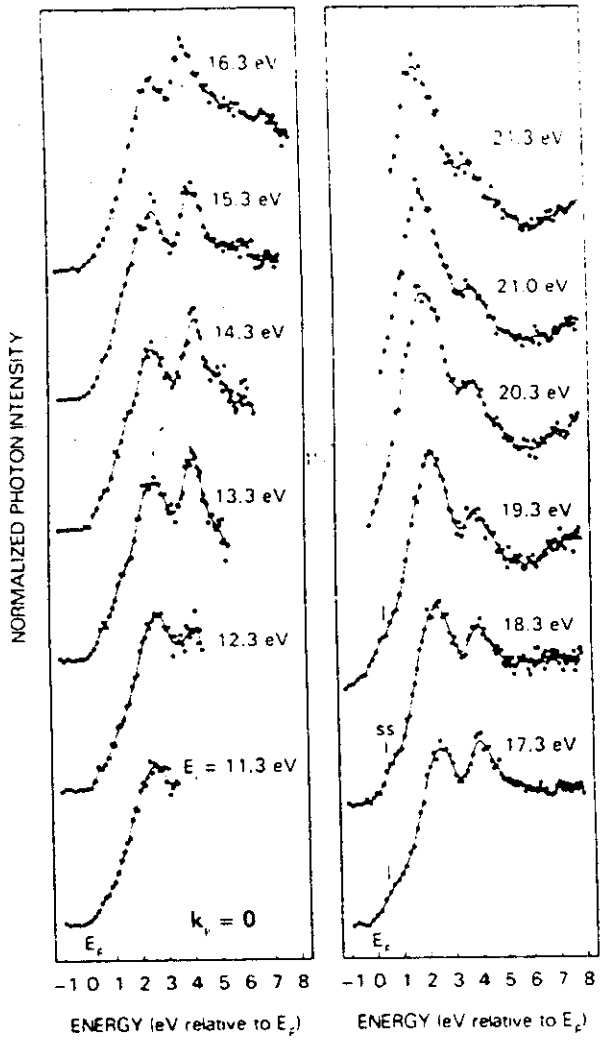

Inverse-photoemission spectra at normal incidence for a range of initial electron energies E_i.

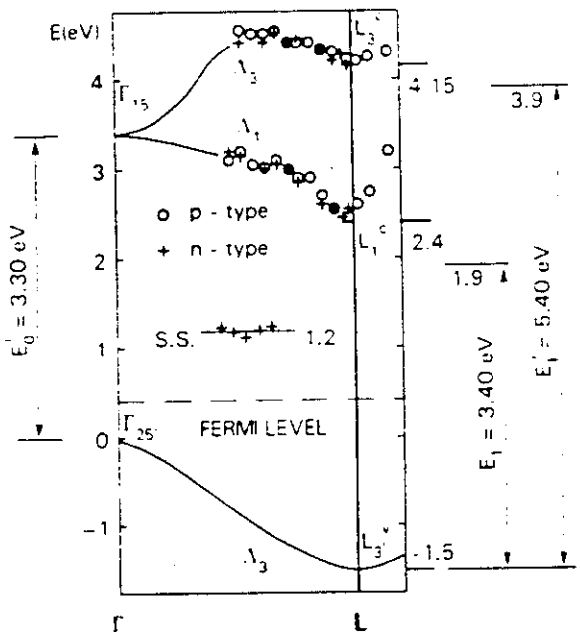

Energy dispersion of conduction-band states along ΓL as derived from inverse-photoemission data. The Λ_3 band is from Ref. 6, and optical transition energies appropriate for $T = 300$ K are from Ref. 7. Data points marked S.S. correspond to an empty surface state on the Si(111) 2×1 surface.

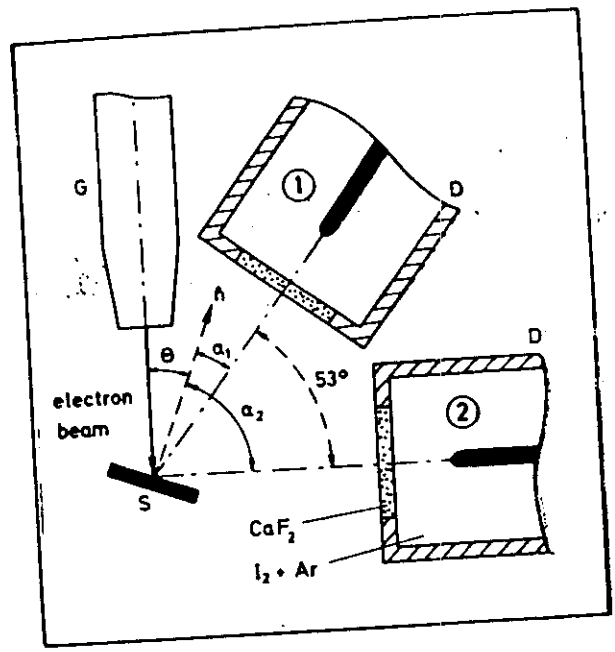

Fig. 1. Experimental setup with two photon detectors (D) for measuring light-polarization effects in inverse photoemission. G = electron gun, S = sample.

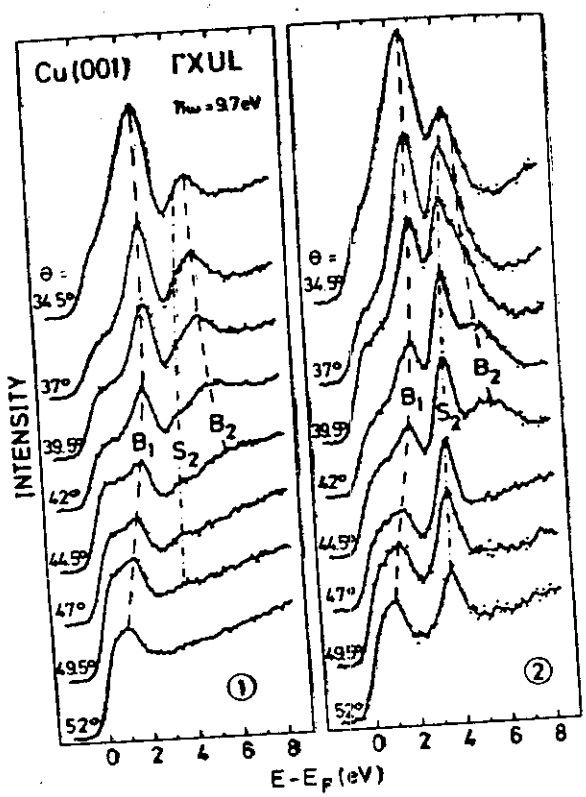

Fig. 2. Bremsstrahlung isochromat spectra of Cu(001) in the ΓXUL-azimuth for various angles of incidence. The left panel shows spectra obtained with detector 1, the right panel those of detector 2. The spectra have been renormalized to equal background intensity at 8 eV.

AES

- **Elemental sensitivity**
  via
  Kinetic energies of AES lines

- **Chemical environment sensitivity**
  via
  Shift of line energies & line shape analysis

- **Quantitative evaluation**
  via
  Line intensity analysis
  & cross section evaluation

- **Structural information**
  via
  Auger electron diffraction

- **Access key to many body realm**
  via
  Spectral line shape analysis & theoretical calculations

$KL_1L_{2,3}$ AUGER TRANSITION

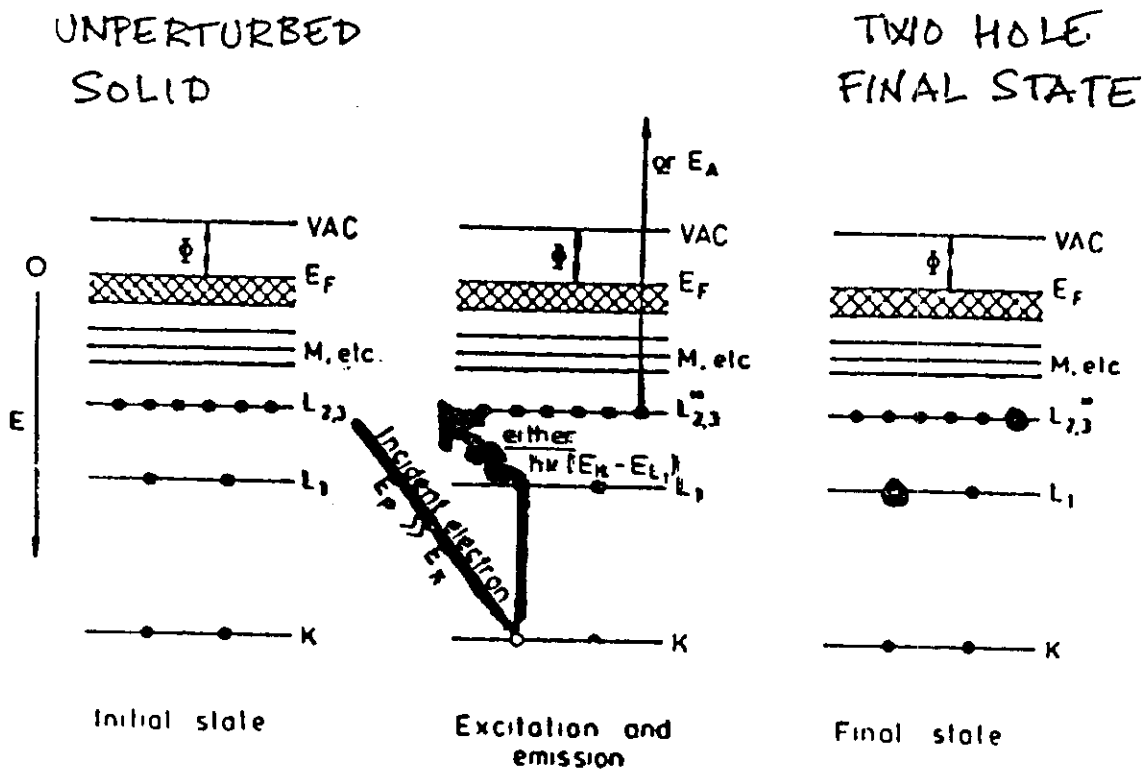

Figure 3.4 Schematic diagram of the process of Auger emission in a solid. The ground state of the system is shown at the left. In the centre an incident electron of energy E_p has created a hole in the core level K by ionization; for this to occur efficiently E_p should be $\geq \sim 5E_K$. The hole in the K shell is filled by an electron from L_1, releasing an amount of energy $(E_K - E_{L_1})$, which can appear as a photon of energy $h\nu = (E_K - E_{L_1})$ or can be given up to another electron. In this example the other electron is in the $L_{2,3}$ shell, and it is then ejected with energy $(E_K - E_{L_1} - E^*_{L_{2,3}})$; $E^*_{L_{2,3}}$ is starred because it is the binding energy not of $L_{2,3}$ in its ground state but in the presence of a hole in L_1. The doubly ionized final state is shown on the right

ENERGY CONSERVATION

$$E(KL_1L_{2,3}) = E_b(K) - E_b(L_1) - E_b(L_{2,3})$$

$$E(ABC) = E_b(A) - E_b(B) - E_b(C) - \mathcal{J} + \mathcal{R}$$

$\mathcal{J}$ = TWO HOLE FINAL STATE CORRELATION EN.

$\mathcal{R}$ = RELAXATION ENERGY

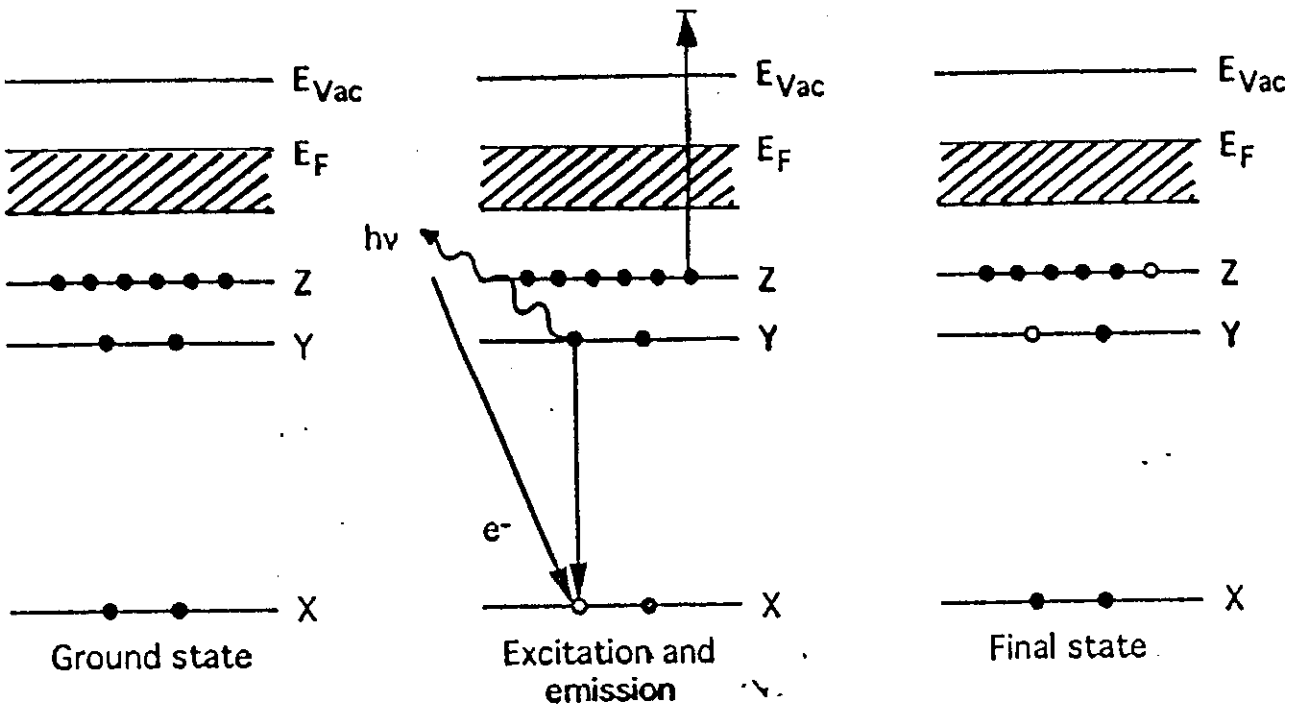
E_{Vac}
E_F
Z
Y
X
Ground state
hν
e⁻
E_{Vac}
E_F
Z
Y
X
Excitation and emission
E_{Vac}
E_F
Z
Y
X
Final state

Fig. 8

ENERGY DISTRIBUTION OF THE e^- EMISSION FROM GRAPHITE FOLLOWING PRIMARY ELECTRON BOMBARDMENT

$E_p = 1000$ eV

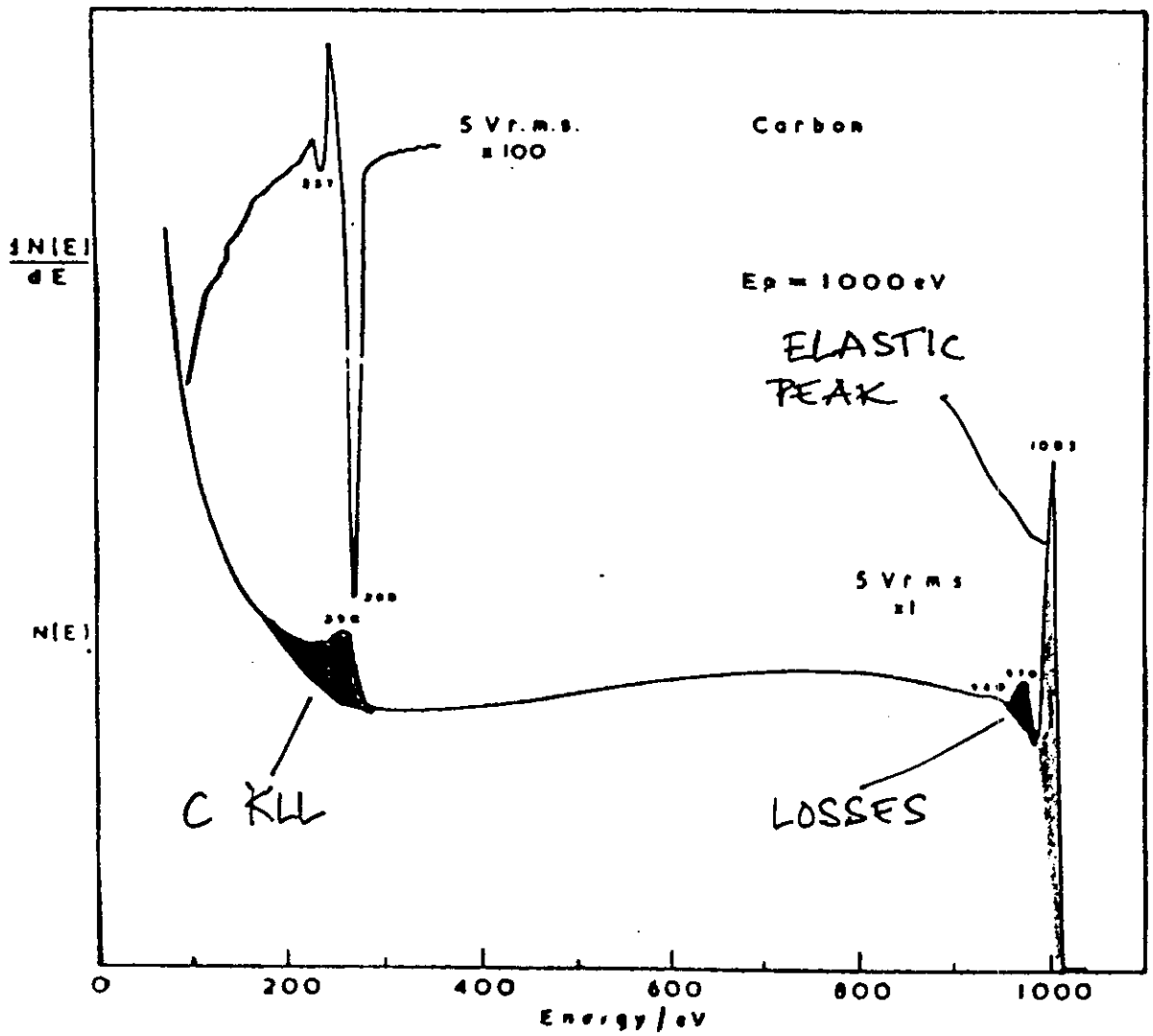

Figure 3.2 Lower curve: distribution of energies of secondary electrons ejected from a graphite surface by incident electrons of energy 1000 eV. Upper curve: differential distribution over the energy range containing the carbon *KLL* Auger peaks. In the differential distribution the peak 'position' is taken to be that of the high energy minimum, by convention

AUGER SPECTRA

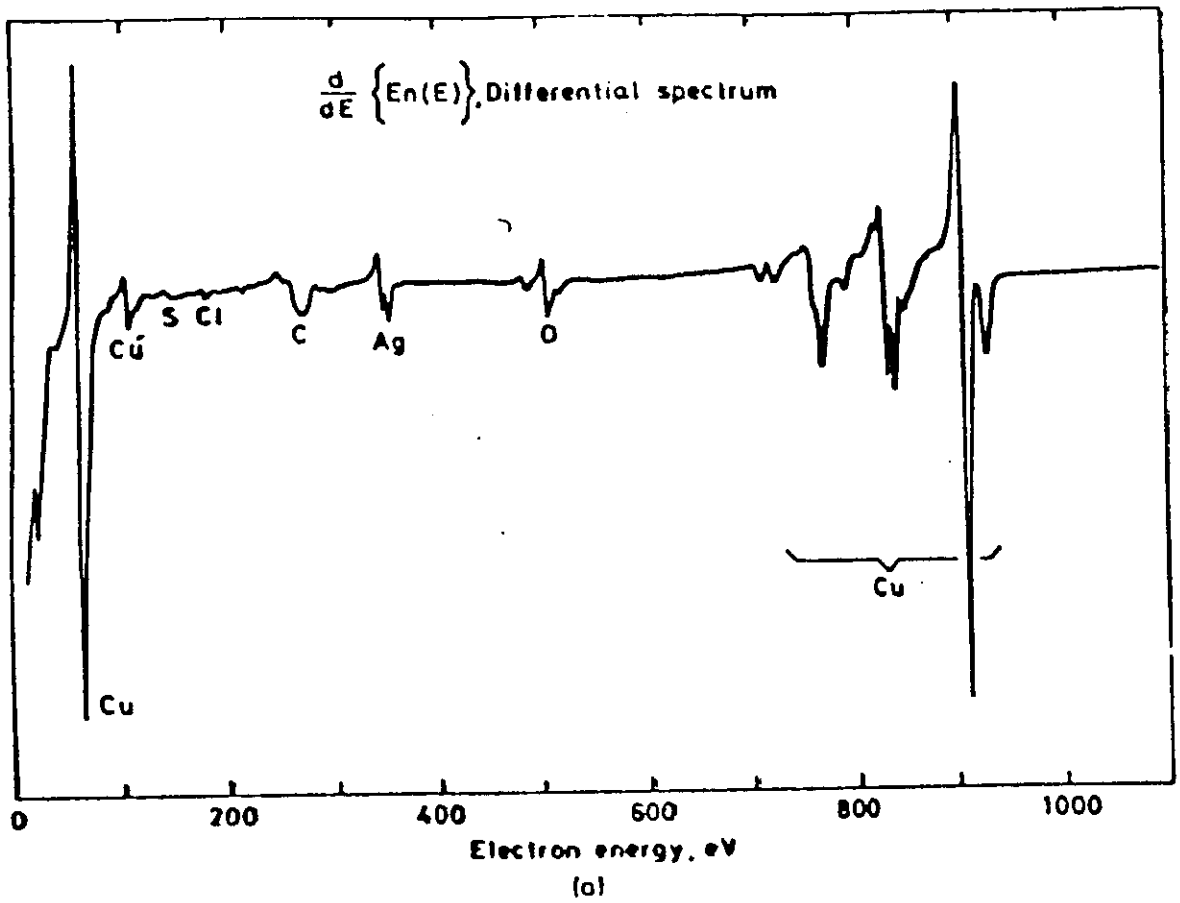

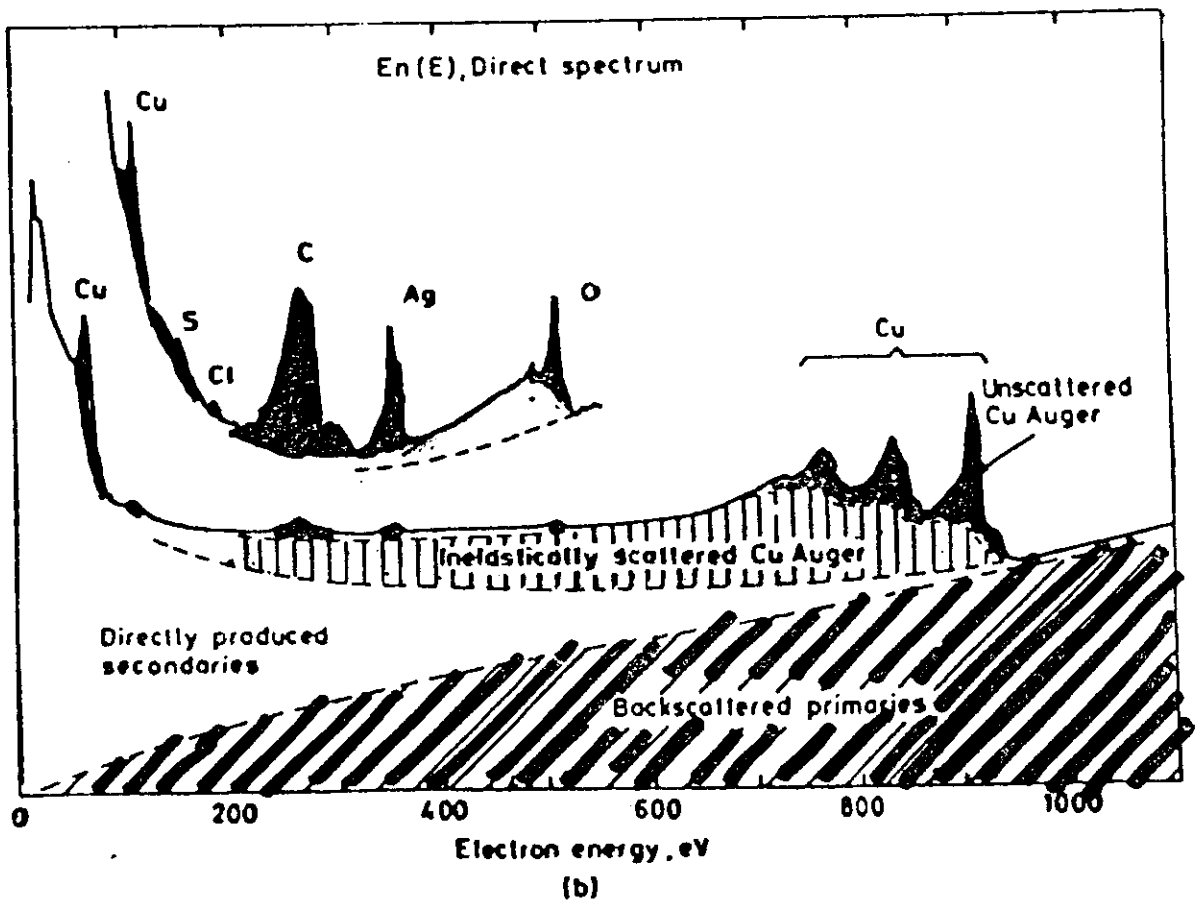

Figure 5.13 Differential and direct electron spectra from contaminated copper. (After Seah[56])

Si AUGER SPECTRUM

DERIVATIVE MODE

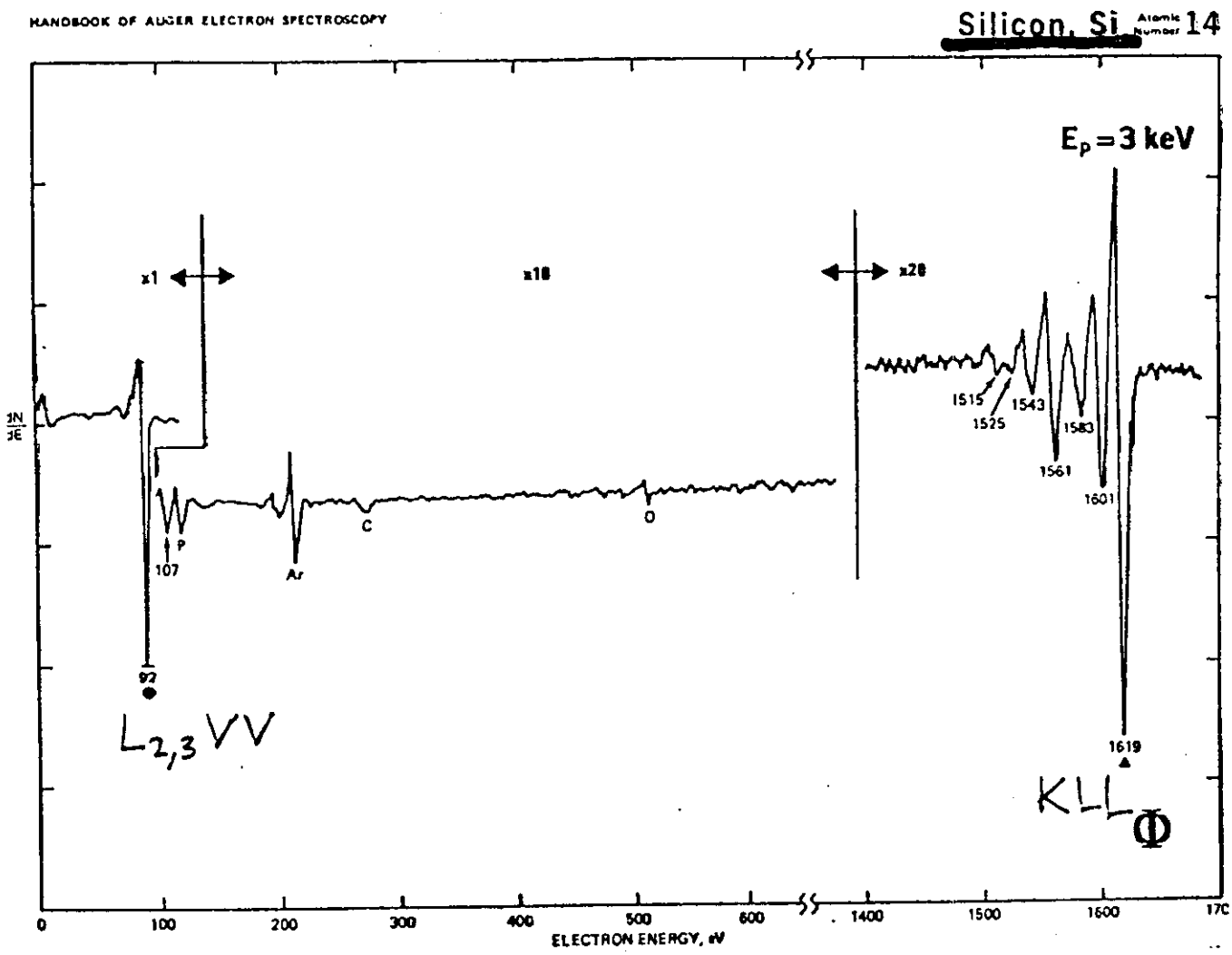

PRINCIPAL AUGER ELECTRON ENERGIES

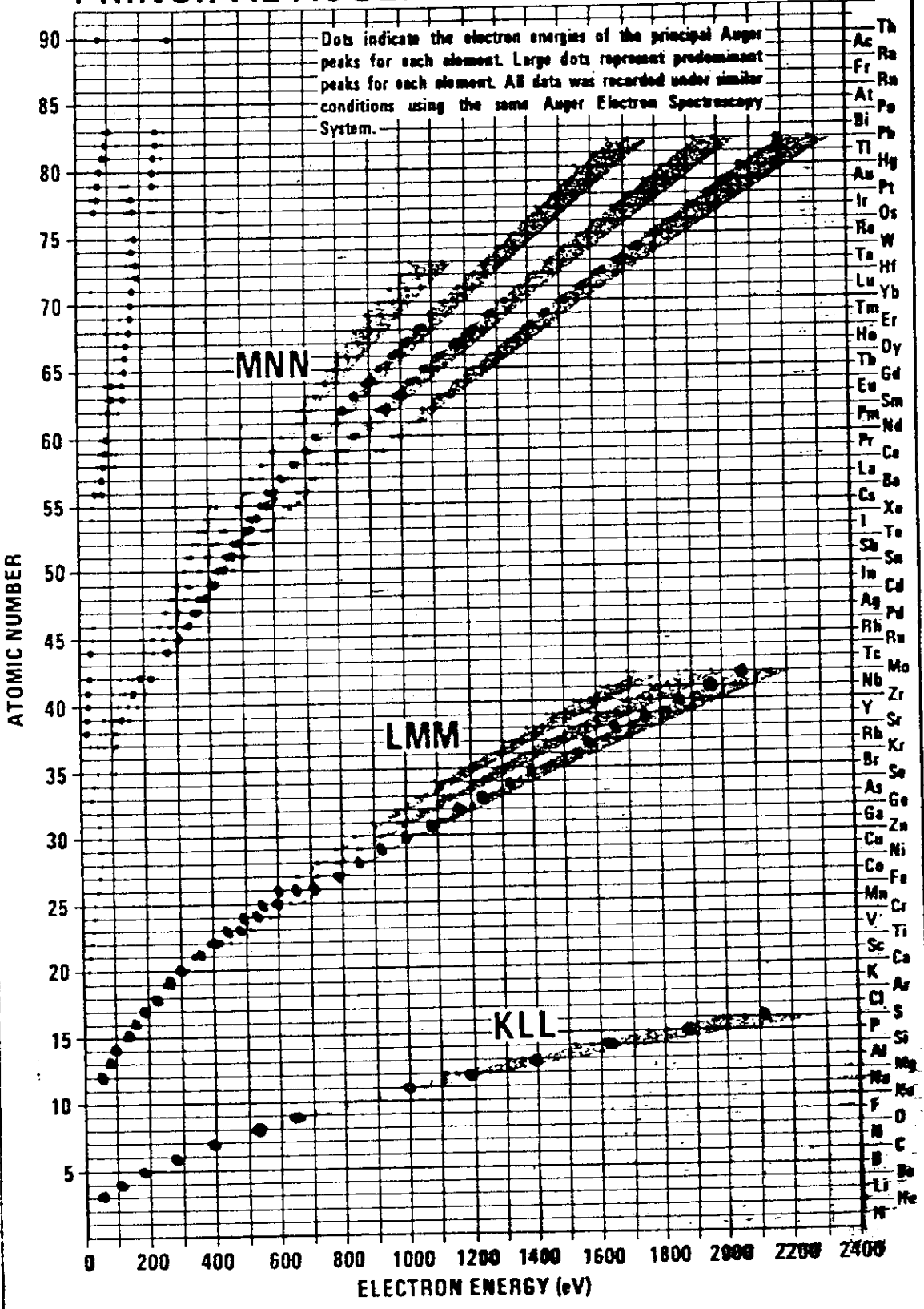

PHYSICAL ELECTRONICS INDUSTRIES, INC.

INTERMEDIATE COUPLING

J-J

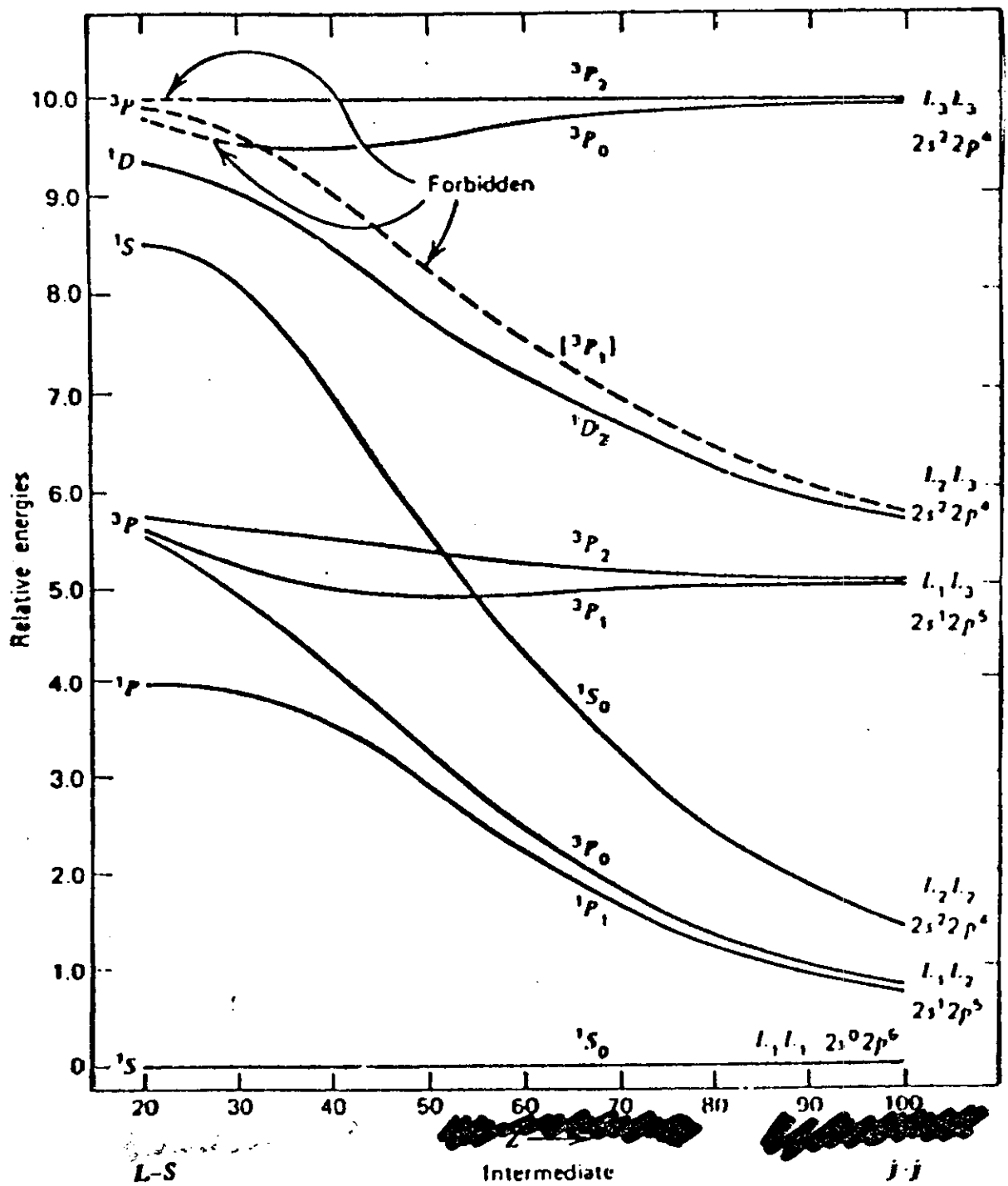

Figure 3.1 The transition from pure *L–S* through intermediate to pure *j–j* coupling across the Periodic Table, and its effect on relative energies in the *KLL* Auger series. (Reproduced from Sevier[2] by permission of John Wiley & Sons Inc.)

DE-EXCITATION PROCESSES FOLLOWING ATOM IONIZATION

PROBABILITY OF AUGER e^- EMISSION Versus PROBABILITY OF X-RAY FLUORESCENCE

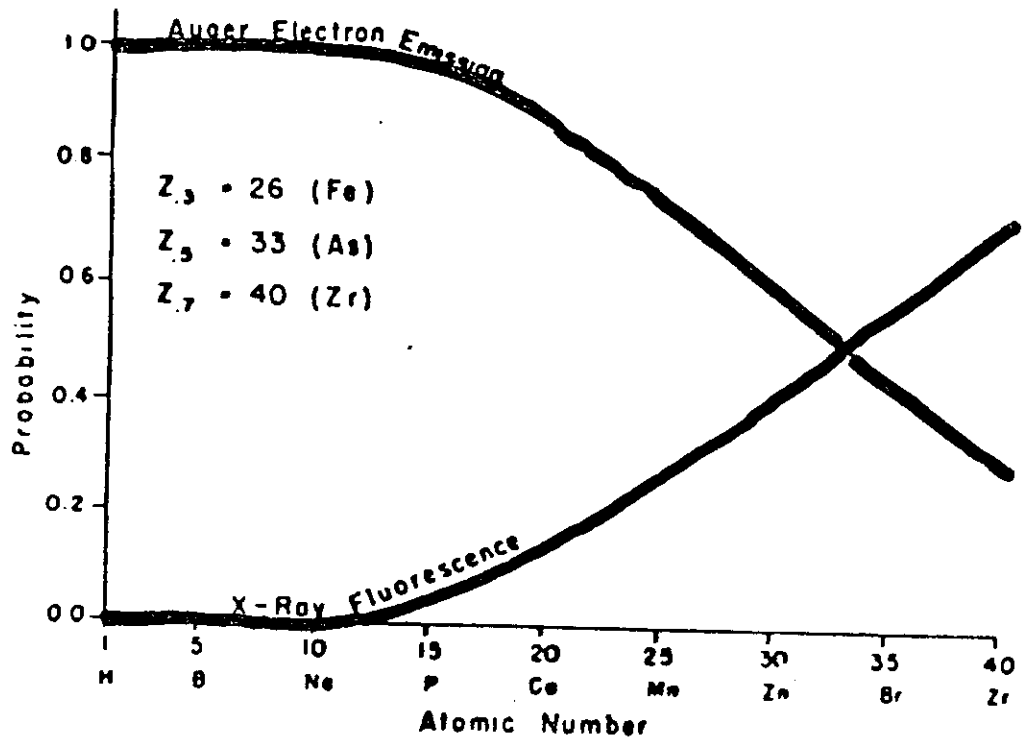

Figure 3.5 Relative probabilities of relaxation by emission of an Auger electron and by emission of an X-ray photon of characteristic energy, following creation of a core hole in the *K* shell

AES
FRAGMENTS OF THEORY

MATRIX ELEMENT

$M_{if} = \langle i | \frac{1}{r} | f \rangle$

$|i\rangle \quad |\psi_A \psi_K\rangle$

$|f\rangle \quad |\psi_B \psi_C\rangle$

- ANGULAR MOMENTUM CONSERVATION
- PARITY CONSERVATION
- CORE - VALENCE - VALENCE CVV

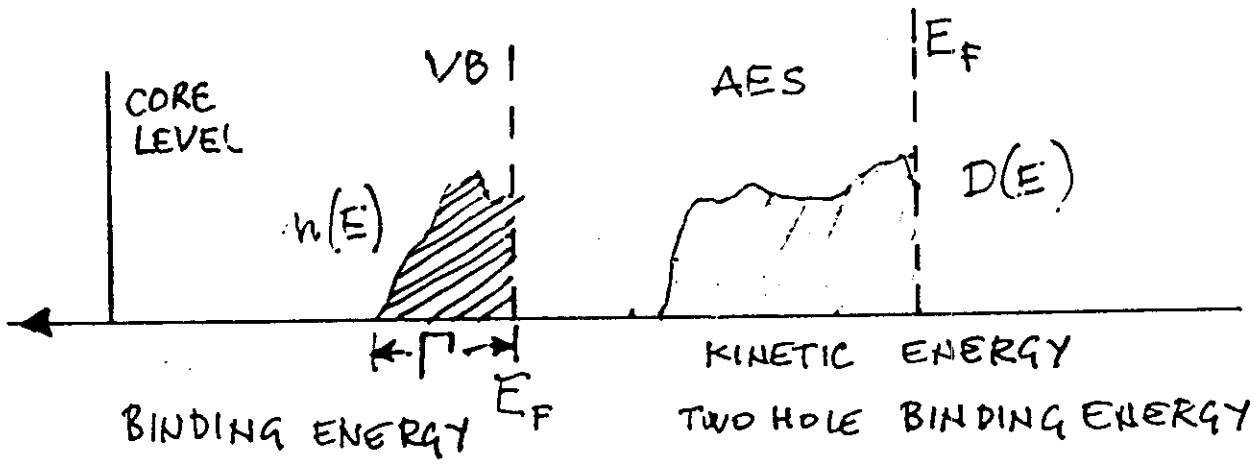

$$D(E) \propto n(E) * n(E) = \int \rho(E-\varepsilon)\,\rho(\varepsilon)\,d\varepsilon$$

SELF-FOLDED DENSITY OF STATES

PROJECTED [illegible] THE CORE HOLE SITE

BASIC COMPONENTS FOR AES

- UHV APPARATUS
- SAMPLE
- ELECTRON GUN
- ELECTRON ENERGY ANALYSER
- ELECTRON DETECTOR
- ANALOG SIGNAL ELECTRONICS and/or PULSE COUNTING ELECTRONICS

ELECTRON GUN

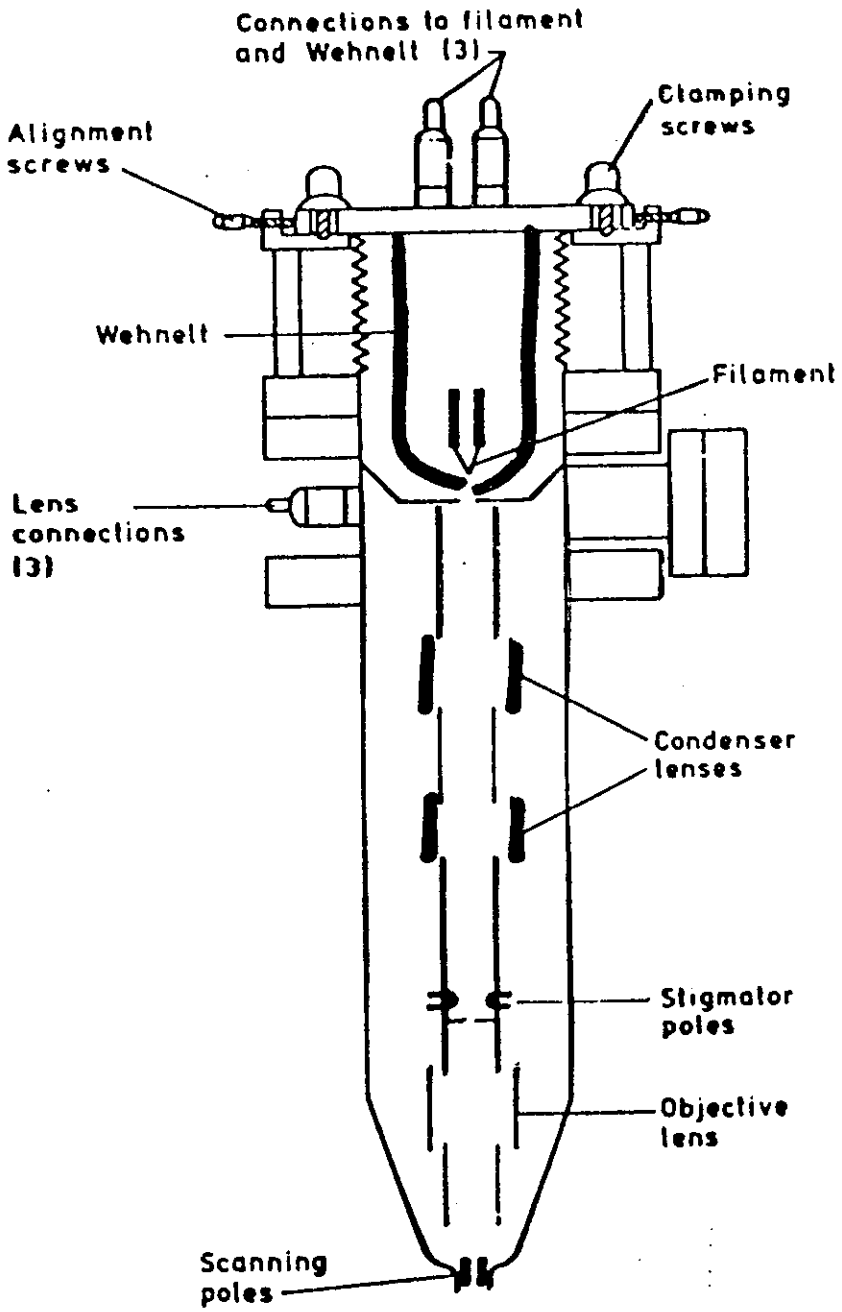

Figure 2.23 Example of an electrostatically focused electron gun for operation at energies up to 10 keV and currents between 1 and 10 nA. The filament and Wehnelt cylinder can be adjusted in position together by screws operating on a flexible bellows. Two condenser lenses and an objective lens perform the focusing, and beam rastering is carried out by a set of orthogonal plates at the end of the electron optical column. Optimum spot size obtainable is about 0.2 μm, but a 0.5 μm spot is more normal in everyday use. (Reproduced by permission of Vacuum Generators Scientific Ltd)

HOW TO DECIDE THE ENERGY OF THE PRIMARY ELECTRON BEAM

IONIZATION CROSS SECTION FOR LEVEL "X"

versus

PRIMARY BEAM ENERGY (E_0/E_{AX})

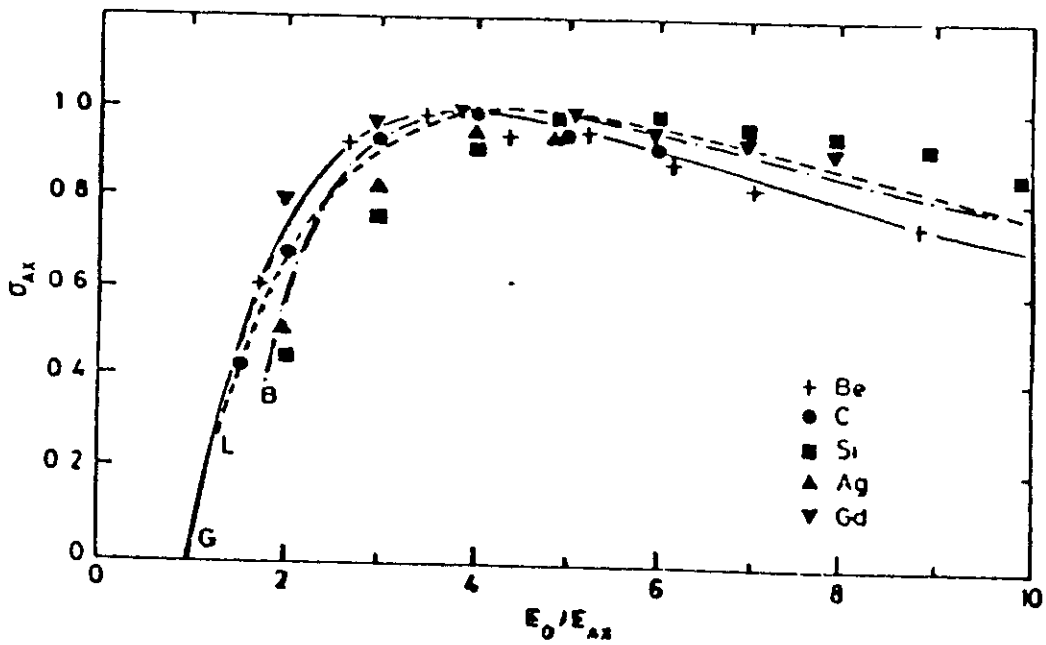

Figure 5.2 The energy dependence of the Bethe,[7] (B) Gryzinski[8] (G) and Lotz[9] (L) cross-sections for ionizing level X, together with experimental measurements for beryllium,[10] carbon, silicon, silver and gadolinium[11]

E_{AX} = IONIZATION ENERGY OF LEVEL "X"

E_0 = PRIMARY BEAM ENERGY

Relative Auger Sensitivities of the Elements

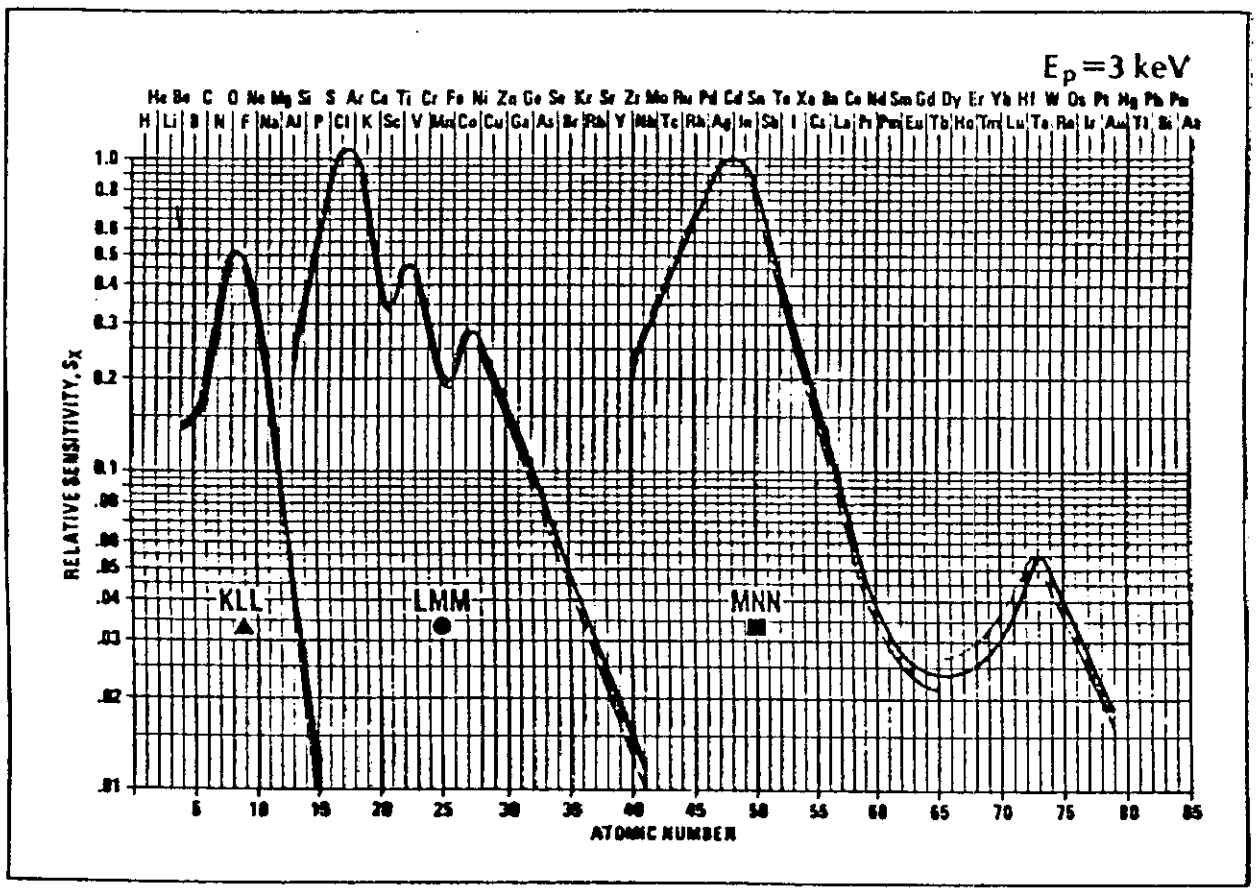

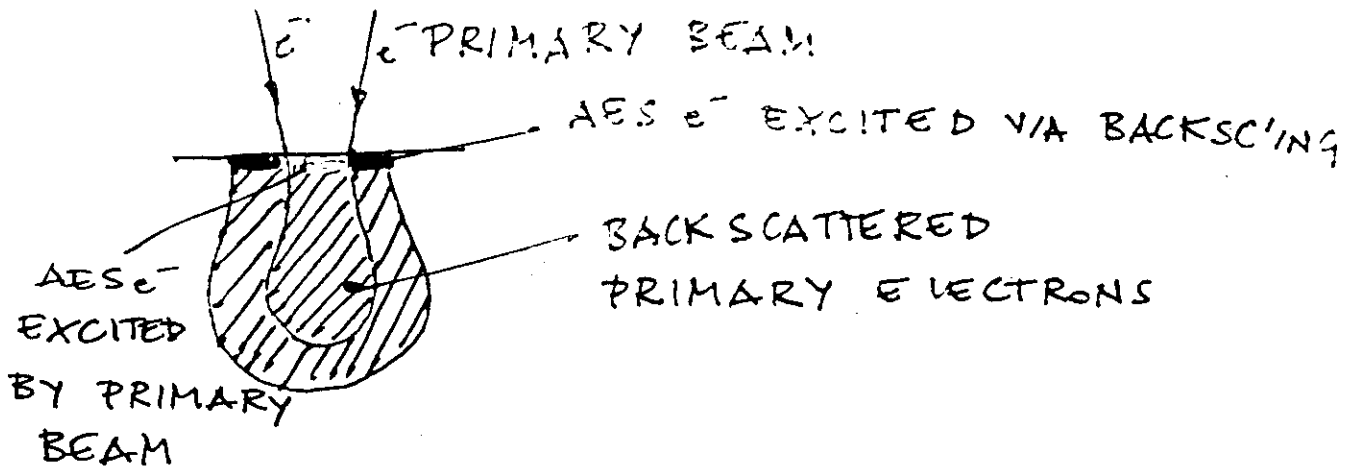

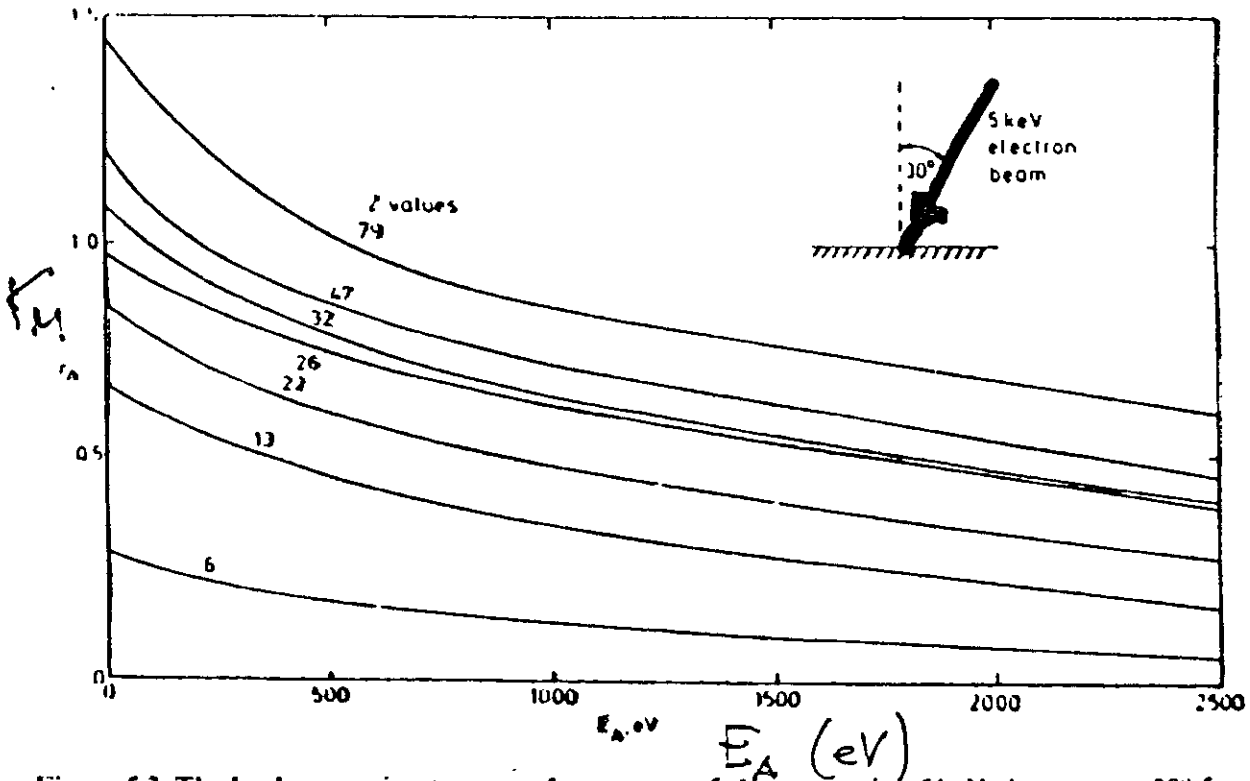

Figure 5.3 The back-scattering term, r_M, for a range of elements using 5keV electrons at 30° from the surface normal, from the calculations of Shimizu and Ichimura[12,13,15]

$$\sigma_{Ax}\left[1 + r_M\left(E_{Ax}; E_o; \alpha\right)\right]$$

r_M BACK SCATTERING TERM (MATRIX DEPENDENT)

BINARY SYSTEMS

TRUE COMPOSITION
versus

COMPOSITION DEDUCED IGNORING THE MATRIX TERM

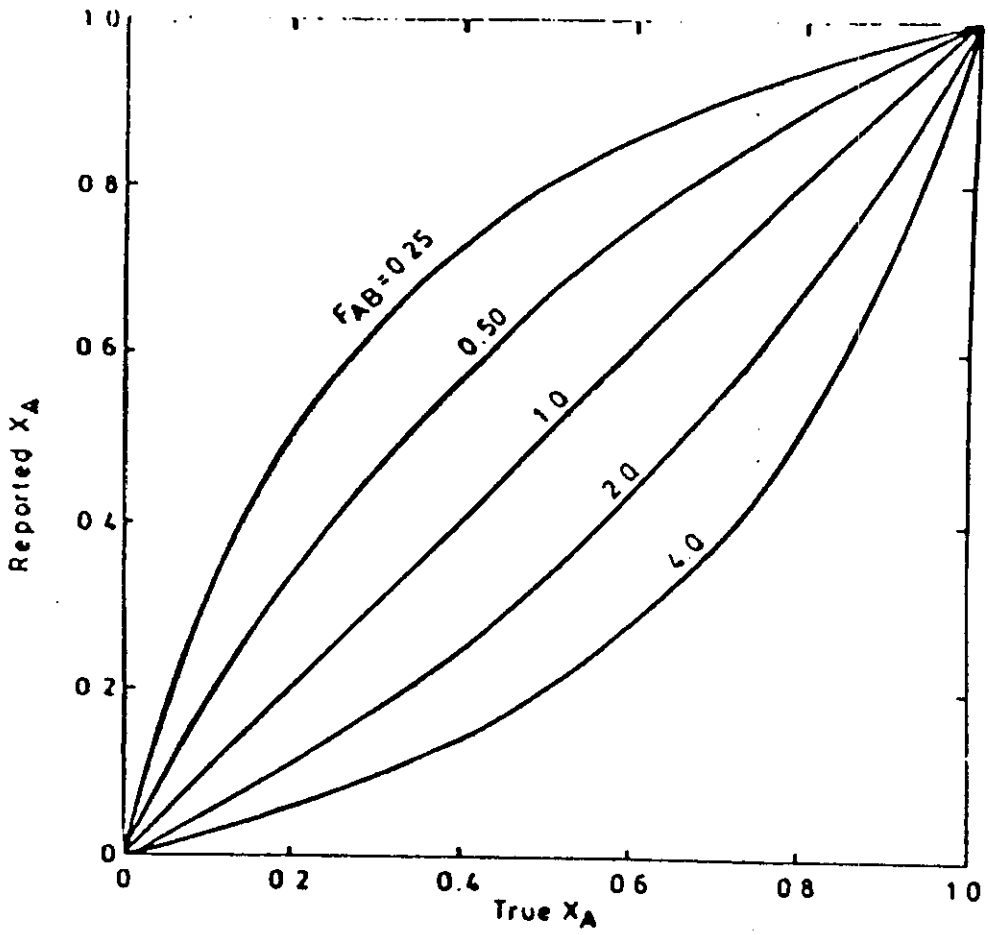

Figure 5.6 A comparison between the true composition and that deduced ignoring the matrix term

AES

GAS PHASE

versus

SOLID PHASE

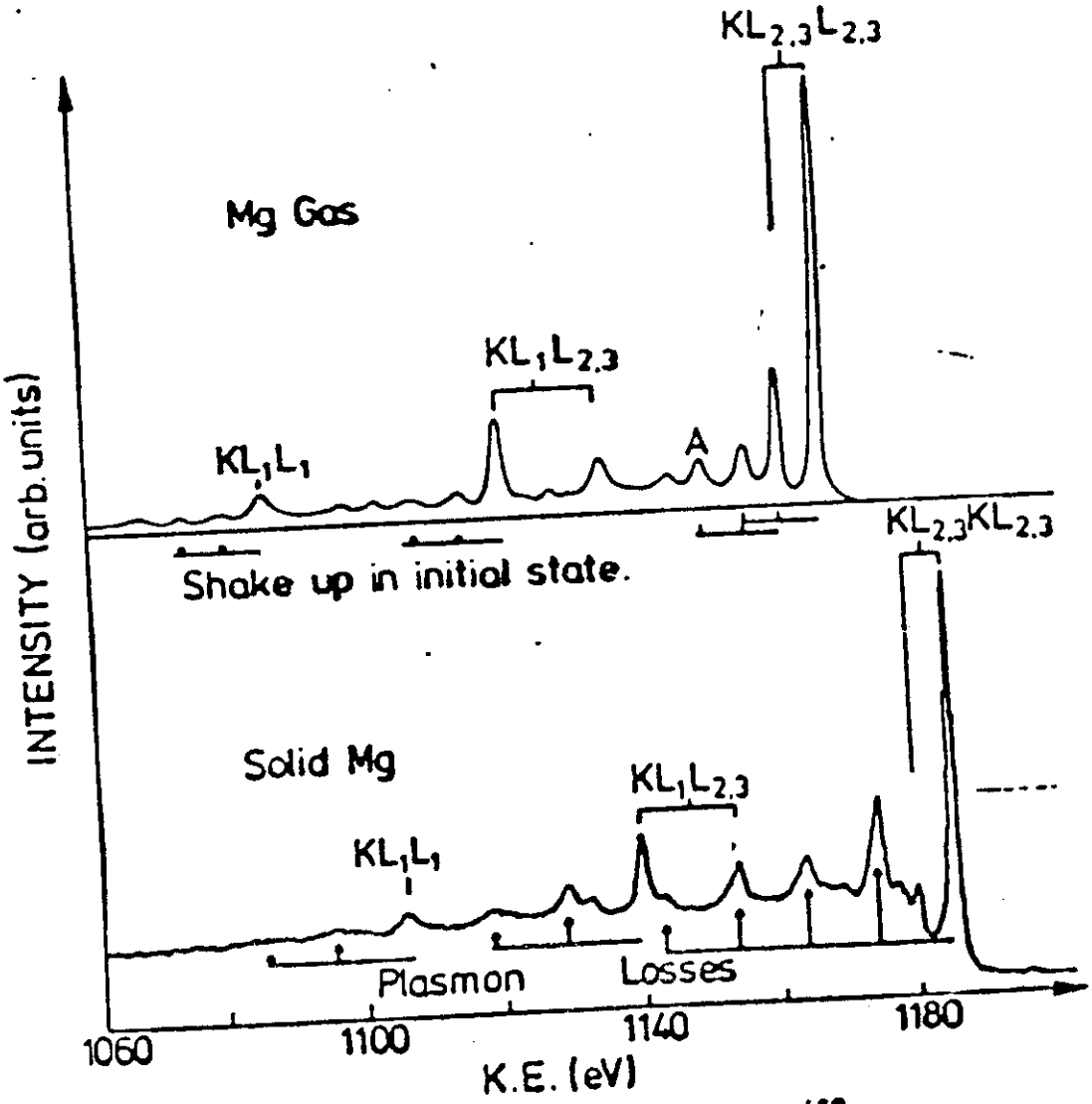

12. The KLL Auger spectra of Mg gas[115] and solid Mg.[189]

AES

- ELEMENTAL SENSITIVITY
  via
  KINETIC ENERGIES OF AES LINES

- CHEMICAL ENVIRONMENT SENSITIVITY
  via
  SHIFTS OF LINE ENERGIES
  ⇕ LINESHAPE ANALYSIS

- QUANTITATIVE EVALUATION
  via
  LINE INTENSITIES ⇕
  SENSITIVITY FACTORS

- STRUCTURAL INFORMATION
  via
  AUGER ELECTRON DIFFRACTION

- ACCESS KEY TO MANY BODY REALM
  via
  LINESHAPE ANALYSIS ⇕
  THEORETICAL CALCULATIONS

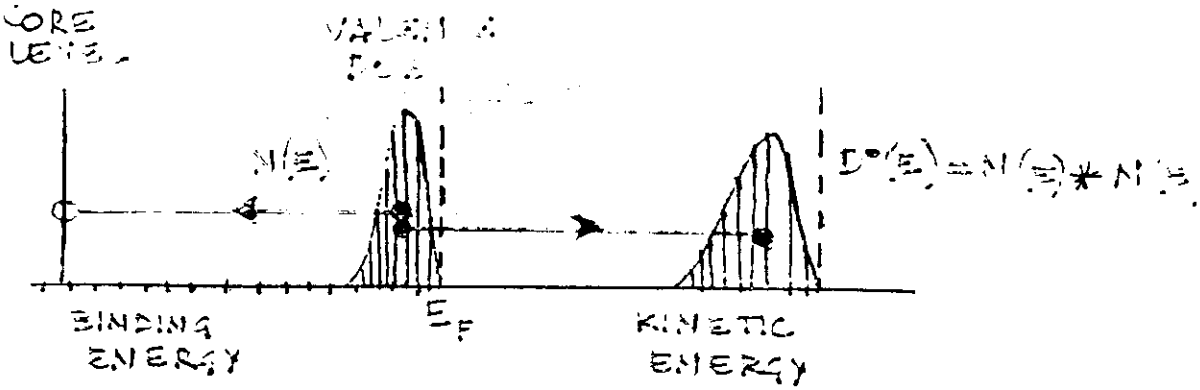

$$I(E) = D^\circ(E) = N(E) * N(E)$$

$$N(E) = N_{\ell'}(E) + N_{\ell''}(E)$$

$$\tilde{N}(E) = \alpha N_{\ell'}(E) + N_{\ell''}(E)$$ WEIGHTED DOS

$$\tilde{I}(E) = \tilde{N}(E) * \tilde{N}(E)$$ SELF-CONVOLUTED TRANSITION DOS

CORE-VALENCE-VALENCE (CVV) AUGER TRANSITIONS IN A PURE BAND-LIKE SCHEME

III-V's $\equiv$ (SP) MATERIALS

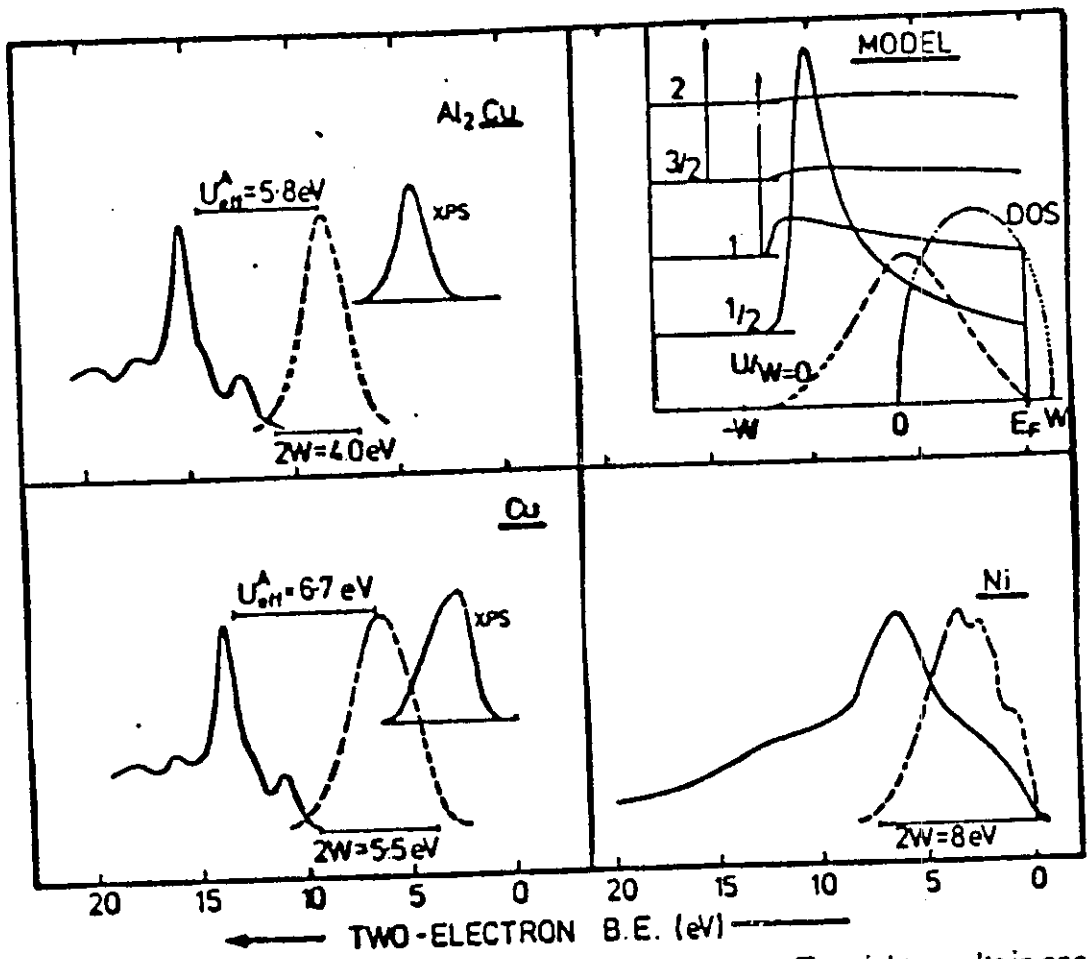

Fig. 9. Illustration of the effect of $U^{A}_{eff}/2W$ on LVV Auger spectra. Top right: results in one band model[124] showing how increasing the Coulomb repulsion first distorts the band and then causes a split-off state to occur. Experimental examples for the multiband case with Cu, Al_2Cu, and Ni are given;[82] (——) AES result, (– – –) self convoluted XPS d-bands for Al_2Cu and Cu and theoretical self convoluted density of occupied states for Ni (from Liebsch[134]). XPS bands of Ni may contain two hole effects[143] and are not given. Note that U^{A}_{eff} should be measured to the centre of gravity of the Auger bands.

CORE-VALENCE-VALENCE AES

SELF-FOLDED VALENCE DENSITY OF STATES

EXPERIMENTAL LINESHAPES

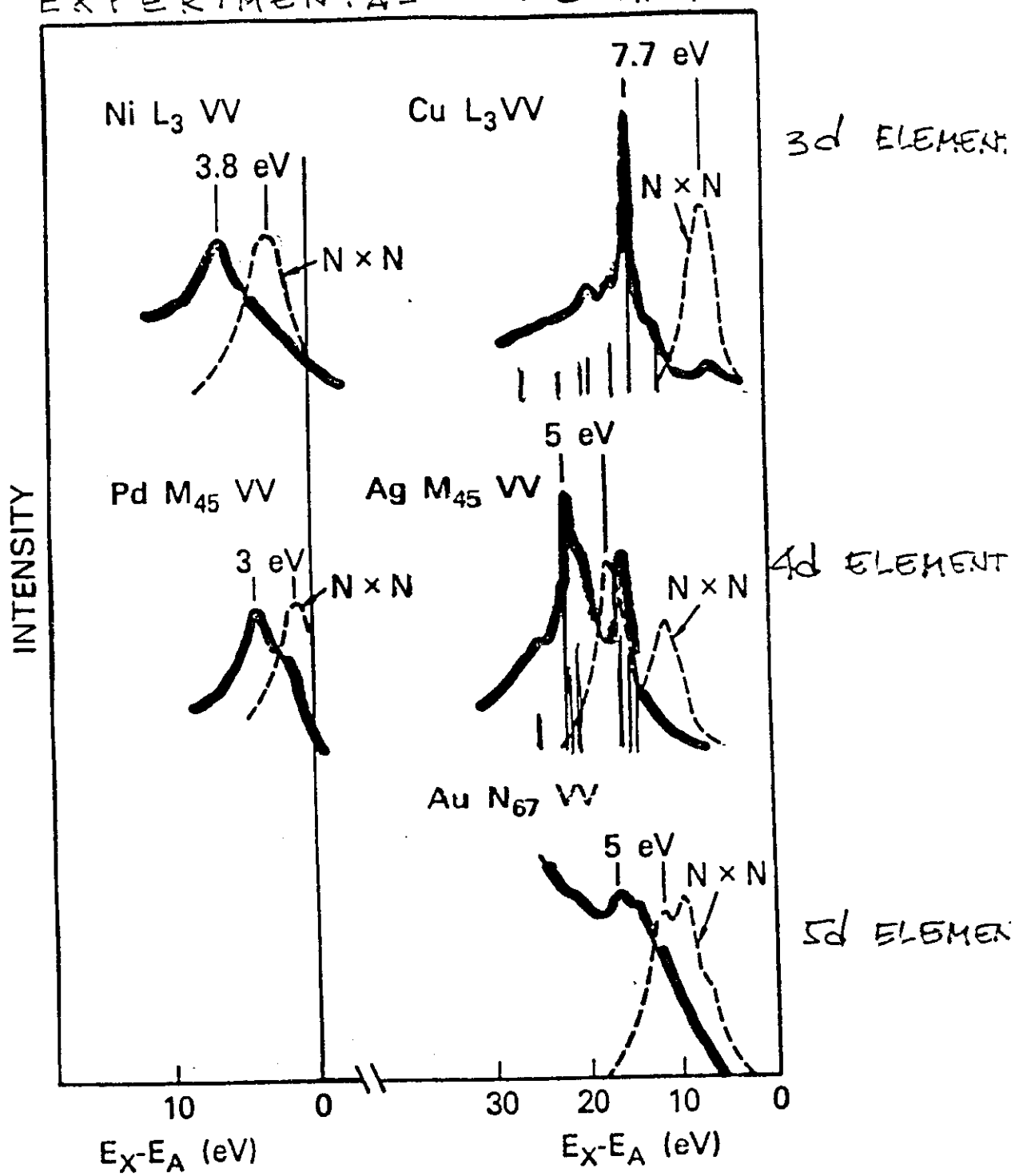

FIGURE 10. Comparison of the CVV Auger line shapes for the transitional metals as indicated in Figure 9 with the fold of the one-electron DOS. The vertical bars from Cu and Ag indicate results from an atomic calculation. E_x is the core-binding energy and E_a the Auger electron kinetic energy. (From Ramaker, D. E., *Chemistry and Physics of Solid Surfaces IV*, Vanselow, R. and Howe, R., Eds., Springer-Verlag, Berlin, 1982, 19. With permission.)

BAND WIDTH (Γ_{nd})

versus

HOLE-HOLE REPULSION ENERGY ($U^e_{nd\,nd}$)

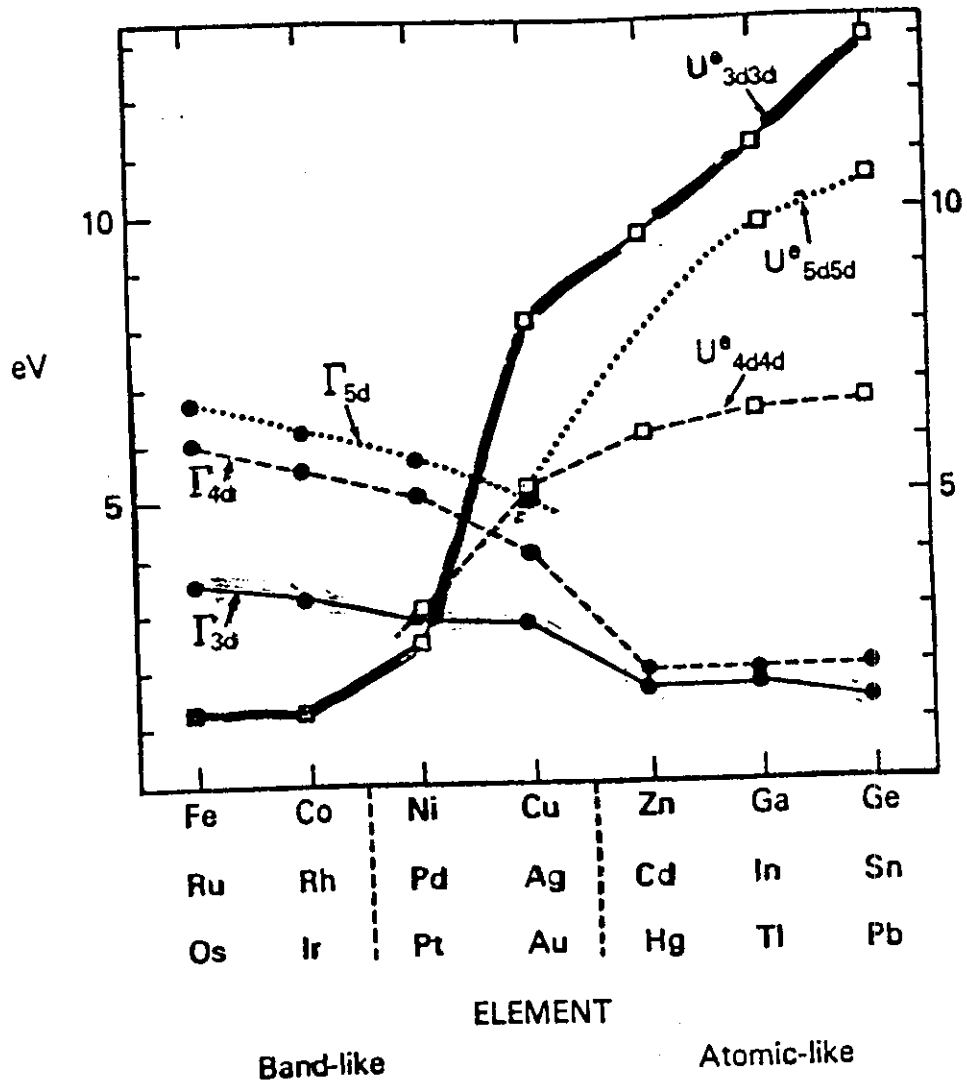

FIGURE 9. Comparison of the bandwidth (Γ_{nd}) with the effective hole–hole repulsion ($U^e_{nd\,nd}$) of the metals with electron configuration d^8s^2 to $d^{10}s^2p^{2.94}$ Metals with bandlike and atomiclike line shapes are indicated; those between the dashed lines are transitional. (From Ramaker, D. E., *Chemistry and Physics of Solid Surfaces IV*, Vanselow, R. and Howe, R., Eds., Springer-Verlag, Berlin, 1982, 19. With permission.)

$U \ll \Gamma$ BAND-LIKE

$U \gg \Gamma$ ATOMIC-LIKE

CARBON-BASED SYSTEMS

SELF-FOLDED DENSITY OF STATES
versus
C KVV AUGER EXPERIMENTAL PROFILES

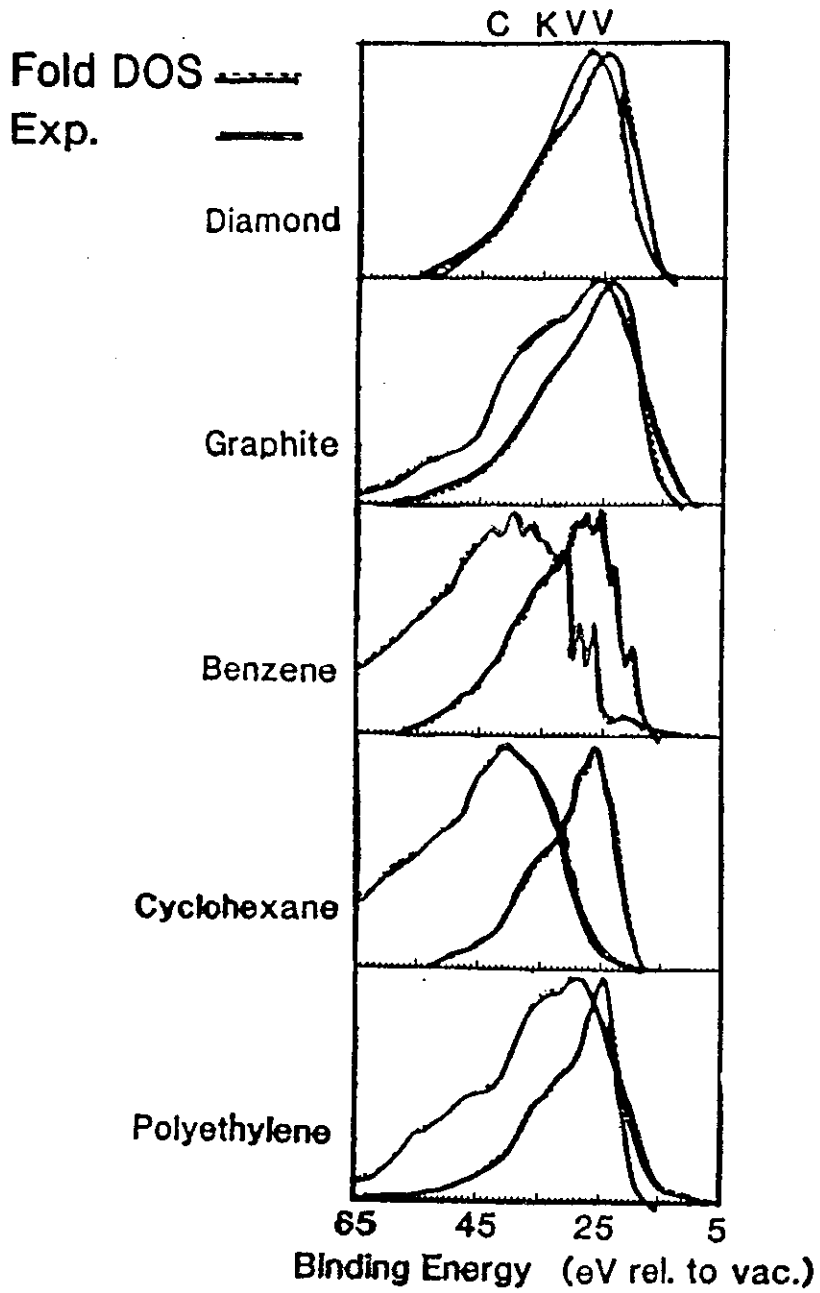

FIGURE 6. Comparison of the experimental C KVV Auger line shapes (solid line) obtained from the literature for diamond,[75] graphite,[67] benzene,[77] cyclohexane,[53] and polyethylene[78] with the self-fold of the DOS (dotted line) obtained as described in the text. (From Ramaker, D. E., *Applic. Surf. Sci.*, 21, 1, 1985. With permission.)

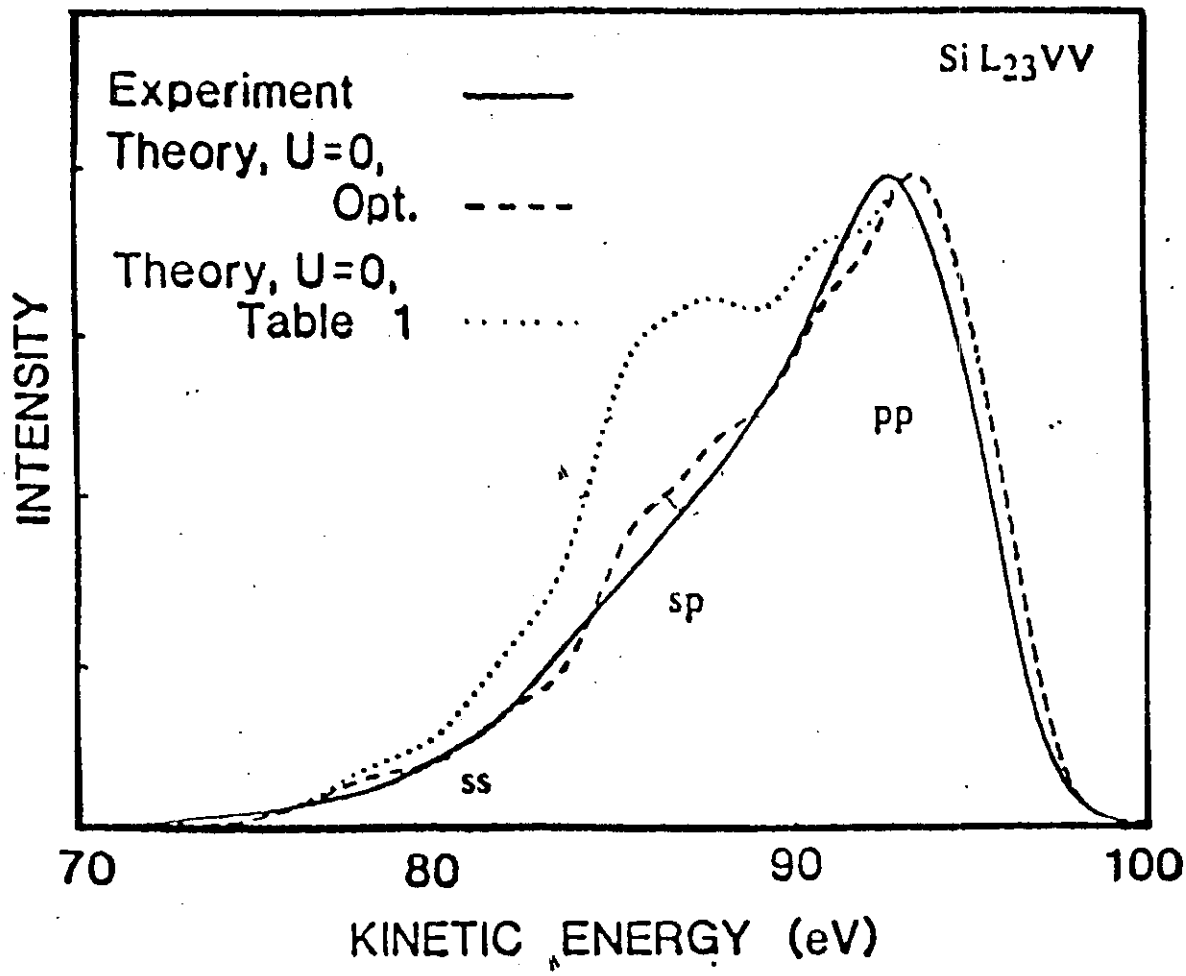
Si $L_{23}VV$
Experiment
Theory, U=0, Opt.
Theory, U=0, Table 1
INTENSITY
pp
sp
ss
70
80
90
100
KINETIC ENERGY (eV)

Fig. 16

CORE - VALENCE - VALENCE

BAND - LIKE SPECTRUM

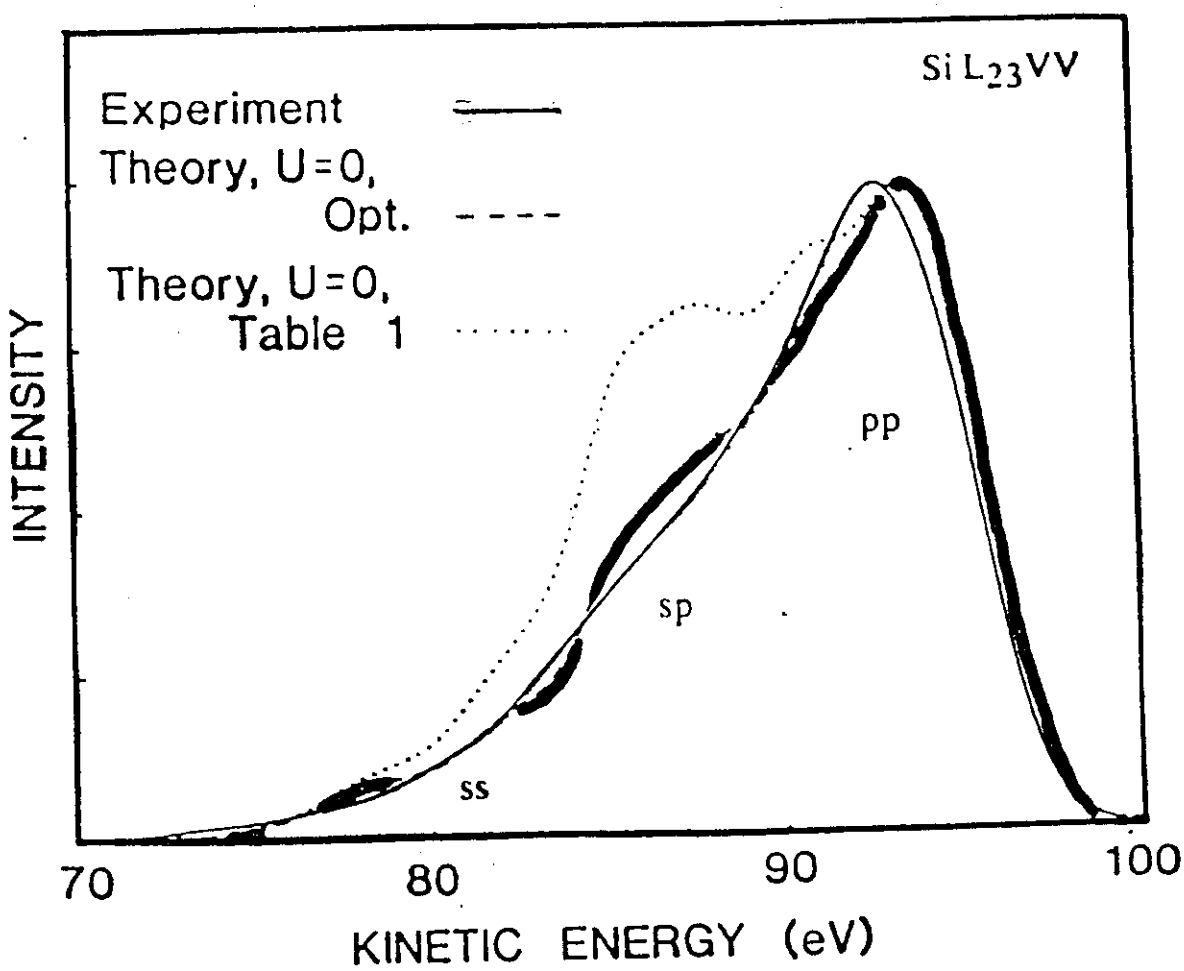

FIGURE 15. Comparison of the experimental Si $L_{23}VV$ Auger line shape for elemental Si with the theoretical line shape obtained by utilizing optimal matrix elements (dashed line) and with the matrix elements predicted from Figure 8 (dotted line) (both sets of matrix elements are given in Table 1). The theoretical fits were obtained with U = 0 in Equation 6.[80] (From Almbladh, C. O. and Morales, A. L., *Phys. Rev.*, B39, 3503, 1989. With permission.)

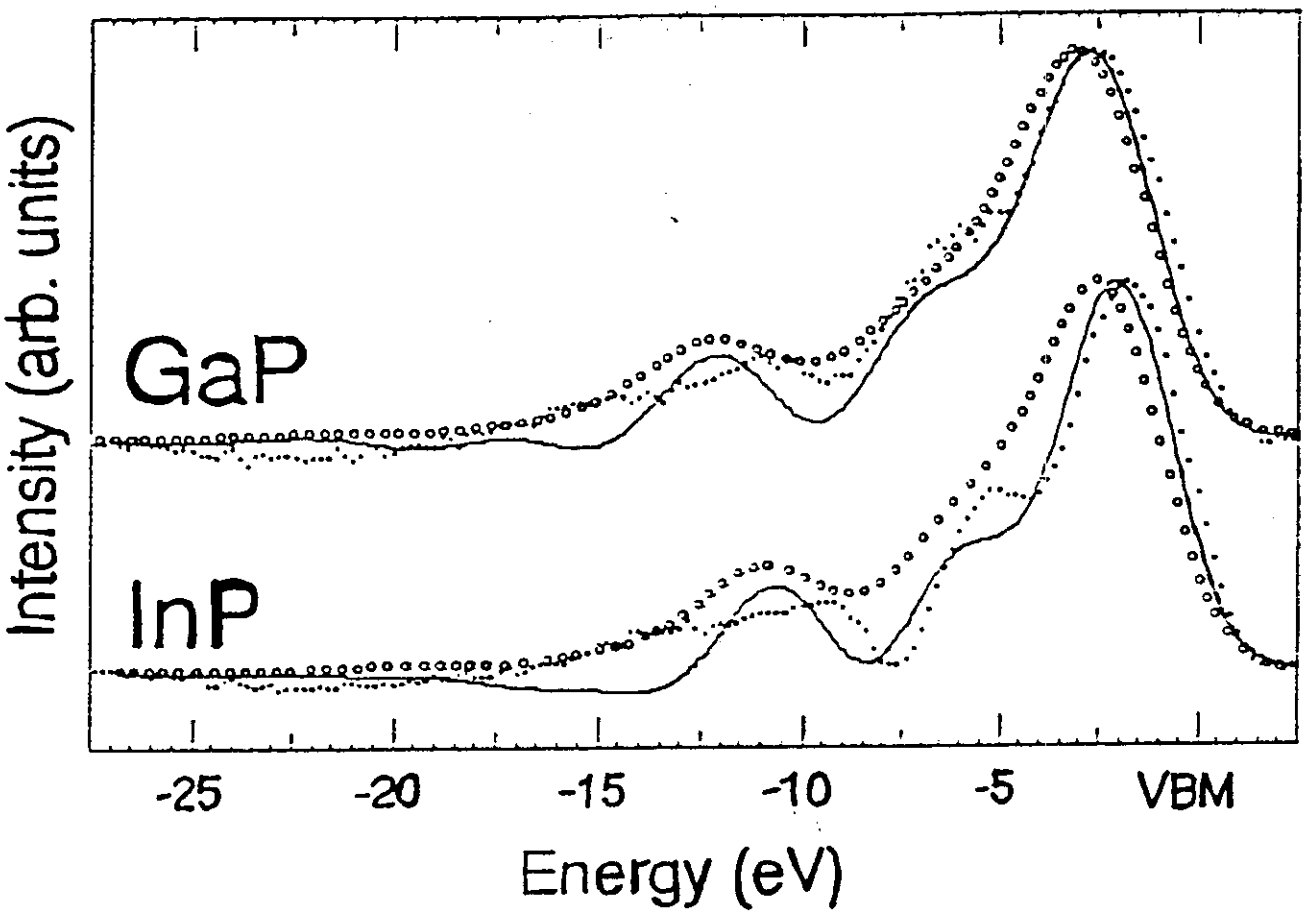

..... EXPERIMENTAL DIFFERENCE CURVE [CLEAVED] − [Sb]

ooooo 1st LAYER SELF-CONVOLUTED TRANSITION DOS

——— THEORETICAL DIFFERENCE CURVE [CLEAN] − [Sb]

SURFACE VALENCE BAND STATES

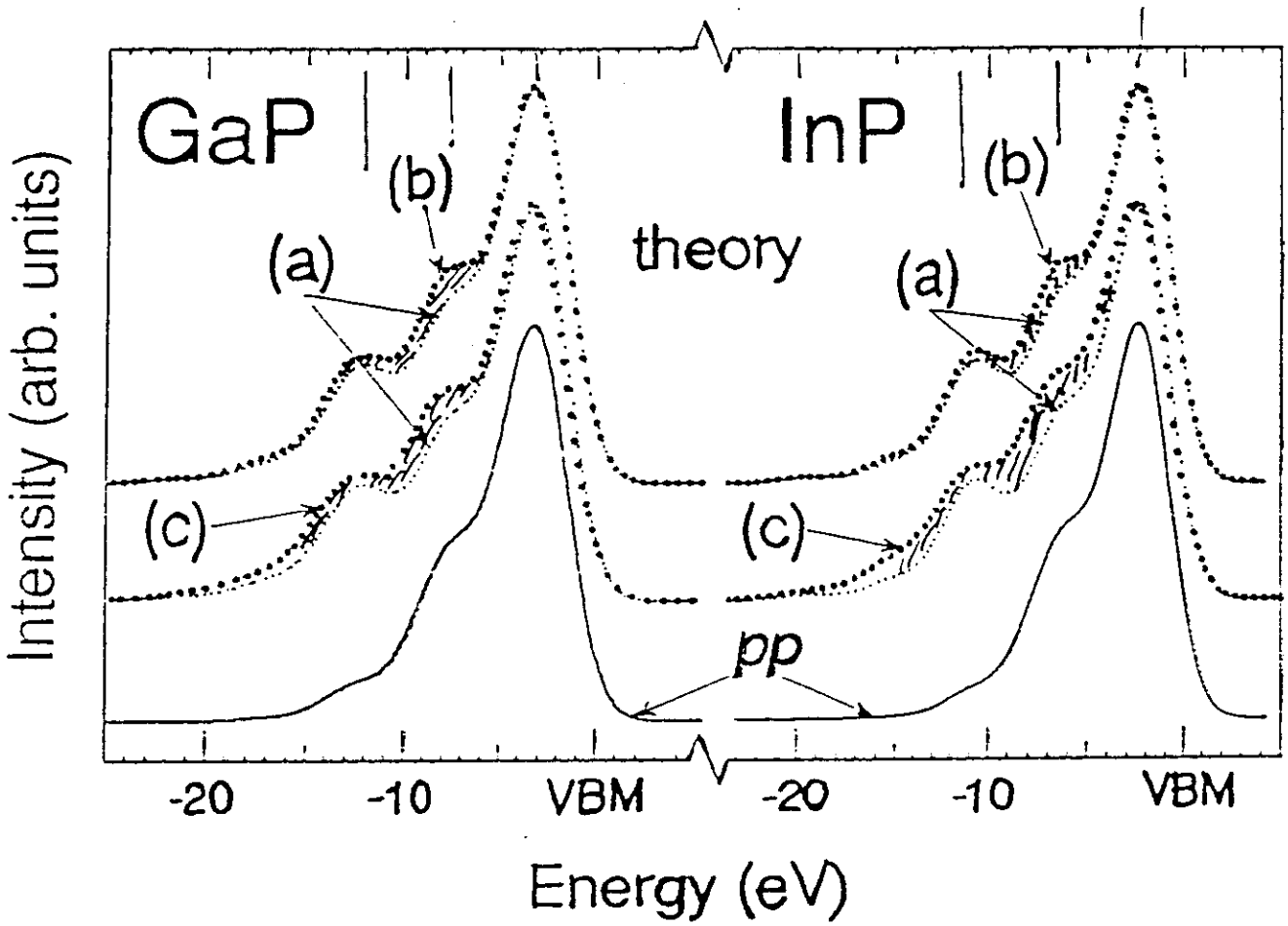

(a) [TOTAL SELF-FOLDED III-V SLAB]

(b) [TOTAL] - [1st SLAB]

(c) [TOTAL] III-V (1x1) SB

THEORY

P $L_{2,3}$ VV

OCCUPIED STATES PROJECTED ONTO Si SITES

Si-$L_{2,3}$VV AUGER LINESHAPE SPECTROSCOPY

EXPERIMENT vs THEORY

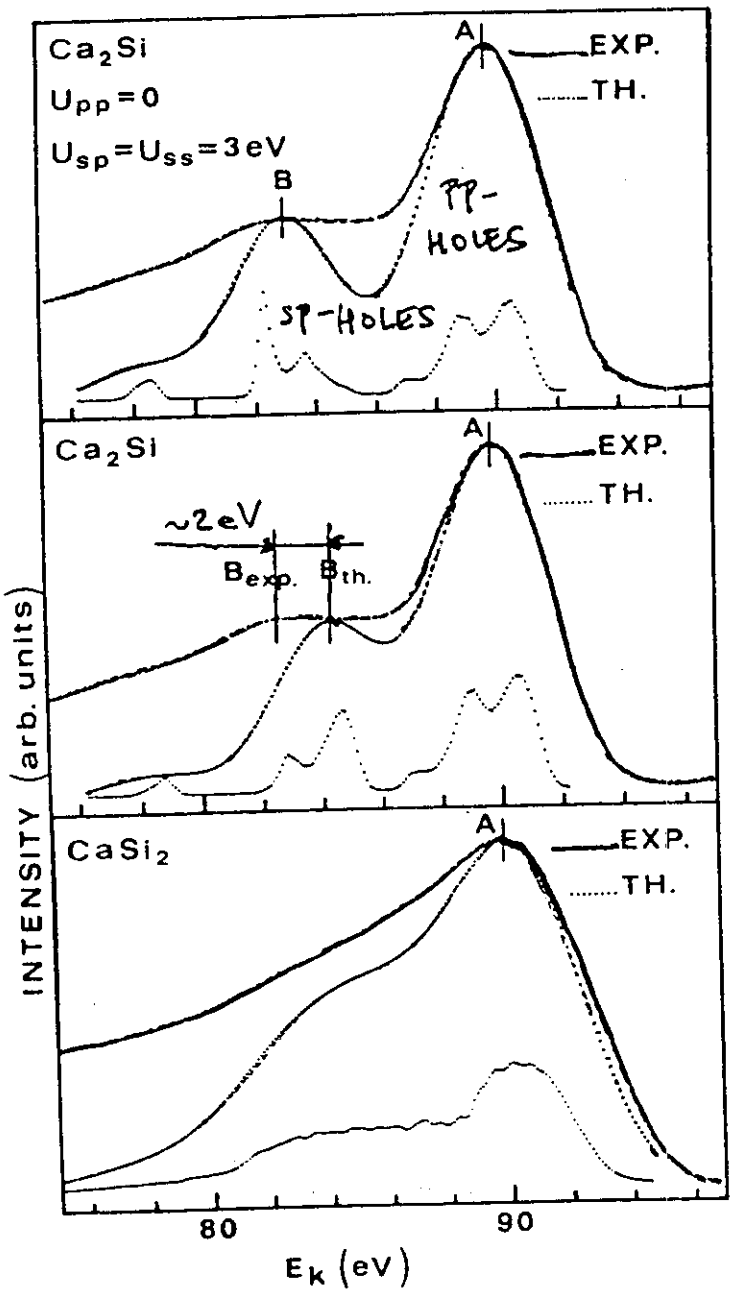

M. SANCROTTI & al PHYS REV B37 (1988) 4805
RAPID COMMUN

$U_{ll'}$ ON-SITE TWO-HOLE CORRELATION ENERGY

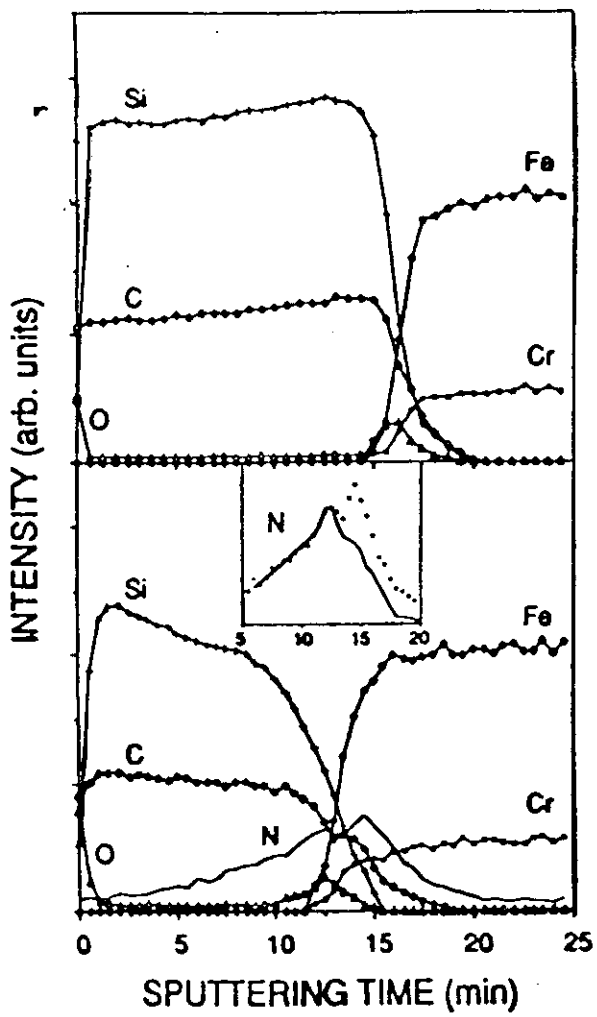

FIG. 10. Auger peak-to-peak heights, in derivative spectra, plotted as a function of sputtering time: (a) upper panel: as-deposited a-SiC film on steel substrate; (b) lower panel: N-implanted (1×10^{17} ions/cm^2) SiC/steel sample. The inset shows the N depth distribution, across the interface, plotted in two different ways; dotted curve: N peak-to-peak height in the derivative Auger spectrum; continuous line: N peak height in the Auger integral spectrum.

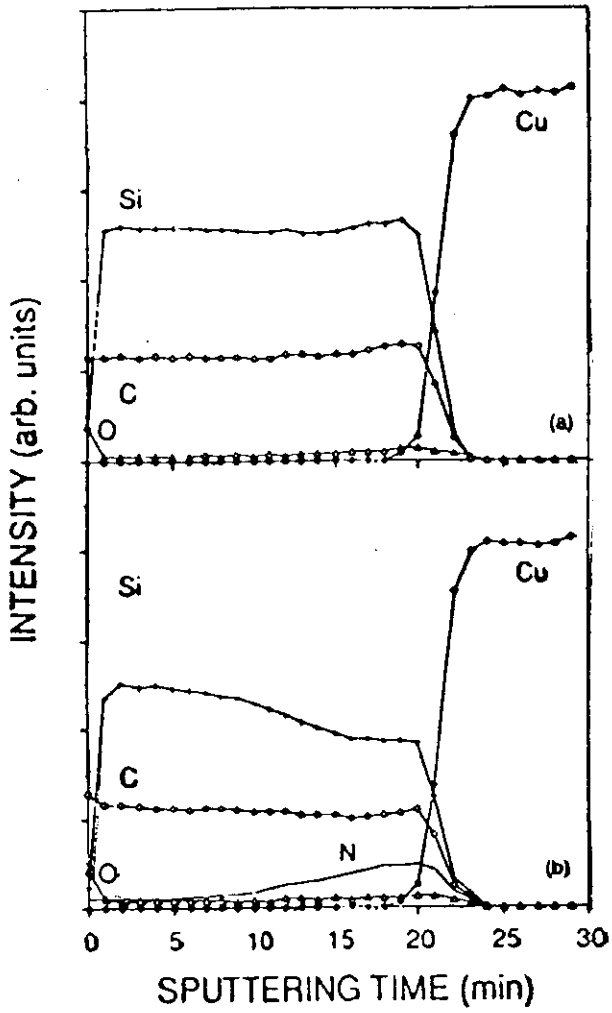

FIG. 11. Auger peak-to-peak heights, in derivative Auger spectra, plotted as a function of sputtering time: (a) upper panel: as-deposited a-SiC film on Cu substrate; (b) lower panel: N-implanted (1×10^{17} ions/cm^2) a-SiC/Cu bilayer.

SiC FILMS ON

STAINLESS STEEL & Cu

NITROGEN IMPLANTATION EFFECTS

N. LAIDANI, A. MIOTELLO, L. GUZMAN,
S. TOCCIO, & L. CALLIARI
J. APPL. PHYS. 76. (1994) 285

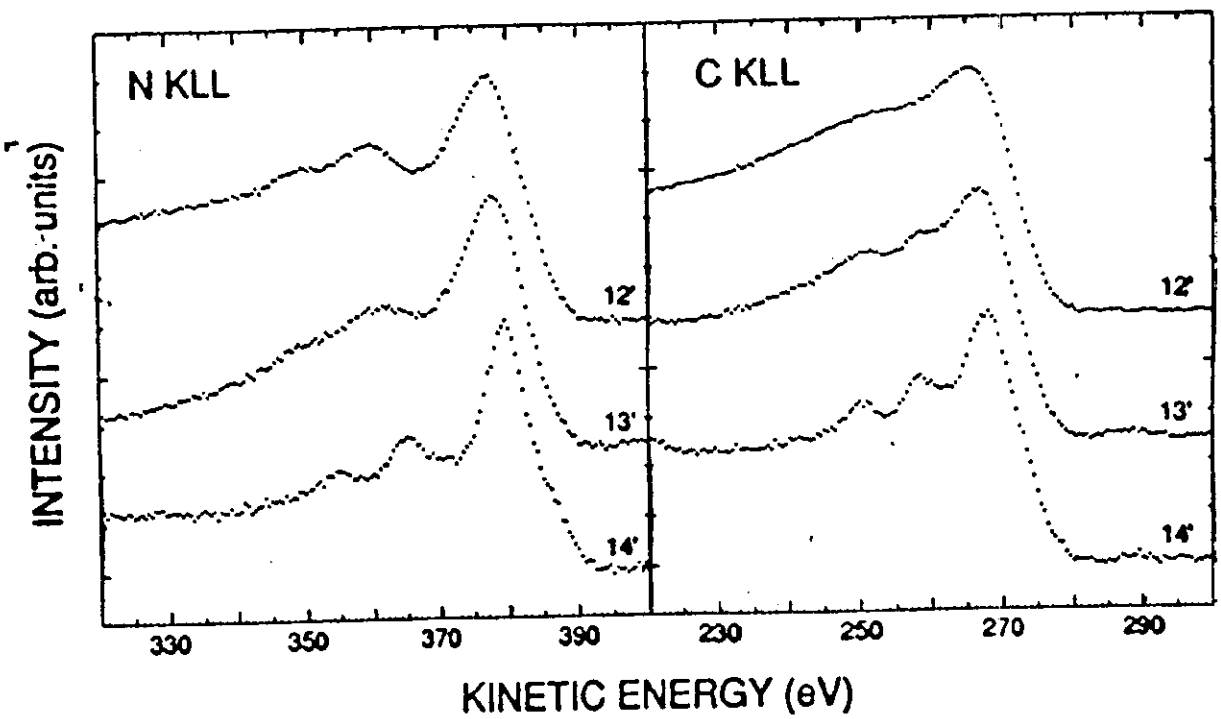

FIG. 12. N *KLL* and C *KLL* Auger integral spectra at three selected points across the *a*-SiC/steel interfaces after 1×10^{17} N^+/cm^2 implantation.

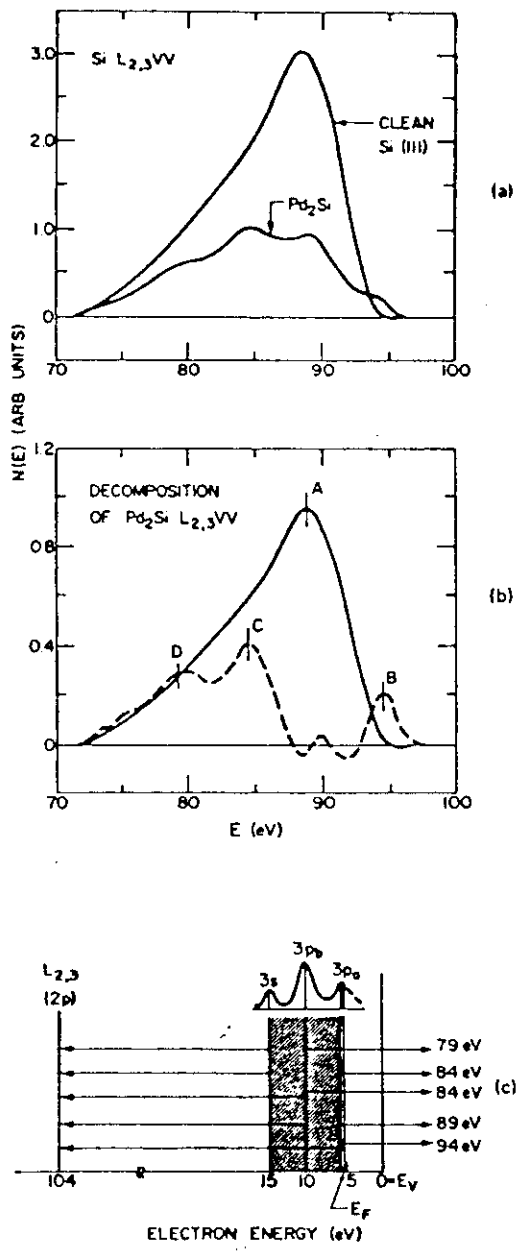

FIG. 2. (a) Comparison of the $L_{2,3}VV$ Auger spectra observed on Pd_2Si and Si (111) surfaces. (b) Decomposition of the Auger spectra into two portions with the solid-line portion proportional to the elemental peak and the dashed-line portion showing the change as a result of silicide formation. (c) Schematics of the Auger transitions for Si $L_{2,3}VV$ in Pd_2Si according to calculated state densities.

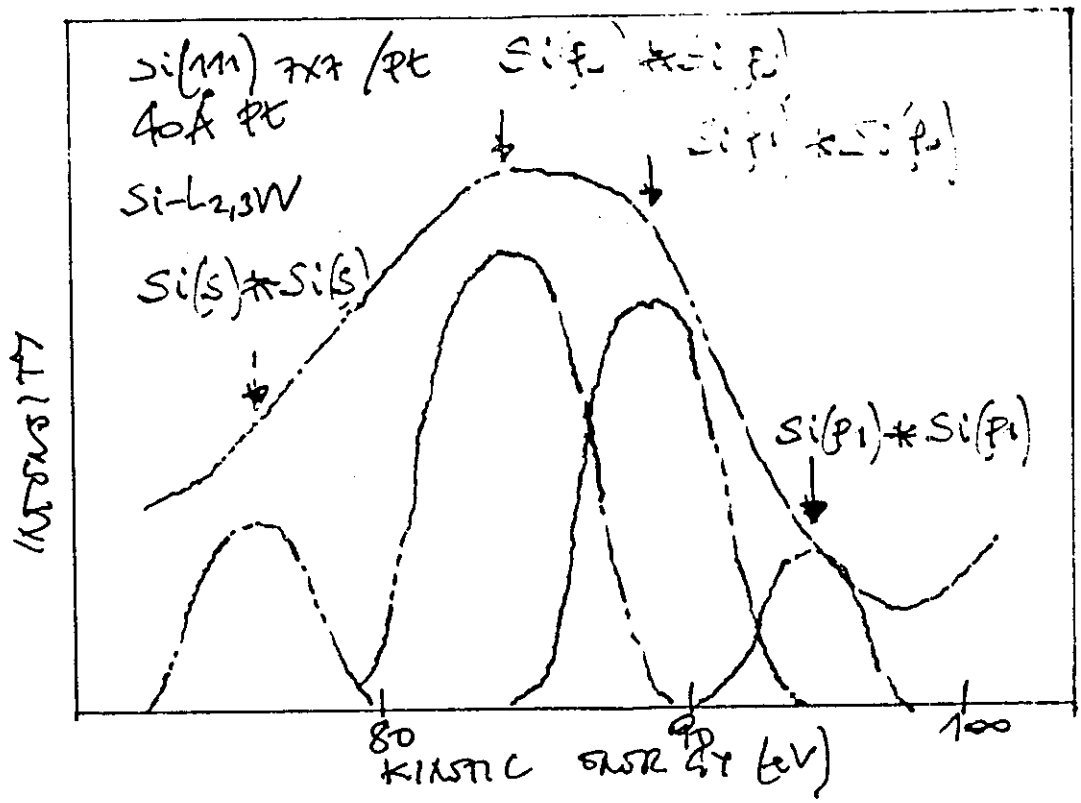

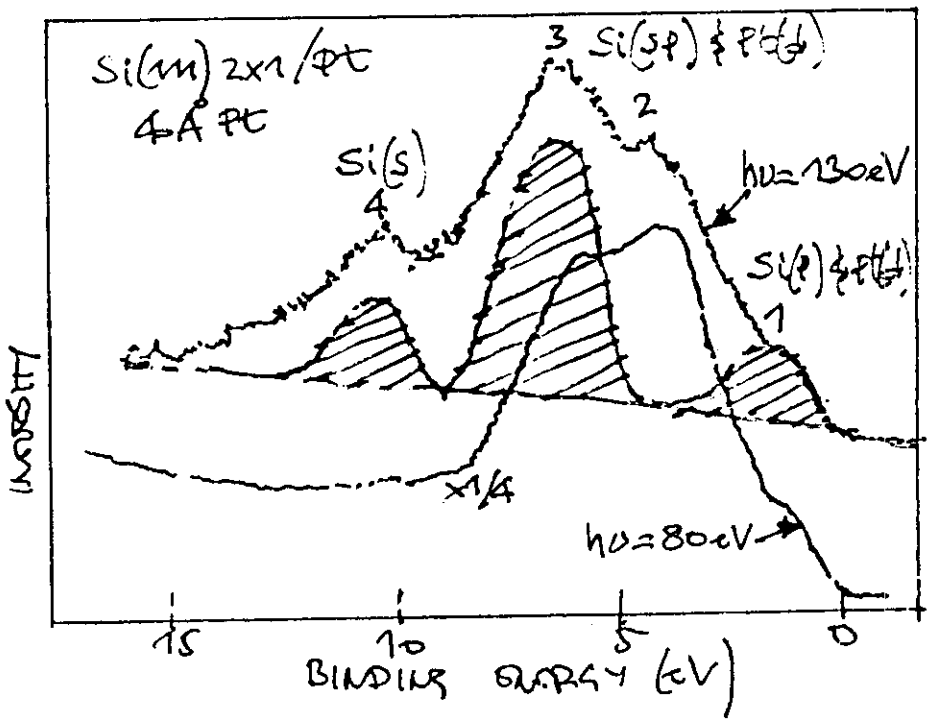

FROM P. MORGEN & al
SURFACE SCIENCE (1987)

Si $L_{2,3}VV$

IN METAL SILICIDES

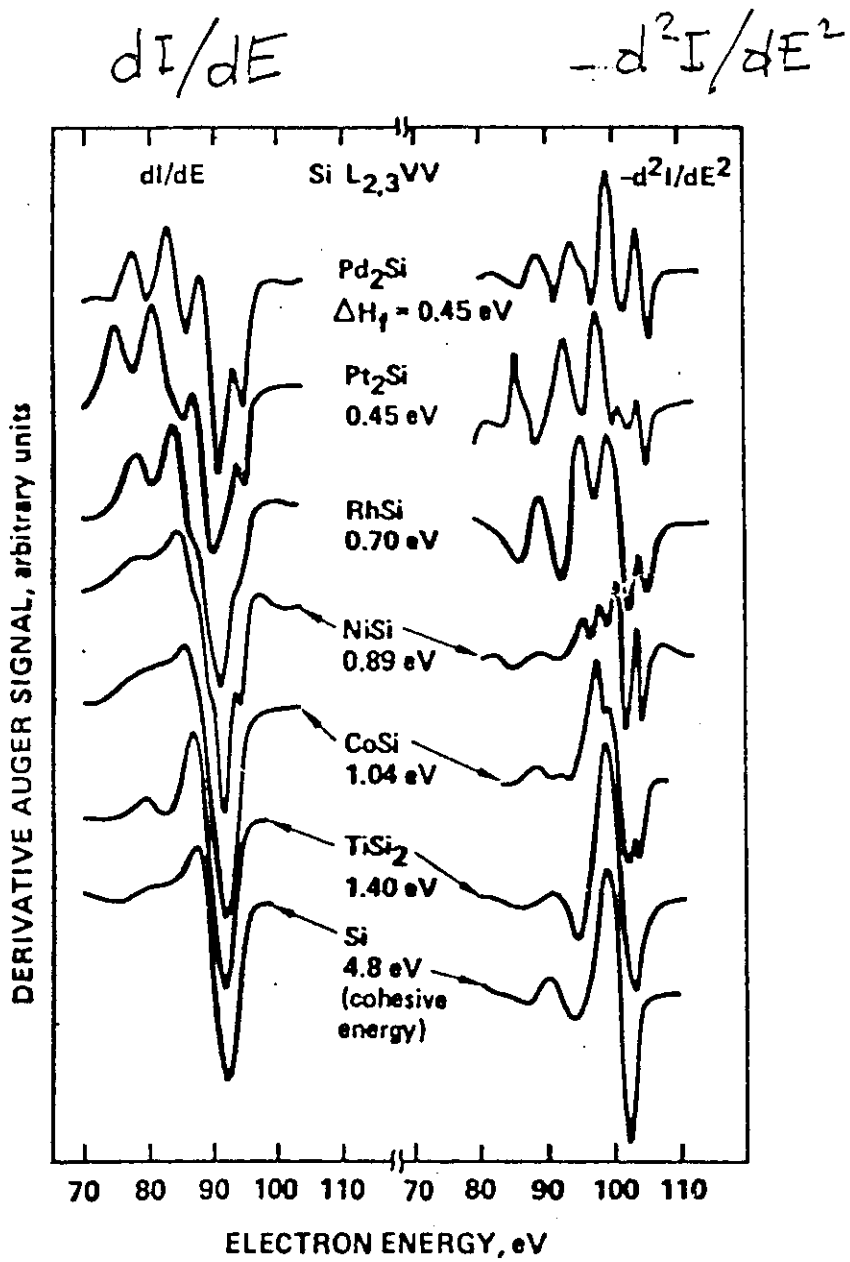

FIG. 3. First- and second-derivative Si *LVV* Auger spectra of several silicides. Scale factors of the individual curves were adjusted to produce similar overall peak amplitudes in the plotted spectra. The silicide enthalpies of formation ΔH_f expressed per metal atom per formula unit are also indicated.

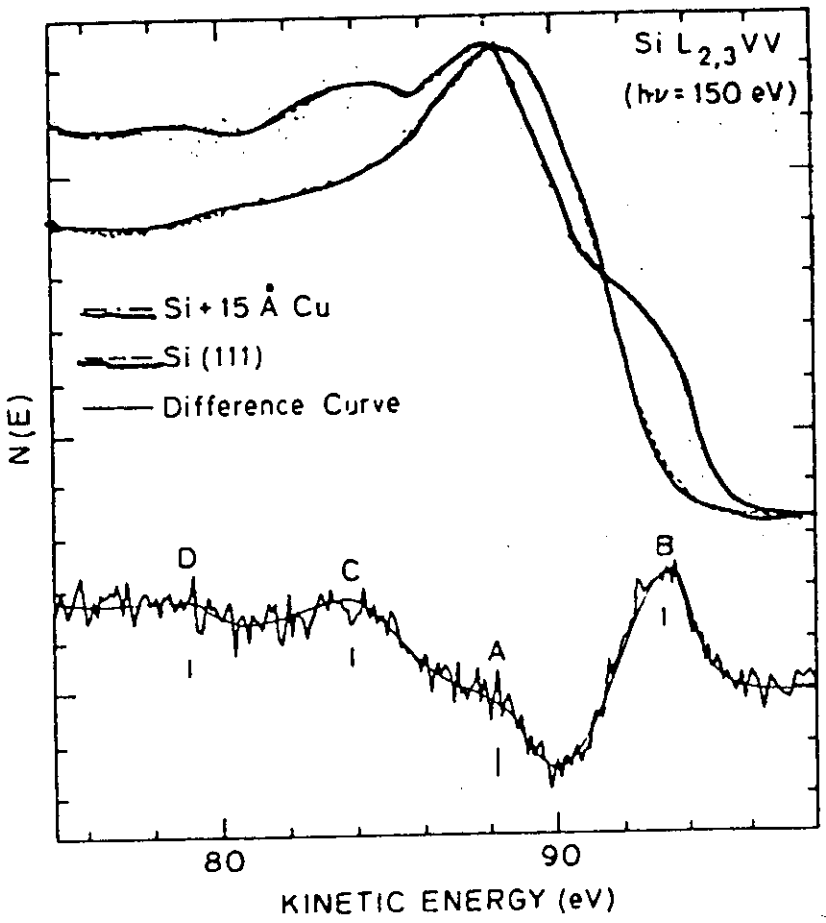

IG. 2. Si $L_{2,3}VV$ Auger lineshape for Si + 15 Å Cu (dots) and Si(111) ashed line) obtained with $h\nu = 150$ eV. The bottom curve (solid) is the fference curve and shows the position of the new peaks (see the text).

OCCUPIED STATES PROBED LOCAL TO THE Si SITES VIA Si $L_{2,3}VV$ AUGER LINE-SHAPE SPECTROSCOPY SHOW A DISTRIBUTION TYPICAL OF (LATED) NEAR-NOBLE METAL SILICIDES AT THE Cu/Si(111) INTERFACE

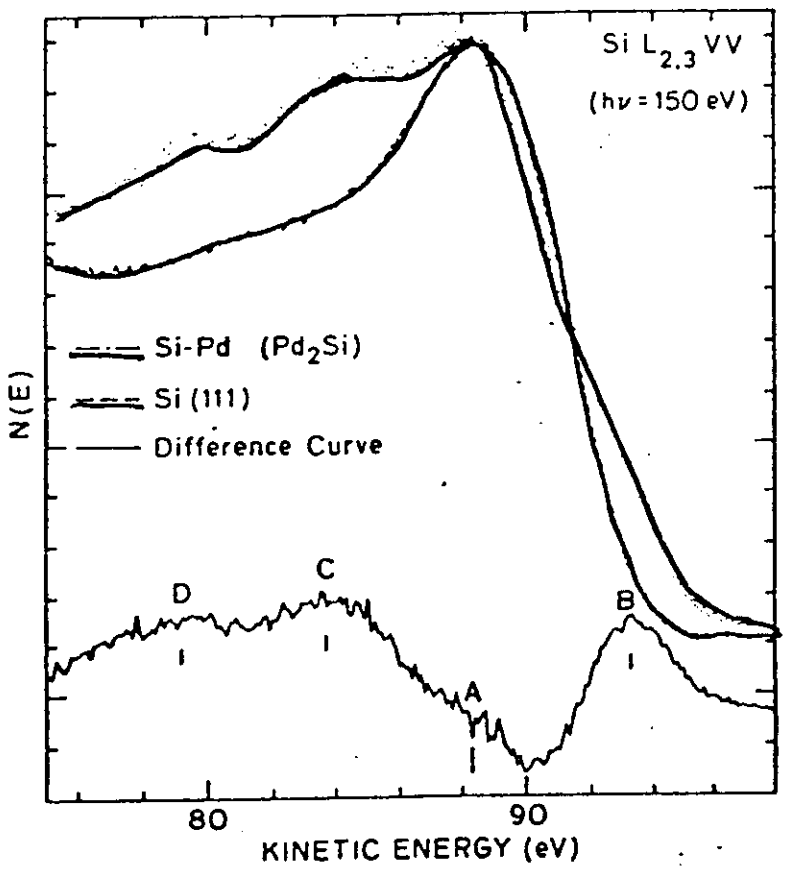

FIG. 2. Si $L_{2,3}VV$ line shapes [$N(E)$] for Si-Pd (Pd_2Si) (dots),

G. ROSSI & I. LINDA PR B 28 (1983) 3589

VALENCE BAND & Si 2p PHOTOEMISSION SPECTROSCOPY

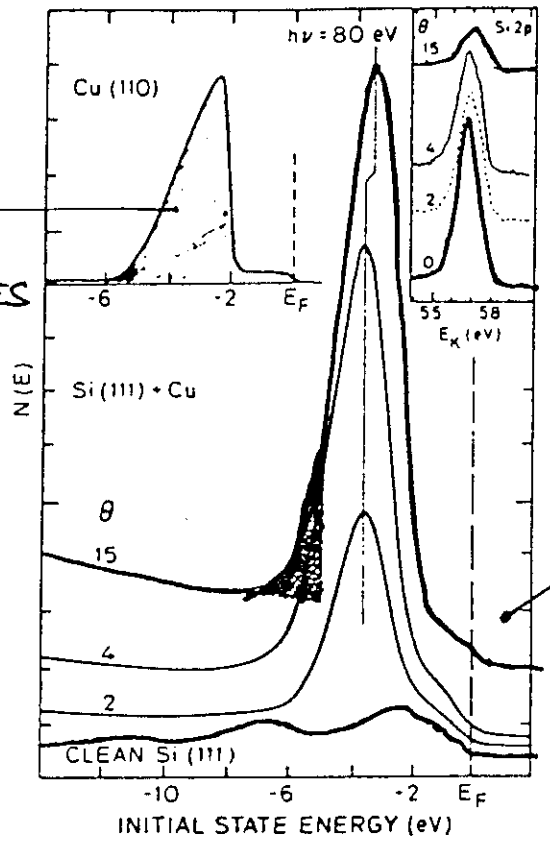

MOSTLY Cu 3d STATES

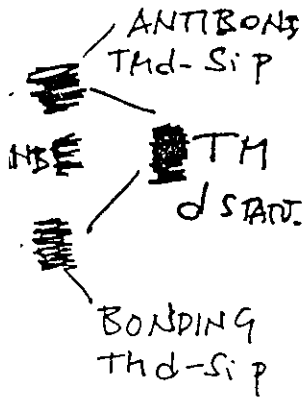

Cu 3d ANTIBONDING STATES ?

FIG. 1. Angle-integrated photoelectron energy distribution curves for Cu(110), Si(111), and Si(111) + Cu as obtained with $h\nu = 80$ eV, and for Si 2p core lines obtained with $h\nu = 160$ eV. The shaded areas correspond to the BE signal between -5 and -6 eV below E_F. Coverages θ are given in Å.

MOSTLY Cu 3d - DERIVED STATES IN BONDING CONFIGURATION WITH Si 3(sp) STATES

G. ROSSI & I. LINDAU PR B 28 (1983) 3597

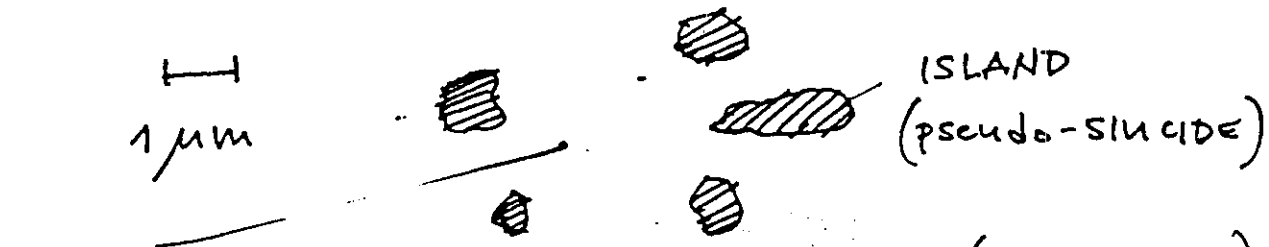

SPATIALLY RESOLVED (~ 200 nm)

pseudo-5x5 Si $L_{2,3}VV$ AUGER LINE-SHAPE

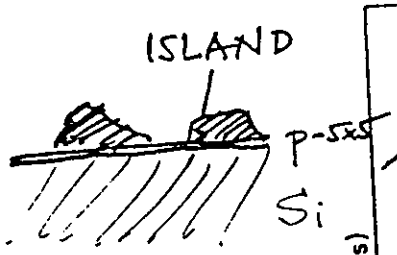

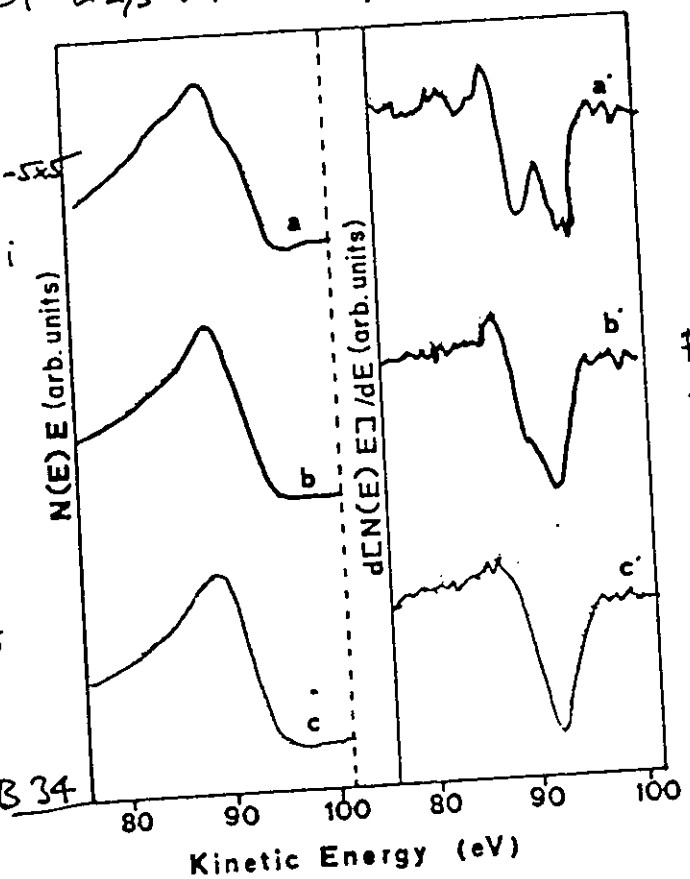

ISLAND

FLAT REGION

FLAT REGION AFTER SOFT SPUTTERING

CALLIARI, MARCHETTI & SANCROTTI PHYS REV B34 (1986) 521

FIG. 4. Spatially resolved Si $L_{2,3}VV$ line shape in the integral form from different sites of a thermally agglomerated Si + 40 ML Cu sample: island, *a*; flat region, *b*; and flat region after a mild sputtering step, *c*. In the right column, the corresponding differentiated curves *a'*, *b'*, and *c'* are shown.

Si (111) 2x1 + +40 ML Cu + ANNEALING @ 450°

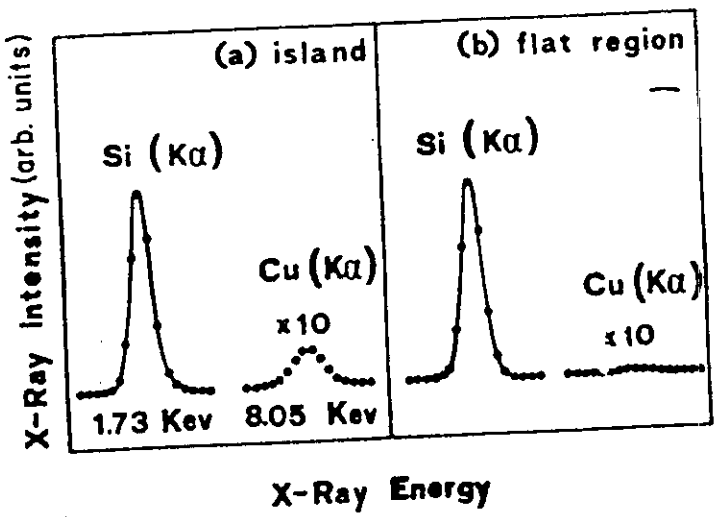

FIG. 6. Characteristic x-ray emission spectra (acquired with an energy-dispersive spectrometer) from an island and a flat re- ... Si + 40 ML Cu sample.

Wire S2 (NiZn/ZnCo) after vulcanization and humidity/temperature ageing

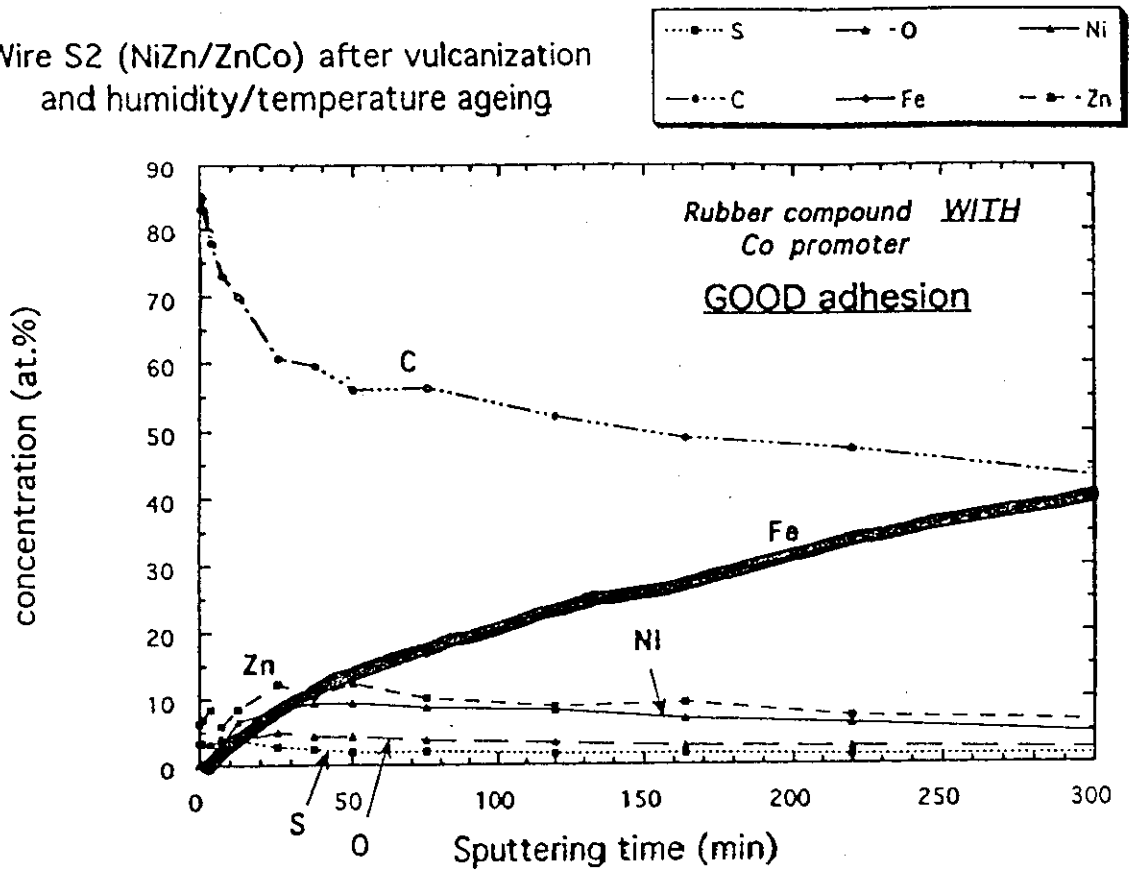

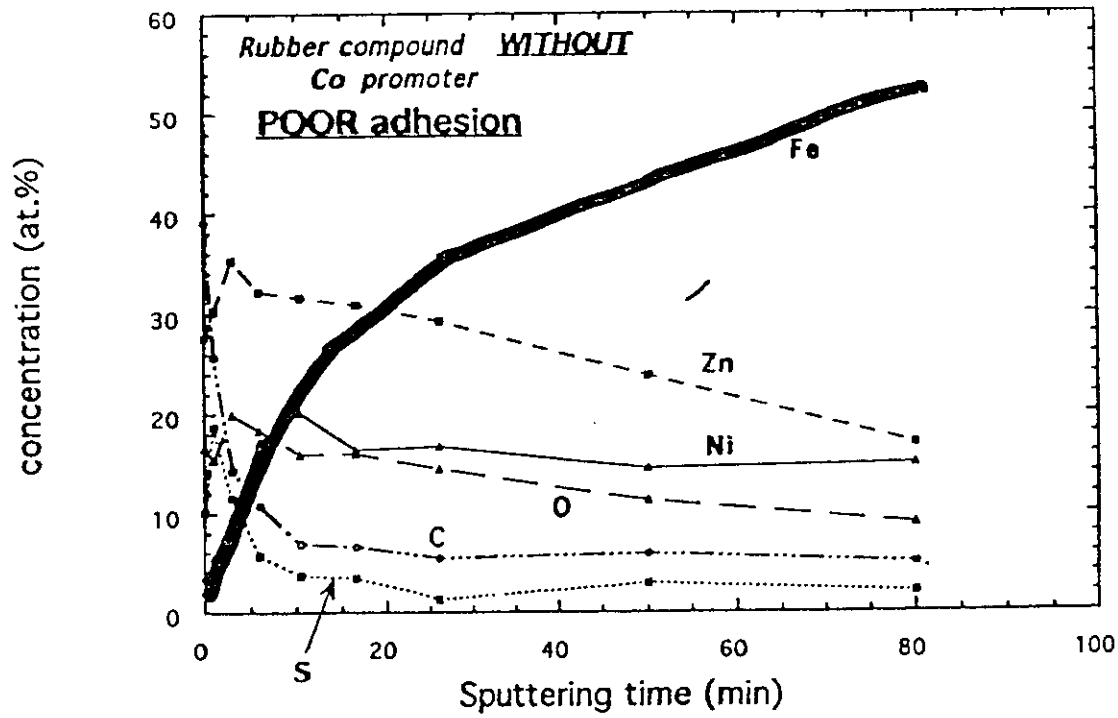

J. Kovač, private Comm.